Effects of Palladium Thin Films on the Hydrogen Permeability of Pd-Cu Alloy Membranes

by

Naser Azzat Al-Mufachi

A thesis submitted to The University of Birmingham for the degree of

DOCTOR OF PHILOSOPHY WITH INTEGRATED STUDIES IN HYDROGEN, FUEL CELLS AND THEIR APPLICATIONS

School of Chemical Engineering

College of Engineering and Physical Sciences

University of Birmingham

April 2015

Surat Al-Fatihah

In the name of God, the infinitely Compassionate and Merciful.

Praise be to God, Lord of all the worlds.

The Compassionate, the Merciful. Ruler on the Day of Reckoning.

You alone do we worship, and You alone do we ask for help.

Guide us on the straight path,

the path of those who have received your grace;

not the path of those who have brought down wrath, nor of those who wander astray.

Amen.

It was a dark and lonely road,

Longest journey ahead,

Over again mistakes were made,

Verily my heart was in dismay,

Encouragement came in the form of an angel,

Enlightenment,

Made of magnificence,

Made me want again,

Away went my plight.

Abstract

The hydrogen permeability of surface modified $Pd_{60}Cu_{40}$ wt% ($Pd_{47.3}Cu_{52.7}$ at%) membranes have been determined for the first time. Surface modification was accomplished through the deposition of Pd thin films of three different thicknesses (95.5 ± 0.1, 797.4 ± 0.2 and $1{,}409.6 \pm 0.2$ nm) on to one side of a range of as-received $Pd_{60}Cu_{40}$ wt% membranes via magnetron sputtering. The $Pd_{60}Cu_{40}$ wt% membrane coated with a $1{,}409.6 \pm 0.2$ nm thick Pd thin film positioned on the feed side (445 kPa of hydrogen pressure) and cycled between 50 and 450 °C achieved the highest hydrogen permeability of 1.09×10^{-8} mol m^{-1} s^{-1} $Pa^{-0.5}$ at 450 °C during the third cycle. This is a 58% increase on the value measured for the as-received $Pd_{60}Cu_{40}$ wt% under the same conditions.

This improvement can be attributed to a Pd-rich Pd-Cu face centred cubic (FCC) phase forming through interdiffusion between the Pd thin film and bulk Pd-Cu membrane as a result of the test conditions used during hydrogen permeability measurements. This introduces a larger hydrogen concentration gradient across the membrane due to the relatively high hydrogen solubility of the Pd-rich Pd-Cu FCC phase resulting in the observed increase in permeability. A hydrogen pressure of 445 kPa produced an increase in interdiffusion rate compared with 100 kPa of pressure. This is related to a higher hydrogen pressure introducing a larger number of vacancy-hydrogen clusters resulting in increased atomic mobility.

The $Pd_{60}Cu_{40}$ wt% membranes coated with a 797.4 ± 0.2 and $1{,}409.6 \pm 0.2$ nm thick Pd thin films retained an almost pure Pd surface throughout cycling between 50 and 450 °C with a feed and permeate hydrogen pressure of 445 and 100 kPa, respectively. For the deposition technique and test conditions used throughout this work, these surface modified membranes appear to stabilise the Pd thin films upon cycling across the critical temperature of 295 °C.

Dedication

Four years ago the civil war in my country began. I humbly dedicate my PhD to the fallen innocent men, women and children of Syria. I also dedicate my work to the innocent lives lost in Gaza and Palestine. It may seem that the world has forgotten you. I haven't.

I have further dedicated my PhD to the memory of my late co-supervisor Dr Waldemar Bujalski. A true inspiration. Gone but never forgotten.

اشتقت لك محمد.

Acknowledgements

First and foremost, I would like to say thank you to Allah for giving me the chance to explore his creations. It has truly been an honour.

I credit my big sister Jeehan Al-Mufachi for my passion of science. She was the first to introduce me to the periodic table, the first element was hydrogen. My uncle Mohammad Raficq Kurimbokus is the reason I am here, he talked me into it and to him I am grateful.

I would like to thank and express my gratitude towards Dr John Speight, Prof. David Book and Dr Waldemar Bujalski for their guidance throughout the duration of my research. Special thanks to Prof. Robert Steinberger-Wilckens and Dr Neil Rees for coming on board last minute, their help and support will always be appreciated.

Many thanks go to the Hydrogen Materials Group and the DTC students for their helpful support throughout the years.

Thank you to NEXUS nanoLab for all of their help and support.

Thanks to Dr Anwar Sattar, a great friend. Also thank you to Rayan Ameen and Dilveen Mohammed for their much needed help and friendship.

Special thanks to Emma, a great woman. Her love and support helped to make this happen.

I am also grateful for the financial support of the EPSRC and the DTC. In addition, special thanks to Johnson Matthey Noble Metals for supply of the Pd-Cu foil used in this work

Modules and mini-projects

I began the doctoral training centre (DTC) in Hydrogen, Fuel Cells and their Applications on November 10th 2010. In addition to the PhD element of this course, it was a requirement to achieve 120 module credits and to complete a series of mini-projects.

Modules

The following modules were successfully passed during the course of the DTC:

- Marketing and TQM
- Materials for Energy Generation and Storage
- Materials for Hydrogen and Fuel Cell Technology
- Presentation Skills
- Coniston Team Building Skills
- Project Management
- Business Methods and Industrial Economics
- Materials for Sustainable Environmental Technology
- Measurement Techniques
- Public Engagement
- The Energy System
- Consultancy Skills
- Electrochemistry

Mini-projects

An industrial mini-project was carried out in collaboration with Johnson Matthey Noble Metals to identify the composition of a range of their Pt-Pd alloy samples using X-ray diffraction (XRD). This 18 month project began in March 2011 and concluded November 2012. A series of heat treatments were used to homogenise the alloy samples prior to characterisation. Using XRD, it was possible to determine the lattice parameter of the alloy samples and from this the composition was calculated. Composition of the alloy samples were also determined using density measurements in order to compare with the compositions obtained using XRD. At the end of the project, a report was compiled for Johnson Matthey presenting all of the findings.

I delivered a talk at the Imperial College London monthly DTC meeting in the summer of 2011 as a part of an interdisciplinary mini-project. The talk briefly described my research to an audience of DTC students and also included a tour of the fuel cell labs. In June 2011, I and a team of students setup a stall at the Gloucester Motor Show where we displayed the hydrogen fuel cell microcabs to the general public and engaged in public awareness of hydrogen fuel cell technology.

During January 2012, I and two other colleagues delivered an outreach talk on hydrogen, fuel cells and their applications at Ninestiles Secondary School to a class of GCSE and BTEC students. This involved a PowerPoint presentation with live demonstrations of a portable hydrogen fuel cell.

Publications and events

Publications

- N. A. Al-Mufachi, N. V. Rees, and R. Steinberger-Wilkens. Hydrogen selective membranes: A review of palladium-based dense metal membranes. Renewable and Sustainable Energy Reviews 47 (2015): 540-551. A majority of the literature review chapter for this thesis has been derived from this article.

- N.A. Al-Mufachi, S. Nayebossadri, J.D. Speight, W. Bujalski, R. Steinberger-Wilkens, D. Book. Effects of Pd thin films on the hydrogen permeability of $Pd_{60}Cu_{40}$ wt% alloy membranes. Submitted to the Journal of Membrane Science.

Events

- Talk given at the 10th ISCARW Hydrogen, Regulations Codes and Standards, 24-28th January 2011 in Belfast, Northern Ireland.

- Poster presented at the 7th International Hydrogen and Fuel Cell Conference, 30th March 2011 in Birmingham, UK.

- Poster presented at the International Hydrogen Research Showcase, 13-15th April 2011 in Birmingham, UK.

- Poster presented at the Research Poster Conference, 15th June 2011 in Birmingham, UK.

- Talk and poster presented at the 2nd Annual Hydrogen DTC Conference, 28th September 2011 in Birmingham, UK.

- Talk and poster presented at the 3rd Zing Hydrogen & Fuel Cells Conference, 1-5th December 2011 in Xcaret, Mexico. Won the abstract competition prize which was an all expenses paid trip to attend the conference.

- Poster presented at the 8th International Hydrogen and Fuel Cell Conference, 29th March 2012 in Birmingham, UK.

- Poster presented at the International Symposium on Metal-Hydrogen Systems, 21-26th October 2012 in Kyoto, Japan.

- Poster presented at the 9th International Hydrogen and Fuel Cell Conference, 20-21st March 2013 in Birmingham, UK.

- Talk given at the 4th European PEFC & H_2 Forum, 2-5th July 2013 in Lucerne, Switzerland.

- Poster presented at the European Technical School on Hydrogen and Fuel Cells 23-27th June 2014 in Crete, Greece.

- Poster presented at the International Symposium on Metal-Hydrogen Systems, 20-25th July 2014 in Manchester, UK. Won the highly commended poster prize.

- Poster presented at the International Conference on Hydrogen Storage Embrittlement and Applications, 26-30th October 2014 in Rio de Janeiro, Brazil.

Table of Contents

List of Figures

List of Tables

List of Abbreviations

BCC	Body centred cubic
FCC	Face centred cubic
XRD	X-ray diffraction
VTXRD	Variable temperature X-ray diffraction
SEM	Scanning electron microscopy
EDS	Energy dispersive spectroscopy
XPS	X-ray photoelectron spectroscopy

1. Introduction

1.1. Introduction

Nowadays, fossil fuel reserves are largely situated in politically unstable countries and rival nations. Climate change has been attributed to rise in anthropogenic CO_2 emissions. Allegedly, peak oil has been reached as a result of the earth's diminishing oil reserves. These factors have created a large demand in alternative green renewable energy and have also become the driving force behind the research and development into new technologies. Movement away from the hydrocarbon economy has brought about the advent of the hydrogen economy which aims at establishing a system for distributing and utilising energy derived from hydrogen.

1.2. The hydrogen economy

Hydrogen is not a primary fuel unlike oil, coal and natural gas. However, like electricity it is an energy carrier. Hydrogen is a secondary form of energy that is produced using primary energy sources [1]. Advocates of the Hydrogen Economy recognise that hydrogen can be an environmentally friendlier source of energy for the consumer, especially in the transport sector whereby no harmful pollutants are released into the atmosphere.

The hydrogen economy is a system for delivering energy sourced from hydrogen through the establishment of a modified infrastructure. Moreover, hydrogen production, distribution, utilisation and storage are fundamental to the realisation of this system. Figure 1.1 is the life cycle of hydrogen when sourced from renewable energies. The diagram also demonstrates that hydrogen is produced from water, which is used in conjunction with oxygen to generate useful energy such as electricity giving water as a product.

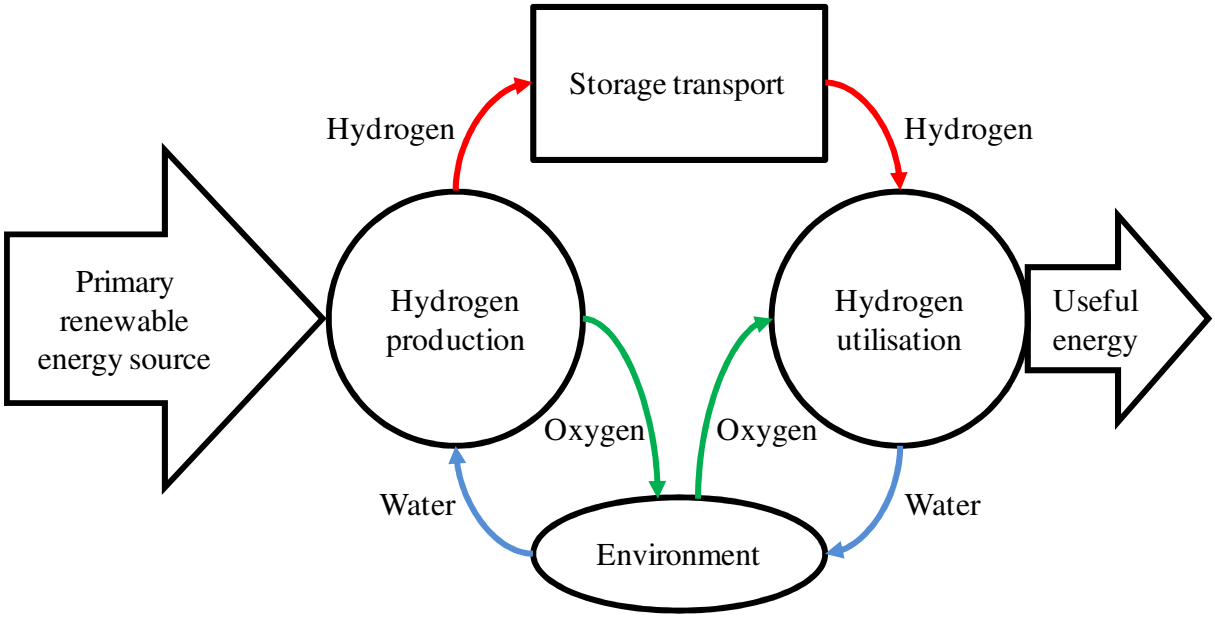

Figure 1.1 Hydrogen life cycle derived from a renewable energy source [1].

1.2.1. Hydrogen production

Hydrogen is the lightest and most abundant element in the universe; however, on earth it only occurs in its free element form in trace amounts. Some conventional methods for the production of hydrogen are steam reforming of natural gas (SMR), partial oxidation of residual oil, coal gasification, steam-iron process and water electrolysis [2]. Hydrogen can be manufactured without producing greenhouse gases through the electrolysis of water using a renewable energy source such as solar or wind energy. This method, however, is relatively costly and energy intensive. Production of hydrogen from biomass using biological processes has been an attractive method in recent times since significant amounts of hydrogen can be harvested from agricultural and municipal waste.

1.2.1.1. Fossil fuels

A majority of commercially available hydrogen (97%) is produced via steam reformation of natural gas and other light hydrocarbons [1]. This method involves two processes the first of which is shown in Equation 1.1:

$$C_iH_j + iH_2O \rightarrow iCO + (i + {}^{j}/_{2})H_2 \qquad \text{Equation 1.1}$$

where i = 1 and j = 4 for a methane feedstock and n = 1 and m = 2.2 for a naphtha feedstock. This stage is strongly endothermic and occurs at a process temperature of approximately 815 °C and 3.5 MPa over a nickel based catalyst. The second exothermic process is known as the water gas shift reaction (Equation 1.2) and is split into two steps, the low temperature shift (LTS) and high temperature shift (HTS). The LTS occurs at 200 °C using a CuO catalyst whilst the HTS operates at 350 °C in the presence of an Fe_2O_3 catalyst [2, 3]:

$$CO + H_2O \rightleftharpoons CO_2 + H_2 \qquad \text{Equation 1.2}$$

Figure 1.2 illustrates the process flow diagram for SMR. The natural gas feedstock is first hydrogenated and then desulphurised in a ZnO bed. Subsequently, the natural gas is reformed producing synthesis gas, a mixture of hydrogen, carbon monoxide and small amounts of carbon dioxide, which then undergoes the HTS and LTS process. Hydrogen is separated from the hot gas mixture in the final step using commercial methods like pressure swing adsorption which is described in more detail in Section 2.1.1.

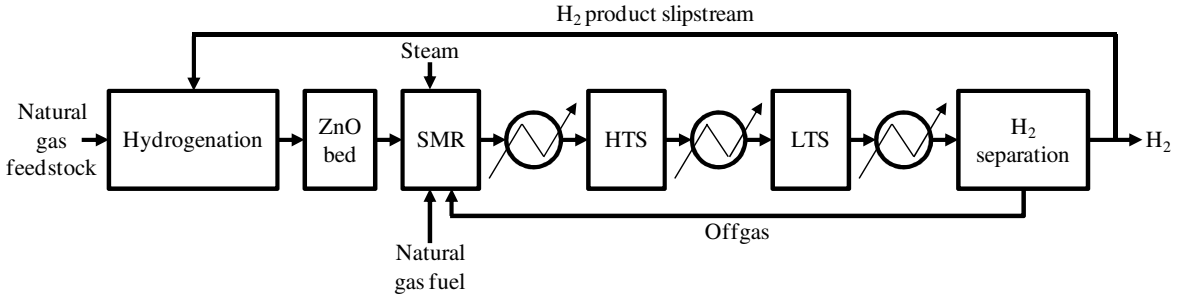

Figure 1.2 SMR process flow diagram [1].

The most recent edition of the United States Department of Energy (U.S. DoE) 2006 technical report states that, based on the lower heating value (LHV) of hydrogen, SMR was approximately 70% efficient with a production cost of U.S.$ 3.00 per gasoline gallon equivalent (gge) [4]. An obvious drawback with the SMR process is the release of CO_2, a greenhouse gas, into the atmosphere from a non-renewable resource like CH_4, although efforts have been made to develop carbon capture and sequestration to tackle this problem [5]. For the meantime, natural gas could be well suited as a temporary solution for establishing the hydrogen economy until which time a renewable energy source substitute is developed.

1.2.1.2. Electrolysis of water

In 1874, Jules Verne realised that fossil fuels were a finite resource and stated that "water will be the coal of the future" and manufacturing hydrogen from water could be a solution [6]. This can be achieved through the electrolysis of water (Equation 1.3).

$$H_2O \rightarrow H_2 + {}^1/_2\, O_2 \qquad \text{Equation 1.3}$$

Figure 1.3 shows a typical schematic of an electrolytic cell. The idea of producing hydrogen in this manner seems attractive considering the vast supply of water. However, the decomposition of water into its constituent molecules is endothermic and requires large amounts of energy to produce an appreciable amount of hydrogen meaning this method is relatively costly. The U.S. DoE reported that in 2006 typical low temperature electrolysis systems have an efficiency of approximately 62% based on the LHV of hydrogen with a production cost of U.S.$ 4.80 per gge [4]. Combining a renewable energy source, such as wind or solar, with an electrolyser could produce and store hydrogen which could be later used as a backup supply to help overcome intermittency in the electrical grid [7].

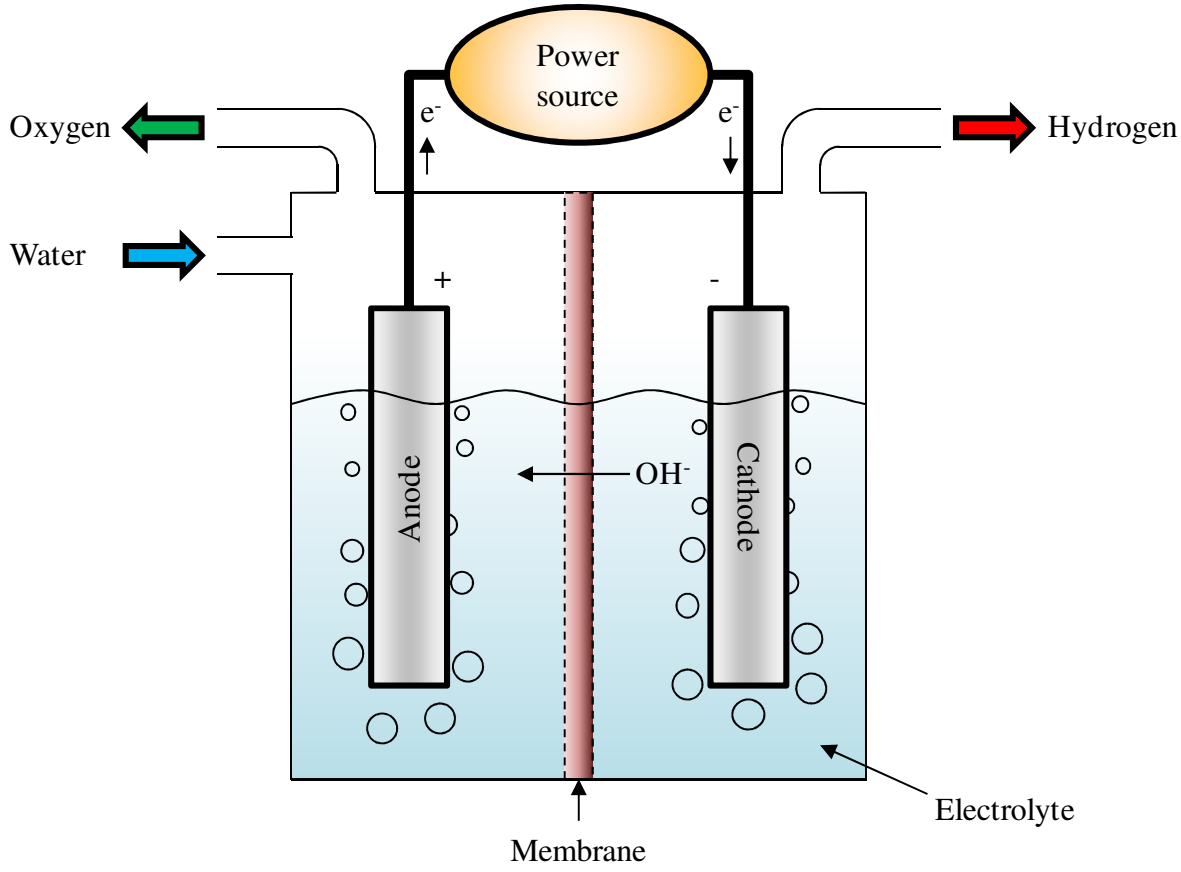

Figure 1.3 Schematic of a typical electrolytic cell for hydrogen production from water.

1.2.1.3. Biomass

A majority of biomass like wood chip and agricultural/municipal waste can contain appreciable amounts of hydrogen. Gasification of such biomass can produce synthesis gas which involves heating the organic material to above 700 °C under a controlled atmosphere of oxygen and/or steam. Gasification of biomass also produces useful by-products such as ethanol and acetate [8].

Biomass also has the advantage of being a naturally abundant renewable resource and having relatively little impact on the environment in comparison to fossil fuels. The U.S. DoE report that in 2005 biomass gasification had an efficiency of > 35% based on the LHV of hydrogen with a production cost < U.S.$ 2.00 per gge [4]. It should be noted, however, that the

hydrogen content of lignocellulose (plant dry matter) is 6 – 6.5 wt% which is significantly lower when compared to 25 wt% in natural gas [9].

Production of hydrogen can be performed sustainably using dark, anaerobic bacterial growth on carbohydrate-rich substrates [10]. This process involves fermentation of the organic feedstock which produces carbon dioxide as well as hydrogen. One of the main drawbacks of this method of hydrogen production is the relatively low yield of 2 mol H_2 mol^{-1} glucose [4].

1.2.2. Hydrogen distribution

Hydrogen can be stored onsite at the point of production as compressed gas, liquid or chemically in a solid-state storage medium. Distribution of the hydrogen would be relatively simple since it can be delivered via pipeline to the point of use.

Currently, in most developed countries there exists a pipeline infrastructure for the delivery of natural gas to homes for the purpose of heating and cooking. Hydrogen could be transported from the point of production to the point of use in a similar manner. In order to tackle hydrogen embrittlement, these pipelines are typically fabricated with low carbon and manganese content, ≤ 1 and ≈ 0.2 wt%, respectively. These low concentrations reduce the yield strength of the steel to < 290 MPa and as a result limit the operating pressure to < 10 MPa, whereby 4 – 6 MPa are commonly used. Research has shown that polymeric coatings for steel pipes and fibre reinforced polymer pipelines are impermeable to hydrogen and can increase the operating pressures to a range of 7 to 25 MPa [11].

In the last two decades, billions of cubic metres of hydrogen were produced and kept in intermediate storage and transported via pipeline to serve the chemical and aerospace industry. For more than 50 years Germany has been using a 200 km pipeline to transport

hydrogen for the chemical industry with virtually no problems. The United States, Japan and Italy also have an established pipeline network for the delivery of hydrogen for industrial applications [8].

Currently, there are only three liquefaction plants in Europe, one operated by Air Liquide in Waziers, France, another by Air Products in Rozenburg, Netherlands and one by Linde in Ingolstadt, Germany [11]. In the United Kingdom, the majority of hydrogen is transported in compressed gas cylinders to the point of use. In some countries, hydrogen is also transported by tanker in either a pressure vessel or in liquefied form. To help facilitate the transition over to a hydrogen economy, the existing pipeline infrastructure used by natural gas could be modified to enable the delivery of a hydrogen/natural gas mixture which could then be followed by the separation of hydrogen at the point of use [4, 11].

1.2.3. Hydrogen storage

One of the biggest hurdles facing the establishment of a hydrogen economy is the issue of storing hydrogen in a safe, compact, reliable and cost effective manner. The U.S. DoE published an online article emphasising that in order for hydrogen to be competitive with conventional technologies it must achieve a vehicle range of 300 miles [4]. However, this is a challenge due to the physical properties of hydrogen.

1.2.3.1. Onboard storage

Hydrogen has a high gravimetric energy content, approximately three times more than petrol yet by volume has an energy content four times less than petrol [12]. This presents a problem when storing hydrogen for mobile applications especially since storage is limited to the space constraints of a road vehicle. In order to achieve the 300 mile range stipulated by the U.S. DoE, utilising existing storage technologies such as compressed hydrogen tanks would

require a space larger than most car trunks. Not only does this provide a space issue but also the added problem of weight. The additional weight of the tank has a two-fold drawback since it reduces vehicle range and fuel economy.

Targets for onboard storage based on a 5 kg hydrogen storage system were put in place by FreedomCAR in January 2002 in conjunction with the U.S. DoE and United States Council for Automotive Research (USCAR) [12]. The aim was to reduce system weight, volume, cost and refuelling time by 2015. It was stated in 2010 by the U.S. DoE that only two technologies were on par to meet the targets. MOF-177, a type of metal organic framework material, was reported to have exceeded the 2010 volumetric capacity target [13]. The second storage method was Cryo-compression which allegedly surpassed the 2015 targets set for gravimetric and volumetric capacities [14].

The more established storage techniques are high pressure tanks which are categorised into four groups based on the tank material and the working pressure. Type I tanks are all-metal containers made from either steel or aluminium. Type II are essentially Type I tanks encased in a glass fibre reinforced polymer (GFRP) winding. The Type III tanks are an improvement on the Type II featuring a composite material such as carbon fibre reinforced polymer (CFRP) with a metal liner made from either aluminium or steel. The modern Type IV tanks are constructed mainly from a CFRP with a polyethylene or polyamide liner [15].

A common method of storing hydrogen is in compressed gas form pressurised inside a tank anywhere between 35 and 70 MPa. Increasing the storage pressure would improve the energy density resulting in a smaller tank but a much heavier system. Hydrogen is a non-ideal gas meaning large amounts of energy are needed to compress hydrogen into smaller volumes. Compressed hydrogen tanks require 2.1% of the energy content to power the compressor [16].

This energy would be lost at the compression step unless recovered otherwise making the system less efficient and more costly. Another major drawback for this mode of storage is the size and weight issue of a compressed tank making it an unattractive option for mobile applications.

Hydrogen can also be stored in the liquid state under cryogenic conditions. Typically, these conditions have hydrogen stored under 35 MPa at -253 °C. Storing hydrogen in a liquid state will improve its volumetric density facilitating containment in a smaller tank. The associated problems with storing hydrogen in this manner include boil-off, energy for hydrogen liquefaction, tank size and the attributed costs. Boil-off can present a significant safety issue in situations where a hydrogen powered vehicle is parked in confined and poorly ventilated spaces since hydrogen is susceptible to auto-ignition. According to the U.S. DoE, approximately 30% of the hydrogen lower heating value is required for liquefaction indicating that this process is energy intensive therefore incurring large costs [4].

Currently, a hybrid system, named cryo-compression, is being developed that provides a pressure vessel which is lighter and more compact than most storage media. Furthermore, the operating temperature is not as low as cryogenic storage meaning there is less of a penalty for hydrogen liquefaction and reduced boil-off [4].

Novel methods involve storing hydrogen either physically or chemically within select materials. Hydrogen can be stored on the surface of a material through adsorption, either in molecular or monatomic form. Hydrogen can also be dissociated into atoms, absorbed into a solid material and stored in the crystal lattice such as in intermetallic hydrides. Other methods include the hydrogen atoms forming strong chemical bonds giving rise to chemical compounds such as complex hydrides and chemical hydrides [12].

The aforementioned, metal organic frameworks (MOFs) store hydrogen through a process known as physisorption. This material is a relatively recent development which has garnered considerable attention due to its high hydrogen uptake. By definition, MOFs are highly ordered structures containing metal clusters and organic ligands as linkers [17]. Essentially, they are highly porous materials giving a vast surface area allowing for storage of hydrogen at the molecular level via adsorption. The infinite combinations of geometric and chemical variations using different secondary building units and linkers give MOFs an endless possibility as a storage medium.

Metal hydrides are formed when certain metals react with hydrogen gas, the most useful metal hydrides react at room temperature under 500 kPa of hydrogen. Examples of metal hydrides are palladium hydride (PdH), magnesium hydride (MgH_2) and lanthanum nickel hydride ($LaNi_5H_x$). Absorption of hydrogen into such metals is an exothermic process, conversely desorption is endothermic meaning that heat energy is required to release the hydrogen.

A majority of metal hydrides form strong bonds with monatomic hydrogen and so more heat energy is required to break these bonds and release the stored hydrogen. Reducing the energy required for hydrogen desorption can be done by using alloys that possess strong and weak hydride formers such as lithium amide, lithium borohydride and sodium borohydride. If the hydride bonds are too weak, then higher pressures will be required to form the hydride eliminating the cost saved from lowering the activation energy. The target for onboard metal hydride storage systems are less than 100 °C for hydrogen discharge [4].

1.2.3.2. Stationary storage

For stationary storage in industrial applications, space is not as important as in mobile applications since the system is not limited to the volume constraints of a vehicle. As a result,

the more traditional and established storage techniques such as compressed, liquid and slush hydrogen are utilised. Slush hydrogen is a combination of solid and liquid hydrogen coexisting together in thermodynamic equilibrium at the triple point which is at a lower temperature than liquid hydrogen and at a higher density.

Hydrogen can also be stored in large quantities underground in caverns, salt domes and depleted oil and gas fields. There are many storage sites across the globe such as the ICI salt cavern in Teesside, England storing 95% pure hydrogen and 3 – 4% CO_2 [18-20]. Between 1956 and 1974 the French gas company Gaz stored syngas in an aquifer in Beynes, France citing no safety issues during this period. Russia has also stored hydrogen underground specifically for their aerospace industry under 9 MPa of pressure [20].

1.2.4. Hydrogen utilisation

Hydrogen can be used to produce useful energy to power a road vehicle in one of two ways. Using an internal combustion engine (ICE), hydrogen can be burnt to convert chemical energy into mechanical energy. A hydrogen fuel cell can use hydrogen to convert chemical energy into electrical energy which can similarly be used to drive a vehicle.

1.2.4.1. Combustion

Like most fuels, hydrogen can be burned in an oxidation reaction. Combustion with a lean air-fuel mixture only produces water in the exhaust gas, whereas a rich mixture can form an exhaust stream containing nitrous oxides, NO_x. The amount of NO_x produced in the exhaust stream is determined by the air-fuel ratio, engine compression ratio, ignition timing, engine speed and whether thermal dilution is used. Trace amounts of CO and CO_2 can be produced if small amounts of oil manage to seep into the combustion chamber. Hydrogen ICEs are designed to function with a high air-fuel ratio or lean mixture in order to decrease the levels of

NO_x in the exhaust stream. For typical ICEs, the conversion of chemical energy to mechanical energy via thermal energy is limited by the Carnot efficiency which is slightly higher for hydrogen-air mixtures (~25%) than compared with petrol-air mixtures [21].

Existing petrol engines can be modified to allow the use of hydrogen instead of petrol by injecting the hydrogen through a specialised spark plug. Modification of an ICE to run on hydrogen is considered unviable, however, due to the low efficiency of the combustion process [22].

1.2.4.2. Fuel cells

In a fuel cell, hydrogen is electrochemically combined with oxygen from air to produce electricity alongside water and heat. Essentially, a fuel cell employs the reverse electrochemical reaction (Equation 1.6) to that used in a water electrolyser to generate electricity. Currently, there exist various types of fuel cells all made distinct by their varying electrolyte material and operating temperatures. A polymer electrolyte fuel cell (PEFC) (Figure 1.4) is commonly used for vehicular applications and as such has been the focus of much research in recent times.

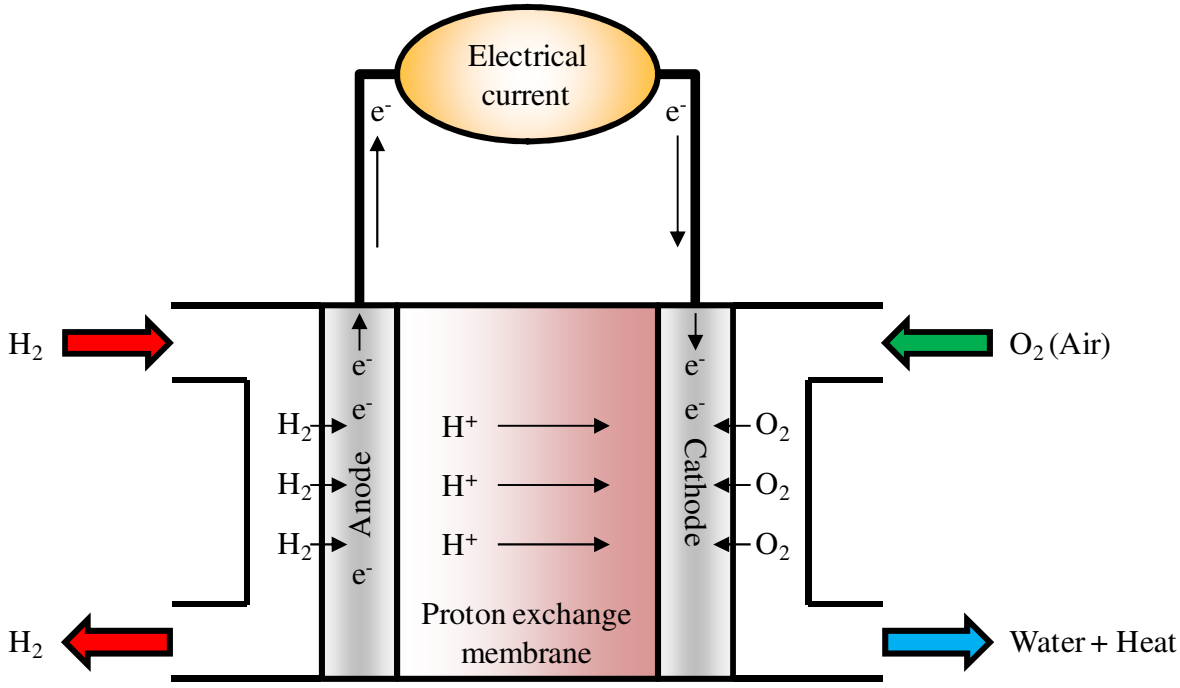

Figure 1.4 Schematic of a PEFC.

In a PEFC, hydrogen is delivered to the anode in order to dissociate the hydrogen molecule into a proton and an electron (Equation 1.4).

$$H_2 \rightarrow 2H^+ + 2e^- \qquad \text{Equation 1.4}$$

The proton migrates across a polymer based ionic conducting electrolyte whilst the electron conducts through an external circuit which provides electrical energy that can be used to power a vehicle. The proton and electron, along with oxygen, from the air intake, combine at the cathode to form water (Equation 1.5).

$$^1/_2\, O_2 + 2H^+ + 2e^- \rightarrow H_2O \qquad \text{Equation 1.5}$$

The overall fuel cell reaction is shown in Equation 1.6.

$$H_2 + {}^1/_2\, O_2 \rightarrow H_2O \qquad \text{Equation 1.6}$$

The PEFC typically operates at temperatures between 50 – 80 °C and hydrogen pressures between 100 – 300 kPa [4, 11, 23] with an efficiency ranging from 50 – 60% and benefits from not being limited by the Carnot efficiency associated with ICEs [21]. The excess heat energy produced during the fuel cell reaction can be reused to further increase the efficiency to above 80% through combined heat and power.

One of the main drawbacks of the PEFC is contamination of the platinum catalyst used at the anode with impurities such as carbon monoxide. Furthermore, several fuel cells are combined to form a stack in order to generate sufficient electricity to power a vehicle. Many challenges still remain with the PEFC including the use of expensive precious metal catalysts, durability and susceptibility to contamination.

1.2.5. Hydrogen separation

Nowadays, steam methane reforming (SMR) is the most common method for hydrogen production. The composition of the SMR product stream is typically 74% H_2, 18% CO_2, 7% CH_4 and 1% CO [24]. The water gas shift reaction involving steam is used to convert CO to CO_2 and H_2, however contamination of the gas stream with CO remains. While CO_2 and H_2O can be removed from the gas stream via condensation, CO requires a further purification step. A majority of applications need a minimum hydrogen purity of 99.99%, whereas, PEFCs require ultra-pure hydrogen (99.9995%) only tolerating contaminants in the parts per million within the feed stream. Any higher would be sufficient to poison the platinum catalyst used by PEFCs. Thus, hydrogen separation is an essential process constituting up to half of the production cost [25].

Membrane technology has been in strong development over the past 50 years and during this period has established a time and tested manufacturing method. Membranes can be used in a

variety of applications including micro filtration of bacteria to reverse osmosis for water clean-up. Membranes hold many advantages such as [26]:

- Typically low energy consumption;
- Ability to carry out separation continuously;
- Mild process conditions;
- Ease of scaling up;
- Absence of additives;
- Possibility to combine with other separation technologies.

Main disadvantages are, depending on the specific membrane type:

- Fouling tendency;
- Low membrane lifetime;
- Low selectivity or flux;
- More or less linear up-scaling factor (whereas competing processes exhibit economies of scale).

Pure Pd and its various alloys have the innate ability to allow monatomic hydrogen to selectively diffuse through its structure to produce purities in excess of $\geq 99.9999\%$ [27], this process is depicted in Figure 1.5. Although, Pd and its alloys are relatively expensive, and so there is a growing need to investigate materials that contain as little Pd as possible without sacrificing membrane properties.

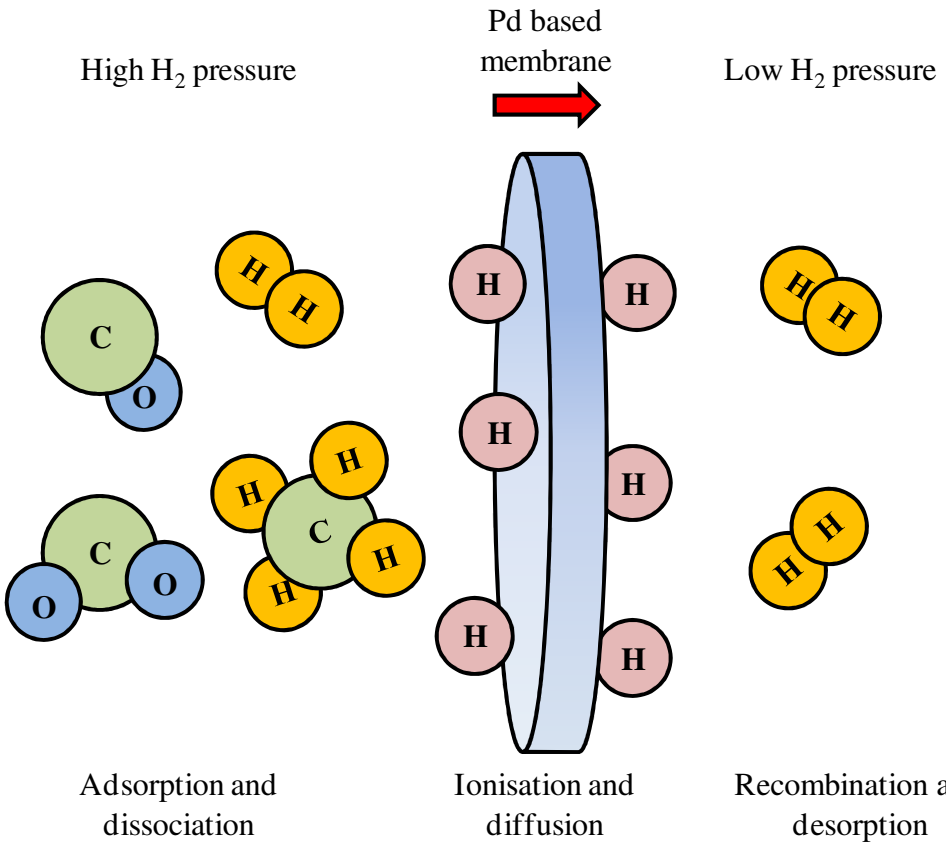

Figure 1.5 Schematic representation of hydrogen separation from a hot gas mixture using a Pd based membrane.

Table 1.1 U.S. DoE technical targets [4]: dense metal membranes for hydrogen separation applications based on a membrane water gas shift reactor with syngas.

Performance criteria	Targets		
	2006	2010	2015
Flux rate[a] (mol m^{-2} s^{-1})	> 0.75	0.94	1.13
Module cost including membrane material[b] (U.S.$ m^{-2})	16,146	10,764	< 5,382
Durability (hours)	< 8,760	26,280	> 43,800
Operating capability[c] (kPa)	1,380	2,760	2,760 – 4,140

[a] Flux rate at 400 °C with a hydrogen partial pressure differential of 345 kPa
[b] Pd does not present a significant cost to the membrane module, major contributors to the figure are the equipment cost, labour, Pd deposition, rolling of foils and drawing of tube.
[c] Pressure differential depends on the application. Many applications require only 2,760 kPa, however, the target for coal gasification is 6,900 kPa.

Dense Pd-based metal membranes offer a convenient way to separate hydrogen from a hot gas mixture to purity levels required by PEFCs either as a standalone device or combined with the

SMR process as a membrane reactor. Commercial dense metal membranes are commonly based on the Pd-Ag binary alloy system that are either cold rolled into a foil or drawn into a tube with an approximate thickness of 50 µm. The hydrogen flux through such a membrane under the conditions stipulated by the U.S. DoE (Table 1.1) is approximately 0.1 mol m^{-2} s^{-1} which is almost an order of magnitude lower than the 2015 target.

Since hydrogen flux is inversely proportional to membrane thickness (see Section 2.1.3 for further details), it has been proposed that Pd-based thin film membranes that are less than 5 µm thick can potentially meet the U.S. DoE flux rate target for dense metal membranes [28]. Using thin films has the added advantage of lowering material cost although at such low thicknesses the tensile strength of the membrane is reduced resulting in less resistance to thermal and mechanical stresses during operation. In order to remedy this, thin films are deposited onto a substrate for mechanical support.

A broad range of porous supports have been investigated over the years such as alumina [29], silicon [30], nickel [31], glass [32] and stainless steel [33]. Porous stainless steel (PSS) substrates are the preferred choice for supporting Pd alloys due to their strength, robustness, similar thermal expansion coefficient as well as ease of welding and sealing [34]. Depositing defect-free Pd and Pd alloy thin films of < 5 µm thickness onto PSS is highly complex. Laser-melting of the PSS reduces the surface roughness and porosity which can facilitate the deposition of a defect-free thin film. Furthermore, dense metallic membranes typically operate at approximately 400 °C which is a temperature that can promote intermetallic diffusion of Fe from the PSS substrate into the Pd-based thin film membrane which in turn can drastically reduce hydrogen permeability [28].

An alternative approach to increase hydrogen permeability and reduce cost of Pd-based membranes is through alloying with a relatively inexpensive metal such as Cu. In the Pd-Cu system, the maximum hydrogen permeability is achieved at a composition of $Pd_{60}Cu_{40}$ wt% [35-37]. At typical membrane operating temperatures (400 °C), this composition corresponds to the ordered BCC phase which exhibits a hydrogen diffusivity two orders of magnitude greater than in the disordered FCC phase [37-40]. In addition, for this composition above 450 °C the disordered FCC phase begins to form and at temperatures higher than 600 °C only this phase is stable. The Pd-rich Pd-Cu FCC phase has relatively high hydrogen solubility [41-43] and an enhanced resistance to H_2S contamination over the BCC phase [44, 45]. Modifying the surface composition of a $Pd_{60}Cu_{40}$ wt% membrane through the addition of Pd may introduce a Pd-rich Pd-Cu FCC layer that may potentially improve hydrogen permeability and its resistance to H_2S poisoning.

1.3. Project aim

The aim of this work is to explore the possibility of creating a Pd-rich Pd-Cu FCC phase on the surface of a BCC $Pd_{60}Cu_{40}$ wt% membrane that is stable under typical operating conditions for hydrogen separation and investigate the effects on hydrogen permeability. This can be achieved by depositing a Pd thin film onto one side of a $Pd_{60}Cu_{40}$ wt% membrane. Annealing the surface modified membrane creates a Pd-rich layer containing the FCC phase produced via Cu interdiffusion out of the bulk $Pd_{60}Cu_{40}$ wt% membrane and into the Pd thin film. Successful manipulation of the $Pd_{60}Cu_{40}$ wt% alloy surface composition could have the potential to produce a membrane with enhanced properties competitive with the more expensive Pd-Y and Pd-Ag alloy systems which currently dominate the Pd-based dense metallic membrane market.

2. Literature review

2.1. Hydrogen separation techniques

A review of hydrogen separation methods is presented with the aim of better understanding the advantages and disadvantages each technique presents for the application of hydrogen purification from hot gas mixtures. There currently exist three commercial methods including pressure swing adsorption, cryogenic distillation and hydrogen selective membranes. Each method yield varying purity levels some of which are used on large industrial scales, whilst others can be scaled down for smaller portable applications.

2.1.1. Pressure swing adsorption

Pressure swing adsorption (PSA) works by passing a gas mixture through a high surface area adsorber which has the ability to adsorb impurity gases whilst allowing hydrogen to permeate through the material. Impurity gas species are adsorbed to an adsorbent material at high gas partial pressures and conversely desorbed at lower partial pressures. A common adsorbent material used is Zeolite. The impurities can be removed by swinging the absorber pressure from the feed to the tail gas (exhaust) pressure coupled with a high purity hydrogen purge. The process is cyclic and more than one adsorber is used in order to maintain a constant flow for the feed, product and tail gas. Each adsorbent material undergoes the same process of swinging; however, the steps are staggered during the procedure. The driving force behind PSA is the impurity gases' partial pressure difference between the feed and tail gas. Typically, hydrogen separation requires a 4:1 pressure ratio between the feed and tail gas.

Two main advantages of PSA are its ability to produce hydrogen at high purities in the range of 99 to 99.999% and filter out impurities down to the region of parts per million (ppm). The

tail gas from PSA is typically utilised as fuel at low pressures which presents an economical benefit, however, large costs are incurred in compressing the tail gas which is comparable to the cost of the PSA unit. Hence, selection of a tail gas pressure is highly important. The hydrogen recovery from the PSA system is greatly reduced upon increasing the tail gas pressure which gives rise to a trade-off between hydrogen purity and tail gas compression costs [46]. Another drawback is the scale of operation and infrastructure. PSA can be adapted from a medium to large industrial scale, but is impractical to use on smaller portable scales.

2.1.2. Cryogenic distillation

This method is highly energy intensive, since the entire process operates under cryogenic conditions. Akin to conventional distillation techniques, cryogenic distillation is able to separate a feed gas mixture due to the ranging boiling points of the gas constituents. The impurity gases condense to form a liquid phase whilst hydrogen remains in a gaseous state since it has the lowest boiling point of the mixture at -252.9 °C. One major disadvantage is the limited purity levels of the extracted hydrogen at approximately 99% [47]. Furthermore, having this process operate at cryogenic temperatures incurs a high cost in terms of gas compression in order to maintain cold conditions, nonetheless the collected hydrogen can be easily stored as a liquid [48]. Similar to PSA, Cryogenic distillation is ideal for large industrial scales, however, unsuitable for small portable applications.

2.1.3. Hydrogen selective membranes

The driving force for hydrogen separation in a membrane configuration is a pressure gradient. Essentially, apply a high pressure feed gas mixture to one end of a hermetically sealed membrane whilst maintaining a relatively low pressure on the opposite side. Large hydrogen partial pressures will initiate mass transport where hydrogen will begin to migrate across the

membrane leaving behind the impurities gases. There are six main types of hydrogen selective membranes and their performance and application can be determined by identifying various parameters for each one. Table 2.1 displays the various properties, characteristics and issues associated with each type of membrane for ease of comparison. Overall, the membranes can operate at a large range of temperatures and pressures and are easily scalable between industrial and portable scales; moreover there are no moving parts, meaning there is no wear of the system.

A nomenclature will be defined in order to identify the various terms used throughout this work. The high gas pressure side of a membrane is referred to as the feed or upstream side whilst the other side is known as the permeate or downstream side (Figure 2.1). Permeation can actually occur in both directions but will be more favourable in the direction of low pressure. The flow of gas on the feed side is aptly named feed flow and the remaining flow of gas on this side after permeation takes place is known as the retentate flow. On the other side, the inlet flow is called the sweep flow and the exit flow is referred to as the permeate flow.

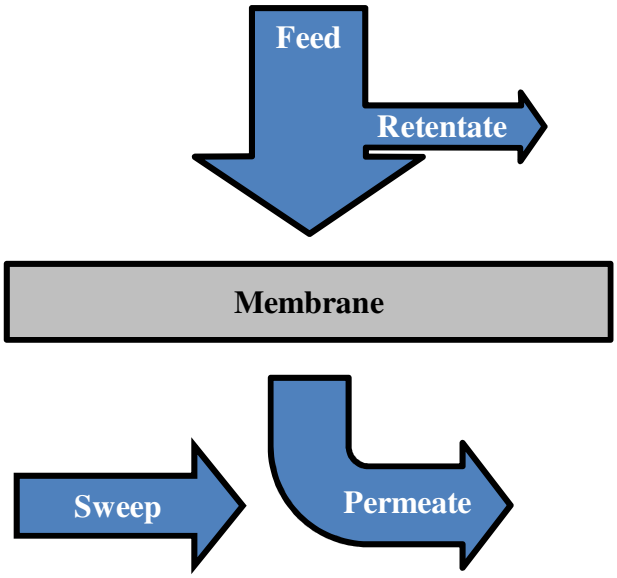

Figure 2.1 Schematic representation of gas flow through a membrane.

The term permeability has several meanings. However, in the context of this work, it is the measure of the ability of certain gases to diffuse through a solid material. Permeability is mathematically modelled and described using Fick's laws of diffusion. A key parameter to consider for hydrogen separation is the hydrogen flux through a membrane. Flux, in this context, can be defined as the number of hydrogen moles diffusing through a perpendicular unit cross-sectional area per unit time. Steady-state flux of gases through a dense solid membrane can be described by Fick's first law which is shown in Equation 2.1:

$$J = -D\frac{\partial C}{\partial x} \qquad \text{Equation 2.1}$$

where, J, is flux of the diffusing species, D is the diffusion coefficient or diffusivity and $\partial C/\partial x$ is the concentration gradient. The negative sign indicates the direction of gas diffusion and can be disregarded. It should be noted that all common driving forces such as gradients in concentration, pressure, temperature and electromotive force can be broken down to differences in chemical potential in a system. Chemical potential is defined as the amount of energy available to an uncharged atom or molecule to perform work in a chemical system. Therefore, flux is ultimately a function of a chemical potential gradient. For example, reverse osmosis requires two driving forces: concentration and pressure however both parameters are interrelated to chemical potential. For simplicity, in the case of gas permeation through a membrane, concentration or pressure gradient will be considered since they can be empirically measured.

In the instance where the gas surface concentration is not known, Henry's law applies (Equation 2.2):

$$S_H = \frac{C_{gas}}{P_{gas}} \qquad \text{Equation 2.2}$$

where S_H is a constant that is defined by the ratio of the non-dissociative gas concentration in a solid or liquid at dilute concentration (C_{gas}) to its vapour pressure (P_{gas}). Since the inlet and outlet gas pressure of a system can be measured relatively simply, the concentration term in Fick's first law can be substituted with pressure. The proportionality constant in Equation 2.2 (S_H) can be referred to as the solubility constant (S) which is expressed as concentration per unit pressure.

Diatomic molecules such as hydrogen dissociate into monatomic form prior to dissolution, therefore a new version of Henry's Law is needed to describe such behaviour. The chemist, Adolf Sieverts, investigated the dissolution of gases in various metals and observed that due to molecular dissociation hydrogen solubility in metals is a function of the square root of its pressure in the gas phase [49]. Sieverts later modified Henry's law (Equation 2.2) to give the following Equation 2.3 known as Sieverts' law:

$$S = \frac{C}{P_{H_2}^{1/2}} \qquad \text{Equation 2.3}$$

Rearranging Equation 2.3 and substituting into Equation 2.1 gives the following expression shown in Equation 2.4:

$$J = DS\frac{\partial P_{H_2}^{1/2}}{\partial x} \cong DS\frac{\Delta P_{H_2}^{1/2}}{\Delta x} \qquad \text{Equation 2.4}$$

where $\Delta P_{H_2}^{1/2}$ is the square root of the pressure difference between the feed and permeate sides of the membrane and Δx is the membrane thickness which can be denoted as simply, x. Equation 2.4 can be further manipulated to compute the total number of moles (Q) permeating through a dense metal membrane by multiplying both sides of the expression by the active membrane area (A) and the time (t) elapsed since gas permeation reached equilibrium to give the following Equation 2.5:

$$Q = JAt = DS\frac{A}{x}\Delta P_{H_2}^{1/2} \cdot t \qquad \text{Equation 2.5}$$

The term DS is merely the product of diffusivity and solubility of hydrogen in the dense metal membrane which gives rise to the term permeability, Φ, shown in Equation 2.6 where all variables are temperature dependent:

$$\Phi = DS \qquad \text{Equation 2.6}$$

Differentiating Equation 2.5 with respect to t gives a formula for determining the flow rate and substituting in Equation 2.6 gives Equation 2.7:

$$\frac{dQ}{dt} = \Phi\frac{A}{x}\Delta P_{H_2}^{1/2} \qquad \text{Equation 2.7}$$

If the steady state flow rate of hydrogen, the membrane active area, the thickness as well as the gas pressure on either side of the membrane are known, then the permeability can be easily determined. The slope of a straight line plot of Q against t can also be used to determine the permeability of the membrane using Equation 2.7.

Equation 2.4 can be further simplified to give Equation 2.8, a general formula for calculating the hydrogen flux through a membrane:

$$J = \frac{\Phi(P_1^n - P_2^n)}{x} \qquad \text{Equation 2.8}$$

where P_1 is the hydrogen partial pressure on the feed side of the membrane and P_2 is conversely the hydrogen partial pressure on the permeate side. The partial pressure exponent, n, also referred to as the n-value can take varying values depending on the assumed transport mechanism (Figure 2.2). For porous membranes Henry's law applies, hence it is assumed that the n-value equals 1 and what is known as Knudsen diffusion occurs. This type of diffusion along with other mechanisms is discussed in detail in Section 2.1.3.1. The n-value is assumed to be 0.5 for hydrogen diffusion though a dense metal membrane and Equation 2.8 reverts to Sieverts' law. This equation shows that flux is inversely proportional to membrane thickness.

It should also be noted that permeability is a material constant and is independent of membrane thickness [50]. In addition, permeability is a temperature dependent parameter that is expressed in the following Arrhenius type Equation 2.9:

$$\Phi = \Phi_0 exp\left(\frac{-E_\Phi}{RT}\right) \qquad \text{Equation 2.9}$$

where Φ_0 is the maximum permeability at infinitely high temperatures, E_Φ is the activation energy for permeation, R is the gas constant and T is the absolute temperature. Similarly, D and S are governed by an Arrhenius type relationship as shown in Equation 2.10 and Equation 2.11, respectively.

$$D = D_0 exp\left(\frac{-E_D}{RT}\right) \qquad \text{Equation 2.10}$$

$$S = S_0 exp\left(\frac{-E_S}{RT}\right) \quad \text{Equation 2.11}$$

where D_0 and S_0 are diffusivity and solubility at infinitely high temperatures, E_D is the activation energy for hydrogen diffusion and E_S is the enthalpy of solution of hydrogen. Furthermore, E_Φ is defined as the sum of the activation energies for both diffusivity and solubility which is expressed in Equation 2.12:

$$E_\Phi = E_D + E_S \quad \text{Equation 2.12}$$

Membranes can also be assessed by looking at other characteristics such as selectivity towards gas mixtures. In other words, selectivity is the measure of the differences in permeability values between various gaseous species and also the membrane separation effectiveness. Consider a gas mixture comprised of gas *A* and *B*, the selectivity factor $\alpha_{A/B}$ can be defined by the following Equation 2.13:

$$\alpha_{A/B} = \frac{y_A/y_B}{x_A/x_B} \quad \text{Equation 2.13}$$

where y_A and y_B denotes the partial pressure of gas *A* and gas *B* on the permeate side whereas x_A and x_B denotes the partial pressure of gas *A* and gas *B* on the feed side of the membrane [51]. There are two further factors which are also important in terms of gauging the effectiveness of a membrane which are the recovery and volume reduction. The recovery (S_r) is defined as the proportion of the feed gas permeating through the membrane and is shown in Equation 2.14:

$$S_r = \frac{q_p}{q_f} \qquad \text{Equation 2.14}$$

where q_p is the permeated flow and q_f is the feed flow. Volume reduction (VR) is the ratio of the feed flow to the retentate flow (q_r) and is shown in Equation 2.15:

$$VR = \frac{q_f}{q_r} \qquad \text{Equation 2.15}$$

Membranes can be divided into two classes: porous and dense. The porous types are commonly micro-porous ceramics or porous carbon which employ molecular sieving as the primary mechanism for hydrogen purification. The dense membrane alternatives can be polymeric, metallic or ceramic based and utilise a solution-diffusion process for hydrogen separation.

Table 2.1 Properties of the various hydrogen selective membrane types adapted from Kluiters [51].

	Dense polymer	**Micro-porous ceramic**	**Dense metallic**	**Porous carbon**	**Dense ceramic**
Temperature range (°C)	< 100	200 – 600	300 – 600	500 – 900	600 – 900
H_2 selectivity	Low	5 – 139	> 1,000	4 – 20	> 1,000
H_2 flux ($\times 10^{-3}$ mol m^{-2} s^{-1}) at ΔP = 100 kPa	Low	60 – 300	60 – 300	10 – 200	6 – 80
Stability issues	Swelling, compaction, mechanical strength	Stability in H_2O	Phase transition	Brittle, oxidising	Stability in CO_2
Poisoning issues	HCl, SO_x, CO_2		H_2S, HCl, CO	Strong adsorbing vapours, organics	H_2S
Materials	Polymers	Silica, alumina, zirconia, titania, zeolites	Pd alloy	Carbon	Proton conducting ceramics (mainly $SrCeO_{3-\delta}$, $BaCeO_{3-\delta}$)
Transport mechanism	Solution/ diffusion	Molecular sieving	Solution/ diffusion	Surface diffusion; molecular sieving	Solution/ diffusion (proton conduction)
Development status	Commercial by Air Products, Linde, BOC, Air Liquide	Prototype tubular silica membranes available up to 90 cm. Other materials only small samples (cm^2)	Commercial by Johnson Matthey; prototype membrane tubes available up to 60 cm	Small membrane modules commercial, mostly small samples (cm^2) available for testing	Small samples available for testing

2.1.3.1. Porous selective membranes

Currently, there exists a variety of porous media for the purpose of hydrogen separation which uses a process known as molecular sieving. Commercially available porous materials are

zeolites, Vycor glass, sintered metals such as nickel and a range of ceramics like alumina and zirconia.

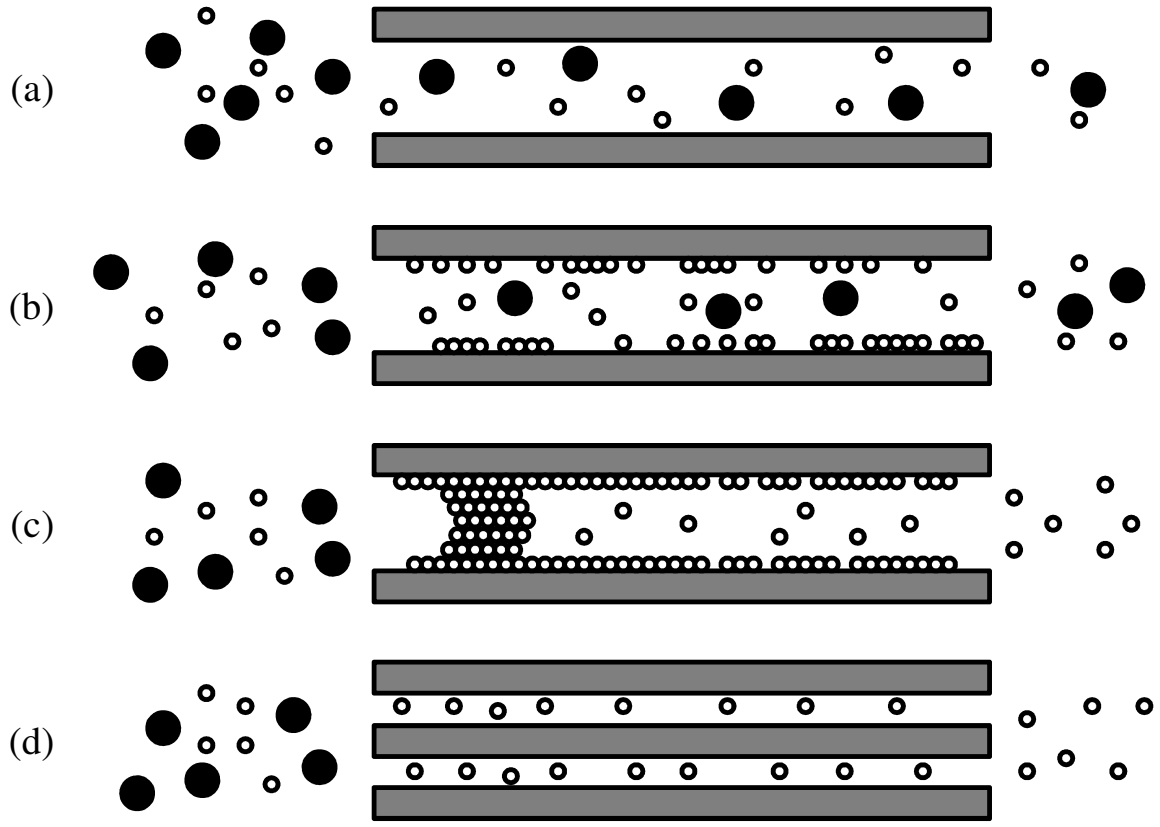

Figure 2.2 Diagram depicting the four transport mechanisms through a porous membrane: (a) Knudsen diffusion, (b) surface diffusion, (c) capillary condensation and (d) molecular sieving [52].

Behaviour of the hydrogen molecules as they manoeuvre through nanometre sized pores can be modelled using Knudsen diffusion as shown in Figure 2.2(a). This type of flow occurs when the mean free path (μ) or the average distance covered by a molecule between molecular collisions is greater than the pore size, resulting in frequent collisions with the pore walls. Knudsen diffusion is the predominant transport mechanism for pore sizes ranging between 2 and 50 nm which are classed as mesopores [53]. Using the Lennard–Jones intermolecular potential approach, Hirschfelder, Curtiss and Bird [54] calculated the mean free path of hydrogen to be 110.6 nm under ambient conditions. Additionally, Knudsen

diffusion is expected to occur when there exists a large Knudsen number (Kn) which is defined as the ratio of the mean free path of the gas component (μ) and the pore radius (L) as shown in Equation 2.16:

$$Kn = \frac{\mu}{L} \qquad \text{Equation 2.16}$$

The diffusion of a gas molecule along a mesopore is directly proportional to pore size and pressure, plus it is inversely proportional to the membrane thickness and the square root of the molecular weight [55]. If the mean free path of a gas molecule is relatively smaller than the pore size then Fick's law of diffusion is prevalent [56].

Figure 2.3 and Figure 2.4 are images of a porous anodic alumina membrane. This material comprises of nano-sized pores arranged in a honeycomb-like configuration which can be used to support thin metal film membranes for the purpose of hydrogen separation. The flow of hydrogen through these nanopores can be modelled using Knudsen diffusion due to the shape and size of the pores.

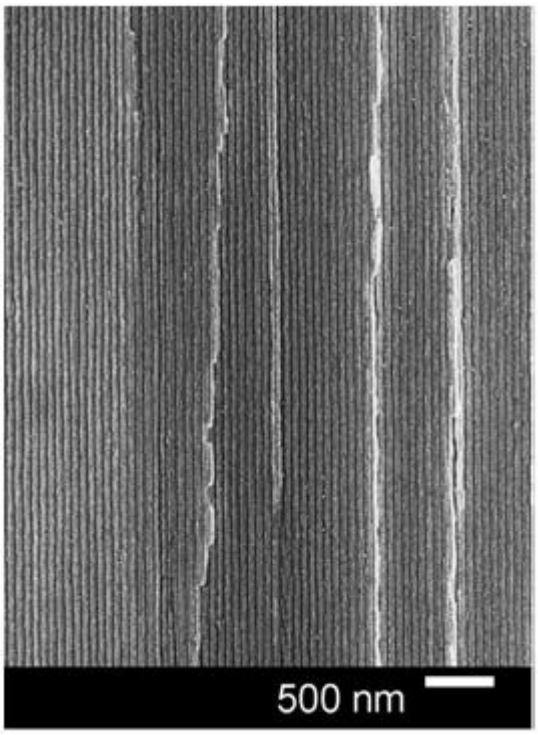

Figure 2.3 Porous anodic alumina membrane cross-section featuring mesopore channels ~25 nm in diameter which lies within the Knudsen diffusion regime. Image taken from Kirchner et al [57].

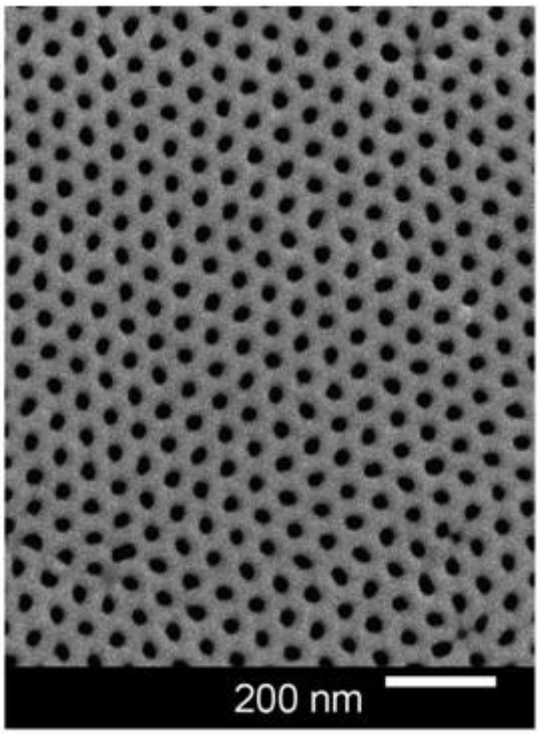

Figure 2.4 Top view of the same porous anodic alumina membrane.

Surface diffusion (Figure 2.2(b)) can occur alongside Knudsen diffusion as gas molecules are able to adsorb and propagate along the pore walls. Permeability will be high for the gas molecules which are readily adsorbed onto the pore walls. Nevertheless, this will result in low permeability for gas particles that are unable to adsorb onto the walls thus increasing the selectivity. Of course, this will result in a decrease in effective pore diameter.

Capillary condensation (Figure 2.2(c)) occurs when a partially condensed gas phase occupies the pore. If the pore is completely filled with the condensed phase then only gas molecules that are soluble in this phase can permeate through the pores. Selectivity and flux are typically high for this mode of gas transport, although it is highly dependent on the gas composition, pore size and pore size uniformity.

Molecular sieving (Figure 2.2(d)) can take place if the pore sizes are sufficiently small. The pore size must be between 0.3 and 1 nm. It works on the basis of filtering and separating out gas molecules that have different kinetic diameters. In general, only gas molecules small enough to fit into the pores may permeate through the membrane.

It can be said that mesoporous materials are only effective at separating hydrogen from the heavier gaseous compounds such as CO_2 and H_2S, although they would seem to be ineffective at extracting hydrogen from the lighter gases such as CH_4 and H_2O. Furthermore, when comparing the hydrogen selectivity of the porous ceramic and carbon membranes to that of the dense ceramic and metallic alternatives, it is evident that dense membranes are by far the more selective as shown in Table 2.1. The highest hydrogen selectivity attainable with porous membranes is when the hydrogen flux is relatively low; therefore, increasing the flux will reduce the selectivity.

2.1.3.2. Dense selective membranes

Hydrogen permeation will occur through the bulk of the dense membrane material. Dense metal membranes display extremely high levels of selectivity; however, the flux is low, whereas porous membranes have high rates of flux but very low selectivity. The transport mechanism for hydrogen through a dense metal membrane can be described using a solution-diffusion model. Upon hydrogen gas coming into contact with a dense metal membrane surface, for example Pd, the molecules dissociate into monatomic form and subsequently ionise to form a single pair of a proton (H^+) and an electron. The proton and electron will diffuse through the membrane to the other side whereby the proton is reduced to form a hydrogen atom that recombines with another hydrogen atom to reform the molecule and finally desorb into the gas phase. The main driving force for this phenomenon is the

difference in hydrogen partial pressure between the feed side and permeate side of the membrane.

Steward [49] successfully compares and contrasts hydrogen permeability data for a range of materials found in literature demonstrating that metals that have a body centred cubic (BCC) crystal structure such as V, Nb and Ta exhibit higher hydrogen permeability values than the face centred cubic (FCC) metals such as Pd and Ni. Moreover, V, Nb and Ta have hydrogen permeability values an order of magnitude higher than that of Pd, however, these metals readily form an oxide layer under ambient conditions which severely hinder hydrogen dissociation and solubility.

The metal data compiled by Steward [49] is displayed in the Figure 2.5 plot. A review by Uemiya [58] on membrane reformers includes a similar plot of the same data set, however, it erroneously includes permeability data for Zr which had never been reported by Steward [49]. In comparison, Adhikari and Fernando [59] present a review on hydrogen membrane separation techniques which features a more accurate plot based on the data found in the Steward [49] review.

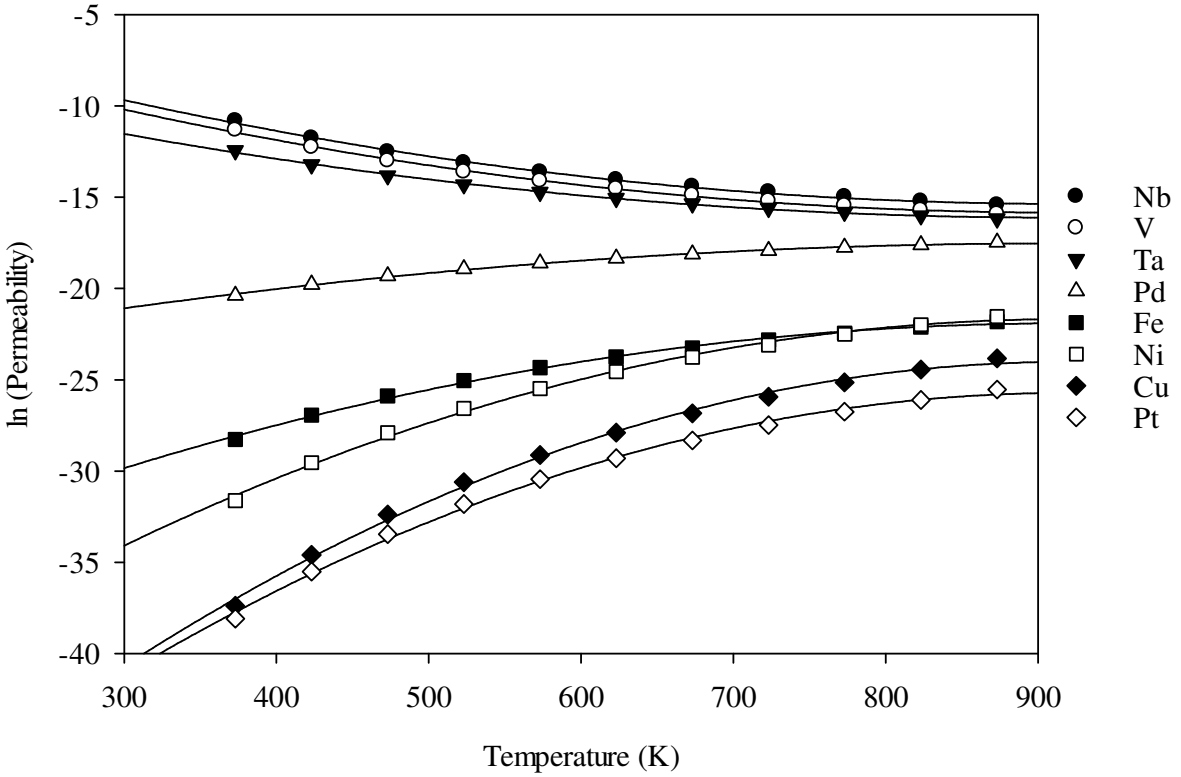

Figure 2.5 Natural logarithm of hydrogen permeability as a function of temperature for various metals plotted using data from Steward [49].

As shown in Table 2.1, dense membranes can be polymer, ceramic or metallic based. Polymer membranes are an existing technology and have been used industrially to separate hydrogen from a gaseous mixture of N_2, CO and various hydrocarbons. These types of membranes can be further subdivided into two categories: glassy and rubbery polymeric membranes. The glassy type has relatively higher selectivity but lower flux, whereas the rubbery kind conversely has higher flux rates and lower selectivity. The main advantages for these membranes are their low cost and ability to cope with high pressure differences. Nenoff, Spontak and Aberg [25], concluded, however, that dense polymeric membranes based on polyamide-imide block co-polymers can benefit from reduced production cost and further development to improve stability at elevated temperatures in order to become competitive with the existing alternative membrane materials.

Table 2.1 shows that polymer membranes have relatively low levels of flux, selectivity, poor mechanical properties and a low operating temperature (< 100 °C). Moreover, they are prone to contamination by HCl, (SO_x) and CO_2 which make these membranes less attractive compared to other membrane types. Table 2.2 shows the hydrogen permeability and selectivity values of various polymeric membranes.

Table 2.2 Hydrogen permeability and selectivity values of various dense polymeric membranes. Conditions are for 300 K at a 206.84 kPa feed pressure [59].

Polymer	Hydrogen permeability ($\times 10^{-16}$ mol m^{-1} s^{-1} Pa^{-1})	Selectivity		
		H_2/N_2	H_2/CH_4	H_2/CO_2
Polysulfone	40.5	15.1	30.3	2.0
Polystyrene	79.6	39.7	29.8	2.3
Polymethyl methacrylate	8.0	2.0	4.0	4.0
Polyvinylidene fluoride	8.0	3.4	1.8	2.0

Overall it appears that polystyrene has the best hydrogen permeability and general selectivity. Adhikari and Fernando [59] note that research efforts have been more focussed towards metallic, carbon, zeolite and ceramic based membranes the latter being the preferred option since this type is inert to poisonous gases.

According to Table 2.1, dense ceramic membranes have very good hydrogen selectivity comparable to that of dense metallic membranes. In a report by Kluiters [51], it is shown that dense ceramic membranes are capable of operating at relatively high temperatures typically between 600 and 900 °C. Contrary to the opinion of Adhikari and Fernando[59], the main disadvantages of these types of membranes are the inherently low flux rates and instability in the presence of CO_2 and H_2S. This class of membranes are commonly fabricated from proton conducting materials also known as perovskites such as strontium cerate ($SrCeO_{3-\delta}$) and barium cerate ($BaCeO_{3-\delta}$) [51]. A past review by Norby [60], mentions the emerging interest in mixed protonic-electronic conductors for the application of hydrogen separation. Moreover,

Norby advocates the versatility of the perovskites as an electrolyte material for solid oxide fuel cells [61].

Phair and Badwal [62] postulate that in order for a dense ceramic membrane to be commercially viable as a hydrogen separator, it must have an electron and proton conductivity in excess of $0.1\ S\ cm^{-1}$ to produce flux rates comparable to dense metal membranes. Generally, these membranes cannot promote spontaneous hydrogen dissociation and re-association on their surface therefore a secondary catalytic phase is required. Song et al [63], have shown that this problem can be alleviated through the addition of Ni to $SrCe_{0.8}Yb_{0.2}O_{3-\delta}$ which improved the hydrogen flux at 900 °C by a factor of 13 from 5.93×10^{-5} to $7.79 \times 10^{-4}\ mol\ m^{-2}\ s^{-1}$. This rise in hydrogen flux is attributed to the Ni enhancing electron conductivity and thus hydrogen permeability. Despite such improvement, this ceramic – metal composite (cermet) is still not competitive with commercially available dense metal membranes.

Supported dense metal membranes undergo interdiffusion between the metal film and porous substrate which can severely hinder hydrogen permeation whereas dense ceramic membranes do not experience such problems. Schwartz et al [64] have demonstrated that unlike metallic membranes, a cermet membrane based on a pyrochlore can easily be hermetically sealed using brazing alloys such as Inconel 600, nevertheless, they report that this membrane achieved hydrogen flux rates a factor of eight less than what is required for industrial processes.

Dense metal membranes can operate between 300 and 600 °C, offer excellent hydrogen selectivity and superior flux rates when compared to other membrane types. The hydrogen purity levels achieved using dense metal membranes are in excess of 99.9999% which is ideal

for PEFCs which make use of a Pt catalyst that is prone to contamination by CO. The main drawbacks are the inherent cost associated with the dense metal membranes which are commonly based on Pd. Efforts are being made to deposit thin films of Pd onto porous substrates in order to reduce material cost and increase hydrogen flux rates since flux is a function of membrane permeability and thickness. An additional disadvantage is the susceptibility of pure Pd membranes to poisoning by H_2S, HCl and CO.

2.2. Dense metallic membranes

2.2.1. Metallic membranes

Hydrogen can rapidly diffuse through refractory metals especially those with a BCC crystal structure, however, these metals have highly inactive surfaces for the catalysis of hydrogen, meaning the rate of absorption and desorption is very slow. Buxbaum and Marker [65] recognised this and developed a Nb (BCC metal) membrane electrolessly plated with Pd (FCC metal) which had a relatively high hydrogen permeability of 3.2×10^{-7} mol m^{-1} s^{-1} $Pa^{-0.5}$ at 425 °C. Although, it was found that the hydrogen flux degraded over time due to interdiffusion occurring between the Nb and Pd film.

In a similar attempt, Paglieri et al [66] previously fabricated a $V_{90}Pd_{10}$ at% membrane with a 100 nm thick pure Pd film deposited on both sides. They claim that this membrane had achieved a hydrogen permeability of 3.86×10^{-8} mol m^{-1} s^{-1} $Pa^{-0.5}$ at 400 °C, yet the membrane had cracked once cooled to 118 °C due to hydrogen embrittlement. Furthermore, Paglieri et al [66] qualitatively tested the endurance of membranes during thermal cycling by measuring the temperature at which a hydrogen charged membrane failed under gradual

cooling. Their findings indicate that membrane endurance under thermal cycling was enhanced by reducing the hydrogen solubility.

Table 2.3 reveals the enthalpy of hydride formation to be exothermic for Nb, Ta, V, Ni and Pd; whereas, Fe and Pt are endothermic. Exothermic, means that this kind of reaction easily occurs and hydrides readily form. Endothermic reactions on the other hand need external sources of heat to proceed, so in this instance Fe and Pt require heat in order to produce their respective hydrides. Phair and Badwal [67] present a list of data similar to that shown in Table 2.3, however, they incorrectly report that the enthalpy of hydride formation for Pd is endothermic (+20 kJ mol^{-1}).

Table 2.3 Hydrogen permeability values of selected metals and the associated enthalpy of hydride formation.

Metal	Crystal structure	Hydrogen permeability at 500 °C (mol m^{-1} s^{-1} $Pa^{-0.5}$) [49]	ΔH of hydride formation (kJ mol^{-1}) [68]
Nb	BCC	1.6×10^{-6}	-60 (NbH_2)
Ta	BCC	1.3×10^{-7}	-78 ($TaH_{0.5}$)
V	BCC	1.9×10^{-7}	-54 (VH_2)
Fe	BCC	1.8×10^{-10}	+14 (FeH)
Ni	FCC	7.8×10^{-11}	-6 ($NiH_{0.5}$)
Pd	FCC	1.9×10^{-8}	-40 ($PdH_{0.5}$)
Pt	FCC	2.0×10^{-12}	+26 (PtH)

2.2.2. Palladium membranes

At this juncture it is important to understand the reason as to why metals such as Pd are popular in the field of hydrogen separation. Hydrogen dissolves in a variety of metals to create either interstitial solid solutions or metal hydrides. Certain metals require high temperatures and pressures to absorb hydrogen whereas some can form stable hydrides at room temperature.

The unique nature of Pd makes the metal ideal for the purpose of hydrogen separation in the sense that it has the ability to dissociate molecular hydrogen into monatomic form ready for fast diffusion through its lattice. Moreover, this metal is capable of absorbing approximately 600 times its own volume in hydrogen whilst maintaining its physical properties and structural integrity, a facet that Thomas Graham discovered in 1866 [69]. It was not until the 1950s that Pd membranes were scaled up from laboratory environments in favour of the nuclear fission industry since there existed a growing demand for separating hydrogen isotopes. Since then, Pd membranes are more commonly used for the production of ultra pure hydrogen for the semiconductor industry [70].

The density of Pd is 12.023 g cm^{-3} and has a melting point of 1,555 °C. Discovered by William Hyde Wollaston in 1803, it is a silvery white metal which is malleable and easily worked. Nowadays, it is widely used in the automotive industry in catalytic converters. In the neutral ground state, Pd has an electron configuration of: $1s^2\ 2s^2p^6\ 3s^2p^6d^{10}\ 4s^2p^6d^{10}\ 5s^0$. There exist overlapping energy bands between the 4d and 5s energy bands which is typical of transition metals. This gives Pd a high affinity for donor electrons from other atoms.

The Pd-H system features an interstitial solid solution (α-PdH) and palladium hydride (β-PdH) phase as shown in Figure 2.6. Both phases have the same FCC crystal structure; however, they differ in lattice parameter. Pure Pd has a lattice parameter of 3.89 Å (10 nm = 1 Å). At room temperature, the α-PdH phase exists up to a composition known as α_{max} and can form alongside the β_{min} up to a H/Pd atomic ratio of ~0.6 whereby each phase has a lattice parameter of 3.895 and 4.025 Å, respectively [71]. The coexistence of these two phases gives rise to a notable feature of the phase diagram shown in Figure 2.6 and is referred to as the miscibility gap. The critical temperature (T_c) for β-PdH formation is approximately 295 °C (below hydrogen pressures of 2 MPa) above which this phase no longer occurs.

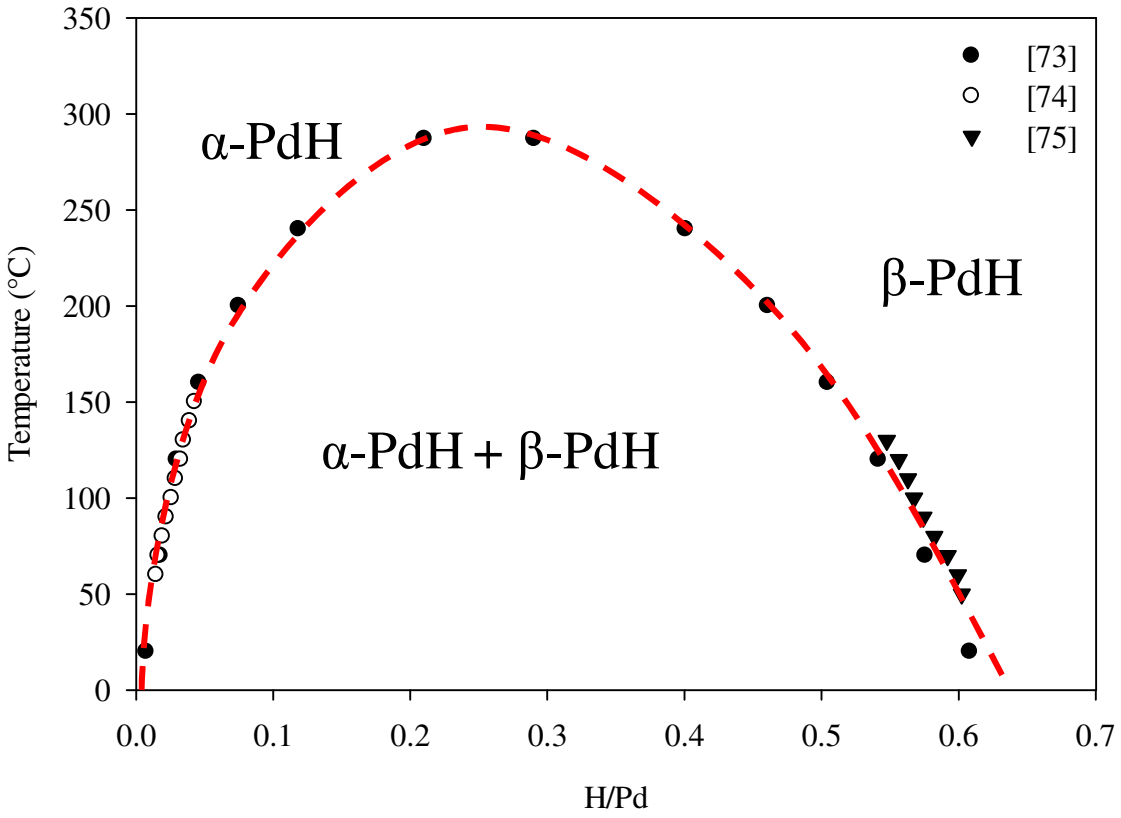

Figure 2.6 The Pd-H phase diagram reproduced from Huang et al [72] who used published data to construct the plot [73-75].

Cycling of a Pd membrane through the miscibility gap can incur a lattice volume expansion in excess of 10%. This occurs due to the disparity between the α- and β-PdH phase lattice parameters and as more hydrogen occupies the Pd lattice, internal stresses are created which ultimately lead to membrane failure. Such phenomenon has been studied using transmission electron microscopy of a Pd-H alloy containing the α-PdH + β-PdH phase showing clear evidence of dislocation production which is a precursor to embrittlement [71]. The effects of embrittlement can be avoided through purging the membrane of any hydrogen prior to thermal cycling in order to prevent crossing the miscibility gap.

As shown in Figure 2.6, the α- and β-PdH phase are able to coexist below the T_c, however, above this temperature the β-PdH phase may only occur at extremely high pressures [76].

According to Dolan [77], the formation of the β-PdH phase is an exothermic process and an increase in this phase content in metals such as Pd can lead to a reduction in hydrogen solubility of the α-PdH phase. An FCC metal like Pd is innately more resistant to hydrogen embrittlement than BCC metals such as V since hydrogen solubility is relatively lower in Pd [77].

The obvious drawback of Pd is the inherent material cost, where its price has rapidly risen reaching a 5 year high of U.S.$ 908.00 per ounce in late 2014, the equivalent of U.S.$ 32.03 per gram [78]. With the continued research and production of Pd alloys, the growing demand for Pd in various other industries also coupled with rising fuel prices will further compound Pd prices. This mere fact makes it ever more difficult to meet the cost target set out by the U.S. DoE. As a result, research aims have been geared towards developing Pd alloy membranes with minimal thickness or fabricating membranes that use less Pd.

2.2.3. Palladium alloy membranes

There exist a plethora of Pd alloys, some yet to be explored, which can bring about superior chemical and physical properties when compared to pure Pd.

Table 2.4 shows hydrogen permeability figures for a range of alloys, however, there are some ternary alloys which are mentioned in literature but have no accompanying permeability data. Several elements such as Ag, Au, Cu, Y and Pt can be alloyed with Pd to form substitutional solid solutions and by doing so can lower the critical temperature (T_c) of the α-PdH → β-PdH phase transformation to below room temperature. The top three alloys in terms of hydrogen permeability and mechanical/chemical performance are Pd-Ag, Pd-Y and Pd-Cu.

Perhaps the most well-known and studied alloy is the Pd-Ag system which has a hydrogen permeability of nearly twice that of pure Pd as shown in Table 2.4. Alloying Pd with Ag lowers the T_c of the miscibility gap such as in $Pd_{23}Ag_{77}$ wt% where the T_c is at room temperature and as a result purging hydrogen from the membrane prior to thermal cycling is not required [77, 79]. Typically, Pd-Ag alloy membranes are used in commercial purifiers, though they exhibit short life cycles due to significant lattice expansion upon hydrogen absorption and undergo grain coarsening at high temperatures [80]. Furthermore, it has relatively low strength when compared to other Pd alloys such as Pd-Y and Pd-Cu. Another issue to note is the onset of rising fossil fuel prices that has a direct knock-on effect on the value of Ag (and Au) which could make this alloy commercially unattractive.

The Pd-Y system has the highest reported hydrogen permeability of the Pd alloys. Harris and Norman [81] discovered that despite Y atoms being ~30% larger than Pd atoms, Y is soluble in Pd up to 12 at%. This is contrary to Hume-Rothery who stated that there is a 15% atomic mismatch limit [82]. Consequently, Pd-Y alloys owe their superior tensile strength to this atomic mismatch. The hydrogen permeability of a $Pd_{92}Y_8$ at% membrane at 400 °C is nearly 2.5 times that of a $Pd_{76}Ag_{24}$ at% membrane and yet has not been commercialised. A probable reason for this is that Pd-Y alloys undergo work hardening during cold work, meaning several costly annealing stages would be necessary to facilitate processing of the alloy into a working membrane.

The Pd-Cu system offers a number of advantages over pure Pd. It gives a maximum hydrogen permeability at approximately $Pd_{60}Cu_{40}$ wt% and although it does not have a higher hydrogen permeability than the Pd-Ag system, it is mechanically superior, more durable to hydrogen cycling and exhibits resistance to H_2S contamination [44, 83]. For the $Pd_{60}Cu_{40}$ wt% composition, the ordered CsCl-type BCC phase is stable and is attributed to the high

hydrogen permeability demonstrated by this system [35, 37]. Piper [39] used electrical resistivity measurements to determine the room temperature hydrogen diffusivity of the $Pd_{60}Cu_{40}$ wt% BCC phase and reported a value of 5×10^{-5} cm^2 s^{-1} which is more than a factor of 300 times greater than that of pure Pd at the same temperature. Opalka et al [84], used atomic modelling to show that sulphur interaction with the Pd-Cu system depended more on electronic characteristics than surface site geometry. Furthermore, dissolved hydrogen has shown to increase the compositional range at which the BCC | FCC + BCC phase boundary occurs in the Pd-Cu system almost acting as a third alloying constituent [39].

Table 2.4 Hydrogen permeability values of pure Pd and miscellaneous Pd alloys (wt%) at 350 °C.

	Permeability ($\times 10^{-8}$ mol m^{-1} s^{-1} Pa^{-n})	*n*	Reference
Pd	1.43	0.5	Fletcher [28]
Pd	1.20	0.5	Holleck [85]
Pd	0.15	0.68	Hurlbert [86]
Pd	0.80	0.5	Kamakoti [87]
Pd	0.73	0.5	Katsuta [88]
Pd	1.07	0.5	Koffler [89]
Pd	1.39	0.5	McKinley [35]
Pd	1.33 0.24	0.5 0.62	Morreale [90]
Pd	1.27	0.5	Toda [91]
$Pd_{75}Ag_{25}$[a]	3.21	0.5	Fort [92]
$Pd_{90}Ag_{10}$ $Pd_{73}Ag_{27}$ $Pd_{60}Ag_{40}$ $Pd_{48}Ag_{52}$	2.44 1.99 0.68 0.10	0.5	McKinley [35]
$Pd_{75}Ag_{25}$	1.65	0.5	Serra [93]
$Pd_{95}Au_5$ $Pd_{80}Au_{20}$ $Pd_{60}Au_{40}$ $Pd_{45}Au_{55}$	1.49 1.35 0.59 0.13	0.5	McKinley [35]
$Pd_{99.5}B_{0.5}$	1.32	0.5	McKinley [35]
$Pd_{94.25}Ce_{5.75}$[a]	2.42	0.5	Hughes [94]
$Pd_{60}Cu_{40}$	1.42	0.5	Decaux [95]
$Pd_{80}Cu_{20}$ $Pd_{60}Cu_{40}$ $Pd_{47}Cu_{53}$	0.17 0.50 0.04	0.5	Howard [37]
$Pd_{80}Cu_{20}$ $Pd_{60}Cu_{40}$	0.17 0.60	0.5	Kamakoti [87]
$Pd_{60}Cu_{40}$	1.07 1.76[b]	0.5	Krueger [96]
$Pd_{90}Cu_{10}$ $Pd_{70}Cu_{30}$ $Pd_{60}Cu_{40}$ $Pd_{55}Cu_{45}$ $Pd_{45}Cu_{55}$	0.68 0.12 1.49 0.25 0.01	0.5	McKinley [35]
$Pd_{60}Cu_{40}$	0.35	0.5	Yuan [97]
$Pd_{92}Gd_8$[a] $Pd_{88.7}Gd_{6.3}Ag_5$[a]	5.33 5.66	0.5	Sakamoto [98]
$Pd_{90}Ni_{10}$	0.27	0.5	McKinley [35]
$Pd_{93.4}Y_{6.6}$[a] $Pd_{90}Y_{10}$[a]	5.39 5.69	0.5	Fort [92]
$Pd_{92}Y_8$[a]	3.82	0.5	Hughes [94]
$Pd_{92}Y_8$[a] $Pd_{85.3}Y_{4.7}Ag_{10}$[a]	3.92 3.70	0.5	Sakamoto [98]

[a] denotes at%.

Using density functional theory (DFT) analysis on an array of Pd_3M alloys, it has been shown that hydrogen solubility is more dependent on electronic structure and less on lattice parameter [99]. As a result, attempts have been made to elucidate and develop a model that is capable of describing the nature of the electronic interaction between the dissolved hydrogen and the host alloy. Furthermore, it has also been demonstrated that the solubility of hydrogen in a metal is mainly dependent on the enthalpy of solution which is strongly related to the density of states (DOS) of the d-orbital for said metal [100].

Consideration should be given to the structure adopted by each alloy component when determining its DOS [77]. Since the introduction of an impurity to a metal can alter its DOS and in addition can change its heat capacity [101]. The DOS for an alloy is typically determined using rigid band approximation, which is based on the assumption that the band shape is unchanged upon alloying; however, the energy of all states is shifted depending on the impurity content [102].

Ebisuzaki and O'Keeffe [100] have applied the rigid band approximation alongside DOS data for transition metals [102, 103] to determine the change in DOS for alloys with different electron per atom ratios. The limitation of this model is that it may only apply to elements with the same crystal structure and are adjacent to each other on the periodic table [104]. Moreover, the rigid band approximation cannot be applied to elements in different blocks due to the increase in valence band width between the 3d and 5d blocks [77]. As a result, other models have been developed such as the tight binding recursion method [105, 106] and the superposition model based on charge transfer between unit cells of constituent metals [104]. Nonetheless, the rigid band approximation has proven to accurately determine the DOS of various alloys [101, 107].

Hydrogen solubility has been predicted using DFT and used to calculate the solubility constant whereby the chemical potential of interstitial and gaseous hydrogen are equated [77]. This technique has been applied to crystalline Pd alloy membranes [87, 99, 108-111], amorphous non-Pd alloy membranes [112-114], AB_2 hydrogen storage alloys [115-117] but currently not to binary higher order BCC Group IV and V alloy membranes.

2.2.4. Hydrogen absorption in palladium and palladium alloys

Before hydrogen absorption can occur in a metal, the hydrogen gas molecule adsorbs onto the metal surface and dissociates to form individual hydrogen atoms. This is a process known as dissociative chemisorption. Following dissociative chemisorption, the adsorbed hydrogen atoms are then ionised to produce a proton (H^+) and an electron (e^-) and subsequently absorbed by the host metal. This reaction is described in Equation 2.17:

$$^1/_2\, H_{2(gas)} \rightleftharpoons H^+_{(metal)} + e^-_{(metal)} \qquad \text{Equation 2.17}$$

Like with most reactions there is an associated activation energy and in certain metal-hydrogen systems dissociation of the hydrogen molecules can be the rate limiting step in the formation of a hydride phase.

Once the hydrogen is in monatomic form, it dissolves into the bulk metal to form either an interstitial solid solution or metal hydride phase. For a period of time it was debated in the chemical literature as to whether the dissolved hydrogen in transition metals exists as a H atom or if this atom donates or even accepts an electron. Svensson [118] observed that the magnetic susceptibility of PdH_x drops linearly with increasing hydrogen content to zero at a H/Pd atomic ratio of 0.6. Similar behaviour was also reported for the Ni-H system [119].

These findings were interpreted as the hydrogen atoms ionising and donating electrons to Pd gradually filling the d-band up until a H/Pd atomic ratio of 0.6 is reached at which point the d-band is full [120].

The dissolution of a single hydrogen atom can be described using the following steps as suggested by Franck [121] and Ebisuzaki and O'Keeffe [100]:

$$H_{(gas)} \rightleftharpoons H^{+}_{(gas)} + e^{-}_{(gas)} \qquad \text{Equation 2.18}$$

$$H^{+}_{(gas)} \rightleftharpoons H^{+}_{(metal)} \qquad \text{Equation 2.19}$$

$$e^{-}_{(gas)} \rightleftharpoons e^{-}_{(metal)} \qquad \text{Equation 2.20}$$

Initially, the hydrogen atom is considered to be ionised on the metal surface to form a proton and an electron (Equation 2.18) which are subsequently absorbed into the bulk metal as described in Equation 2.19 and Equation 2.20, respectively. When the dissolved hydrogen donates an electron to the host metal it becomes a proton and in effect increases the local electron density. From empirical evidence, Ebisuzaki and O'keeffe [100] surmised that the screened-proton model sufficiently described the behaviour of dissolved hydrogen in transition metals.

The concentration of hydrogen inside the metal is described by Sieverts' law (Equation 2.21) which is a variation of Equation 2.3:

$$C = P_{H_2}^{1/2} exp\left(\frac{-\Delta G^0}{RT}\right) \qquad \text{Equation 2.21}$$

where ΔG^0 is the change in standard free energy of the hydrogen solution reaction shown in Equation 2.18. This term can also be defined in Equation 2.22:

$$\Delta G^0 = \Delta H^0 - T\Delta S^0 \qquad \text{Equation 2.22}$$

where ΔH^0 and ΔS^0 are the changes in standard enthalpy and entropy, respectively, for the dissolution of hydrogen into the metal. As a result, the solubility constant (S) shown in Equation 2.2 can be expressed in thermodynamic terms (Equation 2.23):

$$S = exp\left(\frac{-\Delta G^0}{RT}\right) \qquad \text{Equation 2.23}$$

At low C, Sieverts' law provides an adequate description of the variation of hydrogen solubility in a metal as a function of the square root of pressure. Assuming a low value for C is assumed, Sieverts' law is a useful model for predicting hydrogen solubility in a Pd-based membrane under typical operating conditions [122]. As C increases, however, deviation from Sieverts' law occurs for the following reasons [123]:

- Elastic strain energy of the dissolved hydrogen expands the metal lattice to a point where it becomes a significant factor in determining hydrogen solubility.
- The electronic properties of the metal-hydrogen system change as the ratio of free electrons to free metal atoms increase.
- Hydrogen-hydrogen interaction of an attractive or repulsive nature increases.
- The entropy stops representing a random occupancy of dissolved hydrogen within the unoccupied interstitial sites.

The process of hydrogen absorption into the host metal can be represented by the partial molar enthalpy of hydrogen at infinite dilution, ΔH_H, shown in Equation 2.24 [43, 100]:

$$^1/_2\,\Delta H_H = E_{st} + E_{pol} + E_{rep} - E_w + {}^1/_2\,E_{dis} + E_I + E_0 \qquad \text{Equation 2.24}$$

where E_{st} is the elastic strain energy imposed by the proton upon the host metal lattice, E_{pol} is the energy change as a consequence of the conduction electrons becoming polarised by the protons, E_{rep} is the coulombic repulsion energy between the screened proton and ion cores, E_w is the work function of the metal, E_{dis} is the hydrogen molecule dissociation energy, E_I is the ionisation energy of a hydrogen atom, E_0 is the zero point energy.

It has been assumed that all of the energy terms on the right hand side of Equation 2.24 are somewhat constant for various alloys with the exception of E_{st} and E_{pol}. Hence, differences in ΔH_H between various alloys can be attributed to the variation in either E_{st} or E_{pol} [43]. It is interesting to note that Ebisuzaki and O'Keeffe [100] propose that E_{pol} has the most influence on ΔH_H over all other energy terms and have excluded E_{st} from their calculations. At very low hydrogen concentrations, E_{pol} is considered to be constant for different alloys and equivalent to that of its pure metal [124-126].

Figure 2.7 demonstrates the dissolution of hydrogen into metals such as Pd using a simplified diagram adapted from Blagojević et al [127]. Initially, the hydrogen molecule moves towards the metal surface and can be physisorbed onto either an 'on-top' or hollow site through a Van der Waals type interaction. The molecule is then dissociated and the monatomic hydrogen atoms are chemisorbed into subsurface interstitial sites which results in the slight displacement of the above metal atoms. The hydrogen atoms proceed to diffuse further into the bulk metal.

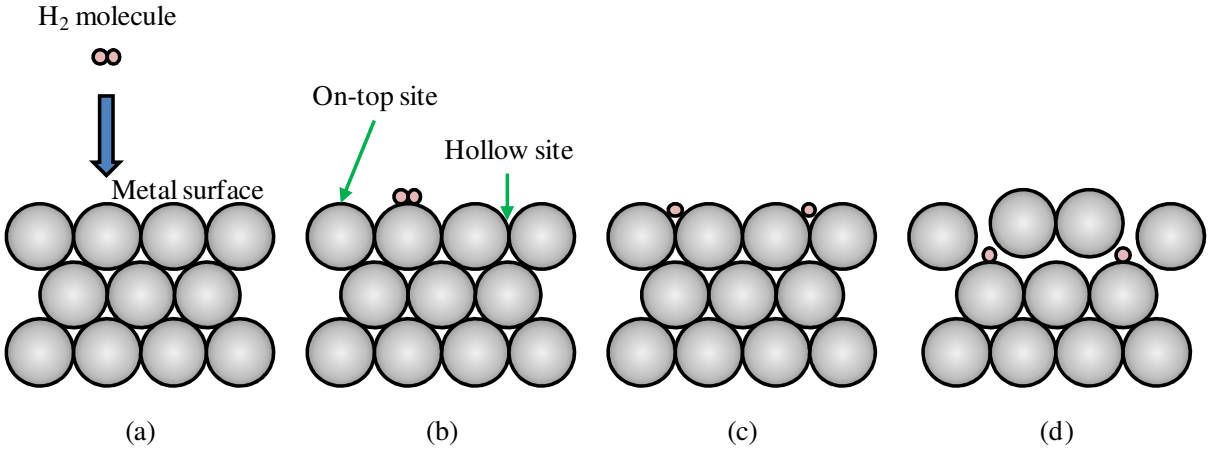

Figure 2.7 Diagram depicting the hydrogen dissolution process adapted from Blagojević et al [127]. Step (a) hydrogen molecule approaches the metal surface, (b) physisorption of the hydrogen molecule onto the metal surface through Van der Waals interaction, (c) dissociation of the hydrogen molecule followed by dissociative chemisorption and (d) occupation of subsurface interstitial sites which is then proceeded by diffusion into the bulk metal. Furthermore, on-top and hollow sites are indicated.

From an energetic perspective, Figure 2.7 can be related to a plot of potential energy as a function of distance into the metal (Figure 2.8). Studies have shown that the metal surface orientation has an influence on hydrogen occupation of subsurface sites. Reconstructed (110) surfaces of Pd and Ni or on less densely packed planes facilitate occupation of subsurface sites at low temperatures (100 K) and hydrogen pressures (10^{-6} Pa) [128-130], while higher temperatures and pressures are required for more densely packed planes [128].

In Figure 2.8, the energy levels represent the chemical potential of each hydrogen state during the dissolution process. Step (a) shows the chemical potential of a single hydrogen atom in the gaseous state, $H_{(gas)}$, moving towards the metal surface. Two hydrogen adsorbed states, $H_{(ads)}$, are shown where step (b) corresponds to the chemical potential of a single hydrogen atom adsorbing onto an on-top site and step (c) relates to the chemical potential associated with a single hydrogen atom adsorbing onto a hollow site. Subsequently, step (d) refers to the chemical potential of a single hydrogen atom in the subsurface interstitial sites, $H_{(ss)}$, which is then followed by diffusion into the bulk metal.

The plot further shows that adsorption is activated in the shallow energy wells of the on-top sites requiring high hydrogen pressure to be filled, whereas adsorption in the hollow sites is non-activated thus occurring spontaneously. In addition, hydrogen absorption is shown to be somewhat endothermic with a high activation energy barrier present between an adsorbed hydrogen atom on a hollow site, $H_{(ads)}$, and the absorbed state, $H_{(abs)}$. The heights of the activation energy barriers and depths of the energy wells depend on the properties of the metal, surface structure and hydrogen coverage. The activation energy barrier between step (c) and (d) could potentially be lowered by high hydrogen coverage or a surface reconstruction [128].

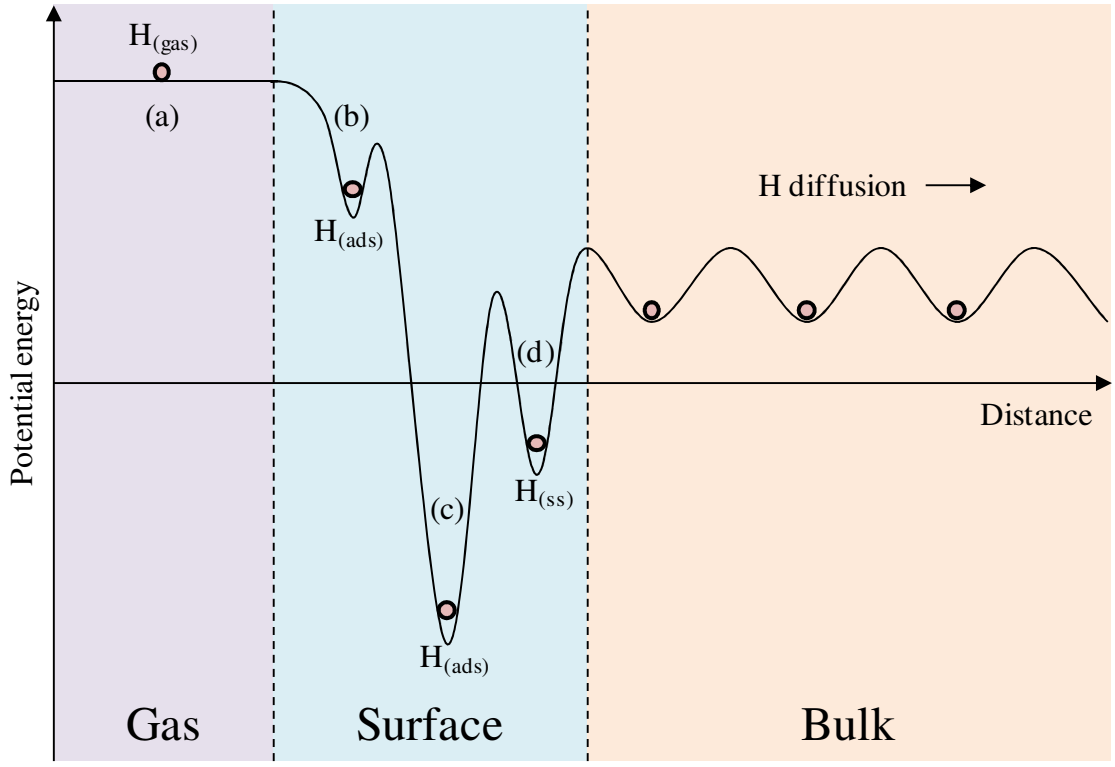

Figure 2.8 Plot of potential energy as a function of distance adapted from Protopopoff and Marcus [131] showing the different states of a single hydrogen atom during the dissolution process. Steps (a), (b), (c) and (d) correspond to the steps shown in Figure 2.7. Step (a) represents the chemical potential for a hydrogen atom in the gaseous state approaching the metal surface, (b) an energy well for hydrogen adsorption ($H_{(ads)}$) onto an on-top site, (c) an energy well for hydrogen adsorption ($H_{(ads)}$) onto a hollow site and (d) an energy well for hydrogen occupation of subsurface interstitial sites ($H_{(ss)}$) and subsequent absorption ($H_{(abs)}$) and diffusion into the bulk metal.

The behaviour of hydrogen solubility with temperature is dependent on the chemical properties of the host metal. This is determined by the tendency of the host metal to either form a solid solution or a stable metal hydride [132]. Examples of metals that exhibit an increase in hydrogen solubility with rise in temperature are Mn, Fe, Co and Ni which are known as endothermic occluders. These metals only form solid solutions with hydrogen occupying random sites [77]. For the purpose of hydrogen separation, metals like Pd, Ti, V, Nb and Zr are popular and are classed as exothermic occluders [133] since they exhibit a decrease in hydrogen solubility with increasing temperature. This is due to the propensity of the metal to form a stable and ordered metal hydride [77].

Commonly, Pd readily accepts donor electrons from other atoms such as hydrogen due to the aforementioned overlapping energy bands located between the 4d and 5s energy bands. The occupancy of the hydrogen atom distorts the lattice and introduces an elastic strain energy. The insertion of four hydrogen atoms into the Pd FCC unit cell results in a volume expansion of 11.5 $Å^3$ hence one hydrogen atom produces an increase in volume of 2.9 $Å^3$ [134].

A pressure-composition-temperature (PCT) diagram is commonly used to understand the thermodynamic properties of a metal-hydrogen system. Figure 2.9 is a PCT diagram for the palladium-hydrogen system featuring a series of isotherms that show the absorption behaviour at different hydrogen pressures. Similar to Figure 2.6, three distinct regions can be shown in the Pd-H PCT diagram which are the α-PdH phase, α-PdH + β-PdH mixed phase and β-PdH phase. The extent of each isotherm plateau defines the miscibility gap which corresponds to the conditions where the α- and β-PdH phase coexist.

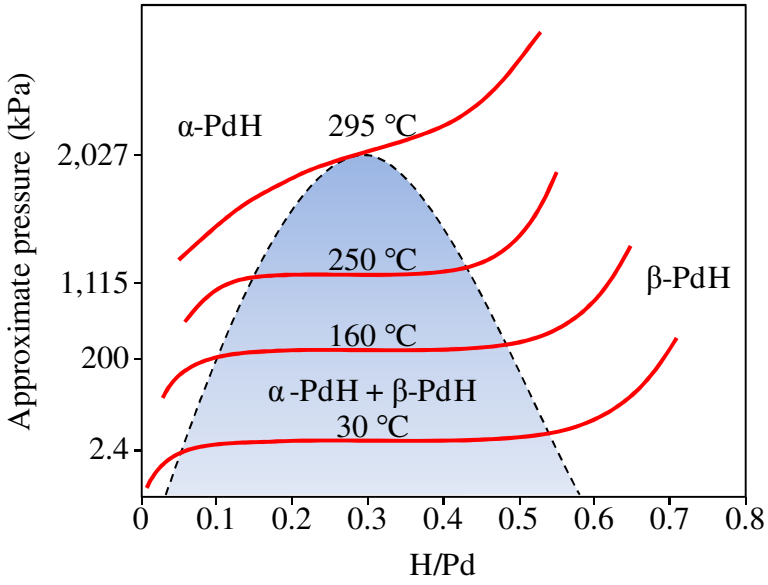

Figure 2.9 Pd-H PCT diagram reproduced from Knapton showing a series of isotherms that define the miscibility gap region [135].

At conditions below 300 °C and 2 MPa of hydrogen pressure, an increase in hydrogen concentration within Pd results in the formation of the β-PdH phase which creates considerable lattice expansion causing stresses to be built up inside the metal. The Pd-Cu system has been selected for this work since the miscibility gap is closed above room temperature meaning that membranes fabricated from this alloy do not suffer from hydrogen embrittlement caused by cycling between the α- and β-PdH phases.

Hydrogen solubility in Pd alloys such as Pd-Cu and Pd-Ag, have been studied through comparison of solubility at a standard pressure of 101.325 kPa [100] and by determining the composition of the hydride phase [136]. In both instances, the findings show evidence of an electronic effect influencing hydrogen solubility. Since Pd-Cu and Pd-Ag have an almost identical electron band structure it would therefore be expected that both alloys have similar hydrogen solubility values yet Figure 2.10 gives evidence to the contrary.

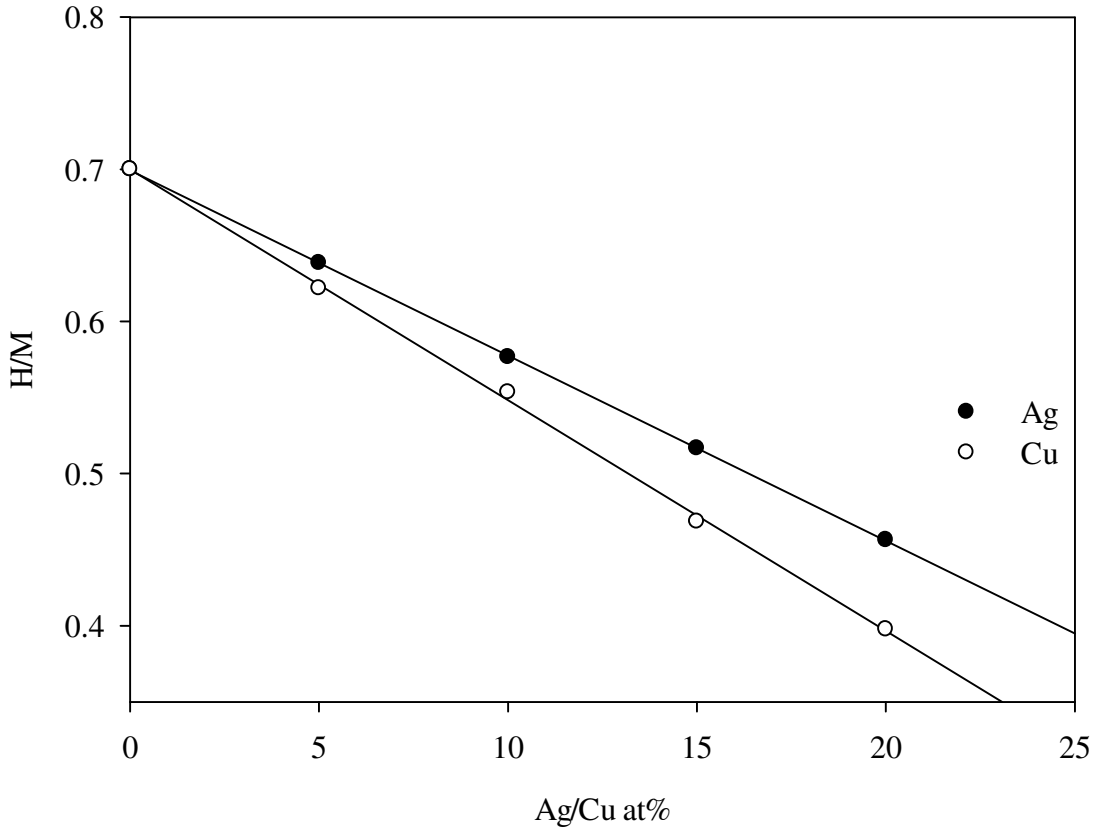

Figure 2.10 Hydrogen solubility at 101.325 kPa and 30 °C as a function of alloy composition for Pd-Cu and Pd-Ag, reproduced from Burch and Buss [43].

At 101.325 kPa of hydrogen pressure and 30 °C, hydrogen solubility (ratio of hydrogen to metal atoms (H/M)) in Pd-Cu alloy decreases more rapidly with increasing Cu content than the Pd-Ag alloy with increasing Ag content. This can be attributed to the difference between lattice parameters of both alloy systems since an increase in Cu content in the Pd-Cu system results in a decrease in lattice parameter whereas the reverse is true upon increase of Ag content in the Pd-Ag system. The relatively larger lattice parameter of the Pd-Ag system means that a proton imparts less strain energy upon dissolution resulting in a decrease in ΔH_H compared with values associated with the Pd-Cu system as shown in Table 2.5:

Table 2.5 Relative partial molar enthalpies and lattice parameters for Pd-Cu and Pd-Ag alloys.

Alloy composition (at%)	ΔH_H (kJ mol^{-1})	Lattice parameter (Å)
Pd	-18.0[a]	3.889[c]
$Pd_{95}Cu_5$	-17.7[a]	3.877[c]
$Pd_{90}Cu_{10}$	-17.4[a]	3.865[c]
$Pd_{85}Cu_{15}$	-16.4[a]	3.853[c]
$Pd_{80}Cu_{20}$	-16.0[a]	3.840[c]
$Pd_{90}Ag_{10}$	-30.8[b]	3.906[d]
$Pd_{80}Ag_{20}$	-39.1[b]	3.926[d]

[a] [43], [b] [136], [c] [137], [d] [138].

Hydrogen solubility of other commercial Pd alloys such as Pd-Y have been investigated by Yoshihara and McLellan [139] at various temperatures. It was shown that hydrogen solubility increased with increasing Y content over the entire Pd-Y solid solution range. Maximum hydrogen solubility was also shown to decrease with increasing temperature due to the exothermic nature of hydrogen absorption in the Pd-Y system. Furthermore, it was observed that the partial molar enthalpy of hydrogen at infinite dilution, ΔH_H, decreased with increasing Y content which was attributed to lattice dilation caused by the addition of Y.

The Pd-Ce alloys exhibit relatively lower hydrogen solubility in comparison to Pd-Y alloys [140] despite Ce expanding the metal lattice more so than Y [81]. Yoshihara and McLellan [139] suggest that Y atoms have a trapping effect on the dissolved hydrogen, whereas Yoshinari et al [141] propose that this phenomenon only occurs at low temperatures of between 100 – 150 K. The hydrogen solubility in the Pd-Y system has been shown to be influenced by the thermal history of the alloy in particular at high Y contents [142].

The improvement of hydrogen solubility in Pd-Y alloys has also been noted by Yoshinari et al [141]. Using an electrolytic method, hydrogen solubility at room temperature was determined for Pd, $Pd_{98}Y_2$ at% and $Pd_{95}Y_5$ at%. The results revealed that compared to pure Pd, the

$Pd_{98}Y_2$ at% and $Pd_{95}Y_5$ at% alloys had an increase in solubility by a factor of 1.7 and 2.3, respectively.

2.2.5. Hydrogen diffusion in palladium and palladium alloys

As previously mentioned, hydrogen propagates through non-porous media such as dense metal membranes via means of solution-diffusion. A mechanism that is not entirely understood, yet nonetheless is used to describe the behaviour of hydrogen with certain metal membranes. The permeated hydrogen from these membranes is sufficient to power PEFCs and in some cases can operate at temperatures corresponding to industrial processes such as the water gas shift reaction (350 °C), steam methane reformation (815 °C) and methanol synthesis (300 °C).

To date, many theories have been proposed in order to elucidate the mechanism behind hydrogen diffusion through a metal lattice and this is still subject to a fair deal of speculation. However, Kehr [143] has suggested several different mechanisms for hydrogen diffusing through metal lattices, such as in Pd, which are all temperature dependent. Figure 2.11 displays the four types of diffusion.

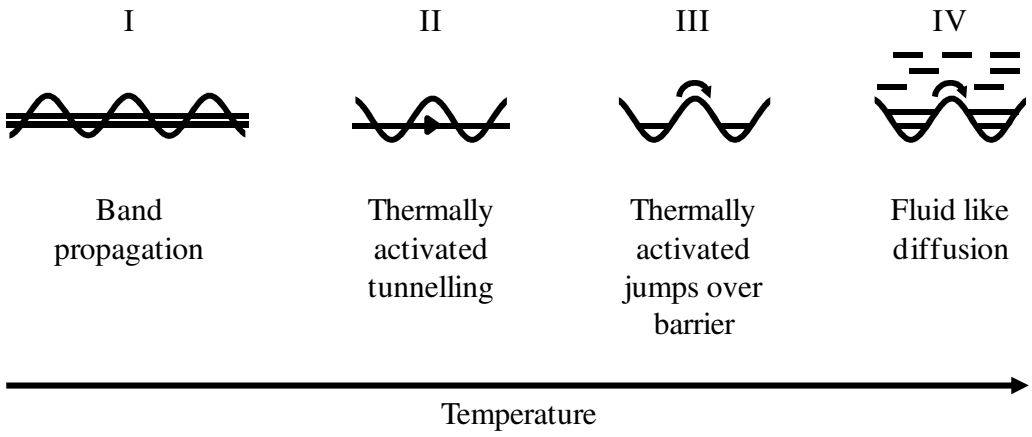

Figure 2.11 Kehr's proposed diffusion models for hydrogen in metals [143].

At extremely low temperatures, there are virtually no thermal vibrations which are also known as phonons (Region I). In this state, hydrogen atoms are able to become "self trapped" due to the relaxation of the surrounding metal lattice. It is then assumed that the hydrogen atoms progress to the adjacent interstitial site via a quantum mechanical process referred to as 'band propagation'. As the temperature increases, hydrogen atoms are transported through a mechanism referred to as thermally activated tunnelling (Region II) which involves phonons. At higher temperatures (Region III), hydrogen atoms are modelled as classical particles and are able to execute over-barrier jumps between neighbouring interstitials sites. At even higher temperatures (Region IV), hydrogen atoms behave more like a fluid similar to the flow of liquids and gases as opposed to being confined to interstices.

Kehr [143] notes that these mechanisms are simply broad qualitative assumptions whereby more than one method of transport can transpire at a given temperature. Region III is of interest as this is expected to occur between 200 – 600 °C which is comparable to the operating temperature of a metal membrane. Therefore, the diffusion mechanism used in Pd and its alloys can be described by the thermally activated jumps over barrier method which involves classical rate theory [144]. The jump rate of a hydrogen atom between interstitial sites (Γ) is expressed in Equation 2.25:

$$\Gamma = n_i v \, exp\left(\frac{-E_A}{k_B T}\right) \qquad \text{Equation 2.25}$$

where, n_i is the nearest number of neighbouring interstitial sites, v is the vibrational frequency of the solute hydrogen atom in an interstitial site, E_A is the activation energy and k_B is Boltzmann's constant. For interstices in a cubic lattice, the theoretically derived diffusivity (D) can be expressed as the following (Equation 2.26):

$$D = a^2 \gamma \Gamma \qquad \text{Equation 2.26}$$

where a is the lattice parameter and γ is the geometric factor which is 1/12 for the FCC lattice and 1/24 for the BCC lattice. Combining Equation 2.25 and Equation 2.26 gives Equation 2.27:

$$D = a^2 \, \gamma n_i v \, exp\left(\frac{-E_A}{k_B T}\right) \qquad \text{Equation 2.27}$$

The activation energy (E_A) term can be separated into two parts as shown in Equation 2.28:

$$E_A = \Delta H - T\Delta S \qquad \text{Equation 2.28}$$

where ΔH is the change in molar enthalpy as a result of lattice distortion created by hydrogen atoms jumping between interstitial sites and ΔS is the change in molar entropy as a result of change in vibrational frequency. Equation 2.27 and Equation 2.28 can be combined to give Equation 2.29:

$$D = a^2 \, \gamma n_i v \, exp\left(\frac{-\Delta H}{RT}\right) exp\left(\frac{\Delta S}{R}\right) \qquad \text{Equation 2.29}$$

Certain terms can be merged into the pre-exponential constant (D_0) to give the simplified Arrhenius relationship (Equation 2.10) previously mentioned in Section 2.1.3.

Equation 2.10 is only valid under certain conditions and as already stated the operating temperatures for membrane applications are normally in the range of 200 – 600 °C where the concentration of hydrogen is relatively low and the diffusion of hydrogen can be sufficiently described by the classical diffusion model (Equation 2.10). Diffusion of solute atoms in

metals becomes non-classical at temperatures below 100 K, at high hydrogen concentrations and with different hydrogen isotopes. Hence, Equation 2.10 is not valid under these conditions and so a quantum theory of diffusion is necessary [145]. To date, no theory has been able to accurately model the diffusion of solute atoms in a metal for each temperature regime.

A variety of methods have been used to measure the diffusion of hydrogen in metals such as mechanical relaxation, X-ray and permeation techniques. A majority of diffusion data is obtained with the aid of non-equilibrium techniques like the Gorsky effect and permeation measurements. The Gorsky effect uses the lattice relaxation effect which involves the diffusion of hydrogen atoms from one side under compression to another side under tension whereby the diffusivity is determined by measuring the time taken for elastic relaxation [145]. This technique negates any surface effects meaning that accurate diffusion data can be obtained. Furthermore, diffusion data can be acquired by determining the jump frequency of hydrogen atoms using equilibrium measurements like quasi-elastic neutron scattering (QNS) and nuclear magnetic resonance (NMR).

The crystal structure has a marked effect on the solubility and diffusion mechanism of a dense metal membrane. The BCC crystal structure features an atom positioned at each corner of the cubic unit cell and one in the centre as shown in Figure 2.12. A range of transition metals form the BCC crystal structure such as W, V, Cr, Rb, Nb, Mo and Ta. Furthermore, Pd alloys such as the Pd-Cu system form an ordered BCC crystal structure which is shown in Figure 2.12.

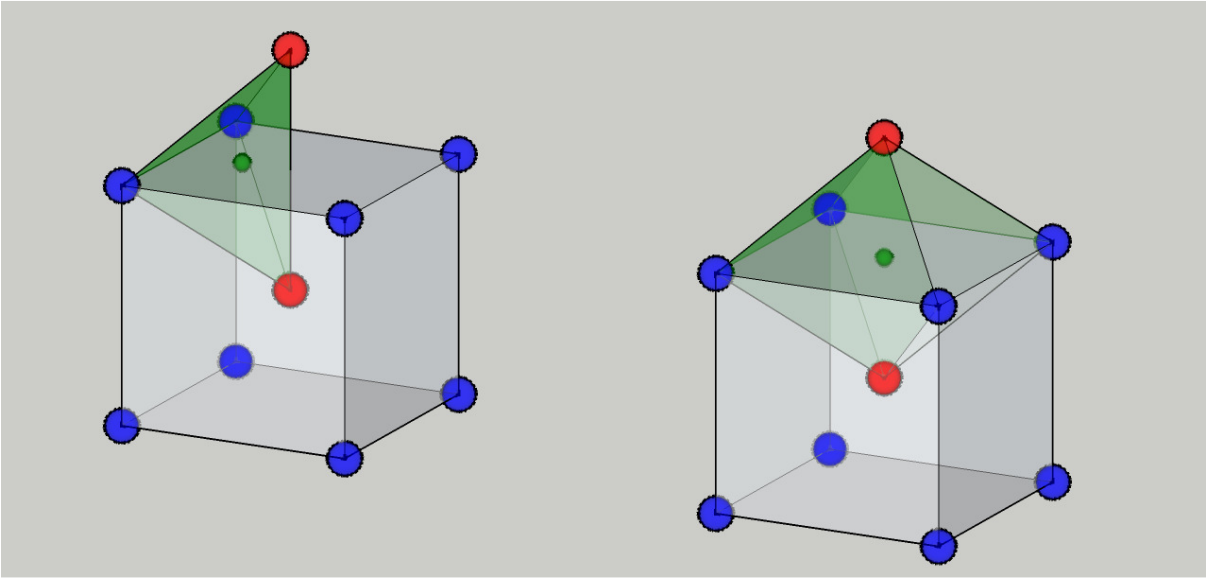

Figure 2.12 A representation of the BCC unit cell, showing the arrangement of Pd atoms (red spheres) and Cu atoms (blue spheres) in this type of crystal structure. An example of a tetrahedral site (left) and octahedral site (right) is also highlighted revealing the position occupied by the hydrogen atom (green sphere) in each case during diffusion.

Similarly, the FCC crystal structure is another type of cubic unit cell, however, an atom is positioned at the centre of each face of the cubic unit cell as opposed to being situated at the centre of the 3D cell as shown in Figure 2.13. This type of crystal structure is adopted by Pd and a variety of Pd alloys. Note, that the length of each dimension of the cubic unit cell is known as the lattice parameter.

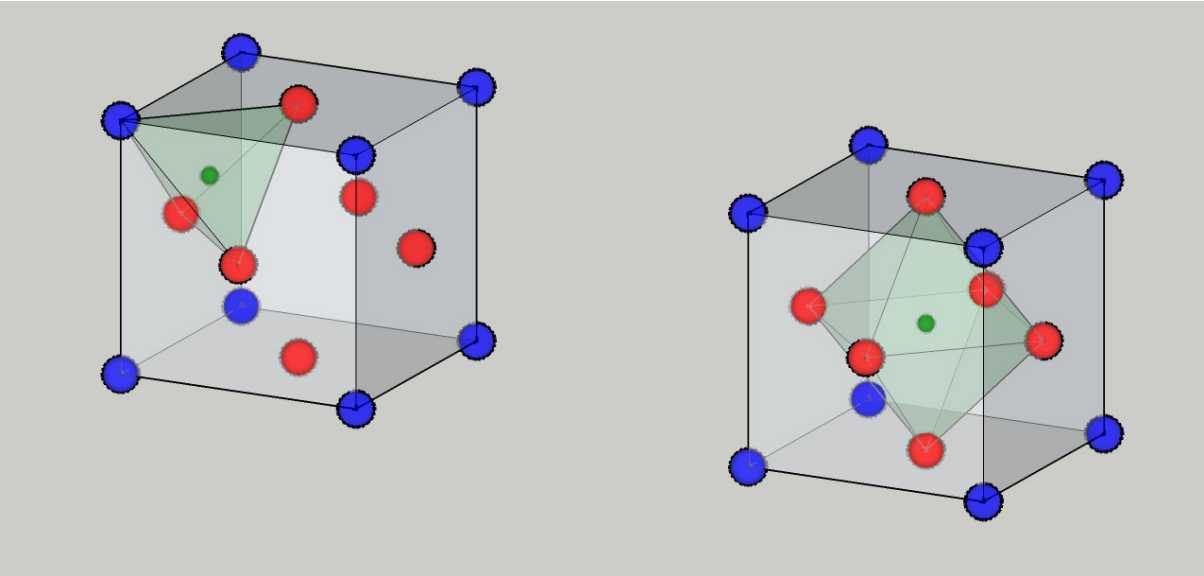

Figure 2.13 A representation of the FCC unit cell, showing the arrangement of Pd atoms (red spheres) and Cu atoms (blue spheres) in this type of crystal structure. An example of a tetrahedral site (left) and octahedral site (right) is also highlighted revealing the position occupied by the hydrogen atom (green sphere) in each case during diffusion.

Both crystal structures feature octahedral (O) and tetrahedral (T) interstitial sites which can be occupied by dissolved monatomic hydrogen. Table 2.6 shows the different concentrations and varying sizes of the interstices existing within the BCC and FCC unit cell that help dictate the hydrogen solubility and transport mechanisms of the metal.

Table 2.6 Crystallographic data for BCC and FCC metals [77].

Structure	**BCC**		**FCC**	
Space group	*Im3m*		*Fm3m*	
Interstitial site	Octahedral	Tetrahedral	Octahedral	Tetrahedral
Number per atom	3	6	1	2
Size relative to M atom radius	0.155	0.291	0.414	0.225
Packing density (%)	68		74	

As shown in Table 2.6, there are 3 times more O and T sites available in the BCC crystal structure compared to that of the FCC crystal structure; however it should be noted that the T sites surrounding the BCC O sites are severely distorted. Furthermore, the T sites in the BCC

crystal structure are larger than the O sites, whereas the reverse is true in the FCC crystal structure [77].

The Nb-H system has been investigated by Gissler and Rother [146] with the aid of quasielastic neutron scattering in order to study the transport of hydrogen in a BCC metal. From this work, Dolan [77] concludes that hydrogen propagates through the BCC metal lattice via a series of hops between O and T sites and further suggest that the (1/4) (111) hexahedral site may also have an involvement in the diffusion process.

Upon dissolution, the hydrogen atom has a tendency to occupy O interstitial sites in the Pd FCC unit cell [100]. Data for diffusion of hydrogen in an FCC metal, such as Pd, was collated from 25 authors by Völkl and Alefeld [40]. The pre-exponential constant and activation energy were calculated to be $D_0 = 2.90 \times 10^{-3}$ cm^2 s^{-1} and $E_A = 22.2$ kJ mol^{-1}, respectively. These values, however, are approximately an order of magnitude higher when compared to Group V BCC metals such as V and Nb.

Conversely, DOS calculations have shown that hydrogen will preferentially inhabit the O sites as opposed to the T sites in the Pd system since the O interstices are far more stable [147, 148]. Although, it has been argued in literature that hydrogen can also occupy T sites as well as O sites in the Pd lattice. In-situ high resolution neutron diffraction studies at 310 °C of Pd loaded with 9 MPa of deuterium revealed significant T site occupation [149]. Furthermore, it has also been cited in literature that the activation energy for diffusion of hydrogen increases with increasing distance between interstitial sites, hence diffusivity is greater in metals with shorter lattice parameters [150].

Theoretical models such as DFT are commonly used in conjunction with experimental data to predict the diffusion of hydrogen in pure metals as well as in ordered and disordered alloys

[151]. The rate of thermally activated jumps between interstitial sites can be determined by calculating vibrational frequencies of the hydrogen atoms in the interstitial sites and the activation energy for jumping which is also known as the transition state [77].

Additionally, DFT has been useful in proving that activation energy for hydrogen diffusion between neighbouring tetrahedral interstices in Group V BCC metals such as Ta is greater than Nb [152]. Moreover, it has also been shown that at temperatures which correspond to the operating temperature of dense metal membranes (~400 °C), hydrogen diffusion was best described by over-barrier thermally activated jumps [77]. This is in good agreement with Kehr's aforementioned model demonstrated by region III in Figure 2.11. In metals with relatively small lattice parameters, thermally activated tunnelling is expected to dominate which is outlined in Kehr's model in region II of Figure 2.11. Hence, alloying metals such as Pd, V, Nb and Ta with smaller elements can increase the contribution of phonon assisted tunnelling in hydrogen diffusion [77].

In most instances, substitutional alloying of Pd with other elements has the effect of reducing hydrogen diffusivity, irrespective of whether the solute atom increases or decreases the lattice volume. An exception to this is the $Pd_{60}Cu_{40}$ wt% alloy which forms the ordered BCC phase below 600 °C [153, 154]. It has been reported, that this ordered phase has the highest room temperature diffusivity ($D = 2.0 \times 10^{-5}$ cm^2 s^{-1}) compared to any metal-hydrogen system and is two orders of magnitude greater than that of pure Pd ($D = 2.0 \times 10^{-7}$ cm^2 s^{-1}) [39]. Despite, such high hydrogen diffusivity, the hydrogen permeability is relatively low since increasing Cu content reduces hydrogen solubility unlike Ag and Y.

The room temperature hydrogen diffusivity was measured by Barlag et al [155] for various FCC Pd alloys which were made using elements that have high hydrogen solubility (V and

Nb) and low hydrogen solubility (Ag, Cu and Ni) relative to pure Pd, the results of which are displayed in Figure 2.14. It was shown that there was little change in hydrogen diffusivity at Ag concentrations of ≤ 20 at%. This observation agreed well with work by Holleck [85] who observed negligible change in E_D from pure Pd to $Pd_{80}Ag_{20}$ at% as shown in Table 2.7. At Ag concentrations greater than 20 at%, a sharp decrease in hydrogen diffusivity is seen in Figure 2.14 reaching a minimum at approximately $Pd_{40}Ag_{60}$ at% and subsequently increasing with further Ag additions up until the value of pure Ag is achieved.

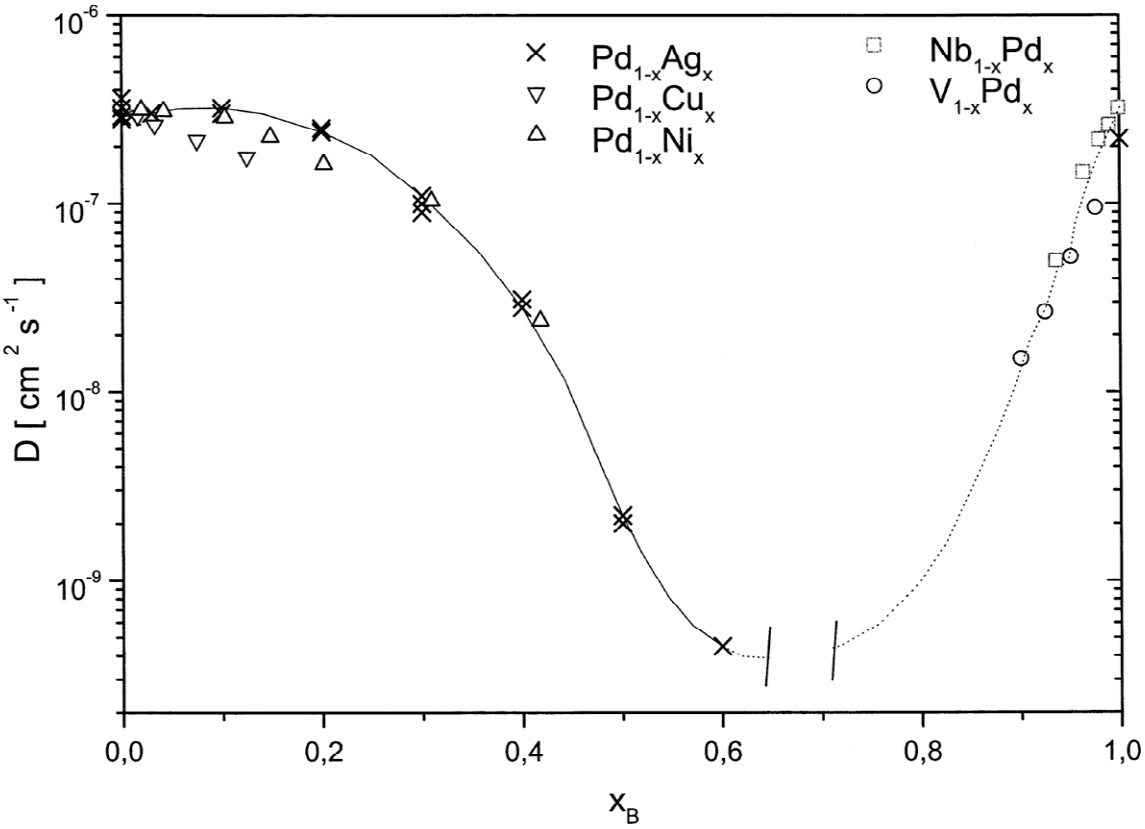

Figure 2.14 Hydrogen diffusivity in $A_{1-x}B_x$ alloys at low hydrogen concentrations where hydrogen solubility in A is greater than in B [61].

Using a Monte Carlo simulation method, Barlag et al [155] was able to explain the variation of hydrogen diffusion as a function of Ag content by proposing a simple two-state model. In

this model, it is assumed that two types of O sites exist giving rise to different hydrogen occupation probabilities or different hydrogen solubility values.

Barlag et al [155] mention that at low Ag additions, the Ag atoms partially obstruct the energetically favourable hydrogen diffusion route in the Pd matrix, resulting in a round-about way trajectory. With increasing Ag content, Pd atoms behave like traps in a Ag matrix thus hindering the diffusion of hydrogen through the lattice. A similar trend is observed in the FCC phase region when substituting Ag with less hydrogen soluble elements such as Ni or Cu. Upon alloying Pd with elements which have relatively higher hydrogen solubility values, such as Nb and V, it was found these metals acted as hydrogen traps in the Pd matrix therefore reducing its diffusivity. From these observations, Barlag et al [155] proposed that alloying Pd with elements with relatively higher hydrogen solubility would result in reduction in diffusivity due to this trapping effect.

Table 2.7 Hydrogen diffusion data for Pd and various Pd alloys with compositions expressed in at%.

	E_D (kJ mol^{-1})	D_0 (cm^2 s^{-1}) × 10^{-3}	Reference
Pd	22.2	2.90	[40]
Pd	22.0	2.94	[85]
$Pd_{90}Ag_{10}$	22.2	2.69	[85]
$Pd_{80}Ag_{20}$	22.3	2.33	[85]
$Pd_{75}Ag_{25}$	25.9	3.07	[93]
$Pd_{75}Ag_{25}$	29.6	1.04	[156]
$Pd_{47.5}Cu_{52.5}$	10	3.0	[39]
$Pd_{92}Y_8$	30.9	1.23	[156]

Electronic effects have also been shown to have a large influence on E_D for several Pd alloys relative to pure Pd. It has been shown by the work of Buchold et al [157] that variation in E_D is proportional to the valence electron concentration (VEC). This quantity is defined as the total number of valence electrons in the alloy per atom. It was suggested that the increase in

E_D with solute concentration is attributed to the filling of the Pd d-band resulting in a reduction in proton screening. Therefore, there appears to be a correlation between E_D and the VEC of the alloy.

Hughes and Harris [94] were able to confirm the theory of Buchold et al by investigating the hydrogen diffusivity in $Pd_{92}Y_8$ at%, $Pd_{75}Ag_{25}$ at% and $Pd_{94.25}Ce_{5.75}$ at% using permeation experiments. Furthermore, the hydrogen diffusivities of these alloys were found to have an Arrhenius-type relationship with temperature. From Table 2.7 it can be seen that $Pd_{92}Y_8$ at% and $Pd_{75}Ag_{25}$ at% have similar E_D and D_0 values which can be ascribed to the similar VEC values. This highlights that the difference in their hydrogen permeability can be attributed to differences in hydrogen solubility in both alloys.

2.3. Pd-Cu system

Currently, Pd-Cu alloy membranes remain of interest for the purpose of hydrogen separation applications due to their high catalytic activity for hydrogen dissociation, high permeability and mechanical robustness. Furthermore, Pd-Cu alloys containing the crystalline FCC crystal structure have shown potential to purify hydrogen feed streams containing impurities such as H_2S [44, 45, 158, 159]. This alloy system exhibits better resistance to hydrogen embrittlement and H_2S poisoning than pure Pd and Pd-Ag alloy membranes [35, 36].

2.3.1. Phase diagram

Ruer [160] conducted preliminary studies into the Pd-Cu binary system using thermal analysis and metallography. Taylor [161]; Jones and Sykes[162]; Nemilov [163]; and Jaumot and Sawatzky [164] have also investigated this system. Nemilov [163], was able to establish the Pd-Cu liquidus using thermal analysis data. Hansen [165] published a Pd-Cu phase diagram

featuring the solidus and liquidus based from data acquired from Ruer [160] and Nemilov [163].

The existence of the ordered $AuCu_3$ type structure was observed in Pd-Cu alloy compositions of less than 20 at% Pd and a tetragonal structure was seen in the compositional range of 20 – 25 at% Pd [162, 164, 166]. Schubert et al [167, 168] theorised that between 18.5 – 25 at% Pd a one dimensional long-period superlattice (1D-LPS) structure forms with a more complex LPS structure occurring between 25.5 – 30 at% Pd. It was later discovered by Watanabe et al [169] that this complex LPS phase was indeed the 2D-LPS structure. The 2D-LPS phase has a large orthorhombic unit cell which is essentially made up of the elementary face-centred tetragonal lattice [170]. The 1D-LPS and 2D-LPS phases have garnered a fair amount of interest in the past and have been the focus of many studies [171-176].

Subramanian and Laughlin [154], have previously calculated and summarised the lattice parameters for the various Pd-Cu phases, however, they have concluded that the symmetry of 2D-LPS phase was monoclinic as opposed to orthorhombic based on the data produced by Watanabe and Ogawa [170]. The Pd-Cu alloy system crystal structure data is outlined in Table 2.8.

Table 2.8 Crystal structure data for the Pd-Cu system.

Phase	Composition (Pd wt%)	Space group	Structur-bericht designation	Prototype	Reference
FCC (α)	0 – 100	$Fm\bar{3}m$	A1	Cu	[153]
Cu_3Pd	~12.1 – 32.1	$Pm\bar{3}m$	$L1_2$	$AuCu_3$	[162]
1D-LPS	~25.5 – 39.4	$P4mm$	-	Cu_3Pd	[172]
2D-LPS	~28.2 – 42.9	-	-	Cu_3Pd	[175]
CuPd (β)	~48.5 – 59.8	$Pm\bar{3}m$	B2	CsCl	[162]

Subramanian and Laughlin [154] more recently modified the phase diagram by slightly amending the solidus and liquidus temperature so that they conformed to the accepted melting points of Pd and Cu. Huang [72] and Li [153] both utilised the calculation of phase diagram (CALPHAD) technique to produce the latest Pd-Cu phase diagram, moreover Li [153] was able to model the phase boundaries to temperatures as low as 200 K (Figure 2.15).

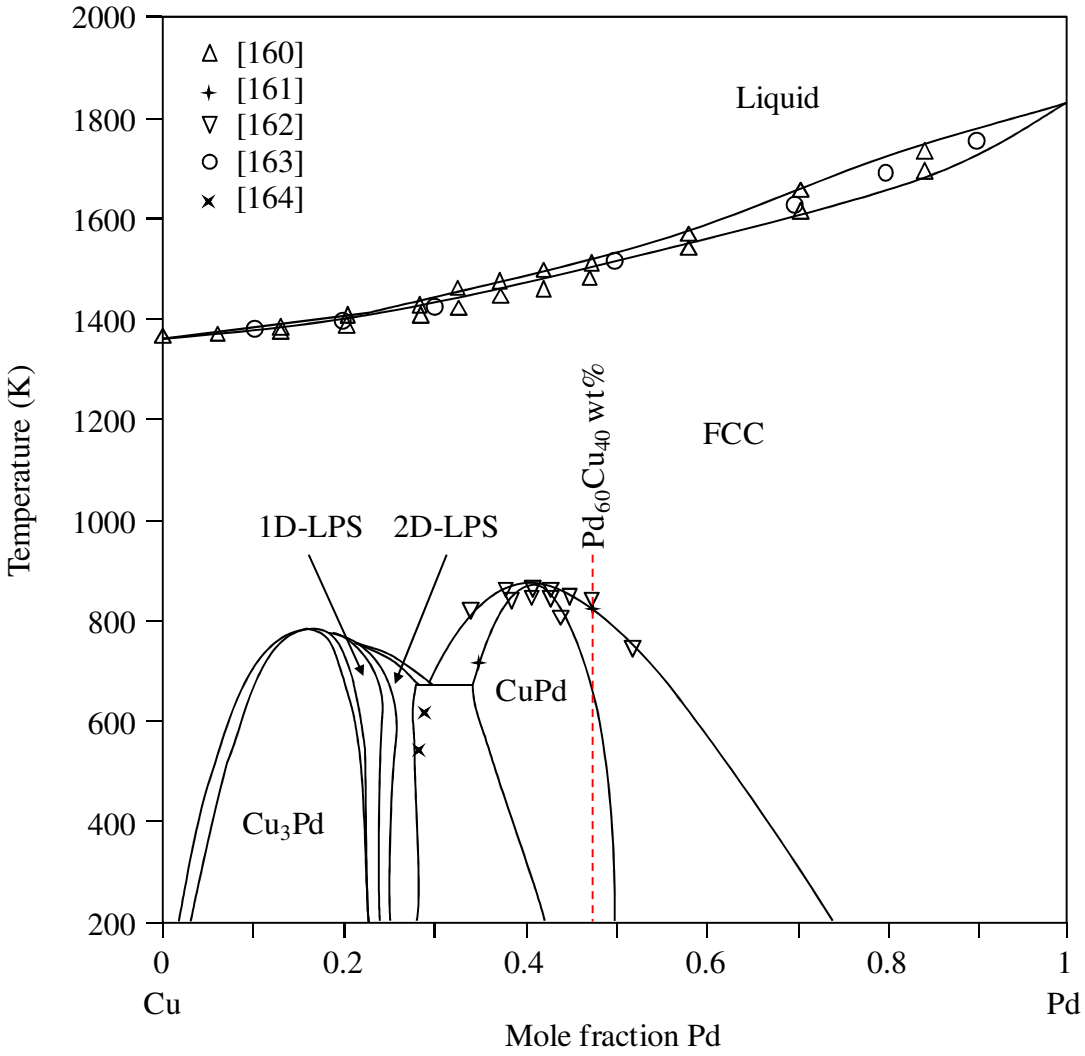

Figure 2.15 Pd-Cu phase diagram adapted from Li et al [153] calculated using the CALPHAD method and compared with literature data [160-164].

2.3.2. The influence of crystal structure on hydrogen permeability

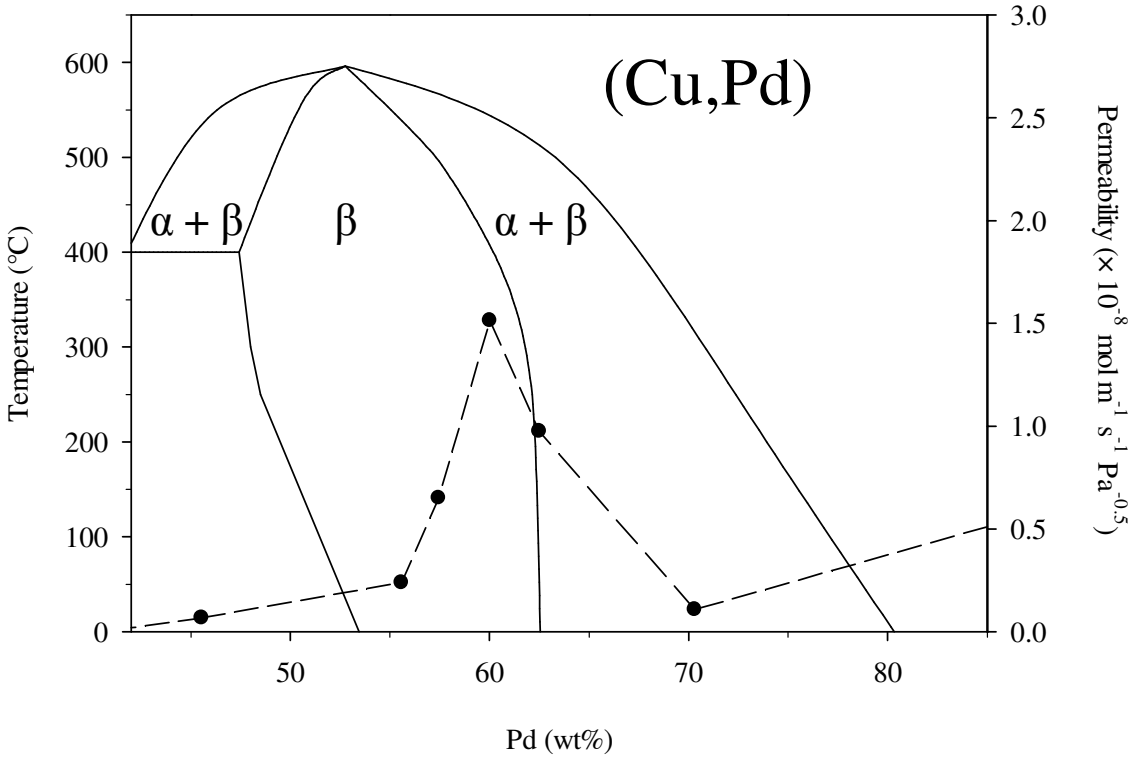

Figure 2.16 The Pd-Cu phase diagram revealing the miscibility gap in more detail, α = FCC phase and β = BCC phase. The phase diagram has been reproduced from literature [153, 154] and also features a hydrogen permeability dashed line plot as a function of Pd content at 350 °C compiled using data from Howard et al [37] and McKinley [35].

According to the Pd-Cu phase diagram (Figure 2.16), the $Pd_{60}Cu_{40}$ wt% composition contains an ordered BCC phase below 450 °C which has widely been reported in literature [35, 36, 39, 135] to possess the highest hydrogen permeability of this binary system. This optimum composition exists in a narrow range since a deviation of 3 wt% or more can result in at least a 50 % reduction in permeability [97].

In the Pd-Cu system, diffusivity of hydrogen in the BCC phase is orders of magnitude greater than in the FCC phase [37-40]. A reason for such relatively low diffusivity in the FCC phase is due to the FCC activation energy for hydrogen diffusion being a factor of three times higher than that of the BCC phase. This could be attributed to the smaller BCC unit cell possessing

three times as many octahedral and tetrahedral interstitial sites than the FCC phase [77] facilitating a much more rapid transport of hydrogen from one unit cell to another. At temperatures above 600 °C, a phase transition from the ordered BCC phase to the disordered FCC phase occurs which comparatively has a lower permeability yet enhanced resistance to H_2S contamination [44, 45]. Furthermore it has been observed that alloying Pd with Cu has the effect of reducing the solubility and increasing the hydrogen absorption pressure of the system [177].

2.3.3. The effects of hydrogen on the Pd-Cu system

Piper [39] had investigated the room temperature diffusivity values of a range of Pd-Cu alloy compositions by measuring the electrical resistivity of the foils. It was observed that dissolved hydrogen had the profound effect of shifting the BCC | FCC + BCC phase boundary to higher Pd compositions. As shown in Figure 2.17, this shift in the phase boundary appears to be greater between 0 and 0.51 MPa as opposed to 0.51 and 12.16 MPa of hydrogen pressure. Huang et al [72] also report a similar effect and furthermore treat dissolved hydrogen as a third alloying element ergo implying that a Pd-Cu-H ternary system exists.

Figure 2.18 shows how hydrogen solubility varies in the BCC phase for different pressures at 320 °C and additionally reveals the shift in the phase boundary with increasing hydrogen concentration. Lässer [74] also observed similar effects, noting shifts in phase boundaries for different hydrogen isotopes dissolved in Pd.

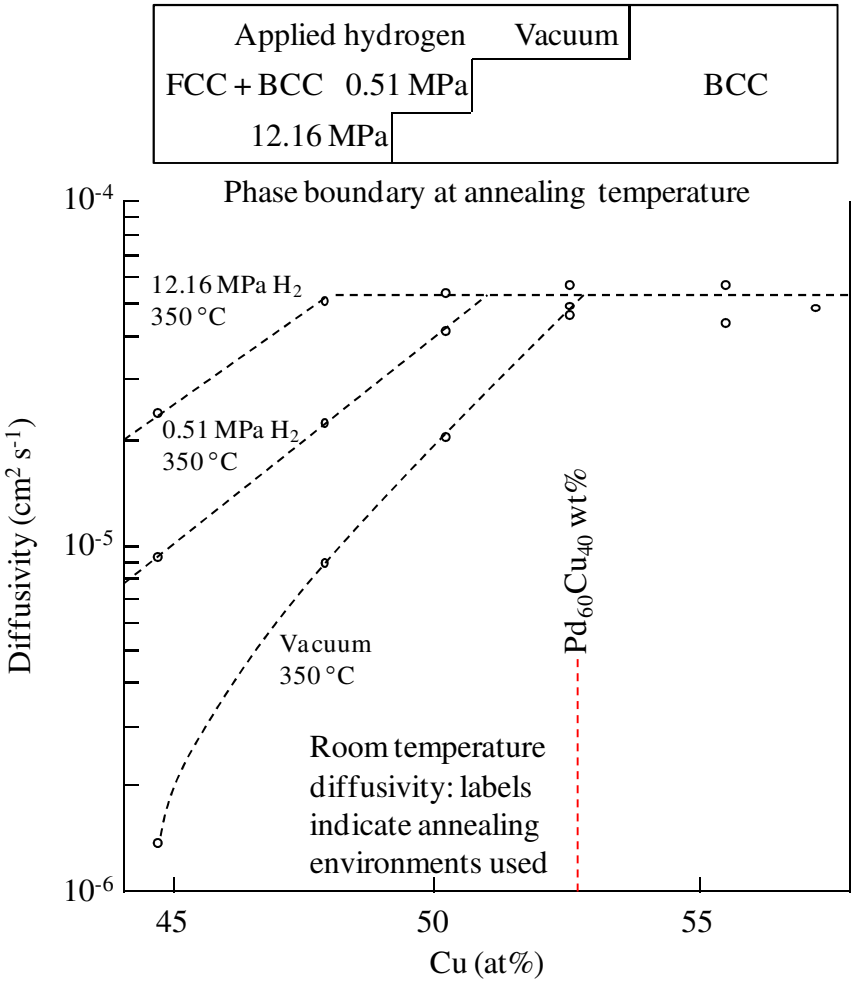

Figure 2.17 Diffusivity values at 25 °C in FCC + BCC mixed phase Pd-Cu alloys. The BCC | FCC + BCC phase boundary has been shown to shift its position upon the application of a hydrogen pressure as indicated at the top of the plot. Recreated from Piper [39].

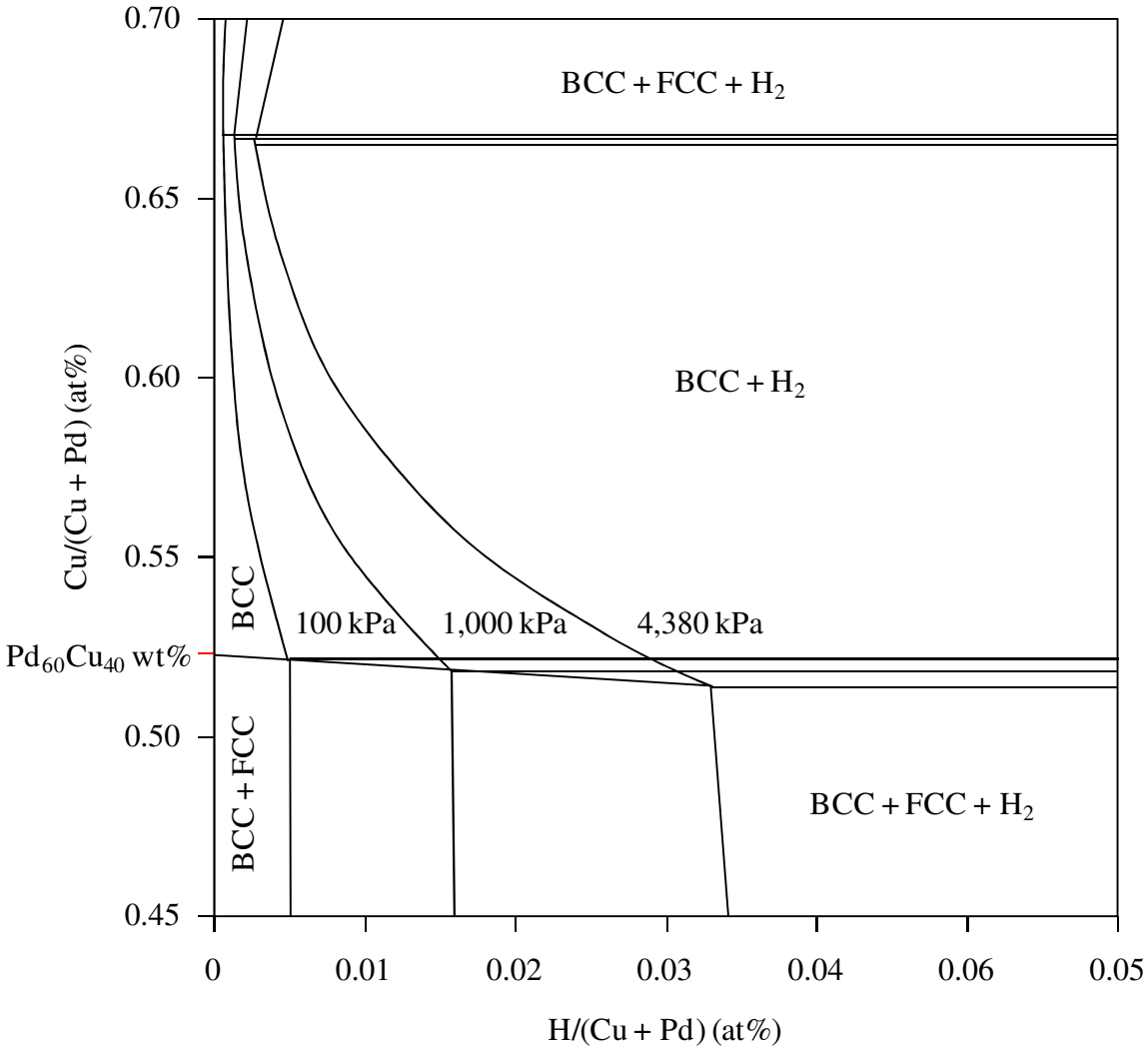

Figure 2.18 A plot revealing the variation of hydrogen solubility in the Pd-Cu system between 45 and 70 at% Cu at 320 °C. In addition the influence of dissolved hydrogen on the position of the BCC | FCC + BCC phase boundary is shown. Image recreated from Huang et al [72].

The formation of the BCC phase appears to be facilitated in the presence of hydrogen. It has been reported that hydrogen helps induce and promote atomic diffusion and rearrangement [178, 179]. Decaux [95] noted that annealing $Pd_{47}Cu_{53}$ at% (~$Pd_{60}Cu_{40}$ wt%) foil under vacuum at 200 °C yielded no sign of the equilibrium BCC phase, however, when annealing was performed under 100 kPa of hydrogen at 250 °C for 26 hours, a mixed BCC and FCC phase began to form.

First principle calculations were carried out by Huang et al [72] predicting the enthalpy of formation of various phases in the Pd-Cu-H system at 298 K. The alleged enthalpy of formation for the Pd-Cu BCC phase is -12.73 kJ mol^{-1} which was the most exothermic of all of the phases reported which suggests it is the most stable.

Hydrogen has another marked influence on the Pd-Cu system such as permeation hysteresis during temperature cycling of ~$Pd_{50}Cu_{50}$ at% membranes through the miscibility gap [97, 180]. It was shown that transition into the mixed FCC + BCC phase region by a Pd-Cu FCC alloy membrane was suppressed during cooling unlike in the heating stage of the cycle. This effect has been linked to non-equivalent phase transformation occurring in the mixed phase region and it has been theorised that a retardation in the FCC(H) → BCC(H) phase transition is delayed due to the existence of a metastable hydrogenated FCC Pd-Cu(H) phase [97].

Cycling of a Pd-Cu membrane through the mixed phase region could present durability issues in the presence of hydrogen. Hydrogen solubility in the FCC phase is approximately one order of magnitude greater than that of the BCC phase [72, 87] and this caveat could lead to the formation of hydrogen pockets at the grain boundaries resulting in the build-up of mechanical stresses. These stresses are the result of an FCC(H) → BCC(H) phase transformation which requires the instantaneous release of dissolved hydrogen into the grain boundaries. If these hydrogen pockets reside deep within the bulk of the membrane, then there will be insufficient time to reach the membrane surface and desorb. This means that either the remaining FCC domains must absorb the surplus hydrogen or internal pressure builds up eventually leading to membrane failure [180].

2.3.4. H_2S resistance

In general, Pd alloy membranes have attracted a lot of attention for their ability to separate hydrogen from coal gasification and steam reforming process streams [181-184], however the presence of H_2S in these streams can deactivate a membrane and significantly reduce hydrogen permeability and selectivity. The Pd-Cu system offers improved resistance to membrane contamination from sulphurous compounds such as H_2S thus being the subject of many studies [44, 45, 83, 159, 185-188].

Edlund [185] observed that hydrogen permeability through a 50 µm thick $Pd_{60}Cu_{40}$ wt% foil membrane exposed to 1,000 ppm of H_2S in hydrogen at 773 K and 700 kPa for 350 hours exhibited no change. Previously, Edlund fabricated a composite membrane composed of a V-based metal, silicon dioxide diffusion barrier and Pd coating and exposed it to H_2S at 700 °C and 894 kPa [189]. Exposure to hot H_2S was shown to corrode the membrane.

McKinley [36] compared the effect of H_2S on pure Pd, $Pd_{73}Ag_{27}$ wt%, $Pd_{60}Au_{40}$ wt% and $Pd_{60}Cu_{40}$ wt% membranes at 350 °C and a pressure differential of 517 kPa. A gas mixture of 4 – 5 ppm H_2S in hydrogen was used to measure the permeability of 25.4 µm thick foil membranes. The hydrogen permeability of a pure Pd membrane decreased by approximately 37% after 6 hours exposure to H_2S and further reduced to 29% after 6 days in comparison to its original value measured in a pure hydrogen atmosphere. The hydrogen permeability of the $Pd_{73}Ag_{27}$ wt% membrane in a pure hydrogen atmosphere was almost double that of pure Pd, however, when exposed to H_2S after 6 hours it dropped to nearly 1% of this value. The hydrogen permeability of the $Pd_{60}Au_{40}$ wt% membrane in a pure hydrogen atmosphere was less than half that of pure Pd, yet showed relatively little change after 6 hours exposure to H_2S with only an 86% decrease in its original value. Furthermore, the $Pd_{60}Cu_{40}$ wt% membrane

achieved a permeability 35% higher than pure Pd in a pure hydrogen atmosphere although when exposed to H_2S for 6 hours its permeability declined to 10% of its original value and then down to 5% after 6 days.

McKinley [36] noted that the membranes used in the study recovered their original hydrogen permeability when the feed gas was reverted back to pure hydrogen. Following H_2S exposure, the Pd-Au and Pd-Cu membranes did not show any signs of corrosion or pitting, however, the Pd and Pd-Ag membranes had a dull appearance. This observation led McKinley to theorise that the decrease in hydrogen permeability seen in the Pd-Au and Pd-Cu membranes was a result of H_2S adsorption as opposed to sulphide formation or chemical attack. This was in good agreement with the work of O'Brien et al [188] who tested the performance of pure Pd and $Pd_{60}Cu_{40}$ wt% membranes in 1,000 ppm H_2S. It was shown that the Pd membrane formed a corrosion product, Pd_4S, during H_2S exposure which was approximately 6.6 µm thick. XPS revealed that sulphur only penetrated 3 nm into the Pd-Cu membrane surface and formed a Pd-Cu-S layer which was responsible for deactivation of the membrane.

Kulprathipanja et al [186] studied the effects of low H_2S concentrations on the hydrogen permeation through Pd and Pd-Cu membranes. They demonstrated that H_2S concentration, as opposed to exposure time, is the main factor in reducing hydrogen permeation in Pd and Pd-Cu membranes. It was also found that hydrogen permeation at 773 K can be completely inhibited by 100 ppm of H_2S in the feed stream while hydrogen permeation was only prevented in a $Pd_{60}Cu_{40}$ wt% alloy membrane at 300 ppm of H_2S. Furthermore, surface roughness had a marked effect on reducing the H_2S tolerance of a membrane. Rough surfaces tend to have broken bonds located at grain boundaries which facilitate the adsorption of sulphur. Therefore, it was concluded that cast and rolled foils possessed better resistance to H_2S contamination over electrolessly deposited metal membranes due to a smoother surface.

Morreale et al [44] showed that the hydrogen permeation of Pd-Cu alloy foils exposed to 1,000 ppm of H_2S experienced little change at temperatures associated with the FCC crystalline phase. Hydrogen permeation in the BCC phase, however, was found to drop by two orders of magnitude under the same conditions. Therefore a clear correlation between H_2S tolerance and crystal structure was established showing that the Pd-rich Pd-Cu FCC phase brings about enhanced protection from sulphide contamination.

2.4. Thin film membranes and deposition techniques

2.4.1. Thin film membranes

Using conventional rolling and drawing techniques a minimum foil thickness of approximately 20 µm can be achieved. Foils fabricated below this thickness can form pinholes and various other defects which can severely reduce the membrane selectivity. Thin film deposition techniques are used to produce defect-free membranes of < 5 µm thick which can help meet the 2015 U.S. DoE flux targets [190]. Thin film membranes are often deposited onto a relatively thick substrate for added mechanical support to fabricate what is known as a composite membrane. A key requirement for the substrate material is to have a thermal expansion coefficient that closely matches that of the film in order to prevent delamination during operation.

Deposition of Pd and Pd alloy thin films onto a range of porous substrates has garnered a lot of research interest over the years. The dense thin film acts as the selective membrane for hydrogen purification and so it is essential that the membrane is free of any defects. Defects in a membrane can vary from pinholes to voids or open pores found in the crystal structure. The presence of pinholes and grain boundary defects in the dense thin film is detrimental to

selectivity as gases are able to flow through a membrane via the Knudsen diffusion mechanism [191].

The most popular types of composite membranes are pure Pd deposited onto either porous alumina or porous stainless steel. The relatively large pore size of certain substrates require an intermediate layer with finer pores which can facilitate the deposition of defect-free thin films [192]. Due to the complex structure of composite membranes, comparison of hydrogen permeability with free-standing membranes is complicated since each individual component must be analysed separately.

Both Pd and Pd alloy thin films have been deposited using an array of techniques such as electroless plating, electroplating deposition, chemical vapour deposition and physical vapour deposition most notably using magnetron sputtering. Each of these deposition techniques are discussed in the following section.

2.4.2. Electroless plating

This technique uses a reducing agent for coating thin films onto a substrate through the reduction of metal complex ions in solution without the involvement of an external power supply. Uemiya et al [32] were the first to employ this method for the fabrication of Pd and Pd alloy composites. Defect-free Pd thin films have been successfully deposited with thicknesses ranging from 1 μm [193] to 33 μm [194].

Electroless plating (ELP) entails the reduction of metallic salt complexes on the substrate surface that requires an activation step since the plated metal behaves as a catalyst for subsequent reactions [195].

Conventional ELP requires sensitisation and activation through seeding of the substrate surface with Pd precursor particles followed by coating of the Pd film on top of the activated surface. An intermediate layer can be applied to the substrate in order to smooth out any rough surfaces. Typically, sensitisation is performed by immersing the smoothed surface into acidic tin ($SnCl_2$ or $SnCl_4$) solutions to attach the Pd particles to the surface in the proceeding activation step.

Typically, ELP baths contain a Pd-amine complex stabilised by a sequestering agent like Na_2EDTA. The plating solution is usually mechanically agitated in order to achieve a uniform coating and can prevent gas bubbles adhering to the substrate surface which can create film defects. The substrate is removed and the plating bath replenished once the Pd solution has been completely consumed. This is repeated until the desired film thickness is obtained. Vacuum annealing is used to achieve a homogenous film.

The advantages of ELP include ease of plating any shapes or geometries, simple setup and low cost [196]. However, the drawback is the complex and laborious task of the pre-treatment steps such as activation and sensitisation before any plating can be performed. Another issue with fabricating Pd alloy films is the different reduction potentials associated with the metallic ions resulting in an uneven coating. This problem was encountered by Bhandari and Ma [197] when fabricating Pd-Ag alloys using ELP which resulted in dendritic growth . This could be remedied by tailoring the reduction overpotential of Ag to closely match that of Pd through adjusting the reactant concentration [198].

Several attempts have been made to co-deposit solid solution Pd-Ag alloy films via ELP with little success [199-201]. The effect of varying the Pd and Ag content of the plating bath on film composition was investigated by Shu et al [201] who noted that Ag preferentially plates

and passivates the substrate therefore hindering the deposition of Pd unless the plating bath is Pd-rich. A plating bath composition of 83.4 at% Pd and 16.6 at% Ag was shown to deposit films containing distinct Pd and Ag phases with small traces of a Pd-rich Pd-Ag solid solution phase. Annealing the film in hydrogen considerably improves homogeneity and produces a composition of $Pd_{44}Ag_{56}$ at% [201].

An alternative method for fabricating Pd alloy thin films is to sequentially deposit distinct metal layers and anneal to produce a homogenous film composition. This technique has been used to produce Pd-Ag [202-208] and Pd-Cu [208-211] membranes deposited onto an array of substrates. Despite giving better control over film composition over co-deposition, other significant discrepancies can occur. Keuler and Lorenzen [202] fabricated multiple Pd-Ag membranes via sequential deposition under the same conditions and produced film thicknesses ranging from 1.4 to 2.16 µm with compositions varying between Pd-Ag_{20-25} wt%. Furthermore, high temperatures are needed in order to fully homogenise the films.

It was observed that annealing of Pd-Cu films at 600 °C was sufficient to achieve compositional homogeneity, however it was inadequate to obtain homogenous Pd-Ag films as a result of non-uniform deposition of Ag [208]. Hou and Hughes [204, 205], were able to produce a homogenous 5 µm thick Pd-Ag film by annealing at 600 °C for 50 hours under hydrogen. It is evident that hydrogen enhances homogenisation by facilitating atomic rearrangement [179].

Annealing at temperatures as high as 800 °C have been used to homogenise Pd-Ag membranes [207], nevertheless, at this temperature appreciable metallic interdiffusion may occur between the film and metal substrate. Non-metallic substrates are not prone to interdiffusion with Pd (alloy) thin films, however, there is a marked difference in thermal

expansion coefficient which could introduce defects at high annealing temperatures and even result in film delamination.

Films deposited using ELP frequently have lower densities than the bulk substrate material due to the formation of voids and presence of impurities. Roa and Way [212] have previously reported a C content of up to 7 wt% of the electrolessly deposited film. Deposition rate, film structure and morphology are dependent on many variables. Using high plating temperatures can increase the deposition rate which consequently results in finer and more closely packed grains within the film. Films with small grain sizes tend to give better selectivity since they contain fewer defects. Paradoxically, if the deposition rate is too high then the films may form voids introducing more defects thus reducing the selectivity [213]. Other factors which influence deposition rate are substrate surface topography, plating bath concentration, substrate composition and activation conditions.

2.4.3. Electroplating deposition

This technique is a liquid phase electrochemical process whereby metal ions are plated onto an electrode substrate under the application of an external electric field. In the electroplating deposition (EPD) setup, the substrate is the cathode typically immersed in an aqueous electrolyte containing mobile metal plating ions which reduce on the substrate surface. She et al [214] and Hsieh [215] describe, in detail, the fabrication of Pd composite membranes utilising EPD. The benefits of using this technique are the ease of controlling film thickness through plating time and current density in addition to the simplicity of the experimental setup [216]. The main disadvantage is that EPD may only be applied to electrically conductive substrates [198].

2.4.4. Chemical vapour deposition

Chemical vapour deposition (CVD) involves the thermal decomposition of one or more volatile precursors close to the substrate surface in order to deposit a thin film. This method has proved to be very useful in fabricating Pd coatings with controlled thicknesses [195]. Ye et al first used this method for depositing ultrathin Pd films onto an α-Al_2O_3 disk using $PdCl_2$ as the precursor [217]. This technique was further adapted by Itoh et al [218] to produce tubular Pd composite membranes via forced-flow CVD to give a 2 – 4 μm thick Pd film with a H_2/N_2 selectivity of 5,000.

Higher quality Pd and Pd alloy films are typically achieved with CVD in comparison to ELP. Thin films produced using CVD often give a partial pressure exponent (*n*-value) close to 1 for hydrogen permeation since hydrogen dissociation becomes the rate limiting step due to the enhanced diffusivity of these coatings [195, 219]. Despite the capability of CVD producing thin films of high quality and selectivity, the method requires Pd precursors that are highly volatile with good thermal stability in order to achieve a short processing time and high yield [217, 219]. Another drawback is the usage of high purity constituents and stringent process conditions which limit the application of CVD. Costly and highly volatile organometallic Pd precursors such as $Pd(C_3H_5)_2$, $Pd(C_3H_5)(C_5H_5)$ and $Pd(C_5H_5)_2$ are used for Pd thin film deposition through metallo-organic CVD (MOCVD) under high vacuum [220]. Moreover, the Pd thin film produced using this technique is prone to contamination from residual C [198].

2.4.5. Physical vapour deposition

Physical vapour deposition (PVD) entails the bombardment of a solid metal target by a high energy beam of electrons or ions in a high vacuum in order to deposit thin film coatings onto a substrate [221]. This technique is similar to CVD, however, without the involvement of

chemical decomposition occurring at the substrate surface since the precursors in PVD are solid metallic targets as opposed to chemical compounds.

A common PVD technique is magnetron sputtering [222] whereby the metal target is bombarded by an excited Ar plasma under a high vacuum to deposit thin films onto a substrate surface. Prior to sputtering, a cleaning run is performed using the gas plasma to remove any contaminants from the substrate surface. Substrates can be rotated within the sputtering chamber in order to improve the uniformity of the deposited film. Moreover, thin films can be sputter deposited onto both conductive and non-conductive substrates with excellent quality.

Magnetron sputtering offers better control over film thickness as it is directly proportional to sputtering time. This method has been effectively employed in the fabrication of thin multilayers such as Pd/$Nb_{40}Ti_{30}Ni_{30}$/Pd supported on porous nickel [223]. It has been shown that Pd-Cu and Pd-Ag solid solution alloy films can be successfully sputter deposited without the need for annealing at high temperatures [224, 225]. Xomeritakis and Lin [222], deposited 110 – 390 nm thick Pd-Ag films onto alumina substrates with a single $Pd_{75}Ag_{25}$ at% target. They produced membranes with the compositions in the following range Pd-$Ag_{13.3\text{-}20.4}$ at% by varying plasma power and attributed these lower Ag concentrations to the dissimilar atomic mass and binding energy of Pd and Ag.

McCool et al [224] attempted to solve this matter by carrying out a pre-sputter routine to clean the surface of the target in order to achieve some degree of surface equilibration during which the substrate is masked to prevent any unwanted deposition. They define surface equilibration as sputtering both elements at the same ratio as the target composition in order to attain the same composition in the deposited film. Pre-sputtering times were varied

between 1 – 15 minutes whereby a greater match in film composition was obtained following longer pre-sputtering times. It was approximated that 100 nm should be removed from the target surface in order to achieve equilibration. Jayaraman and Lin [191] deposited Pd-Ag thin films with thicknesses ranging between 250 and 500 nm onto γ-alumina substrates from a $Pd_{75}Ag_{25}$ at% target resulting in a film composition of $Pd_{77}Ag_{23}$ at%. Mejdell et al [226] prepared free-standing Pd-Ag membranes with thicknesses ranging between 1.3 – 5.0 µm with a similar composition to its $Pd_{77}Ag_{23}$ at% target.

Co-sputtering has also been used to fabricate Pd-Cu [225, 227] and Pd-Ag [228-230] membranes from individual pure metal targets. During sputtering, the voltage to the Pd target is fixed whereas the voltage to the alloying targets is varied in order to control film composition. Yang et al [225] observed a linear correlation between Cu target voltage and Cu concentration in their Pd-Cu sputtered film (Figure 2.19). They deposited a series of films with Cu concentrations ranging between 0 – 60 wt% all of which contained the FCC phase. This is unexpected since according to the Pd-Cu binary phase diagram [154], a mixed FCC and BCC phase occurs above approximately 30 wt% Cu and a purely BCC phase exists between roughly 40 and 55 wt% Cu at room temperature. They further report that the formation of a metastable super-saturated solid solution was formed as a result of an increase in the Gibbs free energy of the nanocrystalline film with respect to bulk Pd-Cu alloys. It was also noted that film thickness increased linearly with deposition time provided a constant deposition rate was maintained [225].

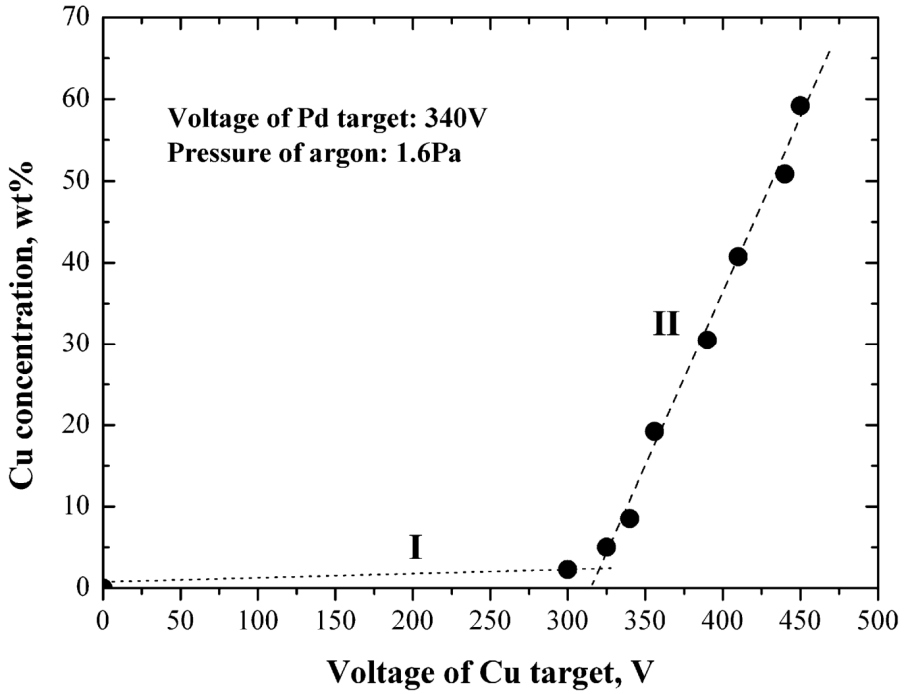

Figure 2.19 Cu concentration in a Pd-Cu sputtered film as a function of Cu target voltage with a constant 340 V Pd target voltage [225].

Zhang et al [228], also utilised co-sputtering to produce 100 nm thick Pd-Ag films with compositions ranging from 0 – 45 at% Ag. X-ray diffraction and energy dispersive spectroscopy were used to determine the film composition and homogeneity. It was seen that at a constant Pd target voltage of 400 V and above a Ag target voltage of 250 V, the Ag concentration in the co-deposited film is proportional to Ag target voltage as shown in Figure 2.20.

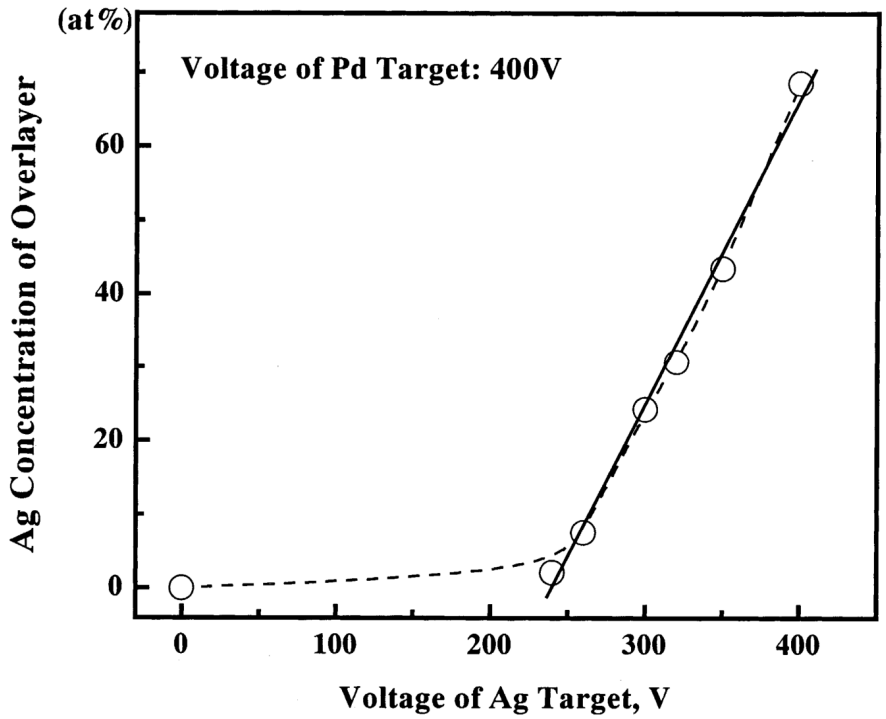

Figure 2.20 Ag concentration in a Pd-Ag sputtered film as a function of Ag target voltage with a constant 400 V Pd target voltage [228].

A disadvantage of using magnetron sputtering is the relatively high cost of the equipment due to the usage of a high vacuum and high power density required to vaporise the target [231]. Furthermore, magnetron sputtering is limited to coating flat substrates as opposed to complex geometries [198].

2.4.6. Pd thin films and diffusion barrier layers

As previously stated, hydrogen migrates through dense metal membranes via a solution-diffusion mechanism. Thus, enhancing the rate at which hydrogen dissolves becomes ever more crucial as membrane thickness is reduced. Metals such as V, Nb, Ta and Zr form a robust oxide layer which severely obstructs surface reaction sites [65, 232] and as a result a thin film protective coating using a non-passive metal, such as Pd, is required.

Interdiffusion occurring between a BCC metal and Pd thin film can reduce membrane performance due to exposure of species which are susceptible to oxidation [233]. Buxbaum [234], highlighted the issues brought about by interdiffusion between an alloy membrane and the catalyst layer and showed that dissolved hydrogen can accelerate the whole process acting as a form of lubricant between the alloying species. Dissolved hydrogen can also place a stumbling block in meeting the 2015 U.S. DoE targets [190] of operating for extended durations at 400 °C due to the adverse effects of interdiffusion on the coated membrane.

Slowing the rate of interdiffusion can allow the use of Pd films of a reduced thickness which will inherently reduce material cost. The use of a diffusion barrier layer between Group IV and V alloy membranes and Pd alloy thin films was introduced by a patent in 2006 held by Eltron Research [235]. The requirement that the barrier layer must permit hydrogen permeation restricts the materials that can be selected for this role and so the aforementioned patent has suggested the use of perovskites, oxy-acids and fluorides whilst others have mentioned the use of metal oxides [236, 237], carbides [238] and chalcogenides [239].

Metal chalcogenides in glass form are a well known proton conductor [240-242]; however, one major drawback is the associated low melting point of these materials. Other research [243, 244] has mentioned the use of high-bond valence metals such as Nb and Ta as an intermediate layer between the Pd thin film and porous support substrate. Alternative diffusion barriers which have been useful in hindering interdiffusion was also proposed by Edlund in the form of porous non-metallic layers composed of refractory oxides in woven, paper or felt [245] arrangements or as porous deposited layers [246].

3. Experimental techniques

3.1. Material and sample preparation

During the course of this work, care was taken to ensure that all samples were handled with nitrile gloves and tweezers in order to minimise surface contamination of the foil and membrane samples. Acetone and a cotton bud were used where necessary to remove any finger prints or dirt from the membrane prior to sputter deposition and hydrogen permeability testing.

3.1.1. Rolled foils

Two batches of cold rolled Pd-Cu foil were supplied by Johnson Matthey Noble Metals (Royston, UK) with a nominal composition of $Pd_{60}Cu_{40}$ wt%. The thickness of each foil was measured using a digital micrometer. Batch 1 had an approximate thickness of 31.0 ± 0.8 µm and Batch 2 had a thickness of 31.3 ± 0.8 µm. Membranes discs (diameter = 21 mm) were cut from either batch for hydrogen permeability experiments. The disc geometry was ideal since it allowed hydrogen permeability measurements, ex-situ X-ray diffraction and microscopy analysis to be performed on the same sample. Square foil offcuts (~5 × 5 mm) were also prepared in order to fit inside the in-situ variable temperature X-ray diffraction pressure cell. In addition, a 67.8 ± 1.8 µm thick pure Pd (99.95%) cold rolled foil, supplied by Goodfellow (Huntingdon, UK), was used during this work acting as a standard.

3.1.2. Magnetron sputtering

For the coated foil and membrane samples, thin Pd coatings of varying thicknesses were deposited onto one side using a closed field unbalanced magnetron sputter ion plating (CFUBMSIP) system produced by Teer Coatings Ltd [247]. Figure 3.1 is a schematic representation of the sputtering system used to prepare the surface modified Pd-Cu membranes during this study.

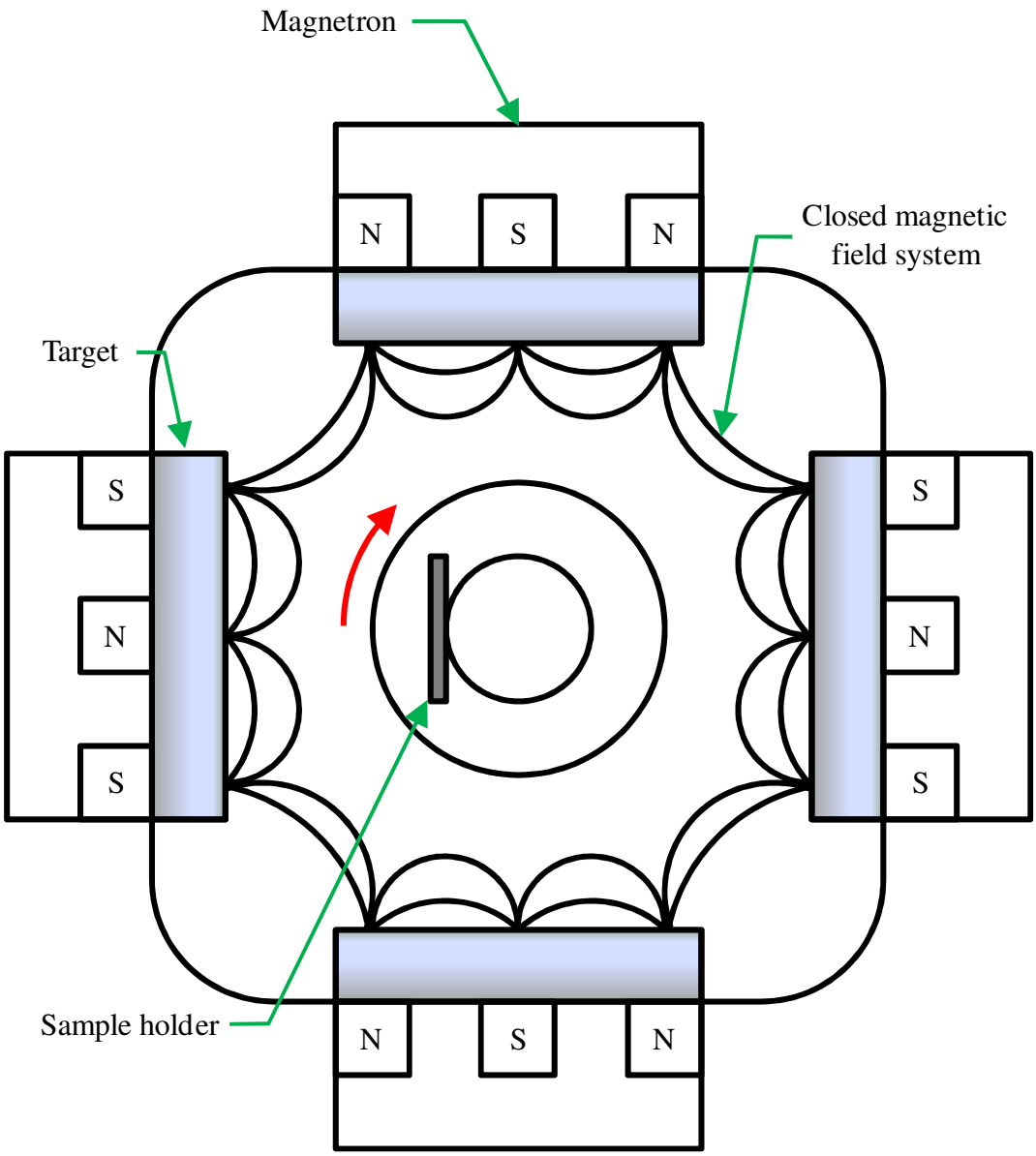

Figure 3.1 Schematic illustration of the sputtering system (CFUBMSIP) used in this work.

A clean surface is crucial for obtaining high quality coatings that achieve good substrate adherence and uniform thickness. A two-step cleaning process was employed during this work for the Pd-Cu membrane disc and foil offcut samples. The first step involved cleaning the samples in an ultrasonic bath for 5 minutes. Subsequently, the samples were mounted inside of the sputtering system, evacuated to 10^{-7} kPa and subjected to an ion cleaning process with an argon plasma prior to sputtering. The sputtering process utilises a Pd target (99.9% purity) which was sputtered onto the samples at a target current of 1 A and argon flux of 25 standard cubic centimetres per minute. Sputtering parameters were kept constant with only the coating durations varied to achieve different film thicknesses. In order to produce a high quality coating the depositions were performed in a single continuous step without breaking the vacuum in order to prevent contamination.

For this work, Batch 1 and Batch 2 Pd-Cu foil membranes were sputter-coated with Pd in order to modify the membrane surface. Coating parameters have been summarised in Table 3.1. Three different coating times were chosen in order to create Pd-Cu foil membranes with varying Pd thin film thicknesses on one side. This was done to investigate the effect of the Pd thin film and film thickness on the hydrogen permeability of a Pd-Cu membrane.

Table 3.1 Summary of coating times used to fabricate the surface modified Pd-Cu membranes investigated in this work. A target current of 1 A has been used.

Type	Coating time (s)
A	50
B	1,000
C	1,800

It should be noted that sputter deposition can be affected by many variables that are difficult to control, for example new targets have a higher sputter rate than worn targets. Furthermore, target surface condition and vacuum level can have an effect on the deposition rate.

Two methods were used to determine the thickness of the Pd thin film coating. The first method involved coating a glass slide with Pd, alongside other samples, with a portion of the glass surface protected with Kapton tape. Removal of the tape revealed the uncoated surface of the glass slide creating a step from which the Pd film thickness could be measured. Profilometry was used to accurately measure the distance between the top surface of the Pd thin film and glass slide top surface to give the film thickness using an Ambios XP-200 Stylus surface profilometer with a scanning speed of 0.1 mm s^{-1} at 2 mg of force on the tip.

The second method for determining film thickness was to weigh the samples before and after sputter deposition using a balance accurate to 5 decimal places of a gram. For simple sample geometries such as membrane discs or square offcuts, the Pd film thickness can be estimated assuming uniformity across the sample surface. The following Equation 3.1 is used to determine film thickness:

$$t_f = \frac{M_{s+Pd} - M_s}{\rho_{Pd} A_s} \qquad \text{Equation 3.1}$$

where t_f is the film thickness, M_s is the mass of the sample before Pd sputter deposition, M_{s+Pd} is mass of the sample subsequent to Pd sputter deposition, ρ_{Pd} density of Pd (12.023 g cm^{-3}) and A_s is sample surface area.

3.2. Hydrogen permeability measurement

3.2.1. Membrane permeability rig

A custom made membrane permeability rig (MPR) was constructed for testing the hydrogen permeability of dense metal membranes. The MPR is designed to apply a controlled gas flow to the feed side of a hermetically sealed membrane and to measure the flow of hydrogen

which permeates through to the other side. The measurement equipment used in the MPR system was monitored and controlled with a PC and SpecView data logging software. Figure 3.2 shows a schematic diagram of the MPR system used in this work.

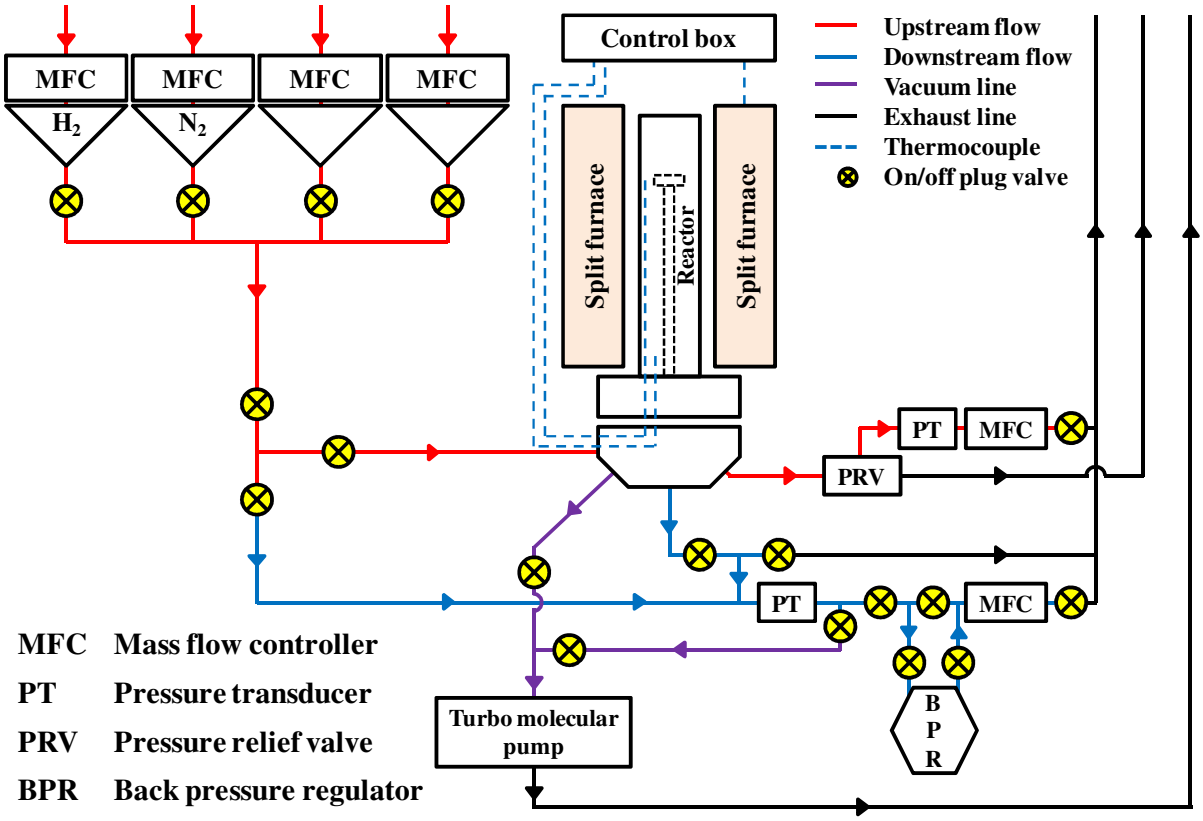

Figure 3.2 Schematic illustration of the MPR system.

Four Brookes 5850S Mass Flow Controllers (MFC) calibrated between 6 – 600 ml min^{-1} with ± 6 ml min^{-1} accuracy were used to control the feed gas to the feed side of the sealed membrane. This enables the inlet of up to four gases meaning the membrane can be tested either under pure hydrogen or a mixed gas feed stream. Air Products supplied the hydrogen (99.99996%) and nitrogen (99.9998%) high pressure cylinders used in the MPR.

To prevent any build-up of contaminants and to maintain a stable hydrogen feed pressure, the feed gas is left continually flowing and bled out through another Brookes 5850S MFC also calibrated between 6 – 600 ± 6 ml min^{-1}. The bleed MFC was connected to the four inlet

MFCs in order to regulate and maintain a constant feed side pressure ranging from 100 to 1,100 ± 0.5 kPa.

An additional Brookes 5850S MFC (6 – 600 ± 6 ml min^{-1}) positioned on the downstream end of the MPR system was utilised to monitor the quantity of hydrogen permeating through the membrane. The precision of the MFC gives a ± 60% instrumental error in the hydrogen permeability measurements for a flow rate of 10 ml min^{-1}, whereas a much lower instrumental error of ± 20% in hydrogen permeability readings is expected at higher flow rates of 30 ml min^{-1}. A Swagelok KFB series back pressure regulator with a range of 100 – 1,800 ± 5 kPa was used to adjust and control the downstream pressure. A Hawco-Direct 408-857 digital pressure transducer with a 100 – 1,700 ± 5 kPa range was used to measure the pressure on both ends of the membrane. A Pfeiffer TSU-071E turbo-molecular drag pumping station with a membrane backing pump is used to evacuate the reactor down to ~10^{-6} kPa.

The temperature of the reactor and membrane was controlled by an Elite Thermal Systems Ltd split furnace capable of a ramp rate ranging between 0.1 and 10 °C min^{-1} and a maximum temperature of 1,100 °C. Three Inconel K-type thermocouples were used to monitor the temperature within the reactor. One thermocouple was positioned inside the furnace heating zone in order to accurately measure the furnace temperature, the second thermocouple was positioned near to the reactor base to measure seal temperature and the third thermocouple was placed 1 mm from the membrane surface to measure membrane temperature.

A single rod of Inconel 625 grade II alloy was machined to fabricate the reactor chamber which features a silver compression gasket to hermetically seal the lid with the mounted base. The reactor has a 1,200 cm^3 internal volume and 5.5 cm diameter which can easily accommodate an array of different membrane geometries. The reactor was designed to have a

maximum operating temperature and pressure of 850 °C and 2,100 kPa, respectively. Swagelok 316L stainless steel fittings were bored through the reactor base to allow the gas pipes to reach inside the reactor and to have the membrane positioned inside the furnace heating zone.

The membranes were mounted in between two hardened 316LN stainless steel conflat vacuum flanges both featuring a hardened 316SS knife edge. Both flanges had a 1.27 cm bore diameter. The bottom flange was welded to a 1.27 cm diameter 316L stainless steel pipe which was positioned inside the furnace heating zone. The top loose flange was used as a cap to produce a hermetic seal around the edge of the membrane. With the membrane resting on the bottom flange knife edge, an ultra high vacuum (UHV) copper gasket was placed on the top side of the membrane followed by the loose flange. Six low thermal expansion hex bolts were used to fasten both flanges together to deform the membrane around the knife edge of the bottom flange creating a gas tight seal. Figure 3.3 shows how the membranes were mounted onto the holder inside the MPR reactor vessel.

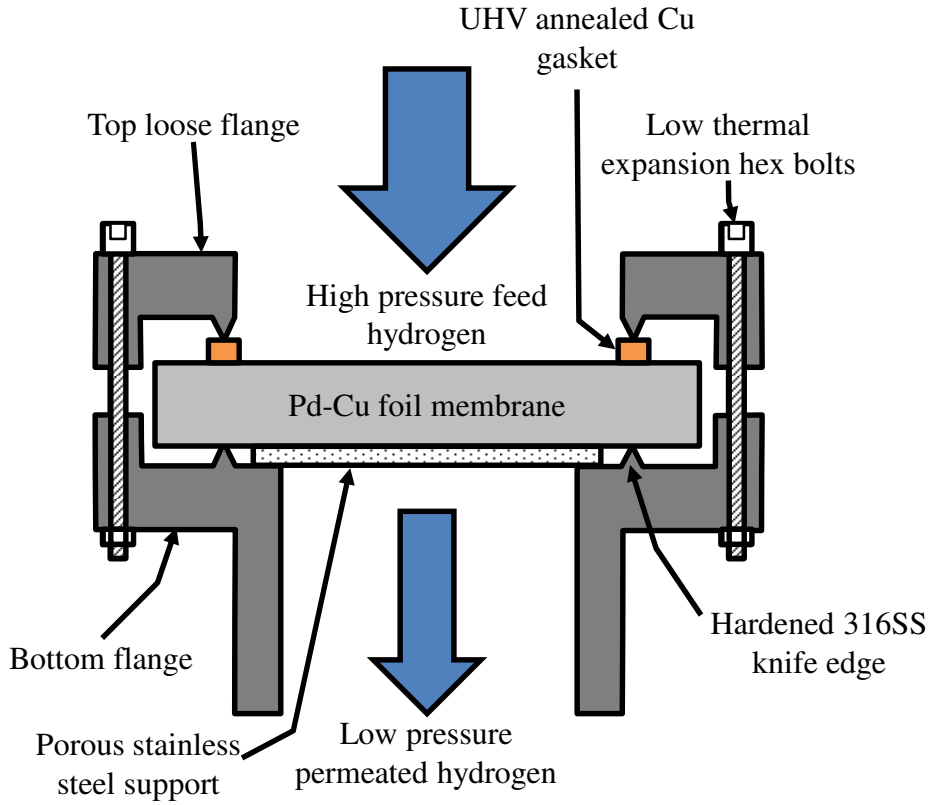

Figure 3.3 Cross section diagram showing the typical arrangement of a membrane mounted inside the MPR reactor vessel.

The integrity of the hermetic seal was tested by applying a 300 kPa N_2 pressure gradient across the membrane. A flow of < 2 ml min^{-1} is below the detectable limit of the downstream MFC, however, if no increase was observed in the downstream pressure after 30 minutes the seal was considered gas tight.

The same testing procedures were used for each membrane in the MPR ensuring consistency in measurements and aiding in fair comparison between all membranes. The testing procedure was similar to those used by past investigators of self-supporting bulk Pd-based foil membranes [28, 94, 156, 248]. All membranes were heated at a ramp rate of 2 °C min^{-1} and then furnace cooled at a cooling rate of approximately 0.5 °C min^{-1}. A maximum hydrogen feed flow rate of 100 ml min^{-1} was used during every measurement.

Typical test conditions in the MPR were isobaric where the membranes were typically cycled up to a maximum temperature of 450 °C using a hydrogen feed pressure of 445 kPa and permeate pressure of 100 kPa resulting in a pressure differential of 345 kPa. These pressures were chosen for ease of comparison with the U.S. DoE dense metal membrane flux targets (Table 1.1) which were based on a 345 kPa hydrogen pressure differential across a membrane. Some membranes were heated to as high as 700 °C in order to measure the hydrogen permeability of the high temperature $Pd_{60}Cu_{40}$ wt% FCC phase. As a precautionary measure, membranes were positioned on a porous stainless steel support to prevent doming and failure during testing.

Three types of hydrogen permeability measurements were performed in the MPR. The first type involved measuring the hydrogen permeability of the as-received pure Pd membrane and $Pd_{60}Cu_{40}$ wt% membrane in order to determine a baseline with which the surface modified Pd-Cu membranes could be compared. The as-received membranes were mounted inside the MPR reactor vessel using the arrangement shown in Figure 3.3.

The second type entailed measuring the hydrogen permeability of the surface modified Pd-Cu membranes with the Pd thin film positioned on the high pressure feed side as shown in Figure 3.4(a). Conversely, the third measurement type involved measuring the hydrogen permeability of Pd coated Pd-Cu membranes with the Pd thin film positioned on the low pressure permeate side which is also shown in Figure 3.4(b) in order to understand the effects this configuration has on hydrogen permeability.

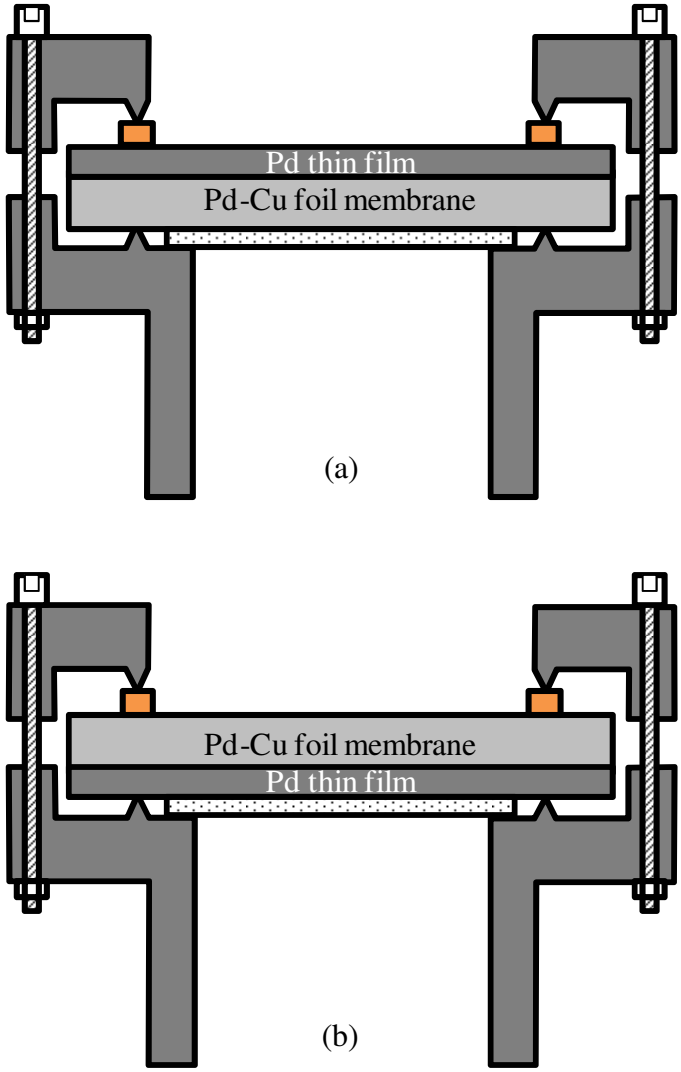

Figure 3.4 Membrane mounting arrangement of the surface modified Pd-Cu membranes inside of the MPR reactor vessel where (a) the Pd thin film is positioned on the high pressure feed side and (b) the Pd thin film is positioned on the low pressure permeate side.

Prior to MPR testing, the membranes were cleaned with acetone in an ultrasonic bath for 5 minutes. After a membrane is mounted inside the MPR reactor vessel, the system is evacuated and a N_2 leak test is performed. If the leak test fails, the membrane is removed, the flanges are inspected and cleaned, the membrane is replaced and secured using a new UHV Cu gasket and the leak test is repeated. Figure 3.5 shows a cross sectional view of the MPR reactor vessel indicating the position of the membrane during testing. Note that the upstream mass spectrometry feed line was not used in this work.

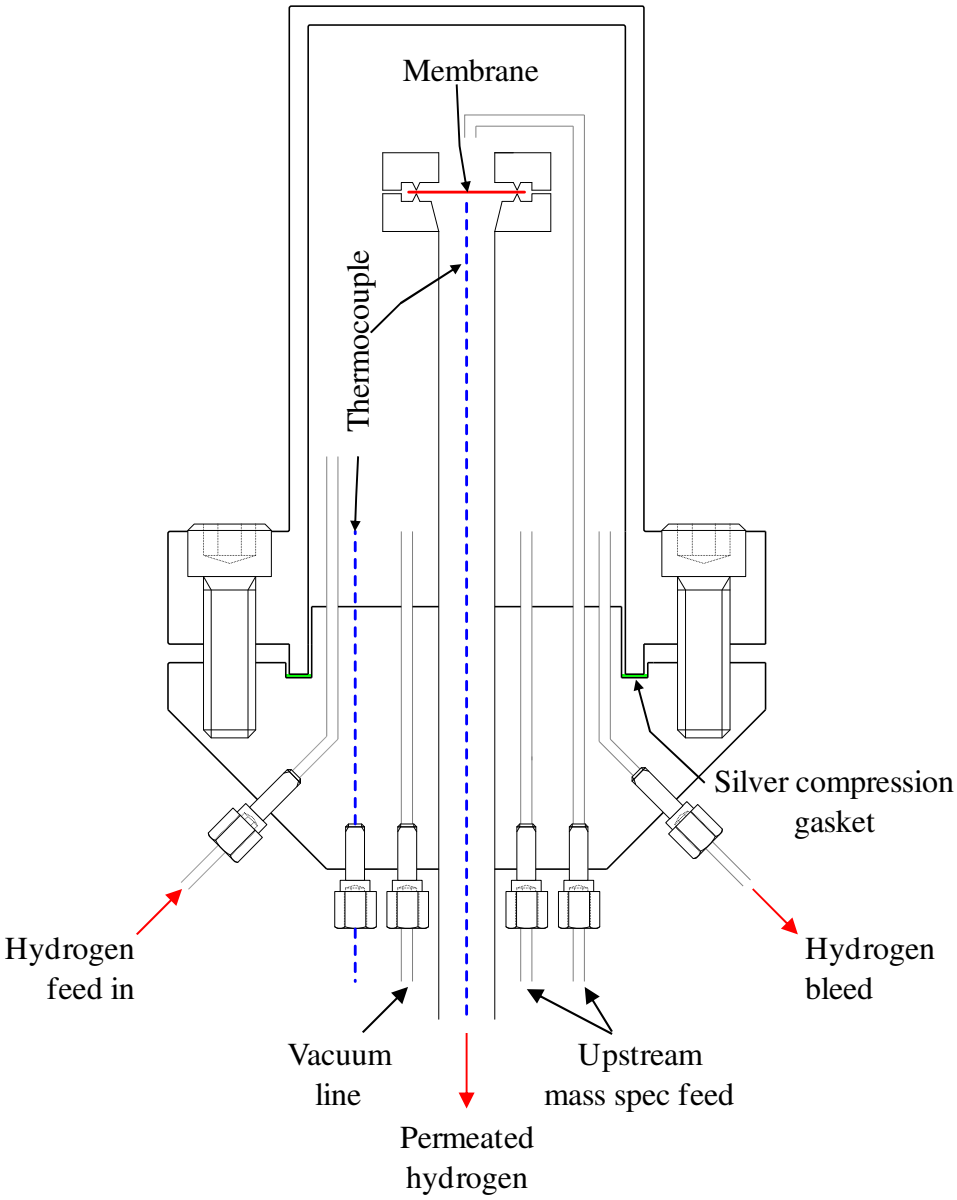

Figure 3.5 Schematic diagram of the MPR reactor vessel [28].

It should be noted that parts of the MPR system were overhauled during the course of this work. Specifically, the downstream MFC was serviced and recalibrated. The original MPR setup had a downstream MFC fitted that was calibrated for N_2 gas whereby the measured flow rate was converted to hydrogen using the following gas factor 1.008 including an additional conversion factor 1.045 for improved accuracy.

Following the MPR refurbishment, the N_2 calibrated downstream MFC was replaced with an MFC calibrated for hydrogen thus negating the need for the conversion factors. Therefore, hydrogen permeability measurements obtained from membranes after the MPR overhaul will be presented and discussed here.

3.3. Material characterisation and analysis

At various stages throughout this work, the membranes were characterised using X-ray diffraction to determine existing phases, phase changes, surface composition and conditions for interdiffusion. Energy dispersive spectroscopy was used for surface chemical analysis which helped verify the surface composition. Furthermore, X-ray photoelectron spectroscopy was used to acquire a compositional depth profile of the membranes to study any changes in surface composition along the thickness. Furthermore, a field emission gun coupled with a scanning electron microscope was used to obtain high resolution images of the Pd thin film microstructure.

3.3.1. Membrane crystal structure and composition

3.3.1.1. X-ray diffraction

Ex-situ X-ray diffraction (XRD) analyses were performed with a Bruker D8-Advance diffractometer using monochromatic $CuK_{\alpha 1}$ radiation (λ = 1.54056 Å). All ex-situ XRD analyses were performed under ambient conditions. XRD patterns were collected for both the top and basal surfaces of the membrane and offcut samples before and after exposure to hydrogen over a 2θ range of 25 to 140° using an approximate step size of 0.028°. It will be common practice throughout this work to perform XRD analysis on a membrane before and

after MPR testing to identify any structural changes that may occur as a result of exposure to high temperatures in a hydrogen atmosphere.

XRD analysis can be used for phase identification, determining phase composition and detecting any interdiffusion between the sputter-deposited Pd thin film and bulk Pd-Cu membrane. Bragg's law was used to calculate the interplanar distance, d_{hkl}:

$$\lambda = 2d_{hkl}sin\theta \qquad \text{Equation 3.2}$$

where θ is the scattering angle in degrees. For the composition of Pd-Cu foil used in this work only the BCC and FCC phases were observed. Table 3.2 shows the Miller indices of the expected diffraction planes for the BCC and FCC crystal structures:

Table 3.2 Miller indices for the BCC and FCC diffraction planes.

BCC	FCC
(110)	(111)
(111)	(200)
(200)	(220)
(210)	(311)
(211)	(222)
(220)	(400)
(300)/(221)	(331)
(310)	(420)

The interplanar distance is related to the lattice parameter (a) through Equation 3.3:

$$a = d_{hkl}\sqrt{h^2 + k^2 + l^2} \qquad \text{Equation 3.3}$$

where h, k and l are the Miller indices of the diffraction plane. Rearranging Equation 3.2 and substituting into Equation 3.3 gives Equation 3.4:

$$a = \frac{\lambda\sqrt{h^2 + k^2 + l^2}}{2sin\theta}$$ Equation 3.4

In order to calculate the lattice parameter for the BCC and FCC phase, the lattice parameter for each *hkl* diffraction plane for that particular phase is calculated using Equation 3.4 and plotted against $cos^2\theta$. The *y*-intercept of this plot gives the value for the absolute lattice parameter. The lattice parameter is of significance in this work as it can be used to accurately determine alloy and phase composition using Vegard's law [249]. This is an empirical rule that stipulates a linear correlation between lattice parameter (*a*) and the alloy concentration of the constituent elements.

In-situ variable temperature XRD (VTXRD) was performed on square foil offcuts using an Anton Paar XRK 900 pressure cell in order to observe any phase transformations and interdiffusion between the Pd thin film and bulk Pd-Cu membrane under similar conditions used in the MPR. One as-received foil offcut was analysed under 445 kPa of flowing helium to determine the phase transition temperatures in an inert atmosphere and a second foil offcut was tested under 445 kPa of flowing hydrogen for comparison. The aim was to investigate the effects of hydrogen on phase transition under conditions similar to those used in the MPR.

Furthermore, VTXRD studies were performed on Pd coated foil offcuts under 445 and 100 kPa of flowing hydrogen to observe the effects of temperature and hydrogen pressures used in the MPR on interdiffusion between the Pd thin film and bulk Pd-Cu membrane. VTXRD scans were conducted isothermally before heating to the next temperature set point. The temperature ramp rate used for all VTXRD experiments was 2.4 °C min^{-1} heating from 30 to 700 °C and then cooled back to 30 °C at approximately 5 °C min^{-1}.

3.3.1.2. Scanning electron microscopy/Energy dispersive spectroscopy

Scanning electron microscopy (SEM) and energy dispersive spectroscopy (EDS) was performed in secondary electron imaging mode using a Jeol 6060 microscope. The Jeol 6060 works in conjunction with INCA EDS software which was used to determine the composition of the as-received Pd-Cu foil and any compositional variation in the membranes before and after MPR testing. A Jeol 7000 microscope equipped with a field emission gun (FEG) was also used to produce high magnification and high resolution images of the Pd thin film microstructure.

3.3.1.3. X-ray photoelectron spectroscopy

X-ray photoelectron spectroscopy (XPS) compositional depth profiling can be obtained using a series of ion beam etch cycles combined with XPS scans of the exposed surface. Using an ion gun, the surface of the sample is etched for a set period of time prior to being switched off to allow XPS scanning of the newly exposed surface. A sequence of etching cycles and XPS spectra acquisition will then be used to construct a plot of composition as a function of depth for a sample.

Depth profiling of the as-deposited surface modified Pd-Cu foil offcuts was used to investigate any interdiffusion between the Pd thin film and bulk Pd-Cu foil taking place during the sputtering process and to identify at which depth the interface occurs. In addition, XPS depth profiling was performed on surface modified Pd-Cu foil offcuts following VTXRD experiments and surface modified Pd-Cu membrane offcuts after MPR testing in order to examine the effects of elevated temperatures and hydrogen pressures on near surface composition.

A Thermo K-Alpha XPS Spectrometer with a monochromated K-Alpha source fitted with a MAGCIS ion gun was used for the depth profile analysis. The charge compensation was on during measurements. The following depth profile settings were used:

- Monatomic Ar gun mode
- Ion energy = 2 keV
- 2×2 mm scan area
- Reference etching rate (Ta_2O_5) = 0.21 nm s^{-1}

An appropriate etch cycle and etch depth was selected according to the Pd film thickness being analysed. Thinner Pd films had a shorter etch cycle compared to relatively thicker Pd films in order to achieve higher resolutions of the interface region. Using a Ta_2O_5 reference, etching depth of the foils was estimated.

4. Results and discussion

4.1. Introduction

Several membranes have been studied throughout the course of this work in order to compare and further understand the effects of a Pd thin film on the performance of bulk Pd-Cu foil membranes for the application of hydrogen separation. Characterisation techniques introduced in Section 3.3 were employed to further relate the influence of crystal structure, phase composition and interdiffusion on hydrogen permeability.

Initially, bulk Pd and two batches (Batch 1 and Batch 2) of Pd-Cu membranes were tested in the membrane permeability rig (MPR) under a pure hydrogen atmosphere to establish a baseline reference against which to measure the performance of the surface modified Pd-Cu membranes. From this, a comparison will be drawn in order to determine which membrane achieves the highest hydrogen permeability. The aforementioned characterisation techniques have been performed pre and post MPR testing in order to understand and explain the hydrogen permeability values achieved by each membrane studied in this work.

Three types of surface modified Pd-Cu membranes have been investigated in this work, referred to as Type A, B and C. Table 4.1 provides further details of the three types of surface modified Pd-Cu membranes giving details of Pd coating times and Pd-Cu foil batch substrate used.

Table 4.1 Description of the three types of surface modified Pd-Cu membranes used in this work.

Type	Pd coating time (s)	Pd-Cu substrate
A	50	Batch 1 and 2
B	1,000	Batch 2
C	1,800	Batch 2

It should be noted that due to a limited supply, only two Type A membranes were prepared using the Batch 1 Pd-Cu foil. The remaining Type A and all of the Type B and C membranes were fabricated using the Batch 2 Pd-Cu foil. The Type A, B and C membranes have been tested in the MPR using the configuration shown in Figure 3.4(a) and (b). The aim was to determine how the hydrogen permeability of the Type A, B and C membranes are affected upon positioning the Pd thin film on the feed side and permeate side during MPR testing.

4.2. As-received bulk Pd foil membrane

4.2.1. Pre-MPR characterisation

Ex-situ XRD scans were performed on both sides of the Pd membrane under ambient conditions before MPR testing. The XRD pattern is shown in Figure 4.1 and clearly indicates a single phase FCC crystal structure present in the as-received Pd membrane with each (*hkl*) diffraction peak indexed. Moreover, the pattern shows preferential texturing in the (220) and (311) diffraction planes which could be attributed to the direction of the cold rolling process. The (222) diffraction plane is present in this pattern, however, due to its relatively low intensity count it may appear invisible.

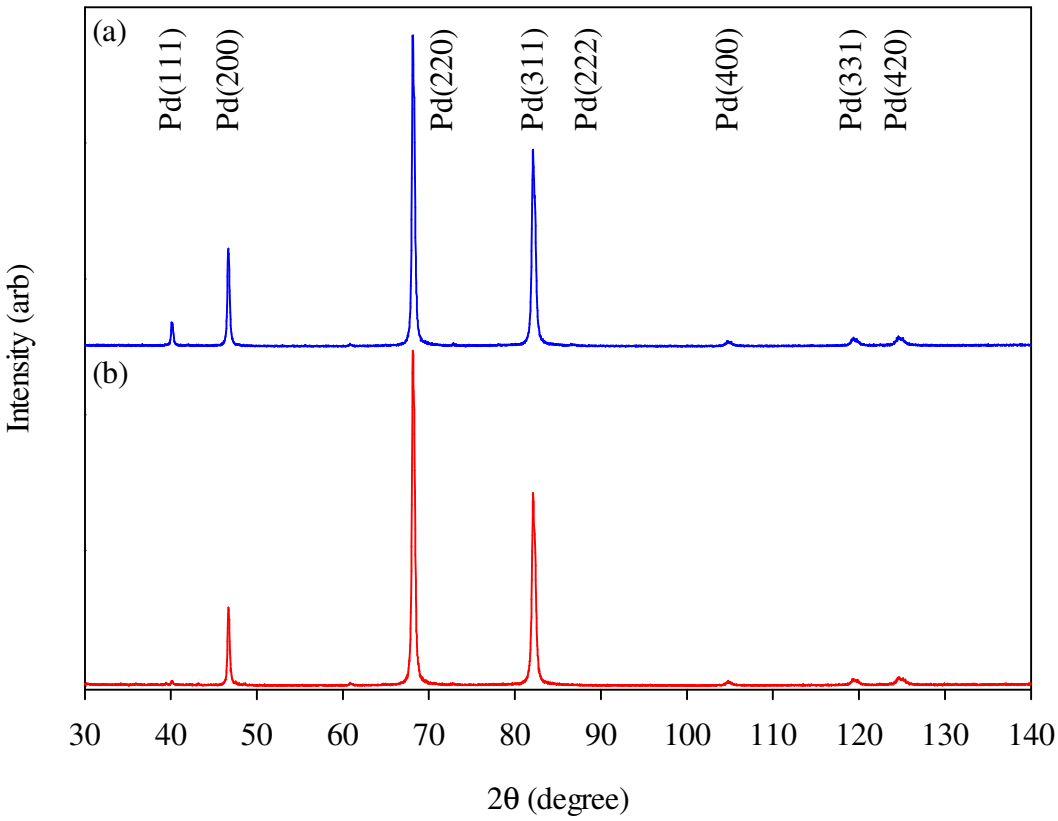

Figure 4.1 XRD patterns of the as-received pure Pd foil membrane prior to MPR testing performed on the feed side (a) and permeate side (b).

4.2.2. MPR results

The hydrogen permeability of bulk pure Pd membranes has been studied extensively over the years [28, 35, 85-91, 250] and is well established. Therefore, the hydrogen permeability of a 67.8 µm thick Pd membrane was measured in the membrane permeability rig (MPR) to validate the system calibration and experimental methodology following the MPR overhaul (see Section 3.2). In order to accurately measure the hydrogen permeability of the Pd membrane, the partial pressure exponent, also known as the *n*-value, must be determined.

It is important, however, to understand the definition of the *n*-value. Consider the physical adsorption of hydrogen by a porous membrane through a process known as physisorption which is described in Equation 4.1.

$$H_{2(gas)} \rightleftharpoons H_{2(adsorbed)}$$ Equation 4.1

In this instance, at dilute concentrations and constant temperature, Henry's law may apply as shown in Equation 2.2. As previously noted in Section 2.1.3, this law stipulates that the concentration (C_{gas}) of hydrogen molecules in the porous membrane, for example, is directly proportional to its partial pressure (P_{gas}) in the gas phase.

$$S_H = \frac{C_{gas}}{P_{gas}}$$ Equation 2.2

The term S_H has previously been referred to as the solubility constant but it can also be seen as the equilibrium constant for the physisorption process shown in Equation 4.1. Now, consider the chemisorption of a hydrogen molecule onto the surface of a dense metal membrane and the subsequent dissociation into monatomic form and absorption (Equation 4.2).

$$^1/_2\, H_{2(gas)} \rightleftharpoons H_{(absorbed)}$$ Equation 4.2

From Equation 4.2, S_H also referred to as the solubility constant, S, can be defined by Sieverts' law (Equation 2.3):

$$S = \frac{C}{P_{H_2}^{1/2}}$$ Equation 2.3

Sieverts' law is valid assuming hydrogen behaves like an ideal gas, hence S can be defined as the ratio of hydrogen concentration in the metal over the hydrogen partial pressure in the gas phase raised to the exponent of the number of moles, in this case 0.5. This exponent is

referred to as the *n*-value, as previously shown in Equation 2.8, and can vary anywhere between 0.5 and 1.

$$J = \frac{\Phi(P_1^n - P_2^n)}{x} \qquad \text{Equation 2.8}$$

An *n*-value close to 0.5 indicates a permeation process that is rate limited by hydrogen diffusion through the bulk membrane whereas an *n*-value approaching 1 means that hydrogen dissociation at the membrane surface is the rate limiting step. Authors have reported *n*-values for free-standing Pd membranes ranging between 0.62 and 0.8 [86, 90, 251, 252].

The reason for the observed deviation from Sieverts' square root dependence on hydrogen pressure has been a matter of speculation. One theory is that the concentration of dissolved hydrogen in the membrane may have an effect on the diffusivity and thus permeability along with the *n*-value [253]. Others postulate that the cause could be hydrogen diffusion through defects in the Pd membrane or even through gaps in the membrane sealing mechanism [252]. Another explanation assumes that when a free-standing Pd membrane is sufficiently thin, hydrogen diffusion across the thickness of the membrane is rapid and surface dissociation becomes the rate limiting step where the *n*-value would deviate from 0.5 and tend towards 1. However, previous work has reported to the contrary that Pd membranes with thicknesses as low as 7.2 µm exhibit diffusion limited permeation [252].

The *n*-value was determined for the Pd membrane used in this work by performing permeability isotherms at 350, 375, 400, 425 and 450 °C. This temperature range was chosen since hydrogen flux was appreciable under the pressure differentials used during measurements. At each temperature, the hydrogen permeate pressure is maintained at 100 kPa and the hydrogen flux is measured at hydrogen feed pressures of 300, 400, 500, 600 and

700 kPa. The permeability isotherms for the pure Pd membrane are presented in plots of membrane flux as a function of hydrogen differential pressure as shown in Figure 4.2 and Figure 4.3. The *n*-values were determined using least squares regression for the experimental data. In Figure 4.2, the data points were constrained to an *n*-value of 0.5 to establish how well the Pd membrane obeys Sieverts' law under the MPR test conditions used. This is measured using the coefficient of determination (R^2). In Figure 4.3, the *n*-value was adjusted to optimise R^2 in order to find its best fit.

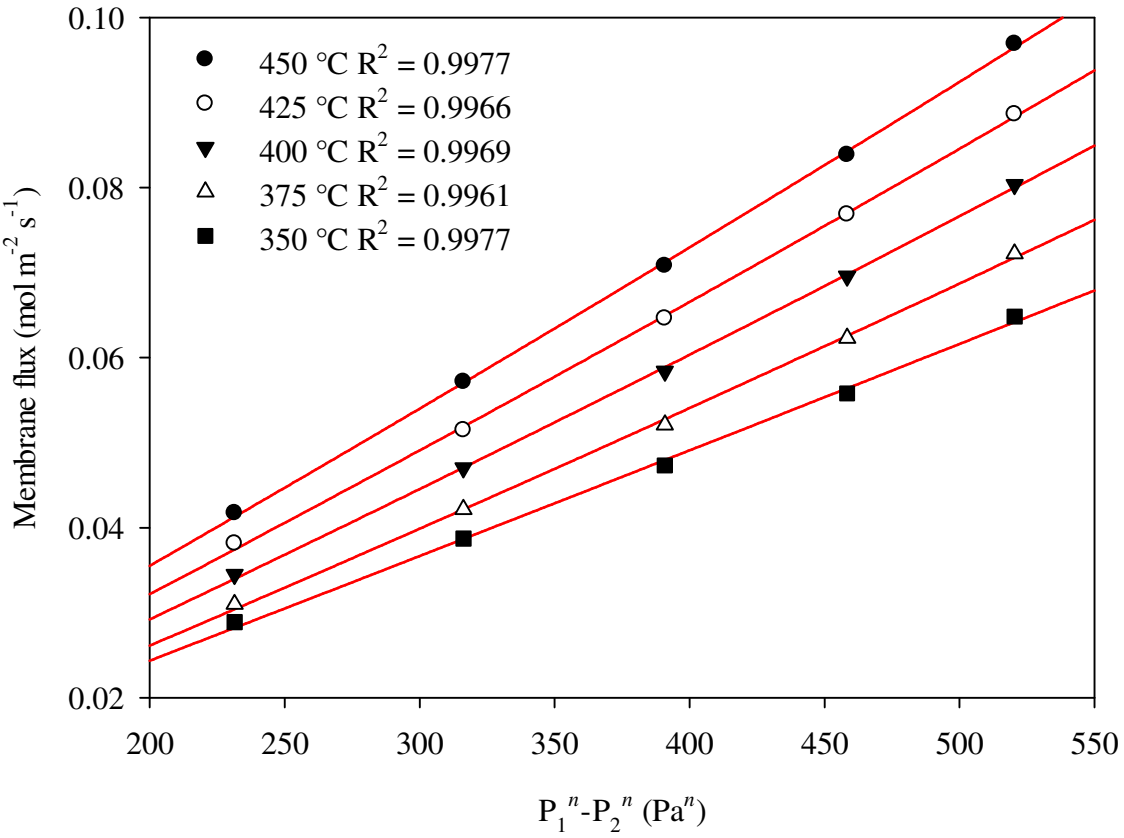

Figure 4.2 Membrane flux as a function of hydrogen differential pressure with *n* constrained to 0.5.

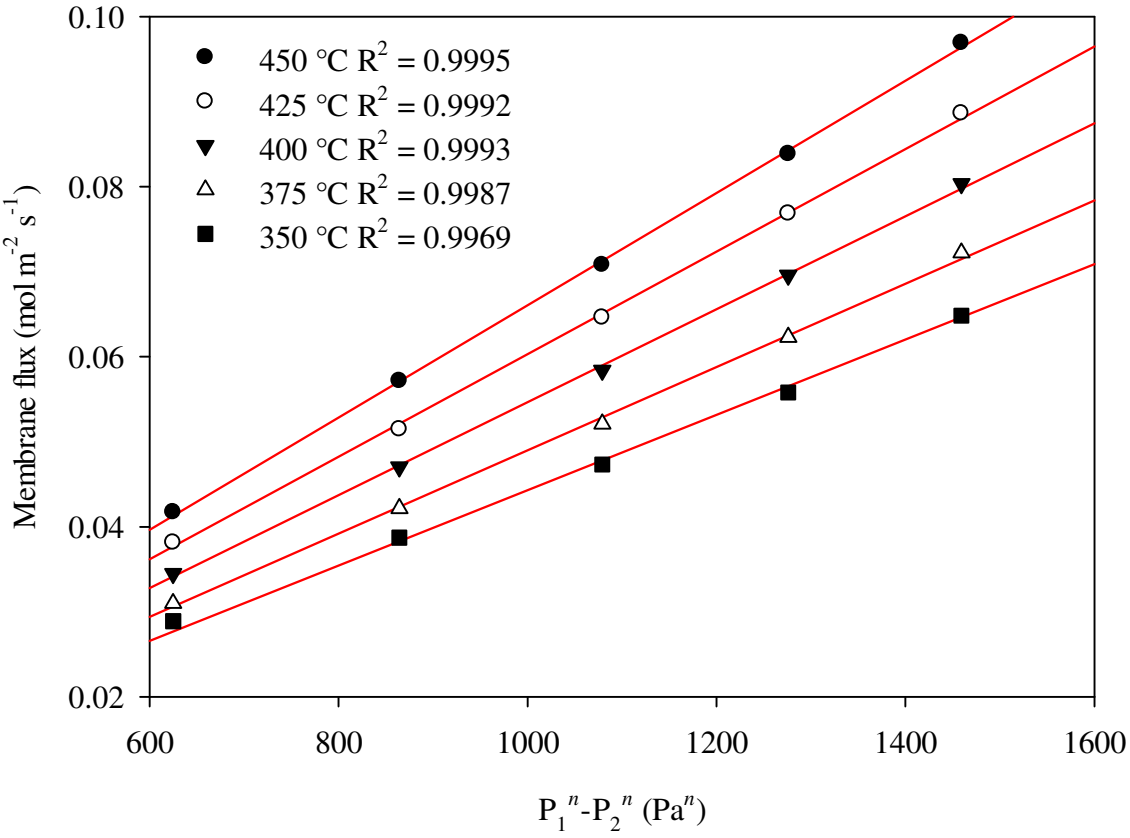

Figure 4.3 Membrane flux as a function of hydrogen differential pressure with *n* constrained to the best fit value of 0.57.

As shown in Figure 4.2, an *n*-value of 0.5 gives high values of R^2 revealing a good linear fit for the hydrogen flux measured across the Pd membrane. Figure 4.3 reveals, however, that an *n*-value of 0.57 gives the best fit for the measured hydrogen flux through the Pd membrane which compares well with the *n*-value of 0.62 reported by Morreale et al [90]. Moreover, it was shown that the *n*-value varied with hydrogen feed pressure where at < 500 kPa an *n*-value of approximately 0.57 was measured and at > 2,500 kPa an *n*-value of 0.65 was observed [90].

Morreale [90] has discussed the effect of hydrogen feed pressure on the *n*-value by relating the dependence of hydrogen permeability to the hydrogen concentration in the membrane.

According to Sieverts' law (Equation 2.3), increasing the hydrogen pressure would increase the hydrogen concentration on the membrane feed side.

Since membrane permeability (Φ) is proportional to the product of diffusivity (D) and the solubility constant (S) (Equation 2.6), an increase in hydrogen concentration at the membrane feed side may influence D and S and therefore Φ.

$$\Phi = DS \qquad \text{Equation 2.6}$$

It would be expected that increasing the hydrogen concentration at the membrane feed side relative to the permeate side would create an even greater driving force for hydrogen diffusion and thus an increase in diffusivity. Holleck [85] observed that under sub-atmospheric conditions hydrogen diffusivity increases with increasing hydrogen feed pressure in a Pd membrane. However, the reverse has been shown to occur in V [254] and Nb-Ta [255] systems. It was suggested that hydrogen diffusivity decreased with increasing concentration as result of a reduced number of available neighbouring interstitial sites that facilitate atomic jumps [255]. In general, a decisive trend has not been established yet between hydrogen concentration and diffusivity.

It would also seem plausible that hydrogen concentration would have an effect on the solubility constant. It has been theorised that an increase in hydrogen concentration can form an non-ideal solution whereby the dissolved H^+ exhibit repulsive forces between each other. As shown in Equation 2.3, an increase in hydrogen concentration would result in an increase in the solubility constant and therefore membrane permeability. By substituting Equation 2.3 into Equation 2.6 it can be seen that Φ is proportional to C (Equation 4.3).

$$\Phi = D\frac{C}{P_{H_2}^{1/2}} \qquad \text{Equation 4.3}$$

Contaminants present on the surface of the Pd membrane could reduce the number of active sites for hydrogen dissociation and absorption into the metal thus decreasing the rate of the dissolution reaction which could be responsible for the observed deviation from Sieverts' law. Nonetheless, the experimentally determined *n*-value of 0.57 indicates that hydrogen permeation through the bulk Pd membrane is still mainly limited by diffusion.

Hydrogen permeability of the Pd membrane was measured as a function of temperature using the MPR. Isobaric conditions were used during membrane permeability measurements where 445 kPa of hydrogen pressure was applied to the feed side and 100 kPa was maintained at the permeate side to produce a constant 345 kPa pressure (50 psi) gradient across the membrane. These conditions are used throughout this work unless otherwise stated. Figure 4.4 shows hydrogen permeability calculated using an *n*-value of 0.5 and 0.57.

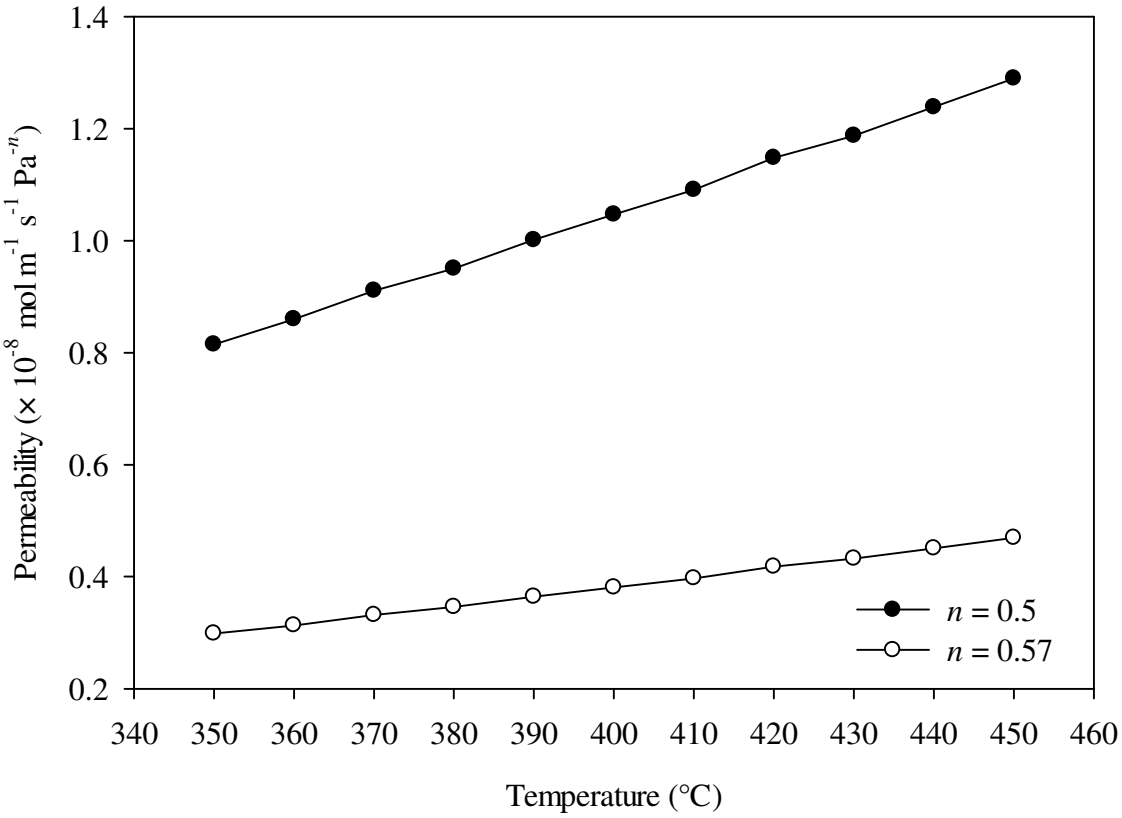

Figure 4.4 Hydrogen permeability as a function of temperature for the 67.8 µm thick pure Pd foil membrane with a hydrogen feed pressure of 445 kPa and permeate pressure of 100 kPa. The solid symbol curve was calculated using an *n*-value of 0.5 whereas the open symbol curve uses the best fit *n*-value of 0.57.

Assuming there are no surface contaminants of the Pd membrane, the behaviour of Φ can be modelled using the Arrhenius type Equation 2.9.

$$\Phi = \Phi_0 exp\left(\frac{-E_\Phi}{RT}\right) \qquad \text{Equation 2.9}$$

Plotting $ln(\Phi)$ against reciprocal temperature, T^{-1}, yields a straight line as shown in Figure 4.5. The slope of this straight line corresponds to the hydrogen permeation activation energy (E_Φ) and the *y*-intercept gives the permeability constant (Φ_0). The two curves in Figure 4.4 were used to construct the plot in Figure 4.5 in order to determine E_Φ and Φ_0 for both *n*-values.

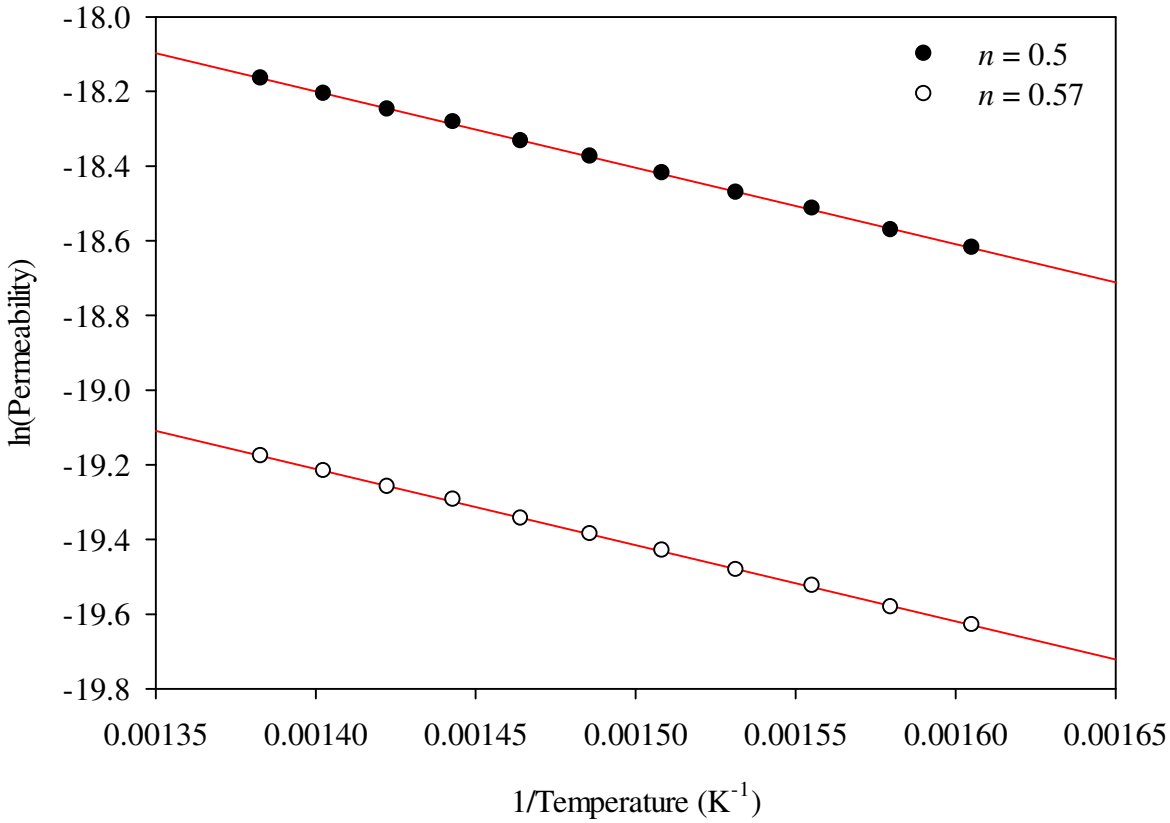

Figure 4.5 Arrhenius plot of the hydrogen permeability data shown in Figure 4.4 between 350 and 450 °C. The solid symbol curve was calculated using an *n*-value of 0.5 whereas the open symbol curve uses the best fit *n*-value of 0.57.

For $n = 0.5$, Φ_0 was determined to be 2.41×10^{-7} mol m^{-1} s^{-1} Pa$^{-0.5}$ and E_Φ was calculated to be 17.54 kJ mol^{-1}. For $n = 0.57$, a Φ_0 of 8.76×10^{-8} mol m^{-1} s^{-1} Pa$^{-0.57}$ and E_Φ of 17.53 kJ mol^{-1} can be calculated. The general permeability formulae (350 – 450 °C) for the Pd membrane have been derived from Figure 4.5 using an *n*-value of 0.5 and the best fit value of 0.57 as shown in Equation 4.4 and Equation 4.5, respectively.

$$\Phi_{n=0.5} = 2.41 \times 10^{-7} exp\left(\frac{-17.54 \times 10^3}{RT}\right) \qquad \text{Equation 4.4}$$

$$\Phi_{n=0.57} = 8.76 \times 10^{-8} exp\left(\frac{-17.53 \times 10^3}{RT}\right) \qquad \text{Equation 4.5}$$

The more realistic *n*-value of 0.57 thus shows that the hydrogen dissolution at the membrane surface has a major impact on the overall permeation mechanism by reducing hydrogen permeability by a factor of approximately three when compared to the theoretical *n*-value of 0.5 assumed by Sieverts' law.

The values for E_Φ and Φ_0 determined for the bulk Pd membrane used in this work fall within the range found in literature (Table 4.2) and as a result validate the reliability of the MPR system and experimental procedure. Therefore, permeability data obtained for other membranes investigated in this work can be compared to those found in literature with high confidence. Furthermore, it can be noted from the data compiled in Table 4.2 that Φ_0 decreases with increasing *n*-value whereas E_Φ remains relatively unaffected by changes in the *n*-value as found in this work and the work of Morreale [90].

Table 4.2 Published data for hydrogen permeability in bulk free-standing Pd membranes.

Thickness (µm)	Geometry	*n*	Φ_0 (mol m^{-1} s^{-1} Pa^{-n})	E_Φ (kJ mol^{-1})	Reference
70	disc	0.5	2.80×10^{-7}	15.40	Fletcher [28]
800 – 2,025	disc	0.5	1.42×10^{-7}	12.81	Holleck [85]
10 – 150	disc	0.68	1.47×10^{-8}	11.91	Hurlbert [86]
940	disc	0.5	3.80×10^{-7}	20.50	Katsuta [88]
486 – 762	disc	0.5	2.20×10^{-7}	15.67	Koffler [89]
1,000	disc	0.5	3.31×10^{-7}	13.81	Morreale [90]
		0.62	5.65×10^{-8}	13.41	
11,500	wire	0.5	1.72×10^{-7}	13.46	Toda [91]
67.8	disc	0.5	2.41×10^{-7}	17.54	Present work
		0.57	8.76×10^{-8}	17.53	

It should also be noted that Fletcher's [28] data was obtained on the same MPR used throughout this work prior to the system overhaul. From Table 4.2, it can be seen that Fletcher's [28] value for E_Φ lies mid-range of the literature values whereas Φ_0 is the second highest of the literature values. For further comparison, Table 2.4 shows that Fletcher [28] has

reported a hydrogen permeability for a free-standing Pd membrane of 1.43×10^{-8} mol m^{-1} s^{-1} $Pa^{-0.5}$ at 350 °C for an *n*-value of 0.5 which is the highest found in literature. Post MPR system overhaul, this work reports a hydrogen permeability for a free-standing Pd membrane of 8.15×10^{-9} mol m^{-1} s^{-1} $Pa^{-0.5}$ at 350 °C and an *n*-value of 0.5, which is 43% lower than the figure reported by Fletcher [28].

Two possible reasons could explain the observed discrepancy. Firstly, Fletcher [28] acquired hydrogen permeability data on the MPR pre-overhaul using a N_2 calibrated MFC, whereas this work obtained measurements post-overhaul using a hydrogen calibrated MFC. Secondly, the Pd membranes studied by Fletcher [28] had undergone bowing during hydrogen permeability measurements as a result of the applied pressure differential. The bowing effect produced a 2.1 mm vertical displacement in the Pd membranes which had to be accompanied by a decrease in membrane thickness and increase in active surface area which led to an apparent increase in hydrogen permeability.

Rather than using the initial membrane active surface area and thickness to calculate hydrogen permeability, Fletcher [28] used the deformed active membrane surface area and thickness instead for improved accuracy. However, the deformed parameters were mathematically estimated as opposed to physically measured. To alleviate this issue, this work used a porous stainless steel support to prevent membrane bowing which had the added benefit of being able to use the initial membrane active surface area and thickness for determining the hydrogen permeability with improved accuracy and reliability.

Comparing the hydrogen permeability data for Pd membranes is difficult since there are many variables that can affect the accuracy of the results. It could be said that purity of the Pd foil, membrane geometry, experimental equipment, conditions and methodology can vary from

author to author. Therefore, measurements obtained by one author may not necessarily be reproduced by another author in a separate location. With that being said, the hydrogen permeability measured for the Pd membrane in this work comfortably lies within the range of the published data displayed in Table 2.4 and Table 4.2 hence it would have greater reliability over the data reported by Fletcher [28].

Morreale [90] noted the effects of hydrogen feed pressure on the *n*-value, although there appears to be no information available in literature on the effects of temperature. Figure 4.6 displays the variation in the *n*-value as a function of temperature for the Pd membrane. At 350 °C, the *n*-value is 0.52 and appears to obey Sieverts' law, however, increasing the temperature to 375 °C increases the *n*-value to 0.58 where it remains stable up until 425 °C and slightly decreases to 0.57 at 450 °C. Deviation from Sieverts' law with increasing temperature could be explained by the endothermic nature of hydrogen diffusion which is expected to increase with a rise in temperature.

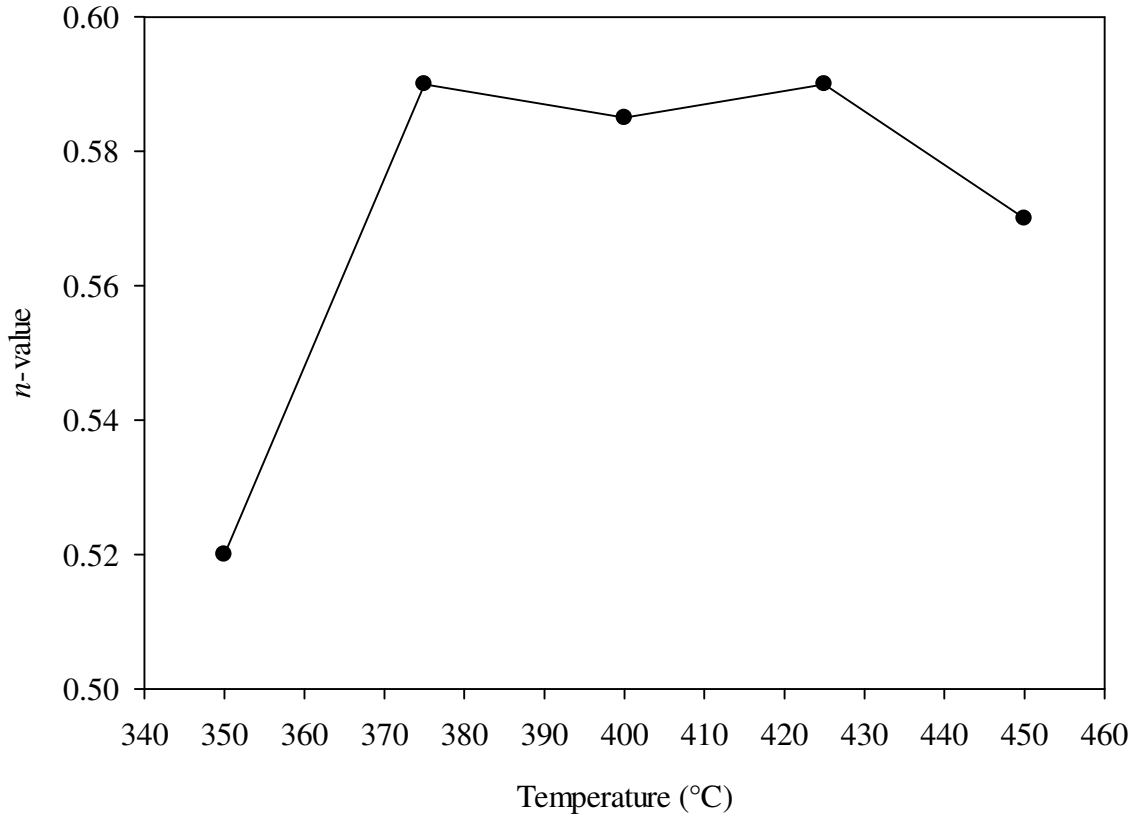

Figure 4.6 Variation of *n*-value as a function of temperature for the pure Pd membrane.

4.2.3. Post-MPR characterisation

Ex-situ XRD scans were performed on both sides of the Pd membrane under ambient conditions after MPR testing to examine the effects of thermal cycling in a hydrogen atmosphere. By comparing Figure 4.1 with Figure 4.7, it can be seen that there are no signs of any phase or structural changes that have occurred as a result of MPR testing. Like Figure 4.1, the XRD pattern shown in Figure 4.7 also indicates the presence of a single phase FCC crystal structure in the Pd membrane with preferential texturing in the (220) and (311) diffraction planes.

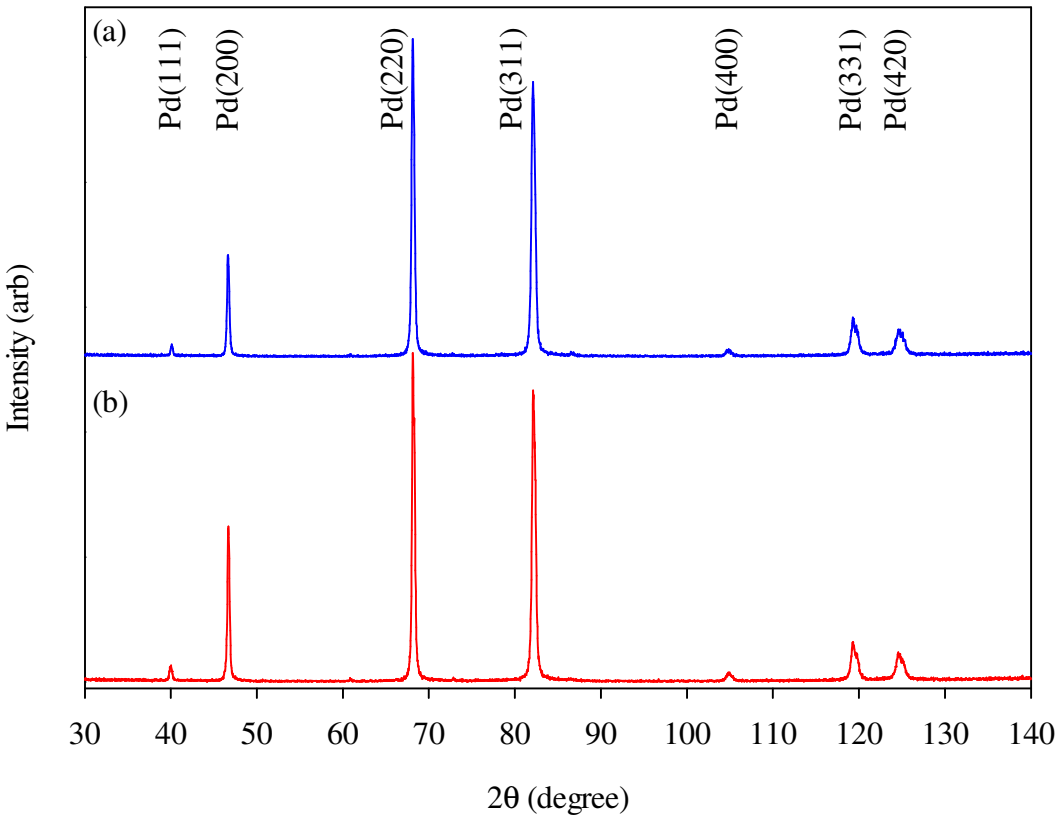

Figure 4.7 XRD patterns of the as-received pure Pd foil membrane following MPR testing performed on the feed side (a) and permeate side (b).

The lattice parameter (a) for the Pd membrane was determined from Figure 4.1 and Figure 4.7. With the wavelength (λ) of the monochromatic $CuK_{\alpha 1}$ X-ray beam known, the value for a can be obtained using Equation 3.4 for each scattering angle (θ) indicated by the position of each diffraction plane.

$$a = \frac{\lambda\sqrt{h^2 + k^2 + l^2}}{2sin\theta} \qquad \text{Equation 3.4}$$

From the XRD data shown in Figure 4.1 and Figure 4.7, the average value for a was calculated to be 3.8905 ± 0.0003 Å. This is in excellent agreement with published values which range between 3.89 – 3.891 Å [28, 34, 38, 77, 85, 256, 257] thus proving the high reliability and accuracy of the XRD equipment and method used for calculating a.

4.3. As-received bulk Pd-Cu foil membranes

4.3.1. Pre-MPR characterisation

In the as-received state, the nominal composition of the Batches 1 and 2 foil was stated as $Pd_{60}Cu_{40}$ wt%. According to the Pd-Cu phase diagram (Figure 2.16), the $Pd_{60}Cu_{40}$ wt% composition contains a CsCl-type ordered BCC equilibrium phase below 450 °C. Figure 4.8 and Figure 4.9 show representative ex-situ XRD patterns of Batches 1 and 2, respectively. The analysis indicates the presence of the disordered FCC structure which could be due to the alloy being quenched from the high temperature FCC phase during the melting process. Furthermore, Figure 4.8(a) reveals a peak at $2\theta = 29.4°$ which coincides with the $Cu_2O(110)$ diffraction plane. It would seem plausible that the Cu used to fabricate either batch may have formed an oxide layer prior to melting which could then explain the origin of the $Cu_2O(110)$ diffraction peak.

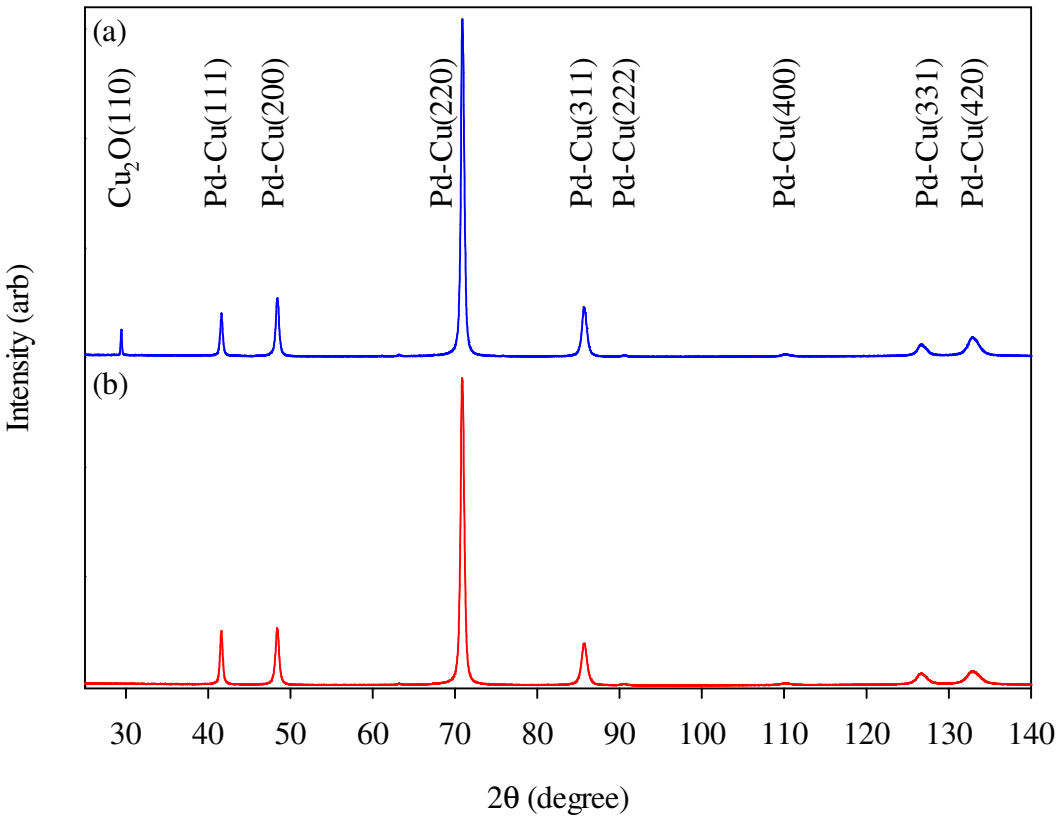

Figure 4.8 XRD patterns of the as-received Batch 1 Pd-Cu foil membrane before MPR testing performed on the feed side (a) and permeate side (b).

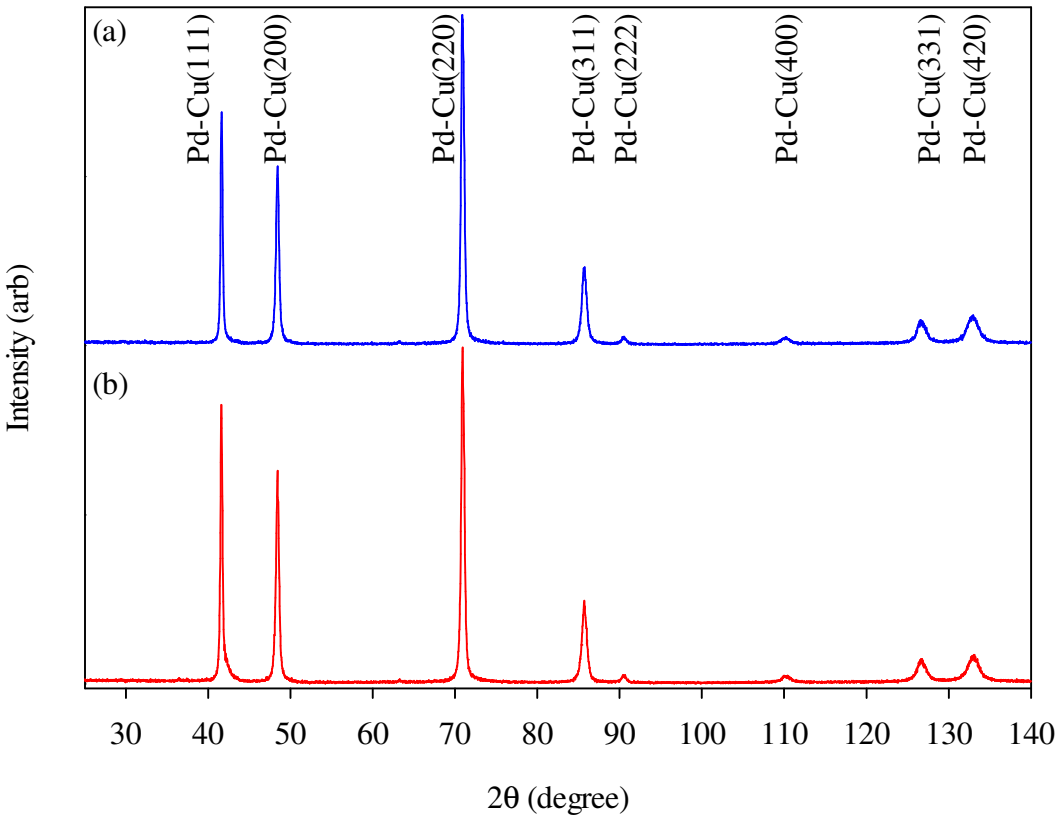

Figure 4.9 XRD patterns of the as-received Batch 2 Pd-Cu foil membrane before MPR testing performed on the feed side (a) and permeate side (b).

From Figure 4.8, the lattice parameter for both sides (Side (a) and Side (b)) of the Batch 1 Pd-Cu membrane in the as-received state can be determined. The lattice parameters were calculated as 3.759 and 3.754 Å for Side (a) and Side (b), respectively, using Equation 3.4. The lattice parameters for the Batch 2 Pd-Cu membrane was determined in a similar manner from Figure 4.9, to give 3.759 and 3.754 Å for Side (a) and Side (b), respectively. These lattice parameters are comparable to published values of the same FCC phase composition which range between 3.75 and 3.764 Å [39, 210, 212, 258-260].

In Table 4.3, the calculated lattice parameters were used in Equation 6.1 to determine the associated FCC phase compositions and compared with the EDS chemical analysis results. Details of the method used to calculate the Pd-Cu FCC phase composition is given in the

Appendix (Section 6.1). It is apparent for both membranes that Side (a) has a different FCC phase composition to that of Side (b) indicating that both batches have compositional inhomogeneity. This observation is corroborated well by the EDS results despite the compositions obtained from either technique not matching exactly. It should be noted that the EDS analysis sampled information from both batches over a relatively smaller area (~150 μm^2) compared to XRD which scans and collects information from the entire membrane surface (~350 mm^2). Hence, the compositions obtained using XRD analysis are considered to be more accurate and therefore it can be said that the average FCC phase composition for both batches of Pd-Cu membranes in the as-received state is $Pd_{61.3}Cu_{38.7}$ wt%.

Table 4.3 A summary of the FCC phase compositions (wt%) determined using XRD and EDS for both batches of as-received Pd-Cu membranes.

	Surface	XRD	EDS
Batch 1	Side (a)	$Pd_{62.0}Cu_{38.0}$	$Pd_{61.7 \pm 0.2}Cu_{38.3 \pm 0.2}$
	Side (b)	$Pd_{60.6}Cu_{39.4}$	$Pd_{58.9 \pm 0.2}Cu_{41.1 \pm 0.2}$
Batch 2	Side (a)	$Pd_{62.0}Cu_{38.0}$	$Pd_{60.8 \pm 0.6}Cu_{39.2 \pm 0.6}$
	Side (b)	$Pd_{60.6}Cu_{39.4}$	$Pd_{57.6 \pm 0.9}Cu_{42.4 \pm 0.9}$

4.3.1.1. Effects of temperature and hydrogen pressure on the as-received Pd-Cu foil

VTXRD experiments were performed on Batch 1 Pd-Cu foil offcuts in the as-received state. Due to the similarity in composition, the results obtained from the Batch 1 Pd-Cu foil offcuts can be representative of Batch 2 also. Initially, a Batch 1 Pd-Cu offcut (Foil 1) was cycled under 445 kPa of helium during VTXRD in order to determine the phase transition temperature in the absence of hydrogen. Figure 4.10 shows the heating stage of the cycle between 250 and 700 °C. XRD scans were recorded at 25 °C increments between 250 and 500 °C in order to capture any sudden phase changes. Above 500 °C, XRD scans were taken every 50 °C up until the end of the cycle at 700 °C. At room temperature, Foil 1 contains only

the disordered FCC phase, denoted α. The BCC phase, denoted β, starts to form at 300 °C and appears to be fully ordered by 475 °C as indicated by the BCC Pd-Cu(100) diffraction peak at 2θ = 30°. 'c' denotes the corundum sample holder. At 325 °C, the FCC phase begins to disappear leaving behind the BCC phase although the FCC phase reforms at 475 °C. By 600 °C, the BCC phase disappears with only the FCC phase present up until the end of the heating stage of the cycle at 700 °C.

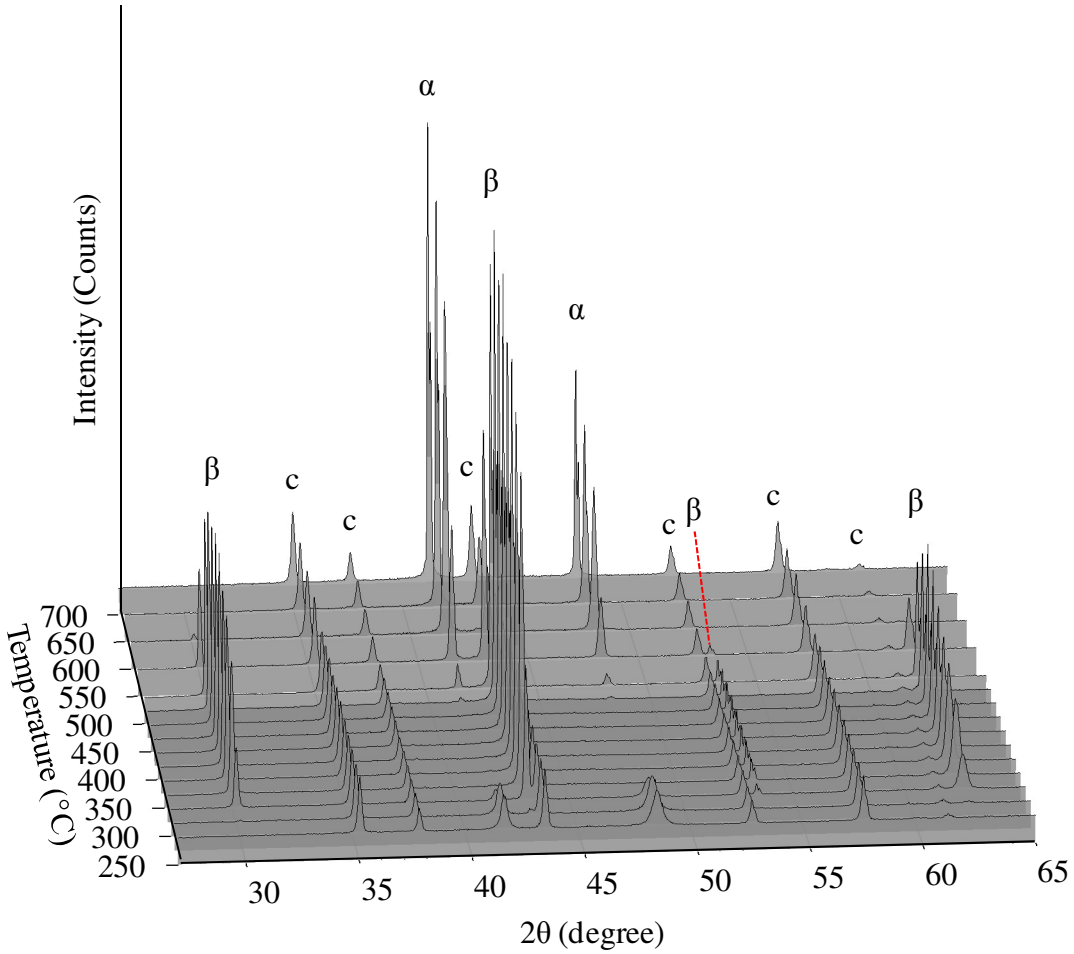

Figure 4.10 VTXRD patterns of Foil 1 showing the heating stage of a cycle under 445 kPa of flowing helium, where 'c', 'α' and 'β' denote the diffraction peaks attributed to the corundum sample holder, FCC and BCC phase, respectively.

Figure 4.11 depicts the VTXRD results during the cooling stage immediately following the heating stage of the cycle (Figure 4.10) where scans were recorded at 50 °C increments. According to Figure 4.11, Foil 1 contains only the FCC phase from 700 to 450 °C. At 450 °C, the BCC phase forms to produce a mixed phase in Foil 1. By 300 °C, the BCC phase is fully ordered and the FCC phase diminishes significantly, however, it does not disappear completely.

Small quantities of the FCC phase remain stable in Foil 1 when cooled to room temperature possibly due to the fast cooling rate of the VTXRD pressure cell which is estimated to be approximately 5 °C min^{-1}. In comparison, the MPR system is capable of much slower cooling rates of around 0.5 °C min^{-1}. A slow cooling rate is essential in facilitating the full phase transformation from the disordered high temperature FCC phase to the ordered equilibrium BCC phase. It proved challenging to achieve a sufficiently low enough cooling rate with the water cooled pressure cell thus causing difficulty in forming a pure BCC phase in Foil 1.

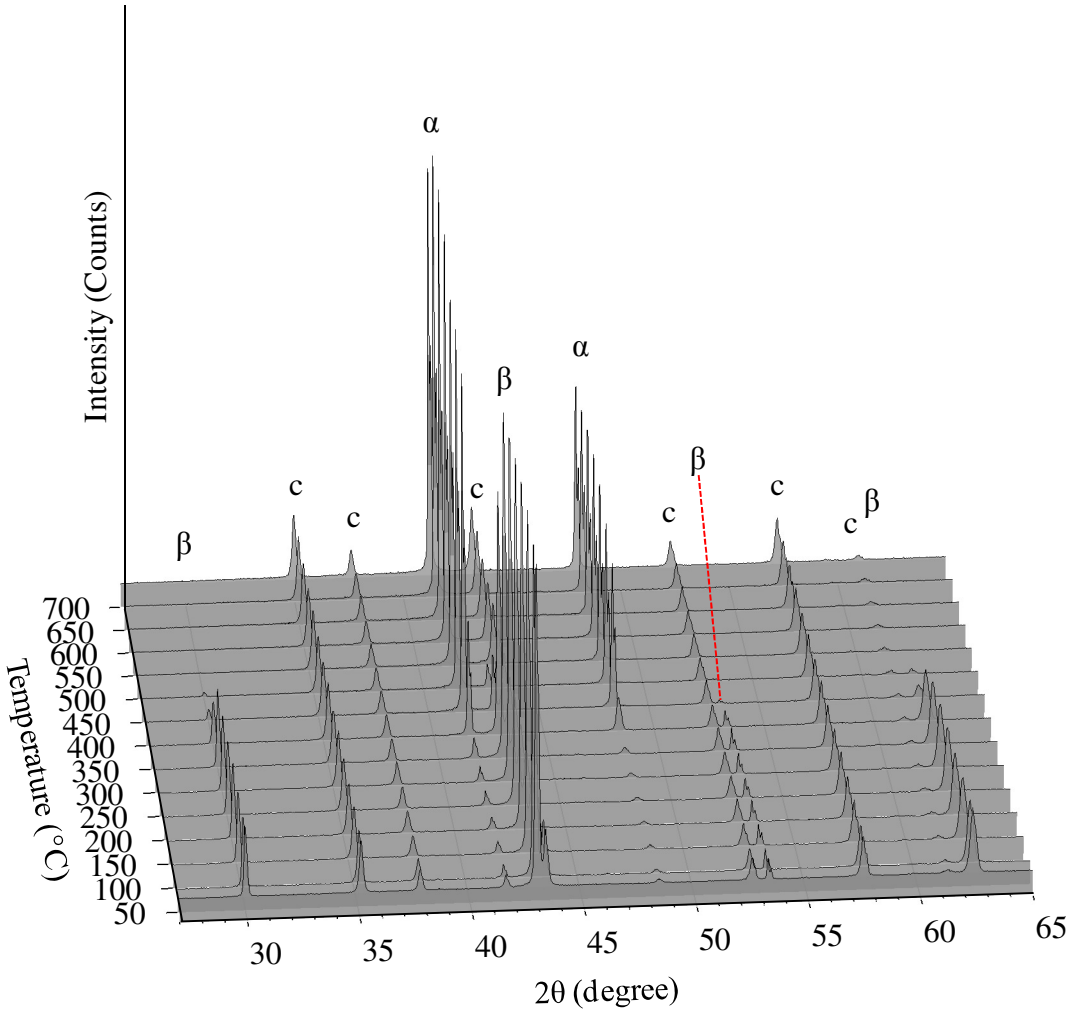

Figure 4.11 VTXRD patterns of Foil 1 showing the cooling stage of a cycle under 445 kPa of flowing helium, where 'c', 'α' and 'β' denote the diffraction peaks attributed to the corundum sample holder, FCC and BCC phase, respectively.

The VTXRD results displayed by Figure 4.10 and Figure 4.11 are summarised in Table 4.4. It is evident that upon heating of Foil 1 under 445 kPa of helium, that the BCC phase is stable between 300 and 600 °C. The Pd-Cu phase diagram illustrated in Figure 2.16 shows that the FCC + BCC | FCC phase boundary occurs at 550 °C for a composition of $Pd_{60}Cu_{40}$ wt%. Subramanian [154], Huang [72] and Li [153] have used data from Jones [162] to construct the Pd-Cu phase diagram which also indicates that for the composition of $Pd_{60}Cu_{40}$ wt%, the FCC + BCC | FCC phase boundary resides at 550 °C. According to these authors, the BCC

phase will not exist above 550 °C; however, according to Figure 4.10 the BCC phase is stable up until 600 °C under the experimental conditions used.

Interestingly, the BCC phase forms at 450 °C during the cooling stage indicating that the FCC + BCC | FCC phase boundary has shifted to a lower temperature. Perhaps this observation is attributed to the non-equilibrium cooling rate encountered by Foil 1 which would not facilitate the formation of the BCC phase at a similar temperature observed during the heating stage. A slower cooling rate may increase the temperature at which the BCC phase nucleates during the cooling stage.

Table 4.4 Summary of results from the VTXRD experiment performed on Foil 1 cycled under 445 kPa of flowing helium from 30 to 700 °C and back to 30 °C. Temperatures are shown at which the FCC and BCC phase are stable during the heating and cooling stage of the cycle.

	Heating (2.4 °C min^{-1})	**Cooling (5 °C min^{-1})**
FCC	30 – 325 °C, 475 – 700 °C	700 – 30 °C
BCC	300 – 600 °C	450 – 30 °C

VTXRD experiments were conducted on a separate as-received Batch 1 Pd-Cu foil offcut (Foil 2) under 445 kPa of hydrogen pressure with the same cycle programme used on Foil 1. The results are summarised in Table 4.5. Figure 4.12 demonstrates that the BCC phase forms at 275 °C and appears to be completely ordered by 400 °C as evidenced by the BCC Pd-Cu(100) diffraction peak. The VTXRD analysis attempts to simulate test conditions in the MPR, however it should be noted that a hydrogen pressure gradient is not present across Foil 2 during the experiment.

Hydrogen also appears to have a marked effect on the Pd-Cu phase diagram. Figure 4.12 reveals that for the composition of Foil 2 ($Pd_{61.3}Cu_{38.7}$ wt% as determined in Section 4.3.1), the FCC phase begins forming at 500 °C to give a mixture of the BCC and FCC phase. By 650 °C, the BCC phase disappears. According to Figure 2.16, at 450 °C the composition of

Foil 2 resides within the mixed phase region close to the BCC | FCC + BCC phase boundary. In addition, Figure 4.12 shows that 445 kPa of hydrogen pressure shifts the BCC | FCC + BCC and FCC + BCC | FCC phase boundaries to higher temperatures and Pd concentrations. A similar effect was reported by Piper [39] showing that larger shifts in the phase boundaries towards higher Pd concentrations are observed at higher hydrogen pressures. Moreover, the BCC phase can be stabilised to higher than normal Pd alloy concentrations with high hydrogen pressures. It is noticeable that the BCC phase is stable over a wider temperature range (275 – 650 °C) in Foil 2 compared with Foil 1 (300 – 600 °C). Furthermore, upon heating the FCC phase disappears at the same temperature (325 °C) and reforms at a higher temperature (500 °C) in Foil 2 compared to Foil 1. This is evidence that 445 kPa of hydrogen pressure is able to accelerate the FCC to BCC phase transformation and stabilise the BCC phase to higher temperatures.

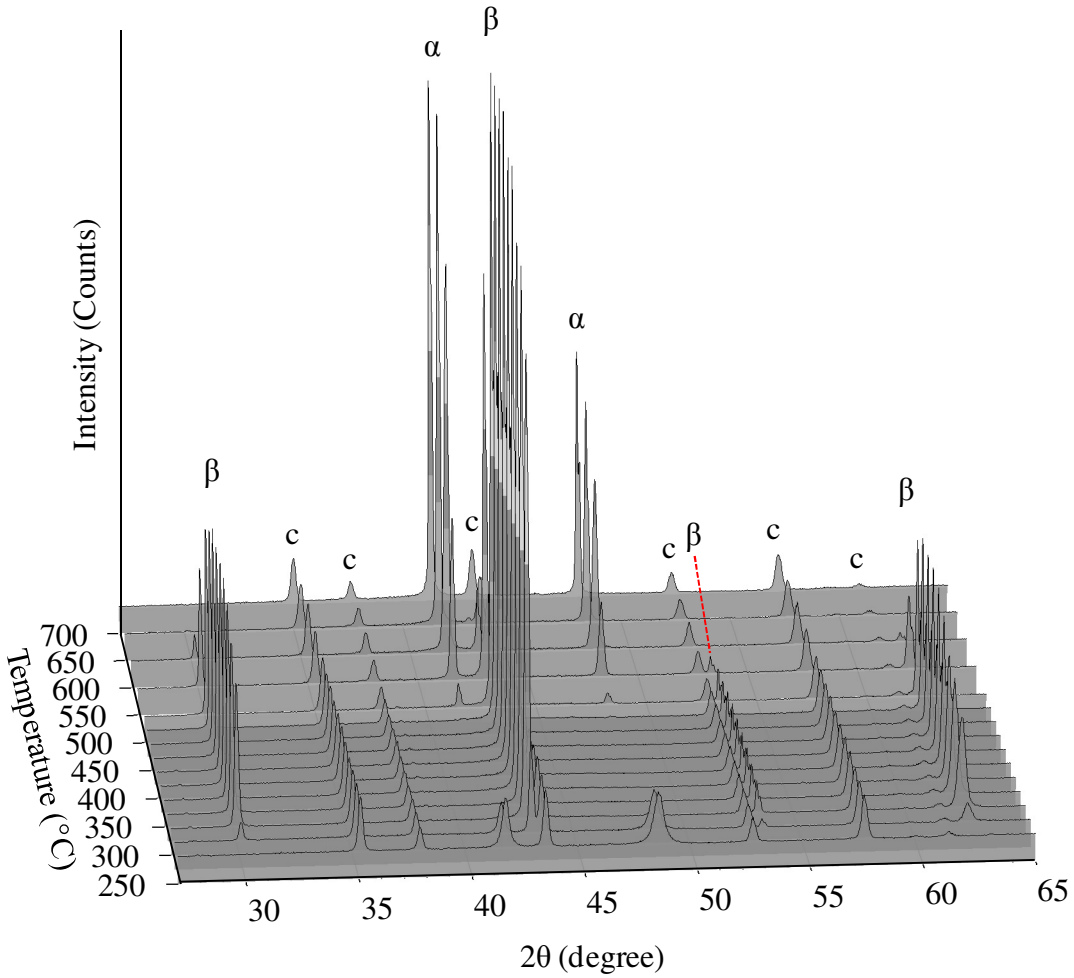

Figure 4.12 VTXRD patterns of Foil 2 showing the heating stage of a cycle under 445 kPa of flowing hydrogen, where 'c', 'α' and 'β' denote the diffraction peaks attributed to the corundum sample holder, FCC and BCC phase, respectively.

The cooling stage of the cycle is shown in Figure 4.13. The FCC phase is present in Foil 2 from 700 to 30 °C, yet like Foil 1, there is a dramatic decline in the FCC phase content at 300 °C. Foil 2 forms the BCC phase at 500 °C during the cooling stage whereas Foil 1 forms this phase at 450 °C. This is further proof that 445 kPa of hydrogen pressure accelerates the FCC to BCC phase transformation. Also, Foil 2 appears to attain a fully ordered BCC phase at 275 °C which is lower than the ordering temperature of Foil 1 (300 °C) during the heating stage suggesting that the presence of hydrogen can increase the rate of ordering.

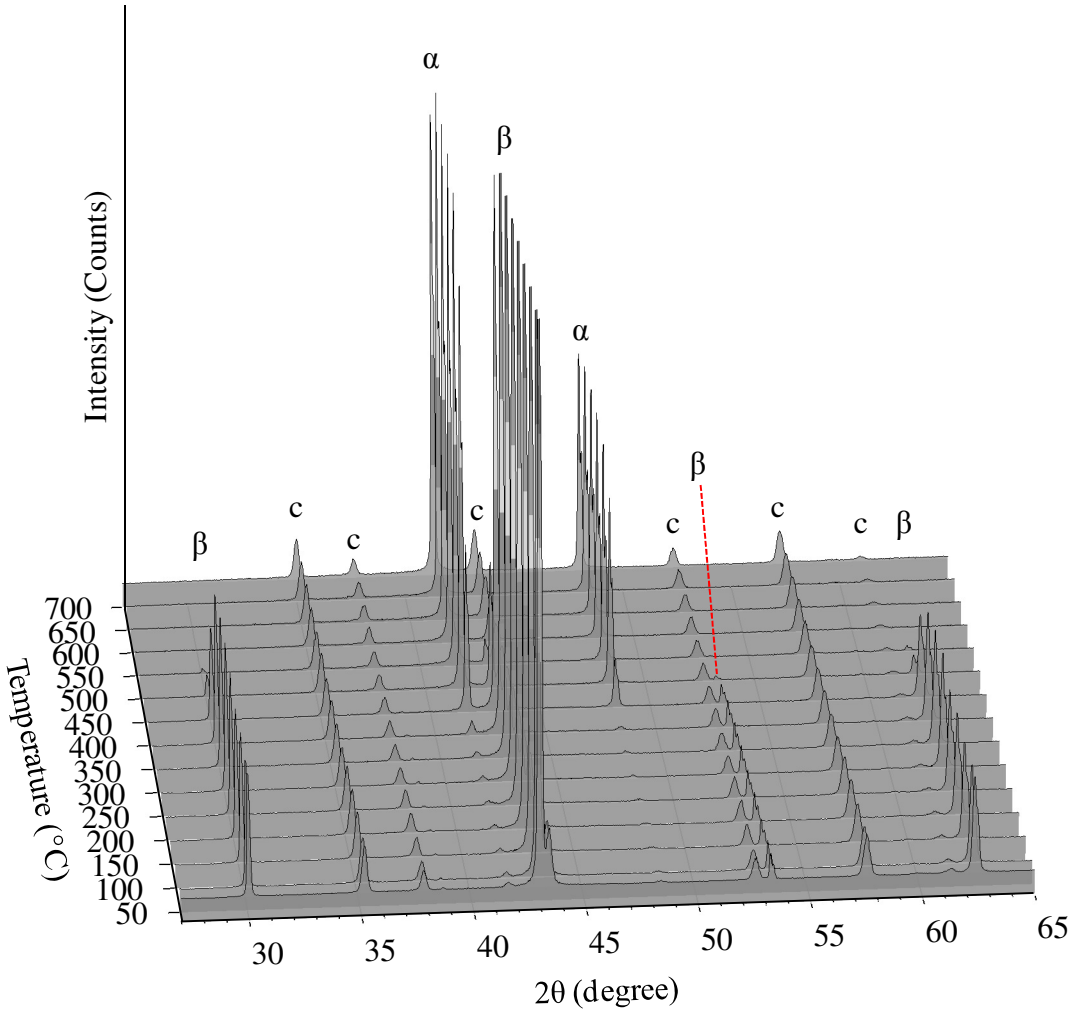

Figure 4.13 VTXRD patterns of Foil 2 showing the cooling stage of a cycle under 445 kPa of flowing hydrogen, where 'c', 'α' and 'β' denote the diffraction peaks attributed to the corundum sample holder, FCC and BCC phase, respectively.

Table 4.5 Summary of results from the VTXRD experiment performed on Foil 2 cycled under 445 kPa of flowing hydrogen from 30 to 700 °C and back to 30 °C. Temperatures are shown at which the FCC and BCC phase are stable during the heating and cooling stage of the cycle.

	Heating (2.4 °C min^{-1})	Cooling (5 °C min^{-1})
FCC	30 – 325 °C, 500 – 700 °C	700 – 30 °C
BCC	275 – 650 °C	500 – 30 °C

4.3.2. MPR results

The hydrogen permeability of the as-received Pd-Cu foil membranes were measured for Batches 1 and 2. The quantity of foil was limited for both batches; therefore measurements were repeated where possible. It should also be noted that hydrogen permeability measurements presented here were obtained on the overhauled MPR.

4.3.2.1. Batch 1

Initially, the hydrogen permeability of the Batch 1 Pd-Cu membrane was measured between 50 and 450 °C in the MPR. Figure 4.14 shows that the first cycle began hydrogen permeation at 410 °C. The first cycle anneals the membrane and brings about a phase transformation from the disordered FCC phase to the ordered BCC phase. Under the test conditions used, only the ordered crystalline BCC phase is stable at 410 °C which is corroborated by the VTXRD results shown in Figure 4.12. Ordering of this phase should occur relatively quickly, especially in the presence of hydrogen [178, 179, 259, 261] since only local rearrangement of the Pd and Cu atoms is required. Additionally, it can be seen that hydrogen permeation begins at 370 °C for the second cycle and 350 °C for the third cycle.

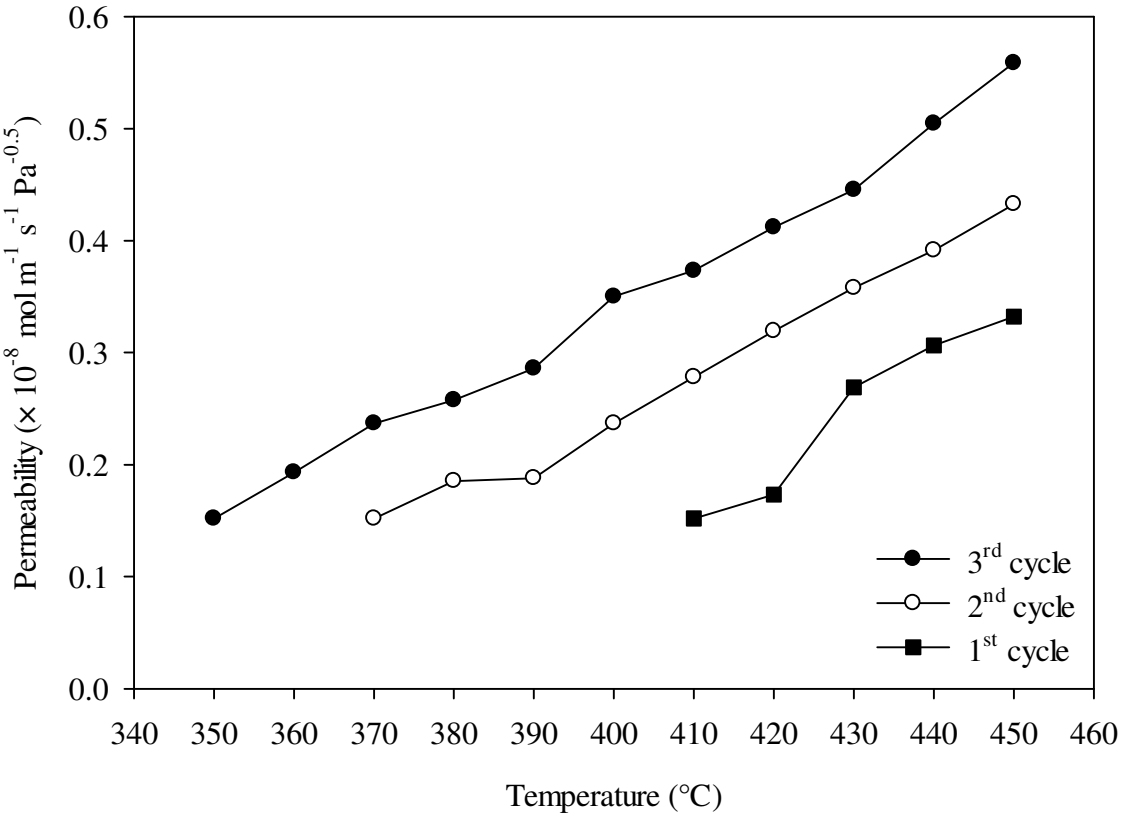

Figure 4.14 Hydrogen permeability as a function of temperature for the 31.0 µm thick as-received Batch 1 Pd-Cu foil membrane showing the first three cycles heated between 50 and 450 °C. A hydrogen feed pressure of 445 kPa and permeate pressure of 100 kPa was applied during measurements assuming an *n*-value of 0.5.

The Pd-Cu BCC phase is a fast diffuser of hydrogen compared to the Pd-Cu FCC phase [154, 165, 262] and therefore more permeable to hydrogen. McKinley [35] reports that hydrogen permeation is enhanced in the presence of the ordered BCC phase, which would explain hydrogen permeation commencing at 410 °C.

It has been shown by Piper [39] and Huang [72] that increasing hydrogen pressure can shift the BCC | FCC + BCC phase boundary to high Pd compositions as shown in Figure 2.17 and Figure 2.18. It should be noted that the feed side is exposed to 445 kPa of hydrogen pressure whereas 100 kPa of hydrogen pressure is applied to the permeate side. This means that for the given composition of the Batch 1 Pd-Cu membrane, more of the FCC phase is converted to

the BCC phase on the feed side as compared to the permeate side throughout the duration of the MPR test.

Evidence for this is shown in Figure 4.33(b) where the small presence of the FCC phase is indentified on the permeate side by the Pd-Cu(111) diffraction peak in a Batch 1 Pd-Cu membrane that was cycled only three times between 50 and 450 °C in the MPR before removal. In keeping with the reporting structure used throughout this thesis, Figure 4.33 can be found in Section 4.3.3 which presents the post-MPR characterisation results for the Batch 1 Pd-Cu membrane.

The permeate side of the membrane will undergo further phase transformation from the less permeable FCC phase to the more permeable BCC phase during each cycle until the FCC phase is diminished. This effect would explain hydrogen permeation commencing at lower temperatures with each successive cycle. For comparison, Figure 4.35 shows a diffraction pattern indicating only a single BCC phase for a Batch 1 Pd-Cu membrane that has completed more cycles than the membrane scanned in Figure 4.33 performing a total of eight cycles, two of which were heated to a maximum temperature of 700 °C.

It has been theorised that rapid phase transformation is due to accelerated atomic diffusion caused by the formation of vacancy-hydrogen clusters [178, 179, 263, 264] which is the trapping of hydrogen atoms in metal vacancies. As a result, the membrane surface exposed to the relatively higher hydrogen pressure on the feed side undergoes a more rapid phase transformation from the FCC to the BCC phase.

Following MPR testing, *n*-value measurements were performed on the Batch 1 Pd-Cu membrane with the results shown in Figure 4.15 and Figure 4.16. An *n*-value of 0.58 gives the best fit for the data shown in Figure 4.16, which is very similar to the

n-value of 0.57 obtained for the Pd membrane indicating that hydrogen diffusion is again the rate limiting step for the Batch 1 Pd-Cu membrane under the test conditions used.

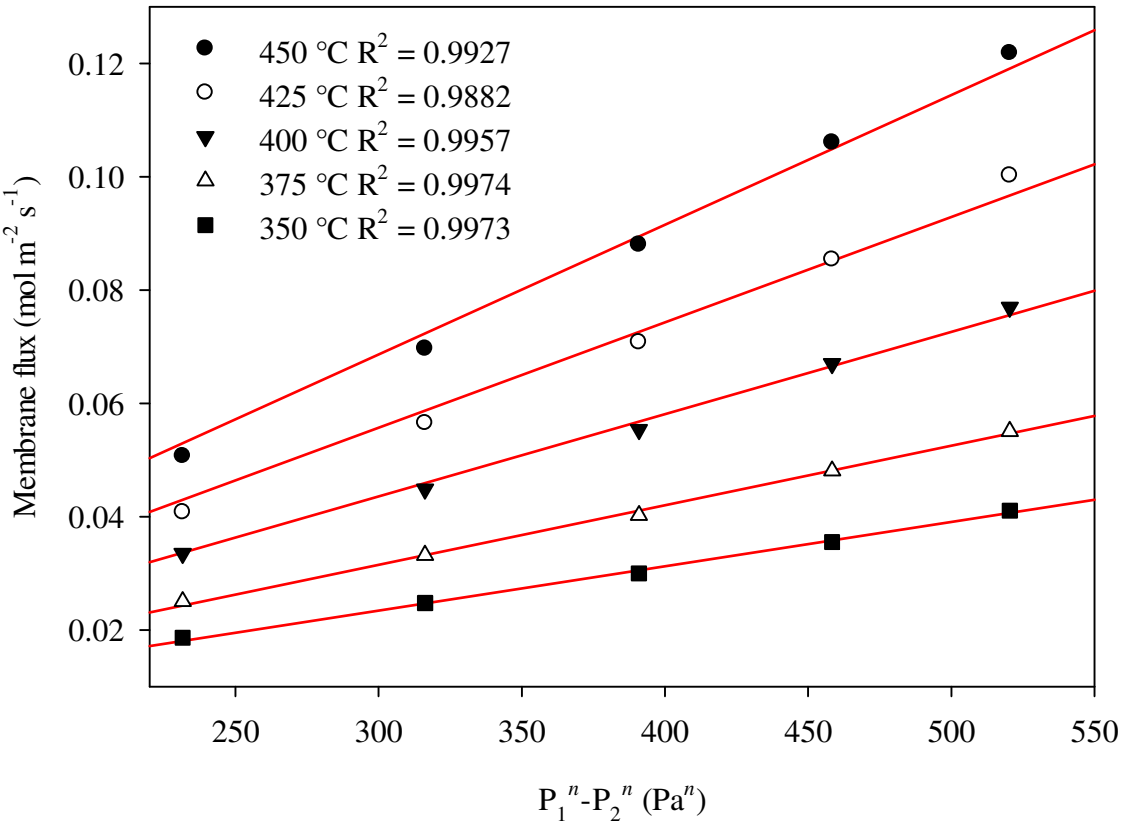

Figure 4.15 Membrane flux as a function of hydrogen differential pressure with *n* constrained to 0.5.

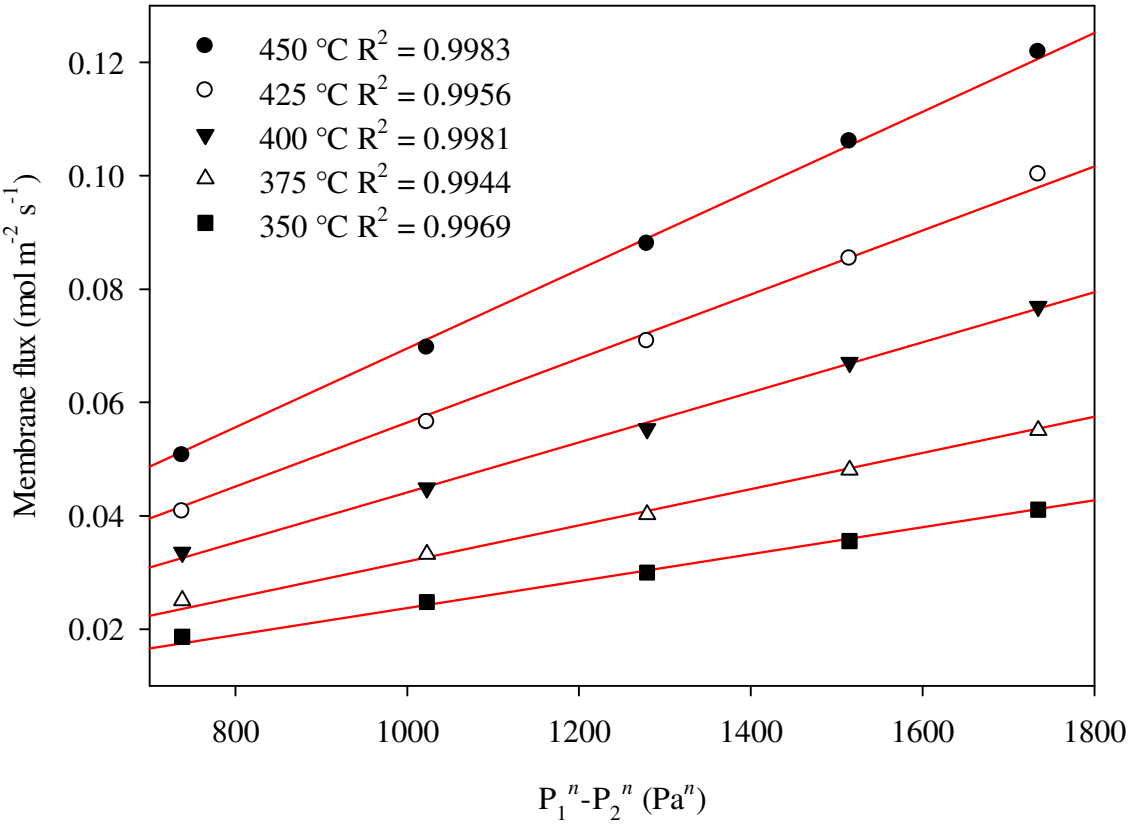

Figure 4.16 Membrane flux as a function of hydrogen differential pressure with *n* constrained to the best fit value of 0.58.

For comparison, Figure 4.17 shows a plot of the third cycle from Figure 4.14 for the Batch 1 Pd-Cu membrane where the solid symbol curve is calculated using an *n*-value of 0.5 and the open symbol curve is calculated using an *n*-value of 0.58.

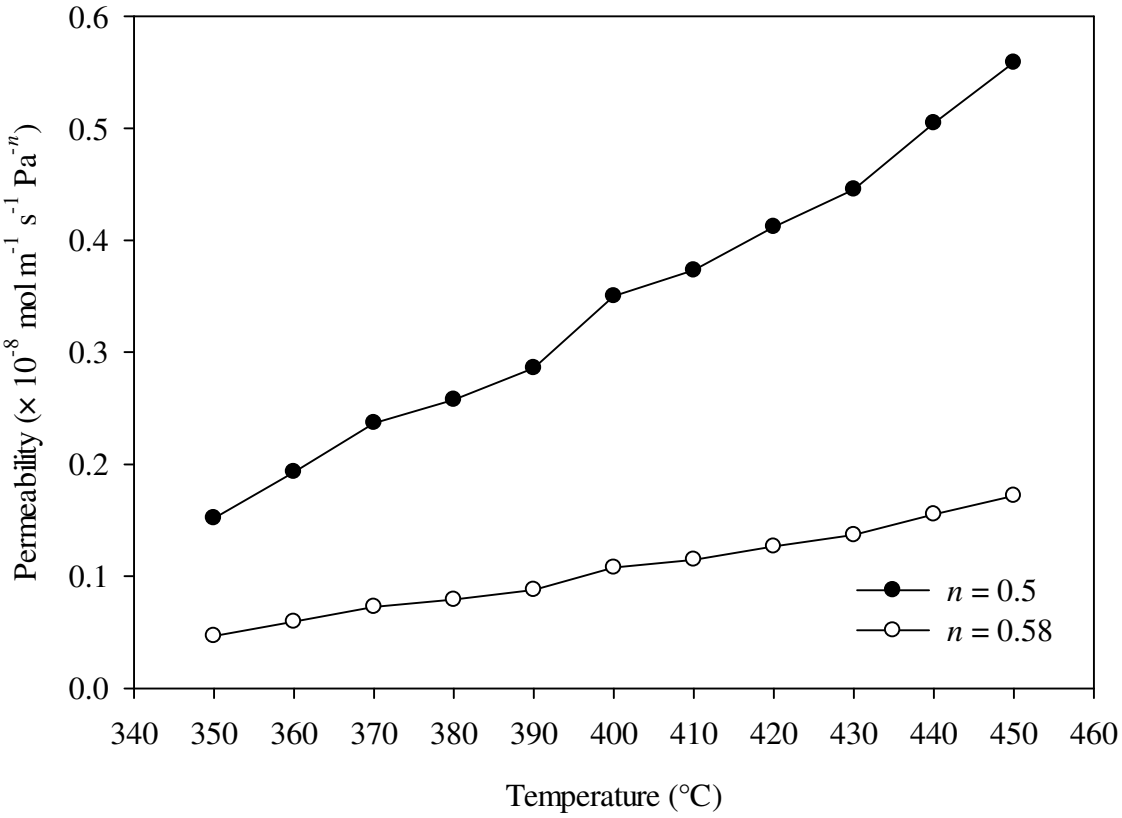

Figure 4.17 Hydrogen permeability as a function of temperature for the 31.0 µm thick Batch 1 Pd-Cu foil membrane showing the third cycle. A hydrogen feed pressure of 445 kPa and permeate pressure of 100 kPa was applied during measurements. The solid symbol curve was calculated using an *n*-value of 0.5 whereas the open symbol curve uses the best fit *n*-value of 0.58.

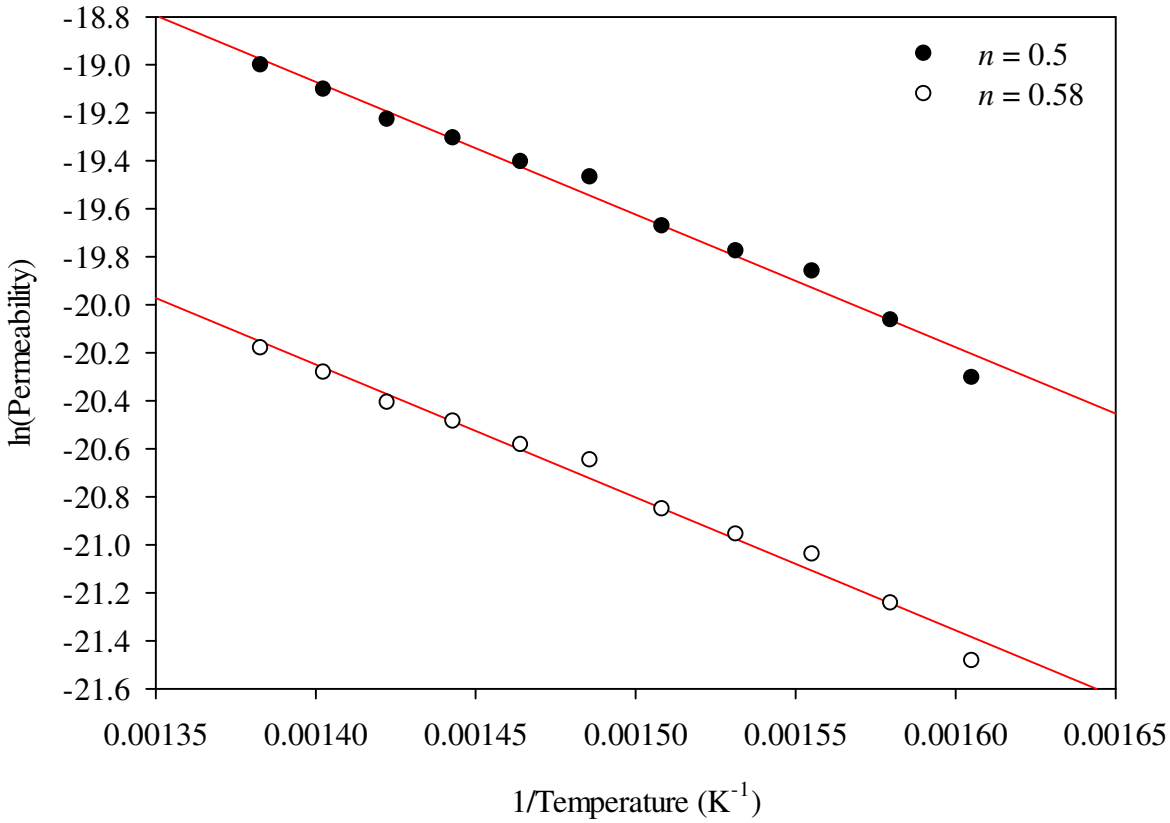

Figure 4.18 Arrhenius plot of the hydrogen permeability data shown in Figure 4.17 between 350 and 450 °C. The solid symbol curve was calculated using an *n*-value of 0.5 whereas the open symbol curve uses the best fit *n*-value of 0.58.

The general permeability formulae (350 – 450 °C) for the Batch 1 Pd-Cu membrane derived from Figure 4.18 using an *n*-value of 0.5 and the best fit value of 0.58 which are shown in Equation 4.6 and Equation 4.7, respectively.

$$\Phi_{n=0.5} = 2.88 \times 10^{-5} exp\left(\frac{-51.09 \times 10^3}{RT}\right) \qquad \text{Equation 4.6}$$

$$\Phi_{n=0.58} = 8.87 \times 10^{-6} exp\left(\frac{-51.09 \times 10^3}{RT}\right) \qquad \text{Equation 4.7}$$

The hydrogen permeability of the Batch 1 Pd-Cu membrane at 350 °C was measured as 1.52×10^{-9} mol m^{-1} s^{-1} Pa$^{-0.5}$ during the third cycle. This is more than a factor of five times

lower than the value measured for the Pd membrane at the same temperature. Also, compared to literature data this value is notably low as shown in Table 4.6. However, it is important to note that the authors in Table 4.6 report hydrogen permeability values at 350 °C which do not agree well with each other since they range between $0.35 – 1.76 \times 10^{-8}$ mol m^{-1} s^{-1} $Pa^{-0.5}$.

Table 4.6 Hydrogen permeability of free-standing $Pd_{60}Cu_{40}$ wt% foil membranes at 350 °C compiled from Table 2.4.

Permeability ($\times 10^{-8}$ mol m^{-1} s^{-1} Pa^{-n})	*n*	Reference
1.42	0.5	Decaux [95]
0.50	0.5	Howard [37]
0.60	0.5	Kamakoti [87]
1.07 1.76[a]	0.5	Krueger [96]
1.49	0.5	McKinley [35]
0.35	0.5	Yuan [97]

[a] denotes measurement taken after heat treatment of alloy membrane.

A likely cause for such low hydrogen permeability observed in the as-received Pd-Cu foil membranes is explained by Krueger [96] who cites that homogenising an as-received $Pd_{60}Cu_{40}$ wt% foil membrane at 1,100 °C in a mildly reducing atmosphere for 40 minutes can improve hydrogen permeability by up to 65%. Such an improvement has been linked to a phenomenon known as coring. This occurs when an alloy melt is cooled to the solid phase under non-equilibrium conditions causing the exterior of the alloy to solidify at a more rapid rate than the interior. The grains that form in the inner region are richer in the higher melting point component; in this case Pd, whereas the outer region grains will be Pd-depleted and so this effect will lead to compositional inhomogeneity within the alloy [96]. Such inhomogeneity can be of detriment to the performance of a Pd-Cu membrane since hydrogen permeability is sensitive to phase composition.

In addition to the effects of coring, Piper [39] demonstrated in Figure 2.17 that annealing at 350 °C in 507 kPa of hydrogen pressure can improve the room temperature diffusivity of a $Pd_{47.3}Cu_{52.7}$ at% ($Pd_{60}Cu_{40}$ wt%) membrane by more than a factor of two over annealing under a vacuum at the same temperature. In general, annealing in a hydrogen atmosphere is beneficial for the membrane to reverse the effects of coring and promote the formation of the equilibrium BCC phase.

It was observed that the *n*-value for the Batch 1 Pd-Cu membrane exhibited a much higher deviation from Sieverts' law with temperature than the Pd membrane. Variation in *n*-value as a function of temperature is shown in Figure 4.19 for the Batch 1 Pd-Cu membrane. Initially, Sieverts' law is obeyed between 350 and 375 °C, however, increasing the temperature results in a maximum *n*-value of 0.69 at 425 °C with a slight reduction to 0.65 at 450 °C.

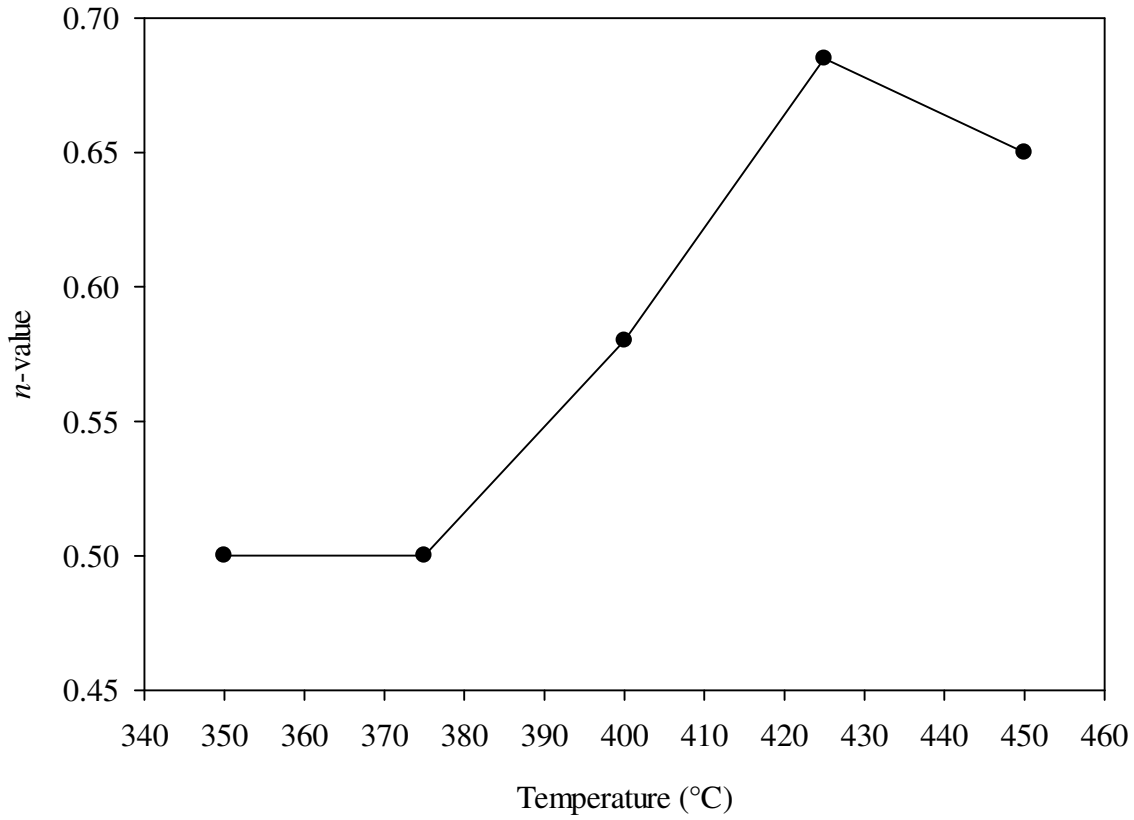

Figure 4.19 Variation of *n*-value as a function of temperature for the 31.0 µm thick Batch 1 Pd-Cu foil membrane.

Further permeability studies were carried out on the Batch 1 Pd-Cu membrane by cycling between 250 and 700 °C immediately after cycling between 50 and 450 °C in order to investigate the effects of the high temperature FCC crystal structure on hydrogen permeability. The results are displayed in Figure 4.20 showing the second cycle. For clarity, the cycle pattern proceeds from A – B – C – D – E – A.

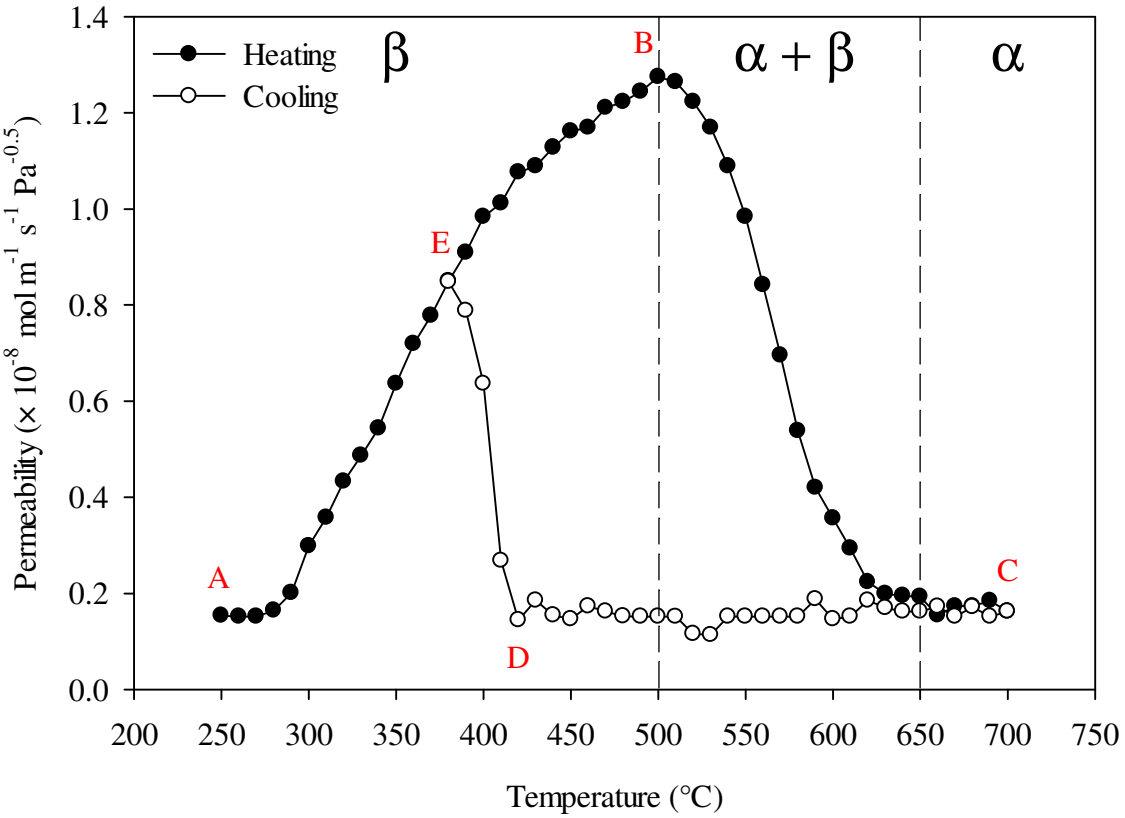

Figure 4.20 Hydrogen permeability as a function of temperature for the 31.0 µm thick Batch 1 Pd-Cu foil membrane during the second cycle between 250 and 700 °C. A hydrogen feed pressure of 445 kPa and permeate pressure of 100 kPa was applied during measurements. The dashed lines represent the phase boundaries of the FCC (α), BCC (β) and mixed phase regions, which were determined from the phase transition temperatures shown in Figure 4.12.

The cycle begins at 250 °C, denoted A, and proceeds to a maximum hydrogen permeability at B which coincides with 500 °C. It is interesting to note that the second cycle up to 700 °C allows the Batch 1 Pd-Cu membrane to begin hydrogen permeation at 250 °C as opposed to 350 °C which was the hydrogen permeation start temperature for the third cycle between 50

and 450 °C (Figure 4.14 and Figure 4.17). At 350 °C, the Batch 1 Pd-Cu membrane achieves a hydrogen permeability of 6.36×10^{-9} mol m^{-1} s^{-1} $Pa^{-0.5}$ which falls well within the literature value range shown in Table 4.6. Moreover, this value is more than a factor of four times greater than that shown in Figure 4.14 and Figure 4.17. The overall increase in hydrogen permeability and decrease in hydrogen permeation start temperature can be linked to the exposure of the membrane to higher temperatures for longer durations which can help remove the effects of coring created during alloy production.

From B to C, hydrogen permeability drops by nearly a factor of eight. According to Figure 4.12, 500 °C corresponds with the formation of the less permeable FCC phase and by 650 °C the membrane contains only the FCC phase. Such decline in hydrogen permeability can be attributed to the lower hydrogen diffusivity of this phase ($< 2 \times 10^{-6}$ cm^2 s^{-1} at room temperature) compared to that of the BCC (4.6×10^{-5} cm^2 s^{-1} at room temperature) [39]. A similar observation has been reported by Kamakoti et al [87] using density functional theory to model the movement of hydrogen between interstices.

Despite not providing data evidence, Piper [39] suggests that hydrogen diffusivity is relatively lower in the FCC phase due to the activation energy for hydrogen diffusion being a factor of three times higher than that of the BCC phase. This could be attributed to the smaller BCC unit cell possessing three times as many octahedral and tetrahedral interstitial sites than the FCC alternative [77] facilitating a much more rapid transport of hydrogen from one unit cell to the next. Hydrogen permeability in the FCC phase was significantly low so that the downstream MFC had difficulty detecting any hydrogen permeation at times since the device was calibrated to measure only as low as 6 ± 6 ml min^{-1} of hydrogen gas flow. With such large error for small gas flows, the activation energy could not be accurately determined.

Hydrogen permeation hysteresis is clearly visible from C, D to E. This effect has been linked to non-equivalent phase transformation occurring in the mixed FCC + BCC region and it has been theorised that a retardation in the FCC(H) ⇋ BCC(H) phase transition occurs due to the existence of a metastable hydrogenated FCC Pd-Cu(H) phase [97]. The VTXRD results shown in Figure 4.11 and Figure 4.13 clearly indicate that the FCC phase is stable down to lower than normal temperatures in the presence and absence of hydrogen during the cooling stage of the cycle. This means that rather than a metastable hydrogenated FCC Pd-Cu(H) phase being the prime cause of the observed hysteresis in Figure 4.20, it is proposed instead that the cooling rate which controls the rate of phase transformation from the FCC to the BCC phase has more of an influence.

At E, it appears as though the FCC phase has transformed to the more permeable BCC phase after which the curve continues its path back to A to conclude the cycle. The effects of hydrogen permeation hysteresis could be remedied by having a more controlled and slower cooling rate as opposed to the natural furnace cooling rate used throughout this work.

Subsequent to cycling up to 700 °C, *n*-value measurements were performed in order to assess any changes brought about by the exposure of the membrane to higher temperatures in a hydrogen atmosphere. Figure 4.21 shows a decline in *n*-value from 0.58 to 0.52. The effects of coring have drawn Pd atoms into the interior of the membrane leaving a Cu-rich surface. The presence of this Cu-rich surface will reduce the ability of the membrane to dissociate hydrogen thus increasing the *n*-value. Cycling of the membrane to 700 °C will facilitate compositional homogenisation through diffusion of Cu atoms into the Cu-depleted interior resulting in the *n*-value tending to 0.5.

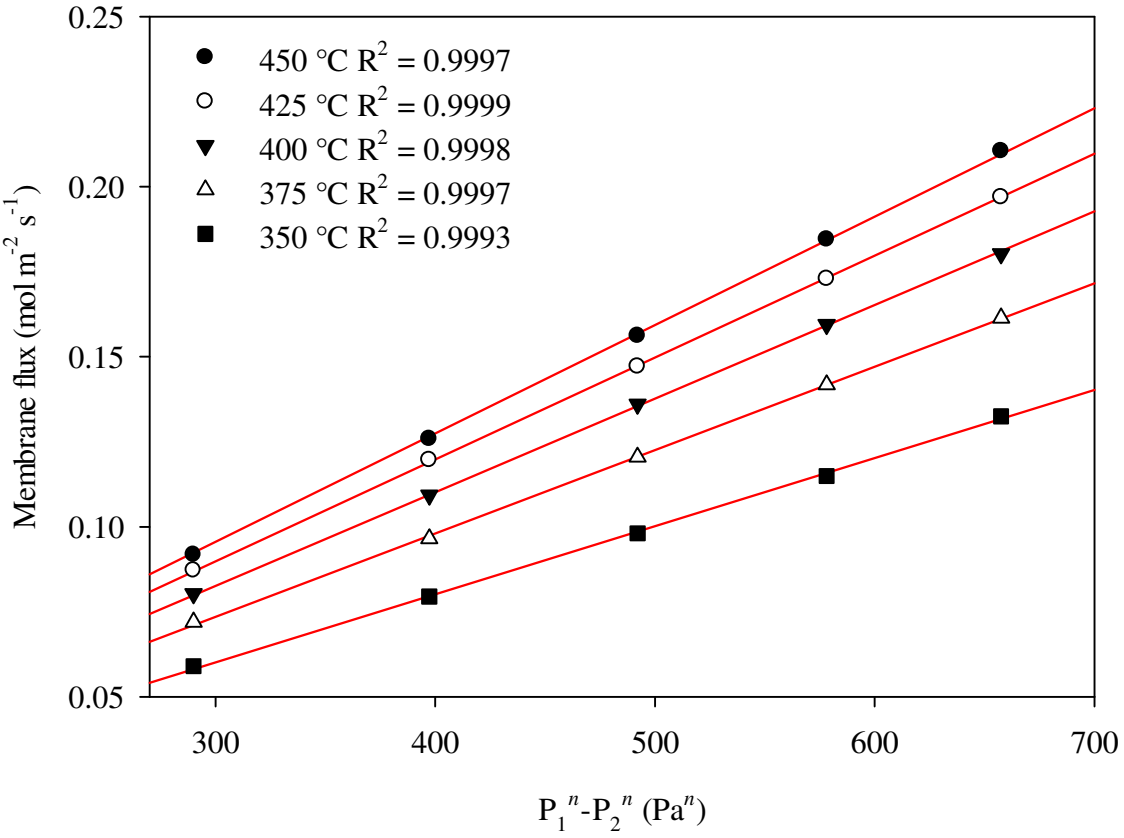

Figure 4.21 Membrane flux as a function of hydrogen differential pressure with *n* constrained to the best fit value of 0.52. This measurement was performed on the Batch 1 Pd-Cu foil membrane following cycling between 250 and 700 °C during MPR testing.

The Batch 1 Pd-Cu membrane was finally cycled between 250 and 450 °C after completing the two cycles between 250 and 700 °C revealing a marked improvement in hydrogen permeability. Figure 4.22 shows that during the third cycle between 250 and 450 °C, the Batch 1 Pd-Cu membrane achieved a hydrogen permeability of 6.98×10^{-9} mol m^{-1} s^{-1} $Pa^{-0.5}$ at 350 °C which is a 360% increase on the value obtained at the same temperature during the third cycle between 50 and 450 °C. In addition, Figure 4.22 shows the third cycle calculated using the new best fit *n*-value of 0.52.

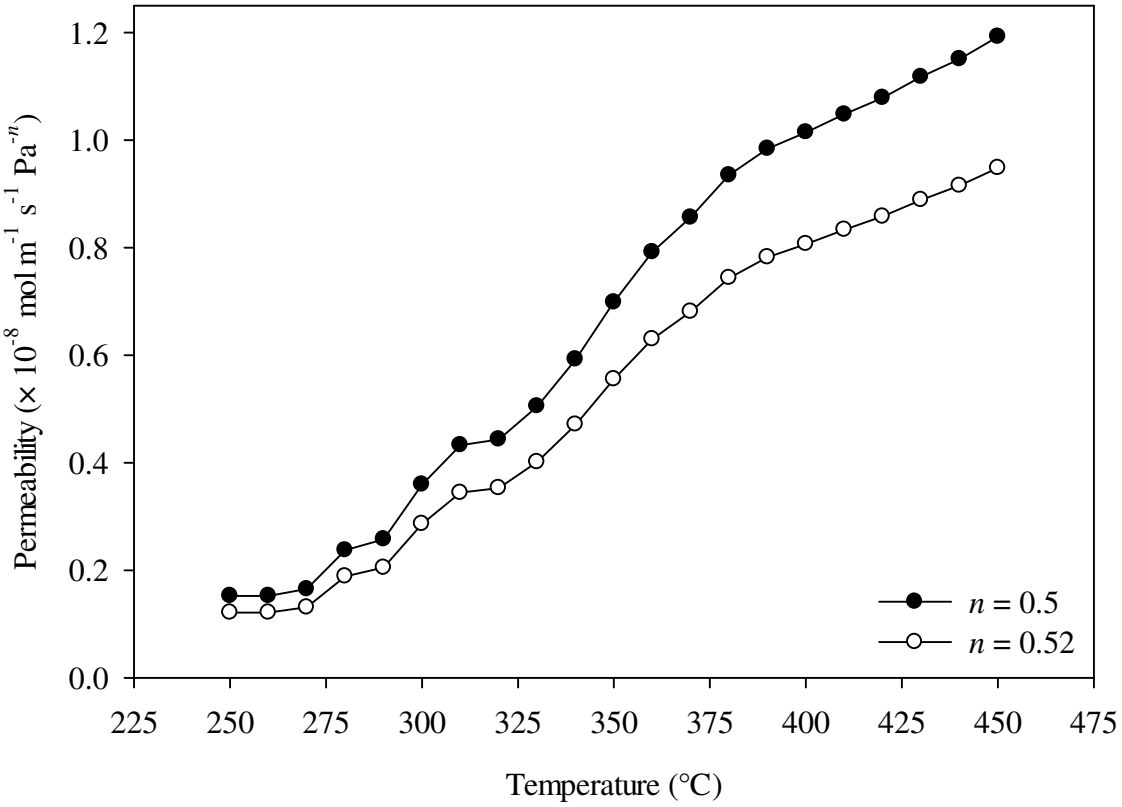

Figure 4.22 Hydrogen permeability as a function of temperature for the 31.0 µm thick Batch 1 Pd-Cu foil membrane showing the third cycle. This measurement was performed after cycling between 250 and 700 °C during MPR testing. A hydrogen feed pressure of 445 kPa and permeate pressure of 100 kPa was applied during measurements. The solid symbol curve was calculated using an *n*-value of 0.5 whereas the open symbol curve uses the best fit *n*-value of 0.52.

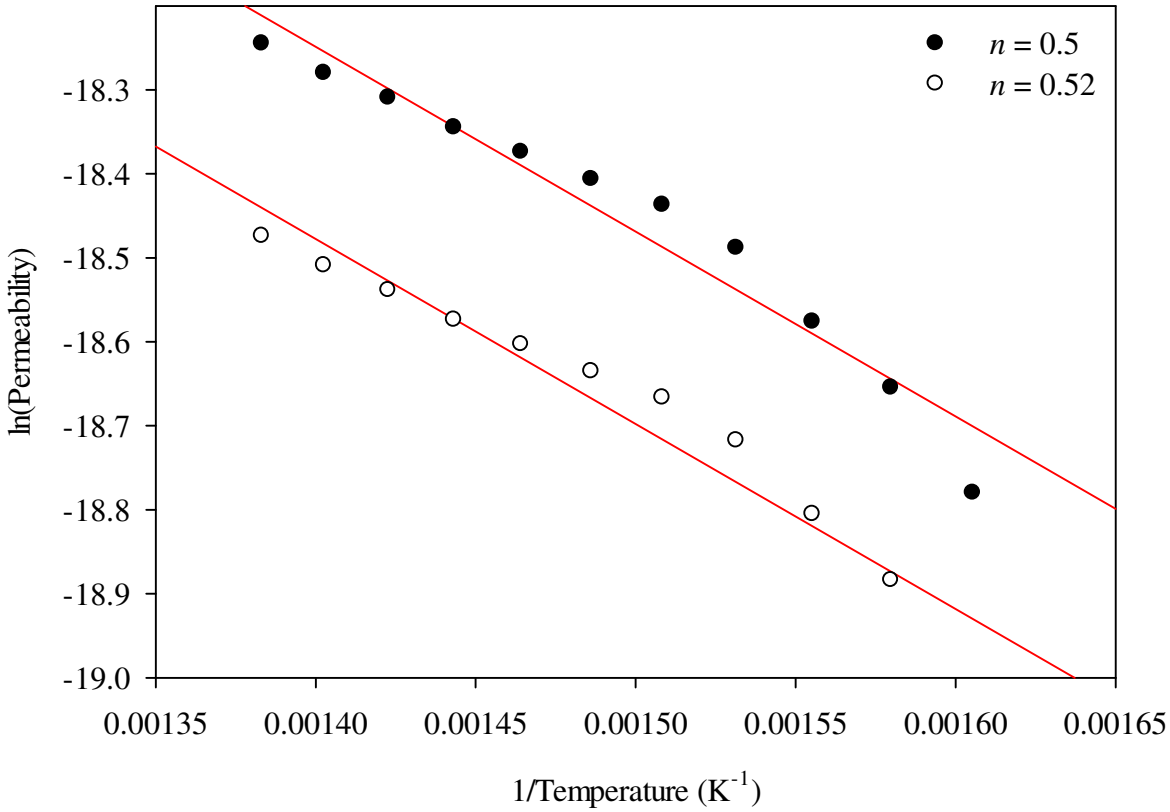

Figure 4.23 Arrhenius plot of the hydrogen permeability data shown in Figure 4.22 between 350 and 450 °C. The solid symbol curve was calculated using an *n*-value of 0.5 whereas the open symbol curve uses the best fit *n*-value of 0.52.

From Figure 4.23, the following general permeability formulae (350 – 450 °C) were derived based on an *n*-value of 0.5 and best fit value of 0.52 as demonstrated in Equation 4.8 and Equation 4.9, respectively.

$$\Phi_{n=0.5} = 3.41 \times 10^{-7} exp\left(\frac{-19.86 \times 10^3}{RT}\right) \qquad \text{Equation 4.8}$$

$$\Phi_{n=0.52} = 2.71 \times 10^{-7} exp\left(\frac{-19.86 \times 10^3}{RT}\right) \qquad \text{Equation 4.9}$$

It is clear that cycling the Batch 1 Pd-Cu membrane up to 700 °C in a hydrogen atmosphere has the effect of reducing the E_Φ from 51.09 kJ mol^{-1}, as shown in Equation 4.6 and Equation

4.7, by 61% to 19.86 kJ mol^{-1}. Furthermore, the test conditions used have also reduced the Φ_0 by one order of magnitude. Figure 4.24 reveals that the *n*-value fluctuates about 0.51 and experiences a slight increase to 0.54 at 450 °C.

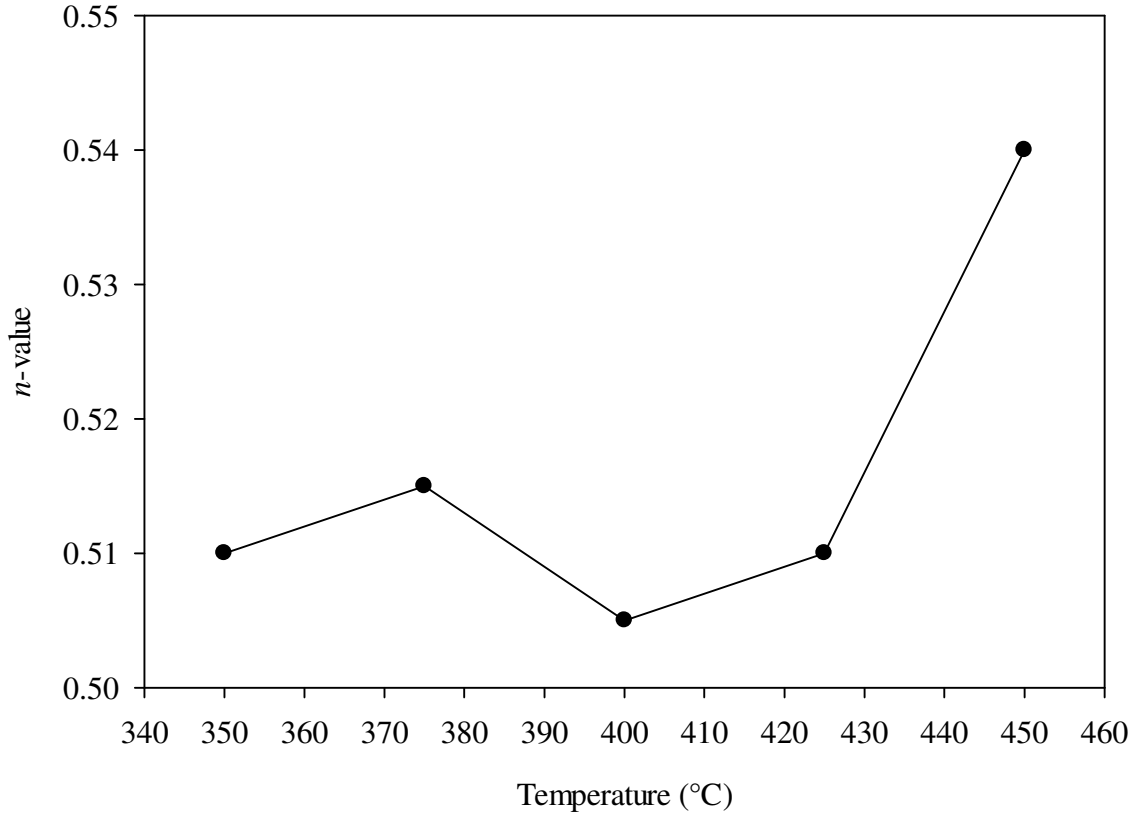

Figure 4.24 Variation of *n*-value as a function of temperature for the 31.0 µm thick Batch 1 Pd-Cu foil membrane following cycling between 250 and 700 °C during MPR testing.

4.3.2.2. Batch 2

Due to a surplus in the Batch 2 Pd-Cu foil, it was possible to only repeat hydrogen permeability experiments on this batch in the as-received state. Therefore, two Batch 2 Pd-Cu membranes were tested in the MPR in order to measure and compare hydrogen permeability data with that obtained for Batch 1. The results are shown in Figure 4.25 with the associated standard error bars.

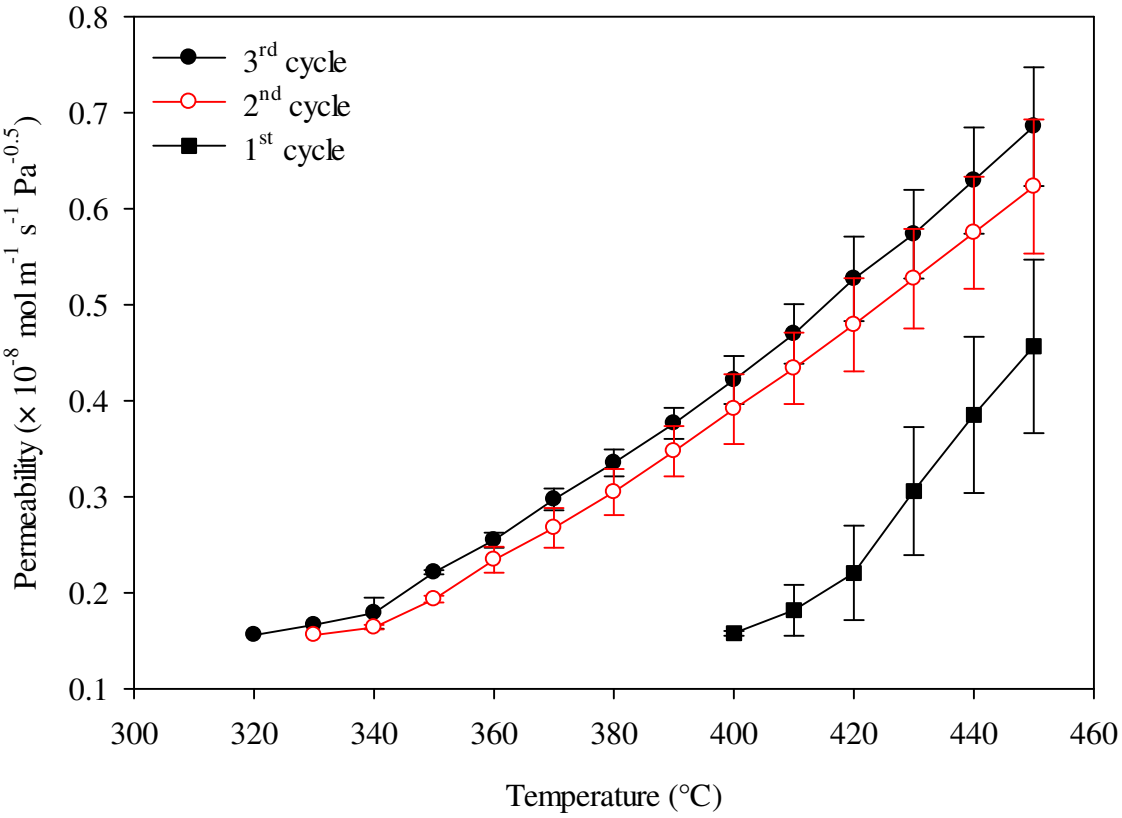

Figure 4.25 Hydrogen permeability as a function of temperature for the 31.3 µm thick as-received Batch 2 Pd-Cu foil membranes showing the first three cycles heated between 50 and 450 °C. A feed pressure of 445 kPa and permeate pressure of 100 kPa was applied during measurements assuming an *n*-value of 0.5.

Similar to what was shown in Figure 4.14 for the Batch 1 Pd-Cu membrane; the Batch 2 Pd-Cu membranes commenced hydrogen permeation at 400 °C. However, the second and third cycle begin at lower temperatures compared to the Batch 1 Pd-Cu membrane suggesting that the Batch 2 Pd Cu membranes likely have a different thermal history and potentially achieved better compositional homogeneity whilst testing in the MPR. During the third cycle, the Batch 2 Pd-Cu membranes achieved an average hydrogen permeability of $(2.21 \pm 0.3) \times 10^{-9}$ mol m^{-1} s^{-1} $Pa^{-0.5}$ at 350 °C which still falls out of the literature value range shown in Table 4.6.

It was decided not to perform *n*-value measurements following the preliminary cycles between 50 and 450 °C since subsequent cycles to higher temperatures can have an influence

on the values obtained as a result of annealing and compositional homogenisation. Therefore, the *n*-value has been determined following cycles between 250 and 700 °C.

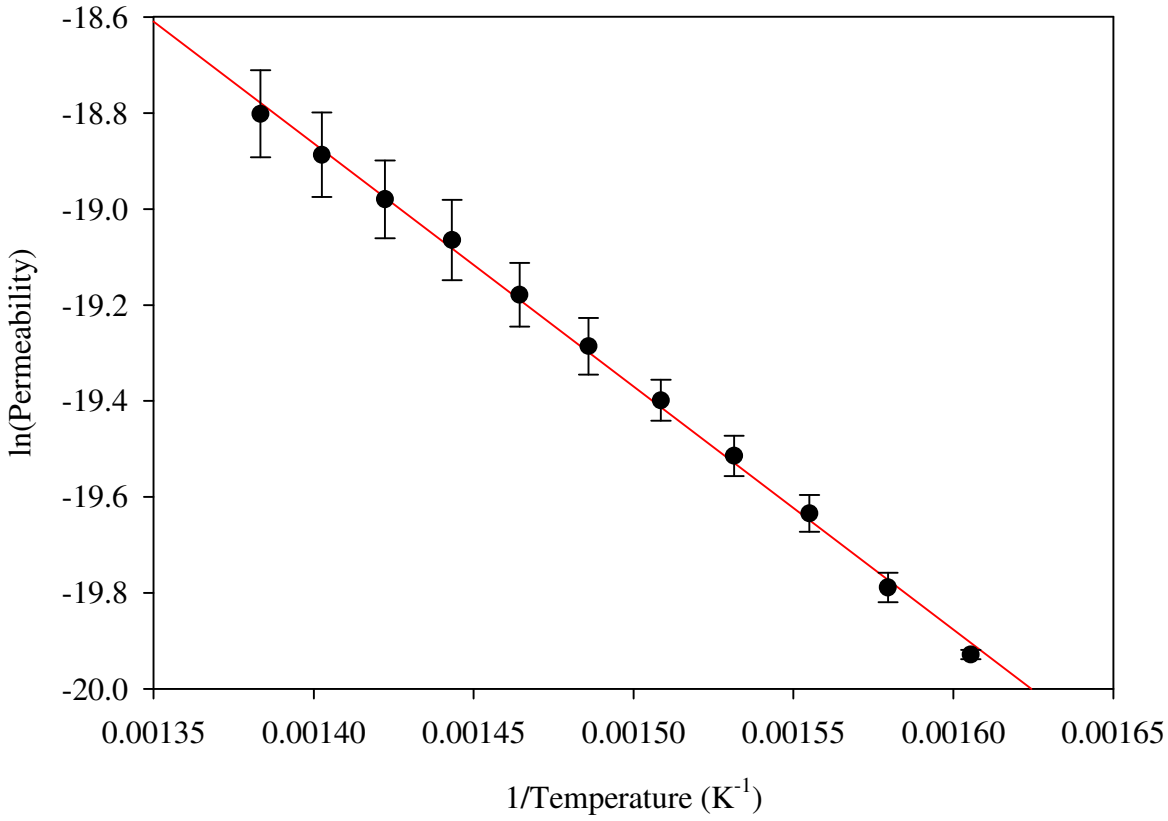

Figure 4.26 Arrhenius plot of the hydrogen permeability data shown in Figure 4.25 between 350 and 450 °C for the third cycle using an *n*-value of 0.5.

From the data displayed in Figure 4.26, the following general permeability formula (350 – 450 °C) for the Batch 2 Pd-Cu membranes was calculated and is shown in Equation 4.10 assuming an *n*-value of 0.5. Despite a similar E_Φ value (41.67 ± 3.4 kJ mol^{-1}), the Φ_0 ($(8.81 \pm 5.12) \times 10^{-6}$ mol m^{-1} s^{-1} Pa$^{-0.5}$) is one order of magnitude smaller than the value shown in Equation 4.6 for the Batch 1 Pd-Cu membrane. The lower E_Φ value for the Batch 2 Pd-Cu membranes helps to explain hydrogen permeation commencing at lower temperatures and achieving relatively higher hydrogen permeability values compared with the Batch 1 Pd-Cu membrane.

$$\Phi_{n=0.5} = (8.81 \pm 5.12) \times 10^{-6} exp\left(\frac{-(41.67 \pm 3.40) \times 10^{3}}{RT}\right) \quad \text{Equation 4.10}$$

Immediately after the Batch 2 Pd-Cu membranes completed three cycles between 50 and 450 °C, two cycles between 250 and 700 °C were performed. Figure 4.27 shows the second cycle completed by the Batch 2 Pd-Cu membranes between 250 and 700 °C.

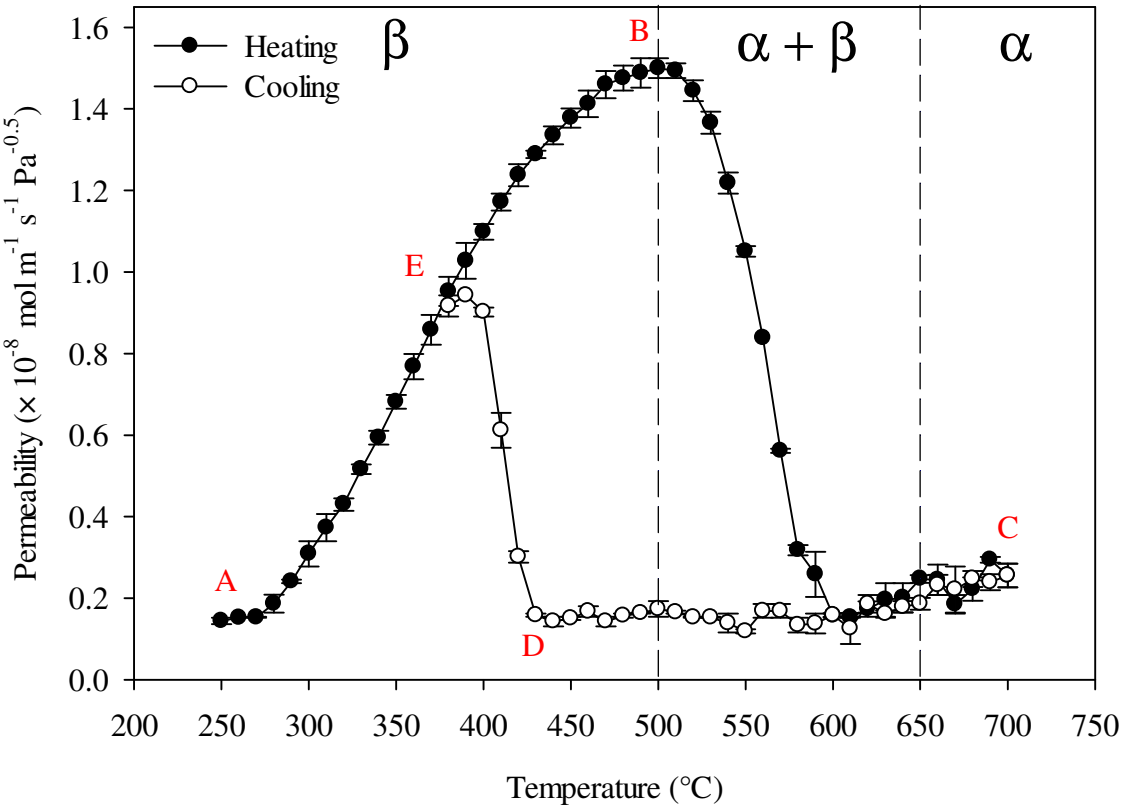

Figure 4.27 Hydrogen permeability as a function of temperature for the 31.3 µm thick Batch 2 Pd-Cu foil membranes during the second cycle between 250 and 700 °C. A hydrogen feed pressure of 445 kPa and permeate pressure of 100 kPa was applied during measurements. The dashed lines represent the phase boundaries of the FCC (α), BCC (β) and mixed phase regions, which were determined from the phase transition temperatures shown in Figure 4.12.

Similar to what has been shown with the Batch 1 Pd-Cu membrane (Figure 4.20), the Batch 2 Pd-Cu membranes follow a very similar cycle pattern. The second cycle begins at A and proceeds to a maximum at B which coincides with 500 °C after which the hydrogen permeability significantly declines to a minimum at approximately 600 °C due to the

formation of the disordered FCC phase. A slight increase in hydrogen permeability is observed up until the end of the heating stage of the cycle at C. The cooling stage proceeds from C to D whereby the hysteresis effect comes into play. This FCC phase begins to disappear at D and at E the membrane predominantly contains the BCC phase at which point the cycle proceeds to the end of the cycle at A. Points A, B, C, D and E occur at very similar temperatures to those shown in Figure 4.20 demonstrating that the Batch 1 and Batch 2 Pd-Cu membranes behave very similar under the same test conditions which further suggest that both batches are almost identical in composition but differ possibly in compositional homogeneity.

The *n*-value measurements were carried out on the Batch 2 Pd-Cu membranes subsequent to the 250 to 700 °C cycles. The data shown in Figure 4.28 has been calculated using an *n*-value constrained to 0.5, whereas the data in Figure 4.29 was determined with the best fit value of 0.59 ± 0.03.

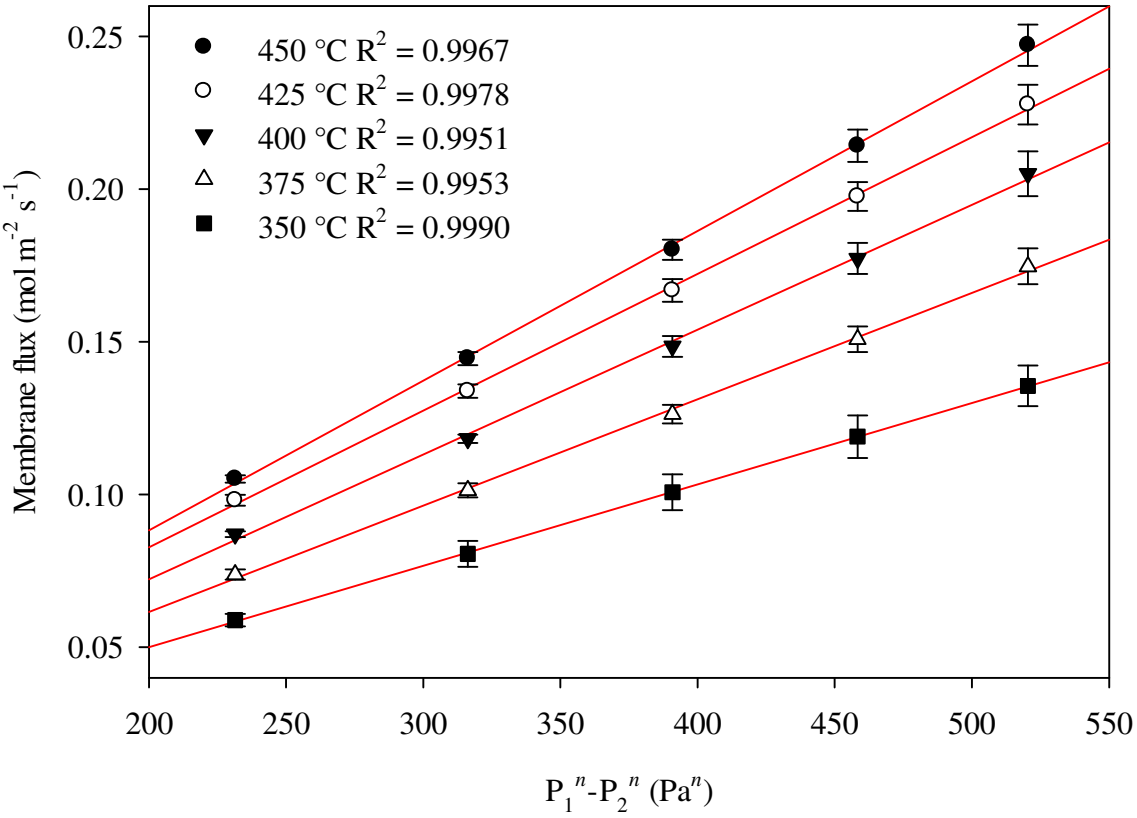

Figure 4.28 Membrane flux as a function of hydrogen differential pressure with *n* constrained to 0.5. This measurement was performed on the Batch 2 Pd-Cu foil membranes following cycling between 250 and 700 °C during MPR testing.

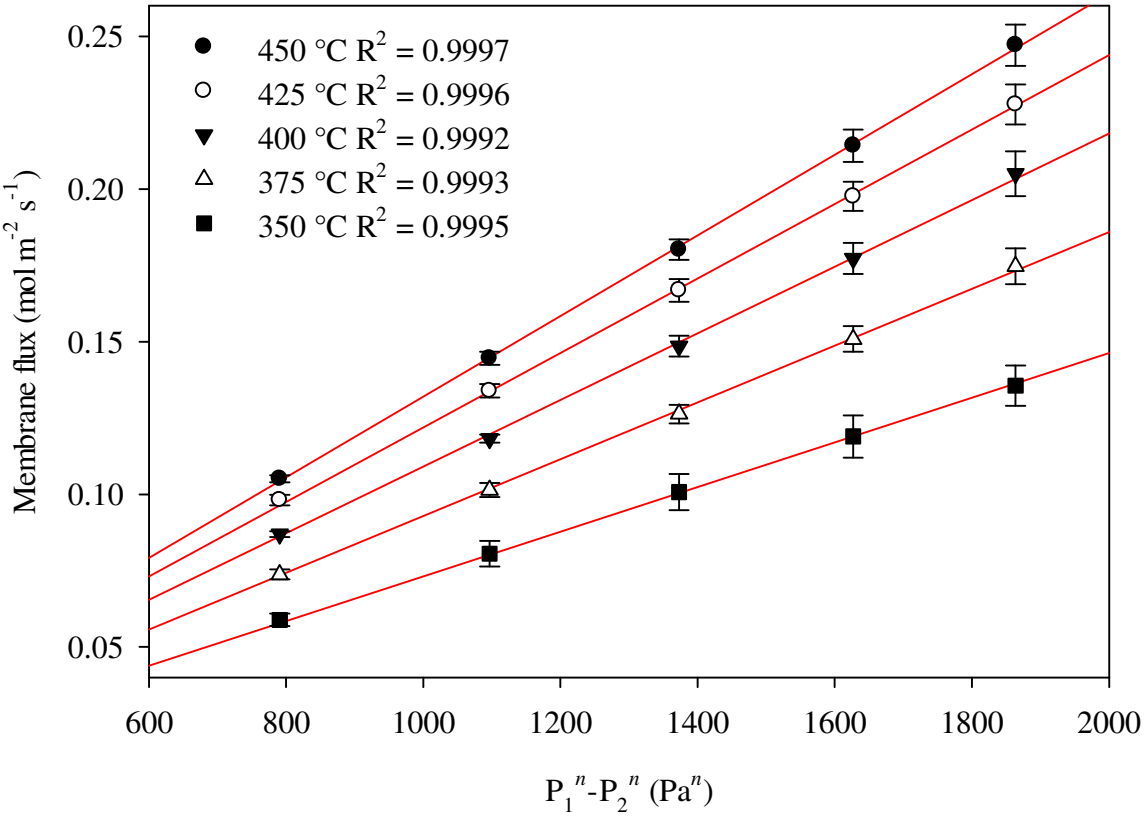

Figure 4.29 Membrane flux as a function of hydrogen differential pressure with *n* constrained to the best fit value of 0.59 ± 0.03. This measurement was performed on the Batch 2 Pd-Cu foil membranes following cycling between 250 and 700 °C during MPR testing.

The calculated average *n*-value of 0.59 ± 0.03 is only 13% larger than that determined for the Batch 1 Pd-Cu membrane, therefore indicating that hydrogen permeation in the Batch 2 Pd-Cu membranes is still diffusion limited. As shown in Figure 4.30, the Batch 2 Pd-Cu membranes achieved an average hydrogen permeability of $(8.49 \pm 1.36) \times 10^{-9}$ mol m^{-1} s^{-1} $Pa^{-0.5}$ at 350 °C which is a 284% increase on what was achieved prior to cycling between 250 and 700 °C. This value is also 21% and 4% higher than the values achieved by the Batch 1 Pd-Cu membrane and pure Pd membrane, respectively, under the same conditions. It is evident that by annealing the Pd-Cu membranes under the correct conditions can significantly enhance hydrogen permeability. For

comparison, Figure 4.30 shows the third cycle calculated using the average best fit *n*-value of 0.59.

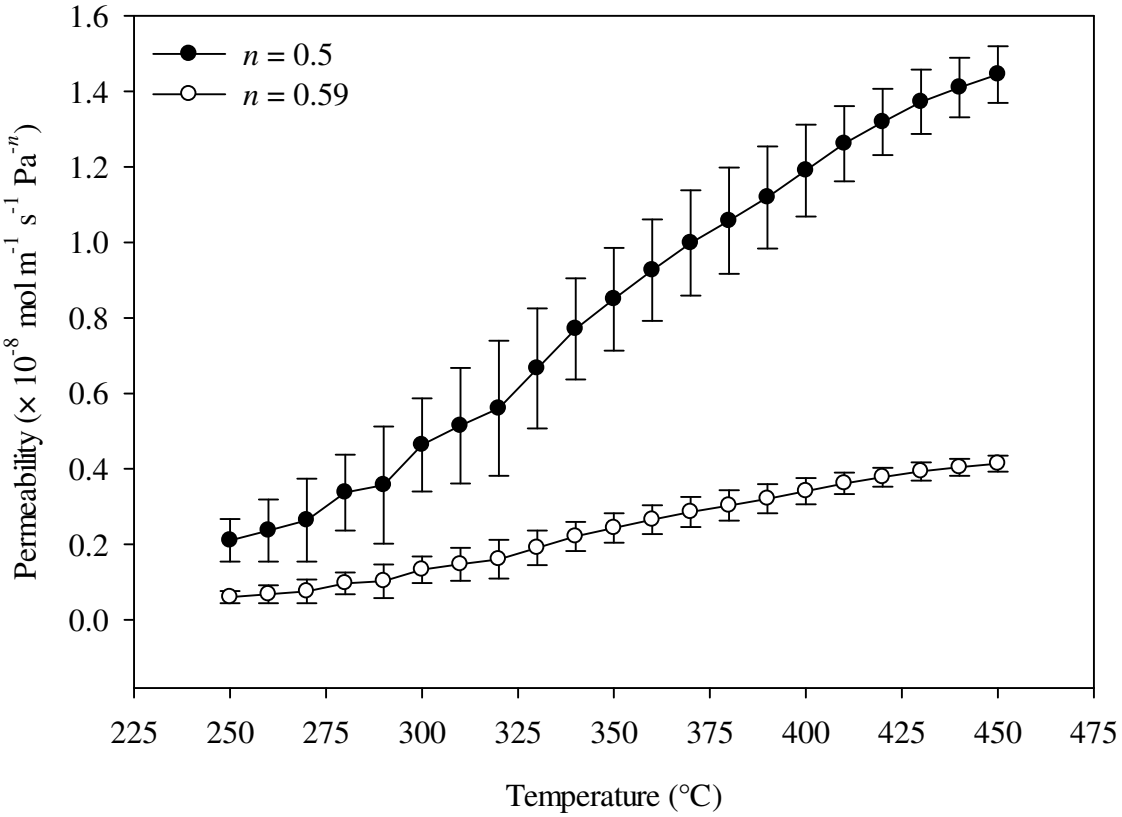

Figure 4.30 Hydrogen permeability as a function of temperature for the 31.3 µm thick Batch 2 Pd-Cu foil membranes showing the third cycle. This measurement was performed after cycling between 250 and 700 °C during MPR testing. A hydrogen feed pressure of 445 kPa and permeate pressure of 100 kPa was applied during measurements. The solid symbol curve was calculated using an *n*-value of 0.5 whereas the open symbol curve uses the best fit *n*-value of 0.59.

Figure 4.8(a), Figure 4.33(b) and also Figure 4.35(a) and (b) show a diffraction peak at $2\theta = 29.4°$ which corresponds to the $Cu_2O(110)$ diffraction plane. The presence of Cu_2O may have an adverse effect on the mechanical properties of the membrane as well as hydrogen permeability. Hydrogen readily dissolves in Cu at approximately 400 °C and rapidly diffuses until it encounters Cu_2O in which case the following reaction occurs (Equation 4.11) [265].

$$2H_{(abs)} + Cu_2O \rightarrow 2Cu + H_2O_{(gas)} \qquad \text{Equation 4.11}$$

The absorbed hydrogen ($H_{(abs)}$) reacts with Cu_2O to produce Cu and steam. Since steam is insoluble in Cu, pockets containing steam form and coalesce with adjacent pockets to form voids which, in extreme cases, lead to membrane failure [265]. Furthermore, these pockets can act as hydrogen traps and could potentially reduce diffusivity and consequently permeability of the membrane. This might be one of the reasons as to why the Batch 2 Pd-Cu membranes achieve relatively higher hydrogen permeability values over the Batch 1 Pd-Cu membrane.

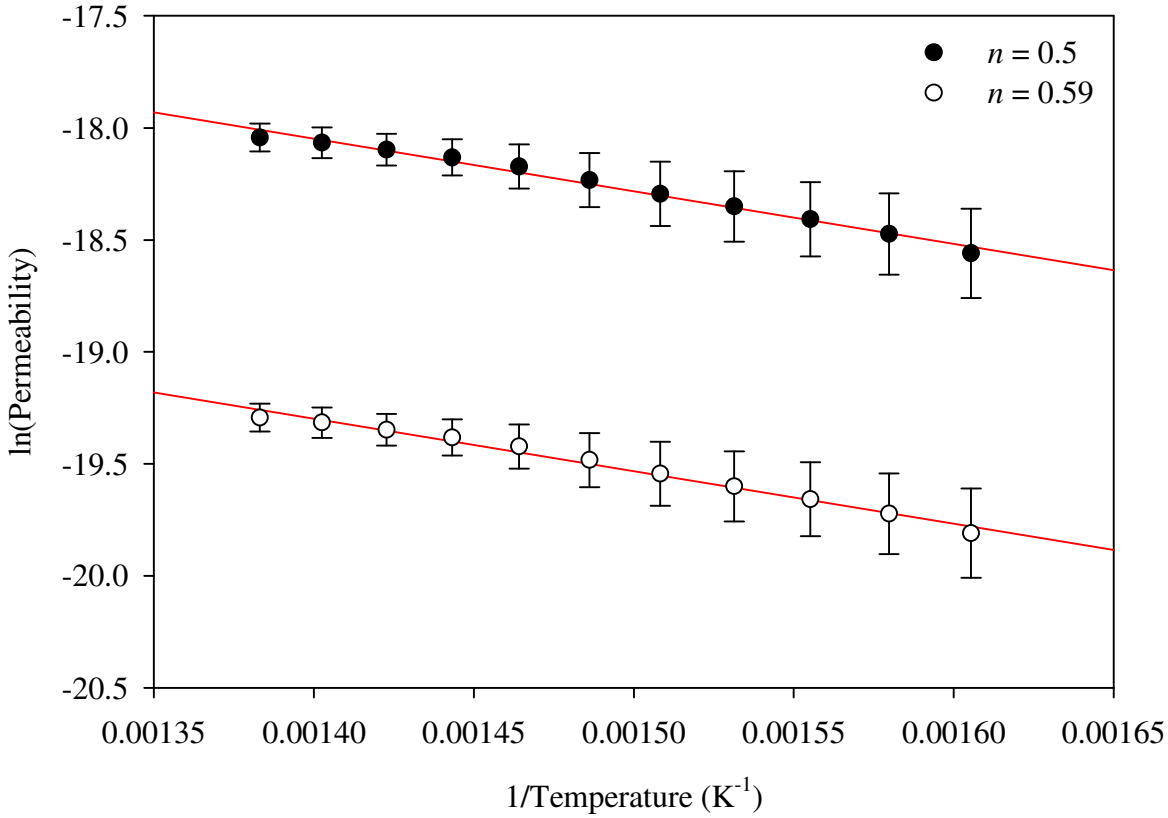

Figure 4.31 Arrhenius plot of the hydrogen permeability data shown in Figure 4.30 between 350 and 450 °C. The solid symbol curve was calculated using an *n*-value of 0.5 whereas the open symbol curve uses the best fit *n*-value of 0.59 ± 0.03.

From Figure 4.31, the following general permeability formulae (350 – 450 °C) for the Batch 2 Pd-Cu membranes were derived using an *n*-value of 0.5 and best fit value of 0.59 ± 0.03 as shown in Equation 4.12 and Equation 4.13, respectively.

$$\Phi_{n=0.5} = (6.32 \pm 4.74) \times 10^{-7} exp\left(\frac{-(19.93 \pm 6.12) \times 10^3}{RT}\right) \quad \text{Equation 4.12}$$

$$\Phi_{n=0.59} = (1.81 \pm 1.36) \times 10^{-7} exp\left(\frac{-(19.92 \pm 6.12) \times 10^3}{RT}\right) \quad \text{Equation 4.13}$$

As shown in Equation 4.12, the Batch 2 Pd-Cu membranes have an E_Φ value of 19.93 ± 6.12 kJ mol^{-1} and Φ_0 value of (6.32 ± 4.74) × 10^{-7} mol m^{-1} s^{-1} Pa$^{-0.5}$ when the *n*-value is constrained to 0.5. In comparison with Equation 4.10, it is apparent that the E_Φ value has more than halved as a result of completing several cycles under a hydrogen atmosphere where two cycles experienced a maximum temperature of 700 °C. This facilitated annealing and homogenisation of the membrane similar to what was witnessed with the Batch 1 Pd-Cu membrane. In addition, the effect of annealing has reduced the Φ_0 value by one order of magnitude which was also observed with the Batch 1 Pd-Cu membrane.

Figure 4.32 reveals the changes in the average *n*-value for the Batch 2 Pd-Cu membranes with temperature. The trend is quite different from that observed for the Batch 1 Pd-Cu membrane. At 350 °C, the *n*-value increases from 0.55 to a maximum of 0.61 between 375 and 400 °C after which a plateau is evident around 0.59 all the way up to 450 °C.

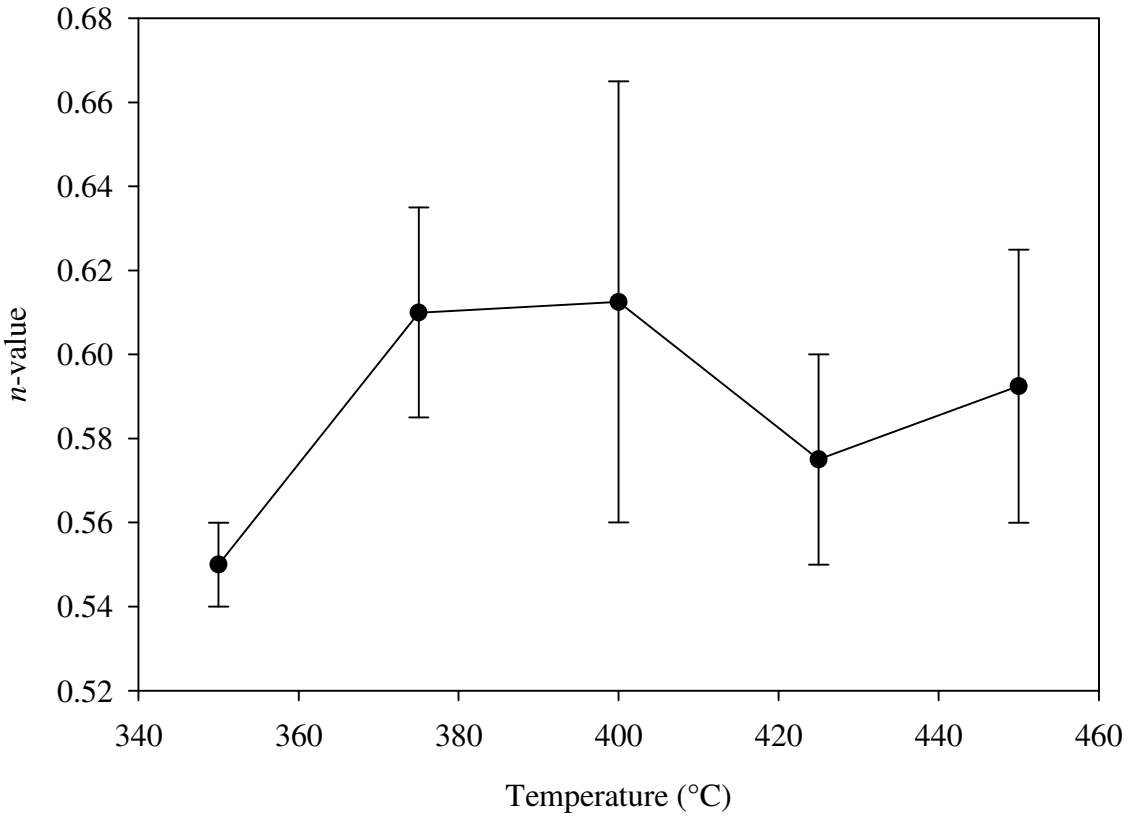

Figure 4.32 Variation of *n*-value as a function of temperature for the 31.3 µm thick Batch 2 Pd-Cu foil membranes.

4.3.3. Post-MPR characterisation

Ex-situ XRD analysis was performed on the Batch 1 and 2 Pd-Cu membranes after hydrogen permeability measurements in order to determine any changes in crystal structure as a result of MPR testing. Figure 4.33 displays an XRD pattern for a Batch 1 Pd-Cu membrane cycled to a maximum temperature of 450 °C. It shows that the membrane contains only the BCC phase on the feed side (Figure 4.33(a)) while the permeate side although predominately BCC also contains some trace of the FCC phase indicated by the Pd-Cu(111)* diffraction peak (Figure 4.33(b)). Similarly, the XRD pattern in Figure 4.34 is for a Batch 2 Pd-Cu membrane also cycled to a maximum temperature of 450 °C showing that the feed side contains only the BCC phase (Figure 4.34(a)) and the permeate side contains mainly the BCC phase with small

amounts of the FCC phase as indicated by the Pd-Cu(111)* and Pd-Cu(200)* diffraction peaks (Figure 4.34(b)).

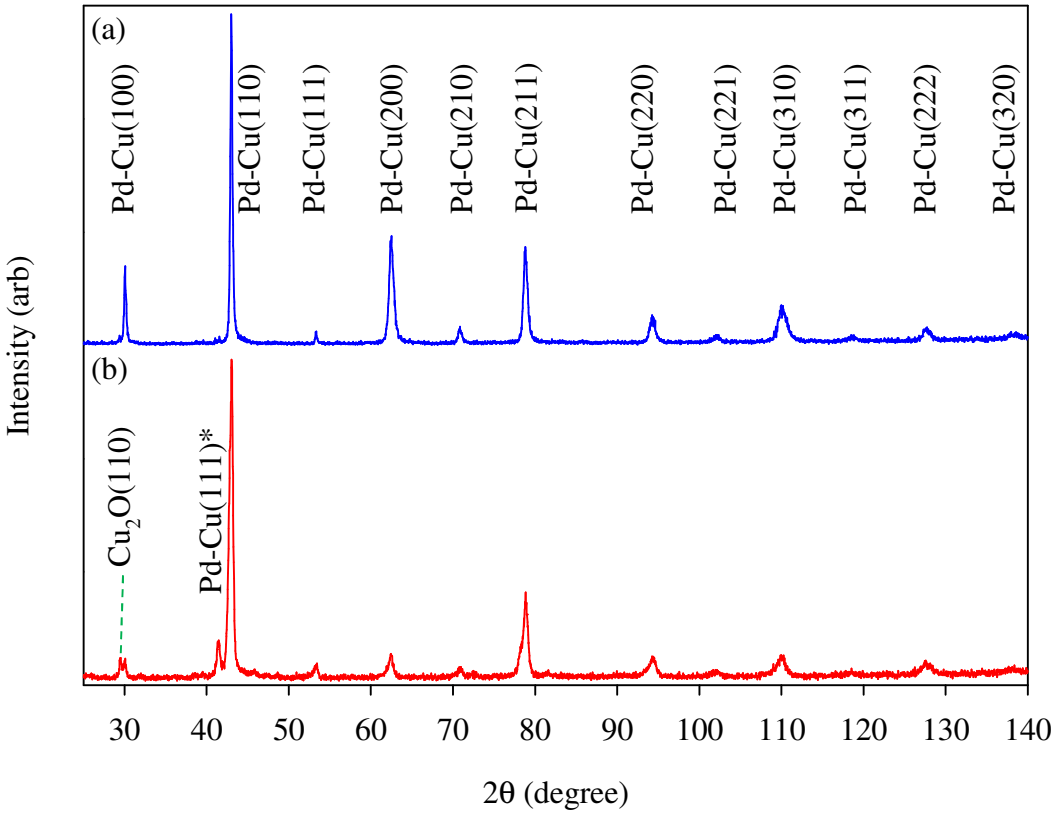

Figure 4.33 XRD patterns of the as-received Batch 1 Pd-Cu foil membrane after MPR testing performed on the feed side (a) and permeate side (b). This membrane was cycled to a maximum temperature of 450 °C. '*' indicates the FCC diffraction peak.

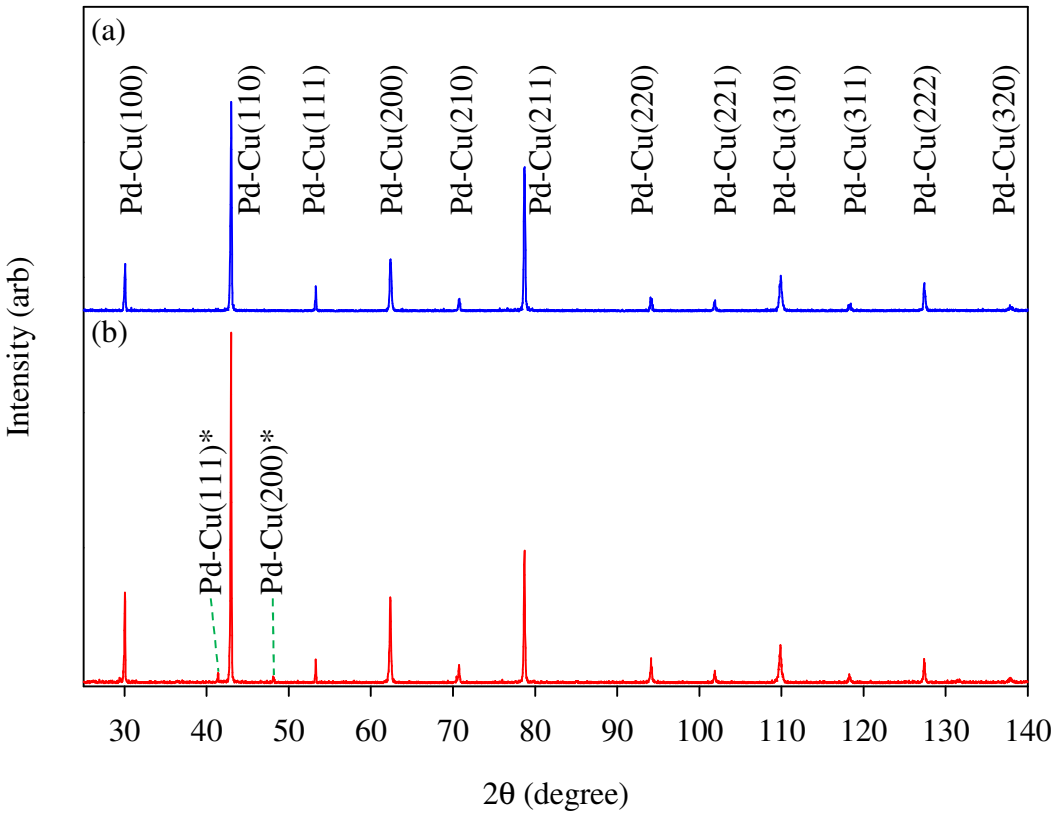

Figure 4.34 XRD patterns of the as-received Batch 2 Pd-Cu foil membrane after MPR testing performed on the feed side (a) and permeate side (b). This membrane was cycled to a maximum temperature of 450 °C. '*' indicates the FCC diffraction peak.

Figure 4.35 and Figure 4.36 show the ex-situ XRD patterns for the Batch 1 and Batch 2 Pd-Cu membranes that had completed several cycles in hydrogen up to temperatures as high as 700 °C under the same conditions described in Section 4.3.2. Both patterns indicate that only the BCC phase is present on either side of the membranes. This is further evidence that exposure to such high temperatures at a hydrogen feed pressure of 445 kPa and permeate pressure of 100 kPa anneals the membranes and promotes the complete phase transformation from the FCC to the equilibrium BCC phase.

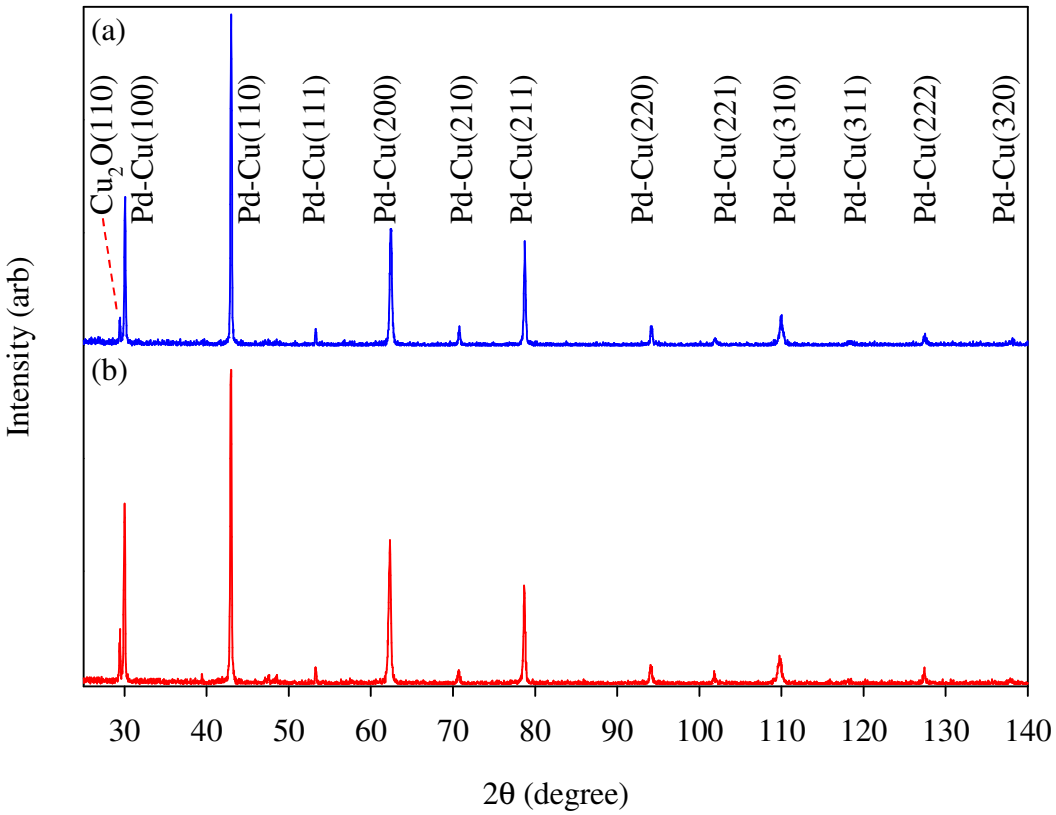

Figure 4.35 XRD patterns of the as-received Batch 1 Pd-Cu foil membrane after MPR testing performed on the feed side (a) and permeate side (b). This membrane was cycled to a maximum temperature of 700 °C.

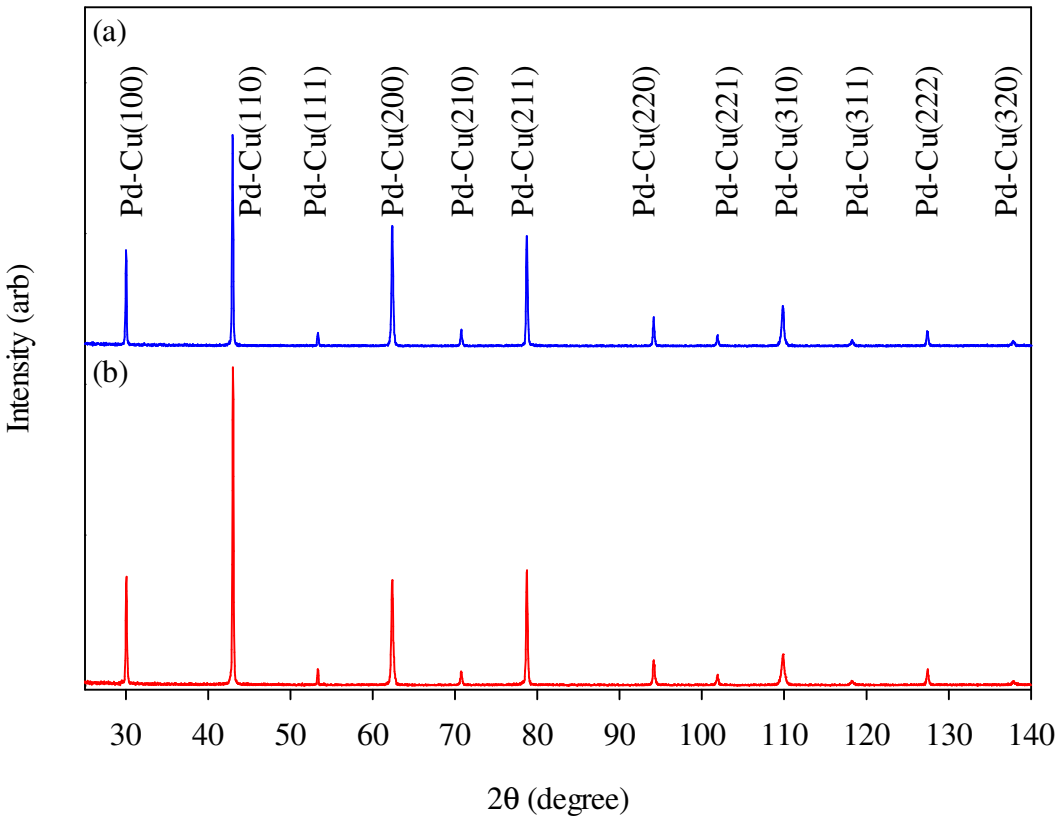

Figure 4.36 XRD patterns of the as-received Batch 2 Pd-Cu foil membrane after MPR testing performed on the feed side (a) and permeate side (b). This membrane was cycled to a maximum temperature of 700 °C.

To accurately determine any compositional changes in the Batch 1 and 2 Pd-Cu membranes as a result of MPR testing, only membranes which were cycled to 700 °C will be used to calculate phase composition since they will have a greater extent of compositional homogeneity over those membranes that were only cycled to 450 °C.

Since the Batch 1 and 2 Pd-Cu membranes largely contain the newly formed BCC phase, which has a lattice parameter different from the FCC phase, a new formula is required to calculate the phase composition similar to Equation 6.1. A description for calculating the Pd-Cu BCC phase composition is given in the Appendix (Section 6.1).

From Figure 4.35, the lattice parameter can be calculated for both sides of the MPR tested Batch 1 Pd-Cu membrane. The lattice parameters for the feed side and permeate side are

calculated to be 2.975 Å and 2.978 Å, respectively. From the XRD data shown in Figure 4.36, the lattice parameters for the Batch 2 Pd-Cu membranes were calculated as 2.978 Å for both the feed side and permeate side. These lattice parameter values agree extremely well with the value range 2.97 – 2.977 Å [39, 210, 266, 267] found in literature for the same phase composition.

Using Equation 6.2, the associated BCC phase compositions are calculated for both Batch 1 and Batch 2 Pd-Cu membranes and summarised in Table 4.7. As indicated by the XRD and EDS data, it can be said that following MPR testing the Batch 2 Pd-Cu membranes possess an identical BCC phase composition on both sides of the membrane unlike the Batch 1 Pd-Cu membrane which exhibits very different compositions on both sides. The homogeneity in the Batch 2 Pd-Cu membrane would most likely be responsible for the higher hydrogen permeability values reached in comparison to the Batch 1 Pd-Cu membrane. It is evident when comparing the compositions presented in Table 4.3 with those shown in Table 4.7 that the conditions used during MPR testing has the effect of homogenising the composition of the Pd-Cu membranes.

Table 4.7 A summary of the BCC phase compositions (wt%) determined using XRD and EDS for both batches of Pd-Cu membrane.

	Surface	XRD	EDS
Batch 1	Feed side	$Pd_{60.0}Cu_{40.0}$	$Pd_{60.7 \pm 0.6}Cu_{39.3 \pm 0.6}$
	Permeate side	$Pd_{61.6}Cu_{38.4}$	$Pd_{65.0 \pm 0.9}Cu_{35.0 \pm 0.9}$
Batch 2	Feed side	$Pd_{61.6}Cu_{38.4}$	$Pd_{62.2 \pm 0.6}Cu_{37.8 \pm 0.6}$
	Permeate side	$Pd_{61.6}Cu_{38.4}$	$Pd_{61.9 \pm 0.9}Cu_{38.1 \pm 0.9}$

4.4. Type A membranes

4.4.1. Pre-MPR characterisation

As outlined in Table 4.1, Type A membranes were prepared by sputtering Pd onto one side of an as-received Pd-Cu membrane for 50 seconds. The Type A membranes which use an as-received Batch 1 Pd-Cu membrane for a substrate are referred to as a Type A-B1 membrane. Similarly, a Type A membrane which has an as-received Batch 2 Pd-Cu membrane substrate is referred to as a Type A-B2 membrane. In total four membranes were prepared: two Type A-B1 membranes and two Type A-B2 membranes.

Furthermore, 'F' and 'P' will be notations to distinguish the position of the Pd thin film during MPR testing. For example, the Type A-B1-F membrane denotes that Pd has been sputter-coated for 50 seconds onto one side of a Batch 1 Pd-Cu membrane and MPR tested with the Pd thin film positioned on the feed side. Similarly, the Type A-B2-P membrane denotes that Pd has been sputter-coated for 50 seconds onto one side of a Batch 2 Pd-Cu membrane and MPR tested with the Pd thin film positioned on the permeate side. The same convention will be used for the Type B and C membranes.

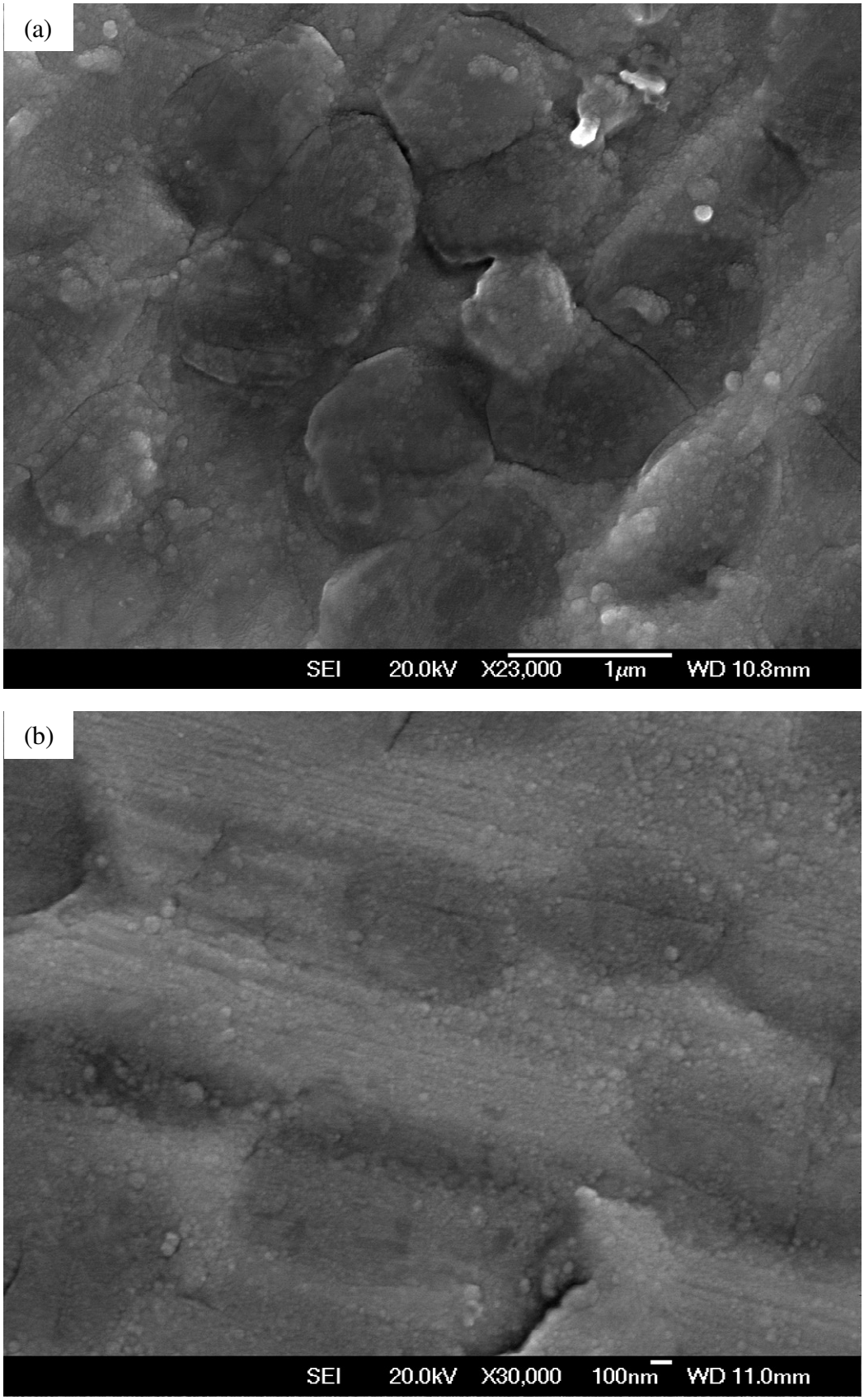

Figure 4.37 SEM micrographs showing the microstructure representative of a Type A-B1 and Type A-B2 membrane. Coating time was 50 seconds with a Pd target current of 1 A.

After the Pd sputter deposition process was complete, SEM micrographs were acquired representative of a Type A-B1 and Type A-B2 membrane in order to view the Pd thin film microstructure (Figure 4.37(a) and (b)). The micrographs show that the Pd thin film is polycrystalline in nature made up of nanometre sized grains. The average grain size can be estimated from Figure 4.37(b) to be approximately 38 nm which is comparable to the 30 nm grain size achieved by Jayaraman et al [268] who sputter-deposited Pd onto porous α-alumina supports under similar conditions to those used in this work.

The thickness of the Pd thin film was determined using the methods outlined in Section 3.1.2. The Type A-B1 and Type A-B2 membranes were weighed before and after Pd deposition and with the use of Equation 3.1, an estimated thickness of 82 ± 4 nm for the Pd thin film was determined.

$$t_f = \frac{M_{s+Pd} - M_s}{\rho_{Pd} A_s} \qquad \text{Equation 3.1}$$

Equation 3.1 assumes that the Pd thin film is fully dense with a continuous and uniform thickness throughout the coated area.

Alongside the Type A-B1 and Type A-B2 membranes, a glass slide with a portion of the surface masked with Kapton tape was Pd sputter-coated for 50 seconds. Following the sputtering process, the Kapton tape was removed to reveal the glass section protected from the Pd deposition. This created a step between the glass surface and the deposited Pd thin film from which the thickness can be measured. Figure 4.38 shows the profilometer trace for the glass slide that was Pd sputter-coated for 50 seconds. The initial 1,050 µm of the *x*-axis represents the non-coated glass surface after which the edge of the Pd thin film is reached. The stylus tip travels just under 1 mm along the top surface of the Pd thin film to complete the

measurement. The trace shows that the Pd thin film thickness is approximately 95.5 ± 0.1 nm thick. From Figure 4.38, the trace reveals that the Pd thin film does not have a uniform thickness along the *x*-axis. The thickness measured using profilometry is larger than that calculated using Equation 3.1 suggesting that the deposited Pd thin film is not completely dense.

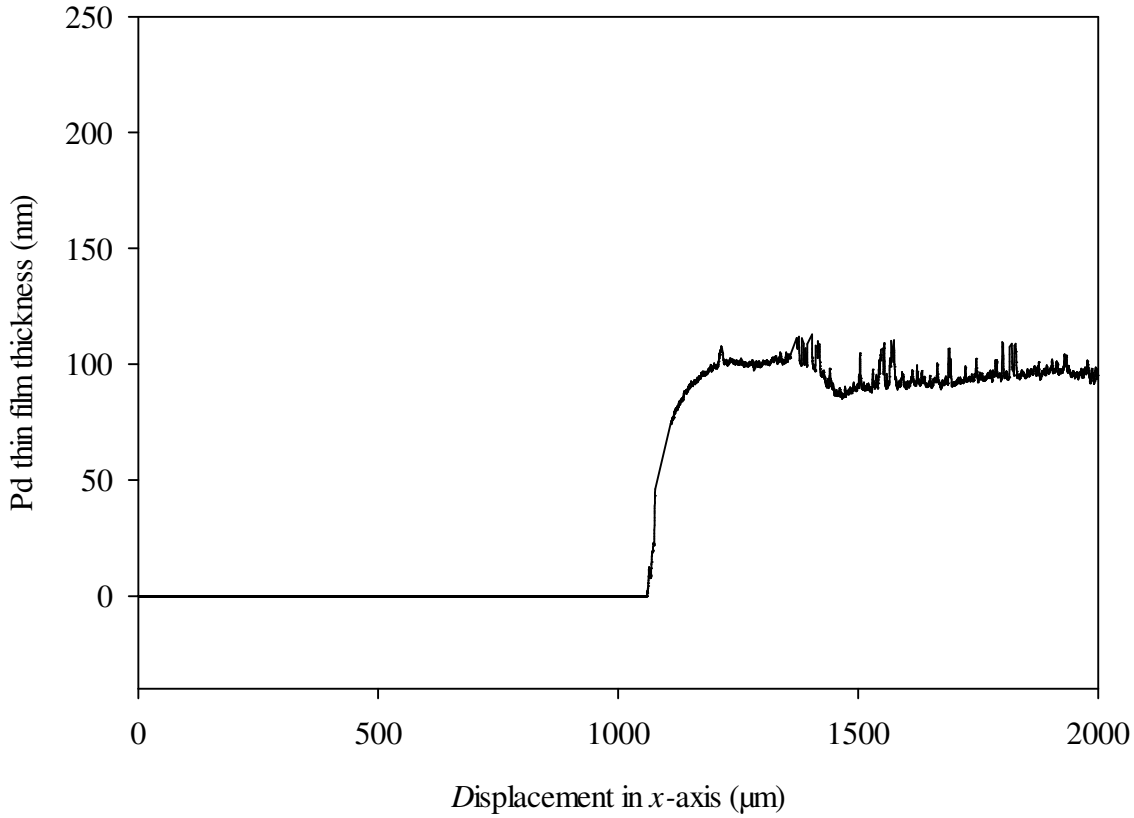

Figure 4.38 Profilometer trace for a glass slide that has been Pd sputter-coated for 50 seconds. The first 1,050 μm of the *x*-axis represents the area of the glass slide masked with Kapton tape during Pd deposition.

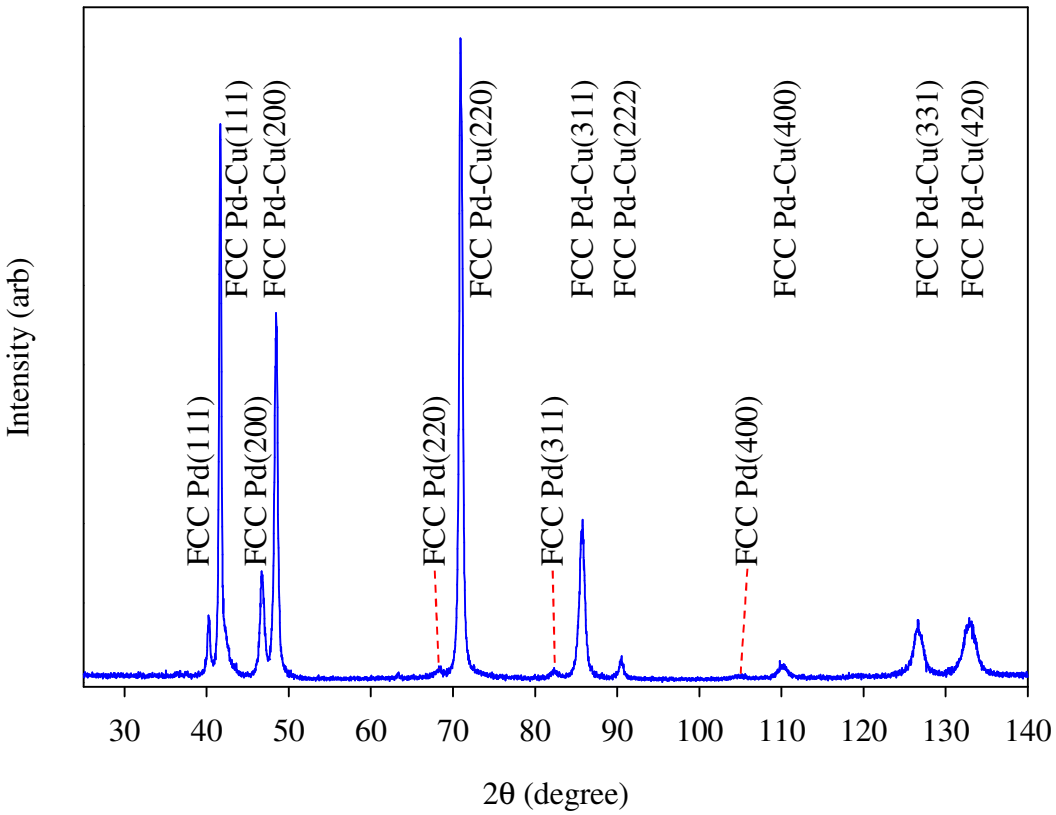

Figure 4.39 XRD pattern which is representative for the Pd sputter-coated side of a Type A-B1 and Type A-B2 membrane in the as-deposited state before MPR testing.

Figure 4.39 illustrates an XRD pattern representative of a Type A-B1 and Type A-B2 membrane. The presence of the Pd thin film is indicated by the Pd(111), (200), (220), (311) and (400) diffraction peaks. A noticeable feature of Figure 4.39 is the peak asymmetry evident in these diffraction peaks. With peak asymmetry, the diffraction peaks themselves are made up of smaller individual diffraction sub-peaks (Figure 4.40(a)) positioned at different scattering angles. Yet the XRD pattern combines the individual peaks into one asymmetric diffraction peak as demonstrated in Figure 4.40(b).

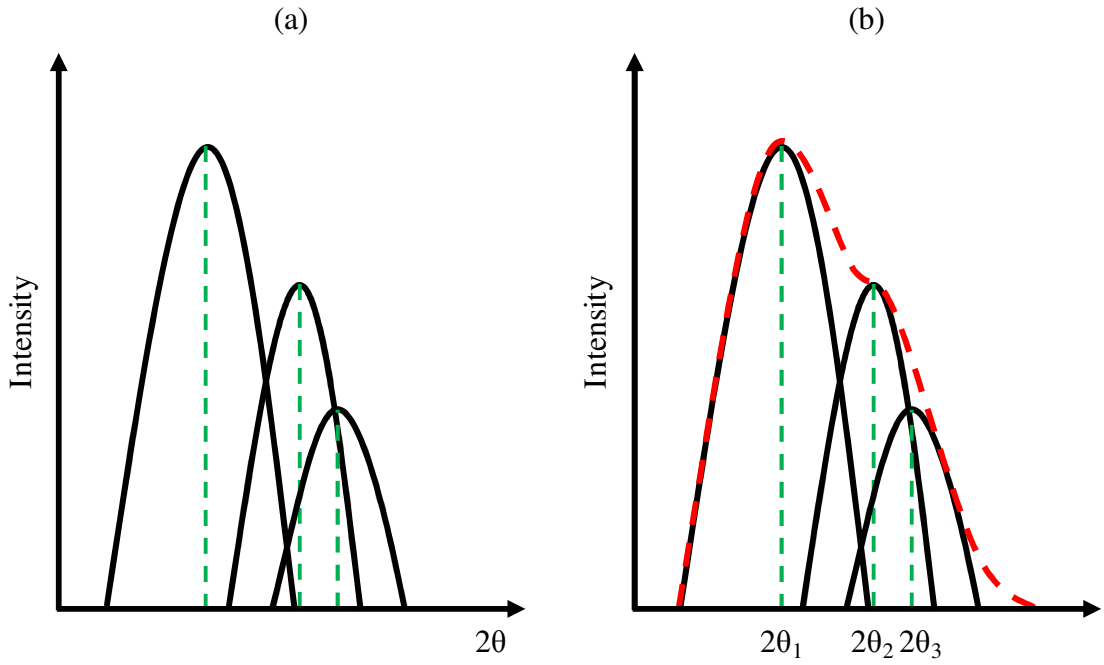

Figure 4.40 Illustration demonstrating peak asymmetry.

The Pd(111) diffraction peak from Figure 4.39 is shown in greater detail in Figure 4.41. Asymmetry in this peak is observed on the right hand side spreading over a range of higher scattering angles. An increase in scattering angle is caused by a decrease in interplanar distance and consequently a reduction in the lattice parameter. As shown in Figure 6.1 in the Appendix, the Pd-Cu FCC crystal structure contracts with increasing Cu content. This may suggest that interdiffusion of Cu atoms from the Pd-Cu membrane into the Pd thin film takes place during the sputtering process producing an interface region that exhibits a range of Pd-Cu compositions.

From points A, B, C, D and E in Figure 4.41, the corresponding compositions were calculated using Equation 3.4 and Equation 6.1 and compiled in Table 4.8. It should be noted that, XRD data points were acquired every 0.028° 2θ in each pattern and it is assumed that this step size is sufficient for a good first approximation. Point A is highlighted with a green dashed line to indicate the 2θ position of the pure Pd(111) diffraction peak.

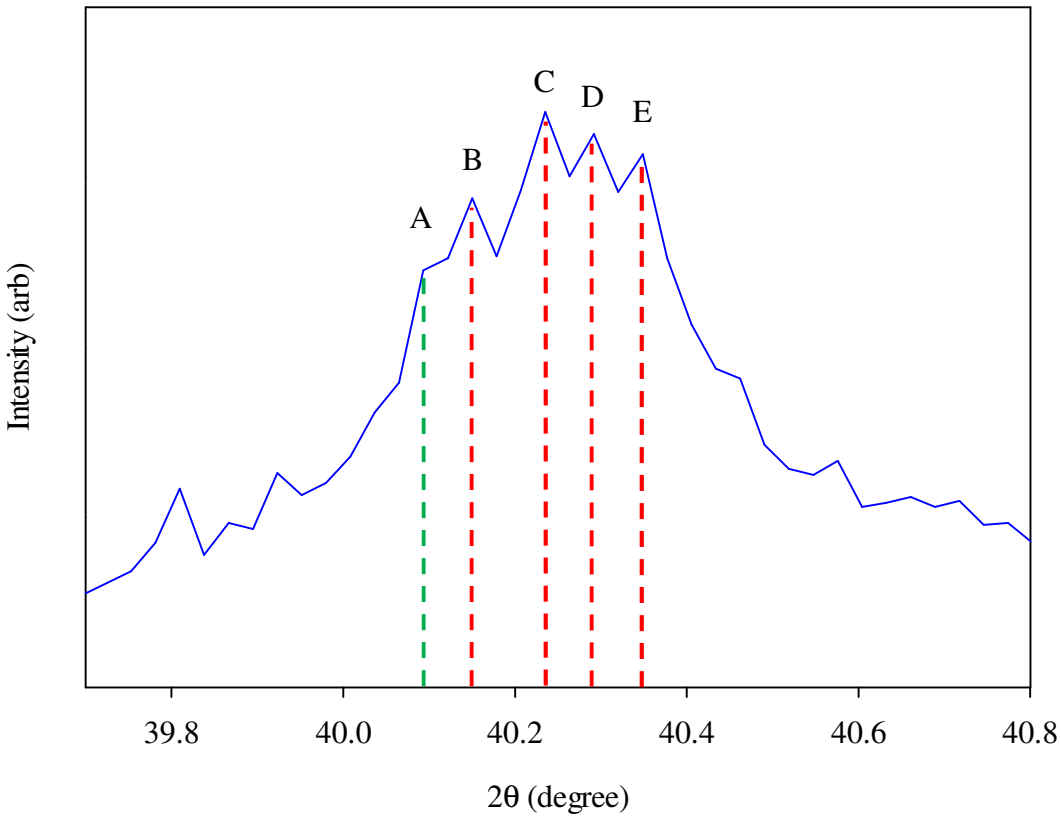

Figure 4.41 Magnification of the Pd(111) diffraction peak shown in Figure 4.39.

Table 4.8 Compositions determined for points A to E in Figure 4.41.

	Scattering angle, 2θ (degree)	Composition (wt%)
A	40.09	$Pd_{100}Cu_0$
B	40.15	$Pd_{97.6}Cu_{2.4}$
C	40.24	$Pd_{95.8}Cu_{4.2}$
D	40.29	$Pd_{94.6}Cu_{5.4}$
E	40.35	$Pd_{93.4}Cu_{6.6}$

Using the scattering angles for the most intense peaks corresponding to each Pd-Cu(*hkl*) diffraction plane (for example point C in Figure 4.41), the composition of the Pd thin film was calculated to be $Pd_{93.4}Cu_{6.6}$ wt%. This has been done using the method detailed in Section6.1.

Three foil offcuts were Pd sputter-coated alongside the Type A-B1 and Type A-B2 membranes. These Pd sputter-coated foil offcuts originate from the

Batch-2 Pd-Cu foil and are referred to as Type A-B2 Foil 1, Type A-B2 Foil 2 and Type A-B2 Foil 3. XPS depth profile analysis was performed on the as-deposited Type A-B2 Foil 1 to observe the variation in Pd and Cu concentration with etch depth as shown in Figure 4.42. An estimate for etch depth was determined from the etch time using an etching rate of 0.21 nm s^{-1} obtained from a Ta_2O_5 standard.

According to Figure 4.42, the top 75 nm of the thin film is pure Pd below which an interdiffusion region exists. Note that the XPS depth profile is performed down to a depth of 200 nm and therefore the interdiffusion region may continue beyond this point meaning greater analysis depths are required in order to reach the composition of the bulk Pd-Cu foil. This is further evidence that interdiffusion between the deposited Pd thin film and bulk Pd-Cu foil occurs during the sputtering process.

It should be noted, however, that XPS scans were performed at 25 nm intervals. A higher resolution or shorter intervals would be required to accurately determine the depth and size of the interdiffusion region. Significant interdiffusion can occur between bimetallic interfaces in bulk metals and alloys at the Tammann temperature [269]. This is defined as half of the melting point (in K) of the constituent metals hence the Tammann temperature for the Pd-Cu system ranges between 679 K (326 °C) for Cu and 914 K (641 °C) for Pd. Therefore it is expected that Cu atoms will be more mobile than Pd atoms during the interdiffusion process.

Various work on this topic [261, 270-274] has shown that significant interdiffusion can occur in Pd-Cu thin films fabricated using deposition techniques such as electrodeposition, thermal evaporation and magnetron sputtering. Bukaluk [274] reports interdiffusion between Pd/Cu multilayers occurring at temperatures as low as 120 °C. The authors have attributed this

phenomenon to the polycrystalline nature of the deposited thin films which introduce grain boundary defects that promote interdiffusion.

Figure 4.37 shows a nanocrystalline Pd thin film with countless grain boundary defects which can facilitate interdiffusion. It may seem unlikely that either a Type A-B1 or Type A-B2 membrane could reach the necessary temperatures in 50 seconds for interdiffusion to take place. However, it should be noted that irrespective of the short coating time, it is possible that the Pd atoms will arrive at the surface of the Pd-Cu membrane with sufficient kinetic energy for interdiffusion to occur.

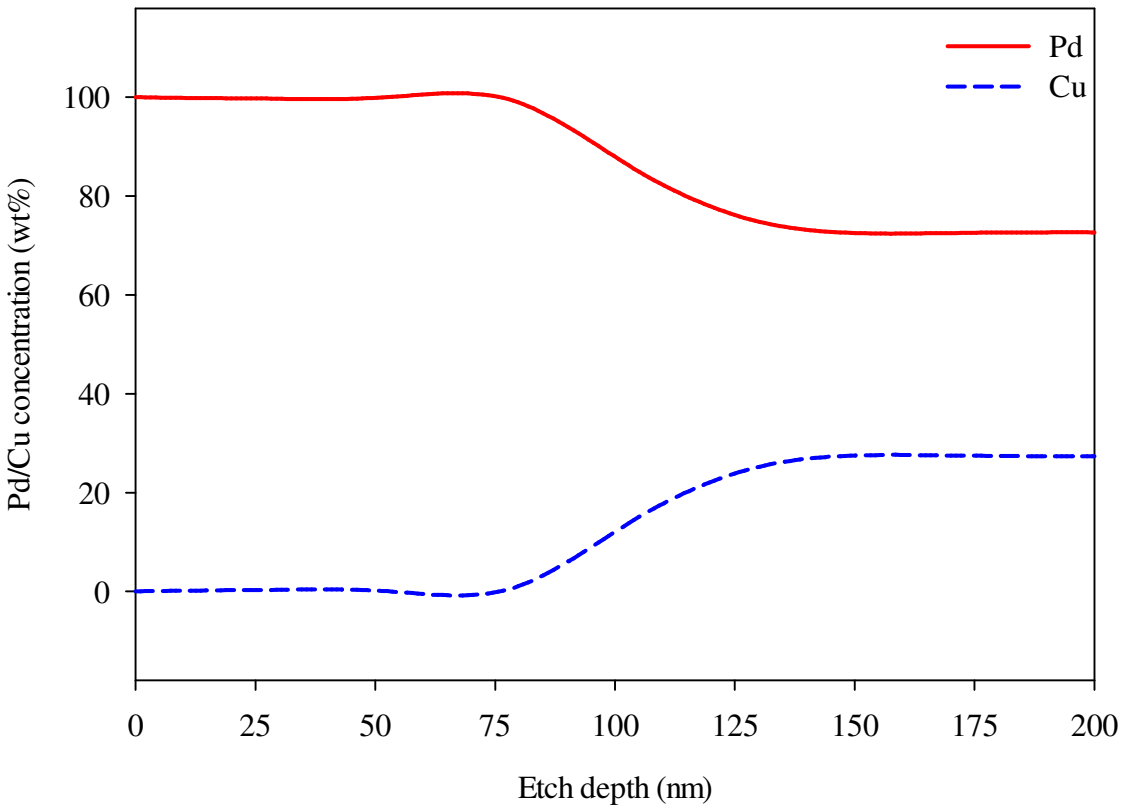

Figure 4.42 XPS depth profile analysis of Type A-B2 Foil 1 in the as-deposited state. The etch depth was estimated using a reference etching rate of 0.21 nm s^{-1} for Ta_2O_5.

4.4.1.1. Effects of temperature and hydrogen pressure on interdiffusion

Type A-B1 and Type A-B2 membranes have been tested in the MPR with the Pd thin film positioned on the feed and also on the permeate side in order to investigate the effect on membrane permeability. VTXRD analysis was performed on Type A-B2 Foil 2 and Type A-B2 Foil 3, which are representative of the Type A-B1/2-F/P membranes, between 30 and 700 °C under conditions similar to those used in the MPR in order to study the influence of temperature and hydrogen pressure on the interdiffusion of the Pd thin film with the bulk Pd-Cu foil.

Type A-B2 Foil 2 was tested under 445 kPa of flowing hydrogen in order to emulate conditions in the MPR on the feed side. Figure 4.43(a) is a contour plot of temperature against scattering angle. It is apparent from this plot that the Pd thin film forms the β-PdH phase at temperatures as low as 30 °C. This is shown by the β-PdH(111) diffraction peak located at $2\theta = 38.30°$. Hence, the Pd lattice parameter expands from 3.89 to 4.067 Å which is a 14.3% lattice volume expansion as a result of 445 kPa of hydrogen pressure. The β-PdH(111) diffraction peak shifts to $2\theta = 39.81°$ at 200 °C indicating the formation of the α-PdH phase as hydrogen is desorbed from the Pd thin film with increasing temperature. Due to hydrogen desorption, the lattice parameter contracts to 3.92 Å. This observation is expected since the enthalpy of hydride formation in Pd is exothermic [68].

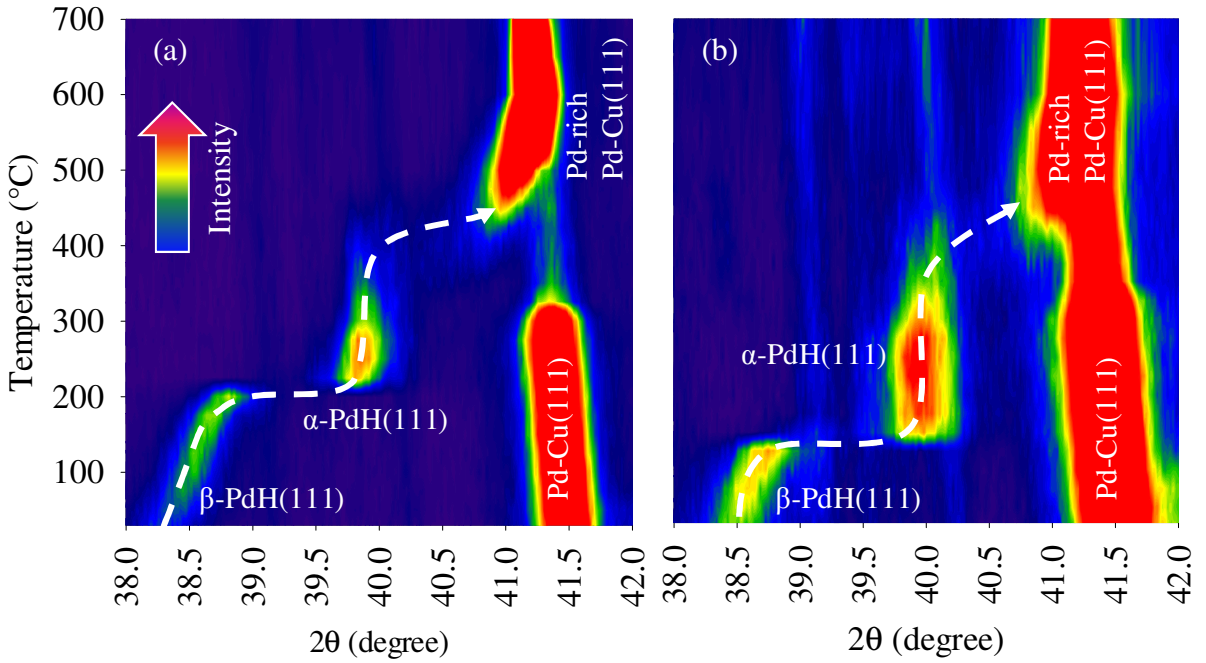

Figure 4.43 VTXRD contour plots tracking the movement of the (a) PdH(111) diffraction peak from the Pd thin film of Type A-B2 Foil 2 under 445 kPa of flowing hydrogen and (b) the PdH(111) diffraction peak from the Pd thin film of Type A-B2 Foil 3 under 100 kPa of flowing hydrogen whilst heating between 30 and 700 °C.

The interdiffusion process takes place between 350 and 600 °C as shown by the movement of the α-PdH(111) diffraction peak to higher scattering angles. This peak shift is indicative of a decrease in interplanar distance and consequently lattice parameter as a result of the Cu concentration increasing in the Pd thin film. At temperatures above 600 °C interdiffusion stops as the α-PdH(111) diffraction peak eventually merges with the newly formed Pd-rich Pd-Cu(111) diffraction peak demonstrating that the Pd thin film has fully interdiffused with the Pd-Cu foil.

Also note that the Pd-Cu(111) diffraction peak attributed to the FCC phase present in the bulk Pd-Cu foil, drops in intensity between 325 and 500 °C. This means that the FCC content in the bulk Pd-Cu foil dramatically drops between these temperatures. This observation was also seen with the as-received Batch 1 Pd-Cu foil offcut (Foil 2) as shown in Table 4.5.

To study the effects of hydrogen permeate pressure on interdiffusion between the Pd thin film and Pd-Cu foil, VTXRD was conducted on Type A-B2 Foil 3 under 100 kPa of flowing hydrogen (Figure 4.43(b)). Similar to Type A-B2 Foil 2, the Pd thin film readily forms the β-PdH phase at 30 °C, however, the β-PdH(111) diffraction peak occurs at a relatively higher scattering angle, 2θ = 38.53°. This scattering angle signifies that the Pd lattice parameter has increased to 4.043 Å as a result of exposure to 100 kPa of hydrogen pressure causing a 12.3% lattice volume dilation. From this it is evident that 445 kPa of hydrogen pressure generates a larger lattice expansion in the Pd thin film compared to a pressure of 100 kPa.

Furthermore, Figure 4.43(b) shows that at 150 °C the β-PdH(111) diffraction peak shifts to 2θ = 39.98° indicating that hydrogen desorption in the Pd thin film occurs to form the α-PdH phase. According to the Pd-H PCT diagram (Figure 2.9), it is expected that hydrogen will desorb from Pd at lower temperatures when at lower hydrogen pressures. The intensity of the α-PdH(111) diffraction peak decreases at 300 °C, however, it is still detectable up until 700 °C suggesting that small traces of the α-PdH phase is stable at such high temperatures under 100 kPa of hydrogen pressure. This also means that minute remains of the Pd thin film can still be detected following interdiffusion with the Pd-Cu foil under these conditions. Similar to what is shown in Figure 4.43(a), interdiffusion takes place between 350 and 600 °C as demonstrated by the movement of the α-PdH(111) diffraction peak to higher scattering angles to eventually merge with the Pd-rich Pd-Cu(111) diffraction peak.

The Pd-Cu(111) diffraction peak associated with the bulk Pd-Cu foil does not disappear during the VTXRD experiment indicating that the FCC phase remains stable throughout the entire temperature range. This implies that 100 kPa of hydrogen pressure is insufficient in promoting the complete transformation of the FCC phase to the BCC phase during the VTXRD run.

Following the VTXRD runs, XPS depth profile analysis was carried out on Type A-B2 Foil 2 and Type A-B2 Foil 3 with the results shown in Figure 4.44 and Figure 4.45, respectively. It appears that the top few nanometres of Type A-B2 Foil 2 contains a Pd-rich phase with a composition of $Pd_{90.2}Cu_{9.8}$ wt%. Similarly, the surface of Type A-B2 Foil 3 has a composition of $Pd_{87.9}Cu_{12.1}$ wt%. Both indicate the presence of the Pd-rich Pd-Cu FCC phase observed in Figure 4.43(a) and (b). This is proof that the Pd-rich Pd-Cu FCC phase forms on the surface of the Type A membranes as a result of interdiffusion occurring between the Pd thin film and bulk Pd-Cu membrane under similar conditions used in the MPR.

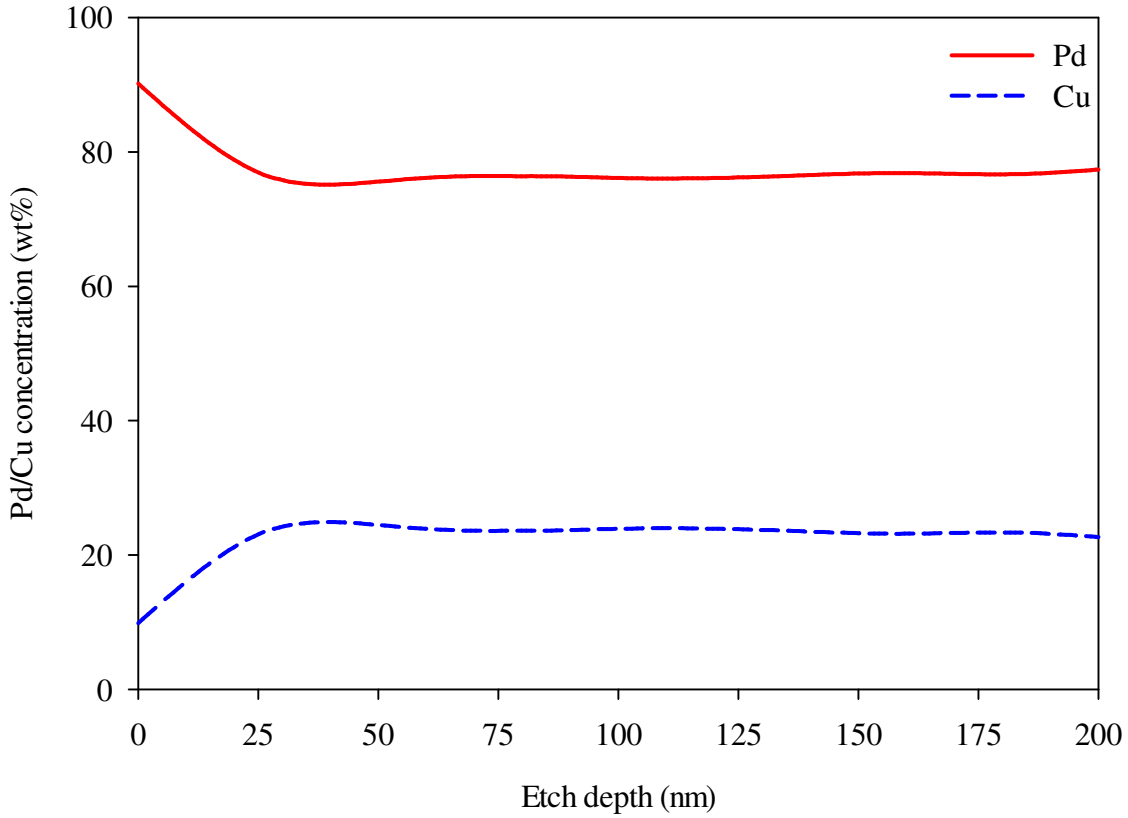

Figure 4.44 XPS depth profile analysis of Type A-B2 Foil 2 following VTXRD under 445 kPa of hydrogen pressure. The etch depth was estimated using a reference etching rate of 0.21 nm s^{-1} for Ta_2O_5.

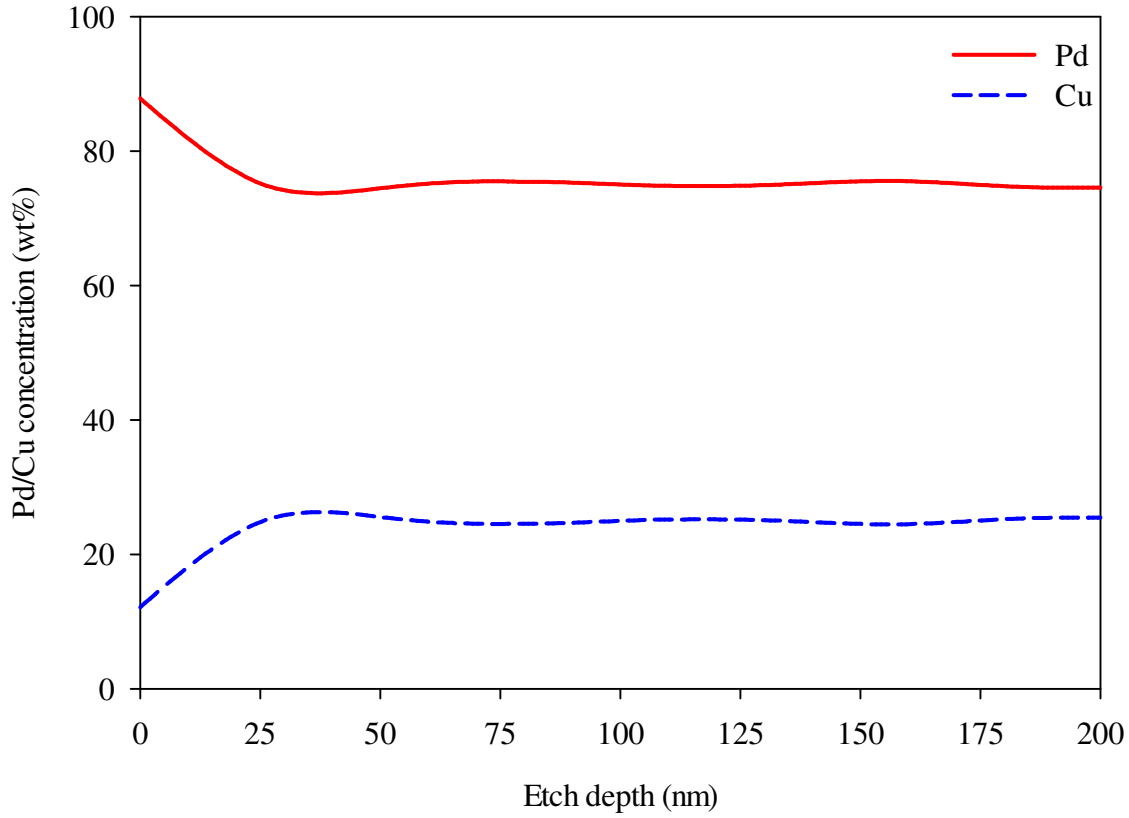

Figure 4.45 XPS depth profile analysis of Type A-B2 Foil 3 following VTXRD under 100 kPa of hydrogen pressure. The etch depth was estimated using a reference etching rate of 0.21 nm s^{-1} for Ta_2O_5.

4.4.2. MPR results

4.4.2.1. Pd thin film positioned on the feed side

Both Type A-B1-F and Type A-B2-F membranes have been tested in the MPR between 50 and 450 °C using an applied hydrogen pressure of 445 kPa on the feed side and 100 kPa on the permeate side. In order to achieve a fair comparison, the performance of the Type A-B1-F and Type A-B2-F membranes will be compared to the initial cycles that the Batch 1 and Batch 2 Pd-Cu membranes completed between 50 and 450 °C as the surface modified membranes were not cycled between 250 and 700 °C.

Figure 4.46 shows the first three cycles for the Type A-B1-F membrane. The Type A-B1-F membrane begins hydrogen permeation during the first cycle at 350 °C whereas the as-received Batch 1 Pd-Cu membrane commenced permeation at 410 °C as shown in

Figure 4.14. Compared to the Batch 1 Pd-Cu membrane, the second and third cycles for the Type A-B1-F membrane begin at much lower temperatures, 250 and 220 °C, respectively. In addition, both the second and third cycles have permeability values that vary similarly with temperature. Remarkably, the Type A-B1-F membrane achieves a maximum hydrogen permeability of 1.05×10^{-8} mol m^{-1} s^{-1} $Pa^{-0.5}$ at 450 °C during the third cycle which is almost double that achieved by the Batch 1 Pd-Cu membrane at the same temperature and cycle.

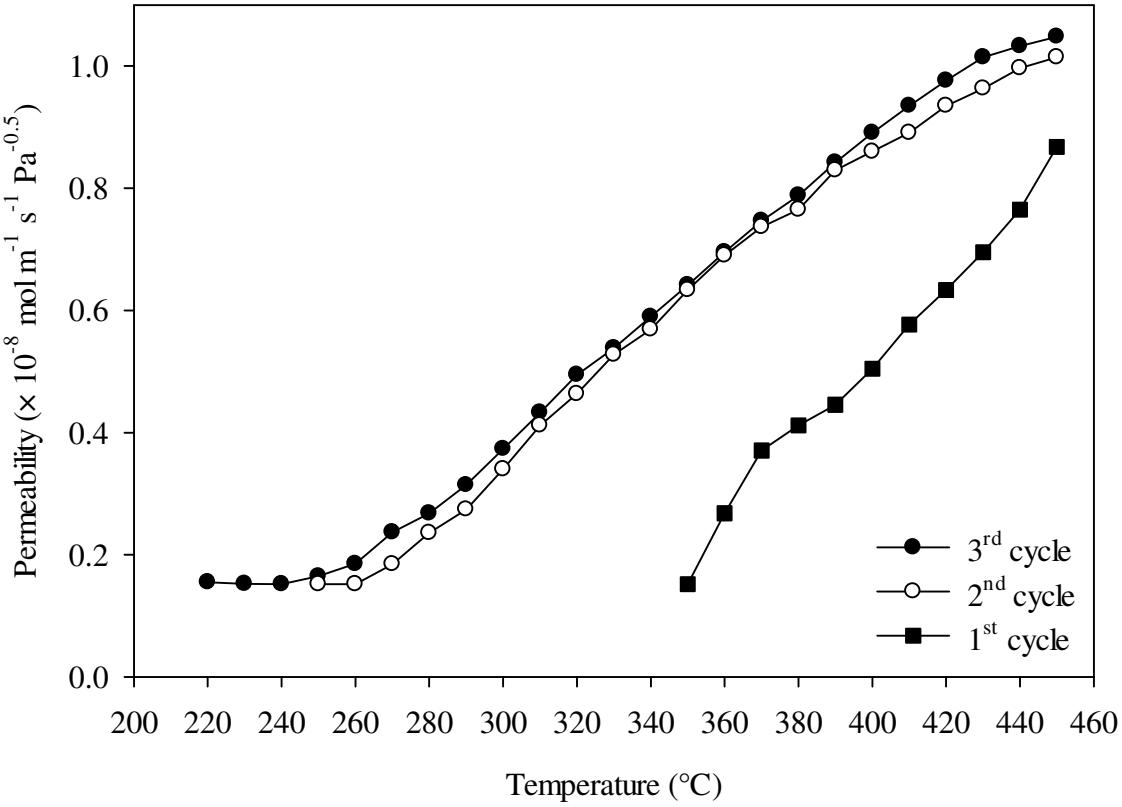

Figure 4.46 Hydrogen permeability as a function of temperature for the Type A-B1-F membrane. The plot shows the first three cycles heated between 50 and 450 °C using a hydrogen feed pressure of 445 kPa and permeate pressure of 100 kPa assuming an *n*-value of 0.5.

Routine *n*-value measurements were conducted on the Type A-B1-F membrane to determine whether the Pd thin film positioned on the feed side affects the partial pressure exponent. The data in Figure 4.47 is constrained to an *n*-value of 0.5; however, the best fit value was

calculated to be 0.55 as shown in Figure 4.48. This is a slight reduction from the *n*-value of 0.58 obtained for the Batch 1 Pd-Cu membrane.

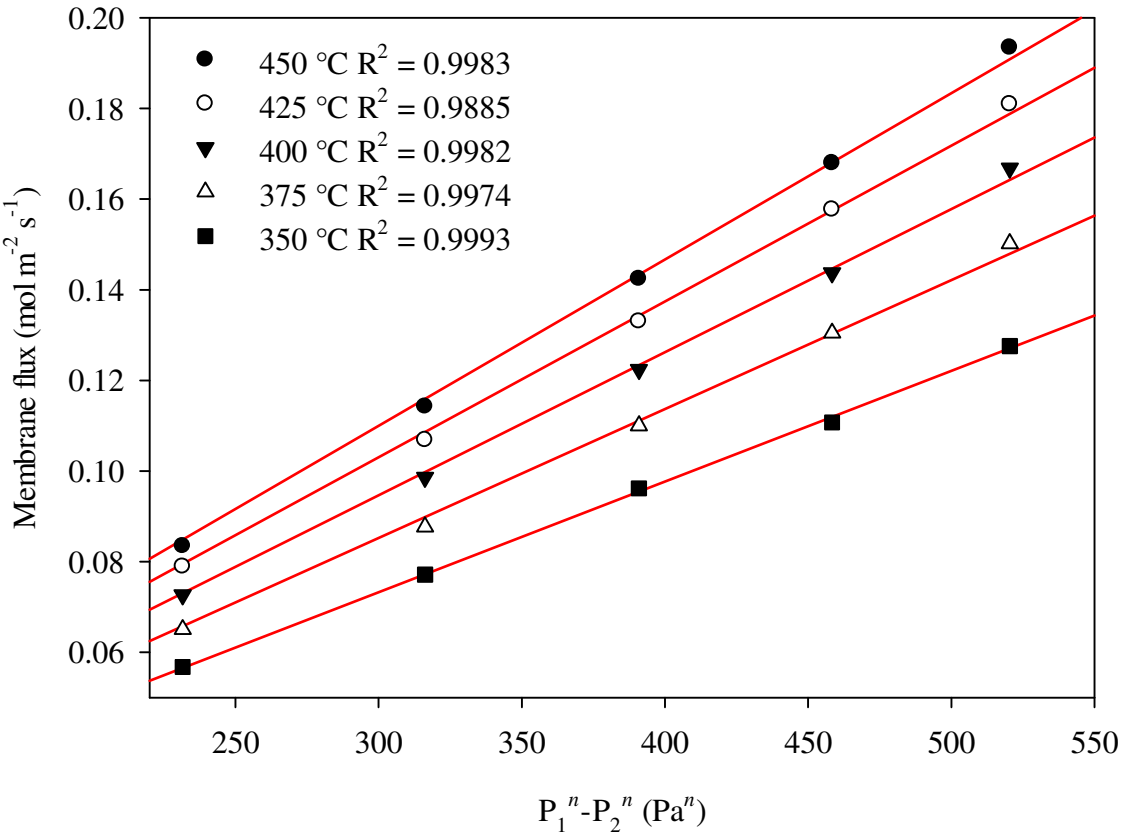

Figure 4.47 Membrane flux as a function of hydrogen differential pressure with *n* constrained to 0.5.

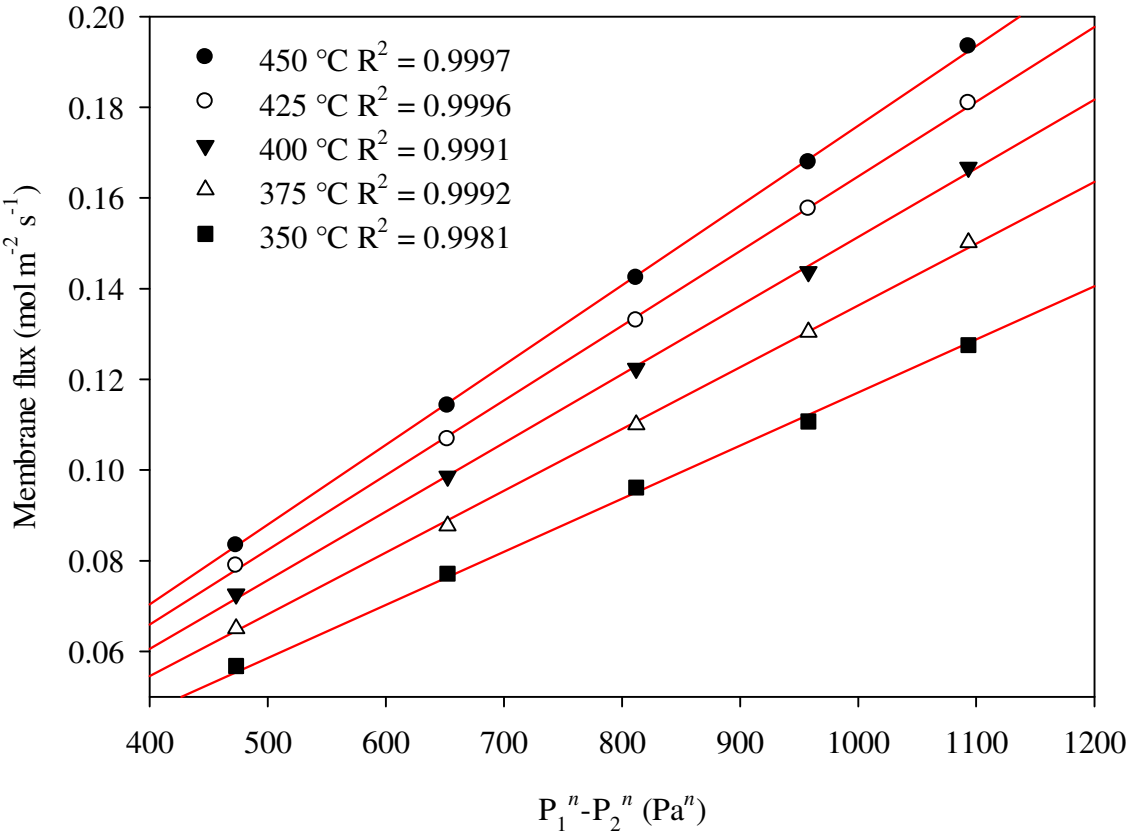

Figure 4.48 Membrane flux as a function of hydrogen differential pressure with *n* constrained to the best fit value of 0.55.

Figure 4.49 depicts the third cycle completed by the Type A-B1-F membrane with the solid symbol curve determined with the *n*-value constrained to 0.5 and the open symbol curve calculated using the best fit *n*-value of 0.55 for comparison.

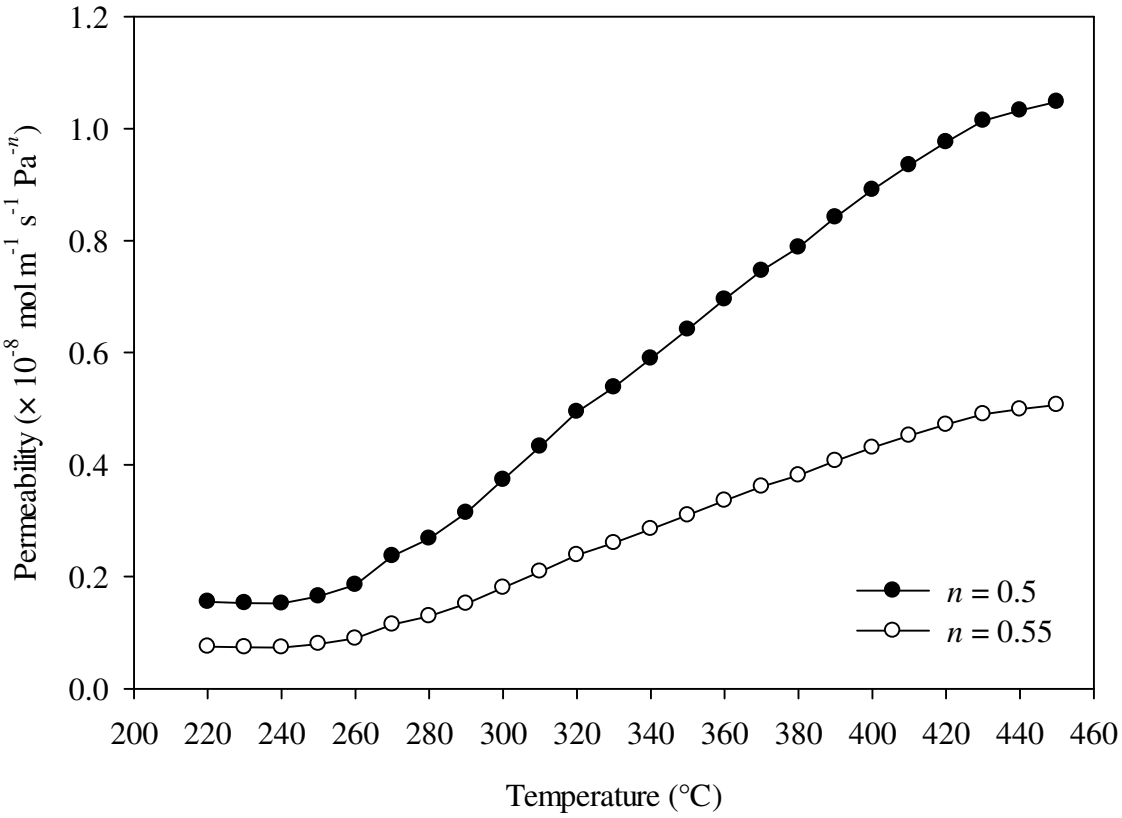

Figure 4.49 Hydrogen permeability as a function of temperature showing the third cycle for the Type A-B1-F membrane. A hydrogen feed pressure of 445 kPa and permeate pressure of 100 kPa was applied during measurements. The solid symbol curve was calculated using an *n*-value of 0.5 whereas the open symbol curve uses the best fit *n*-value of 0.55.

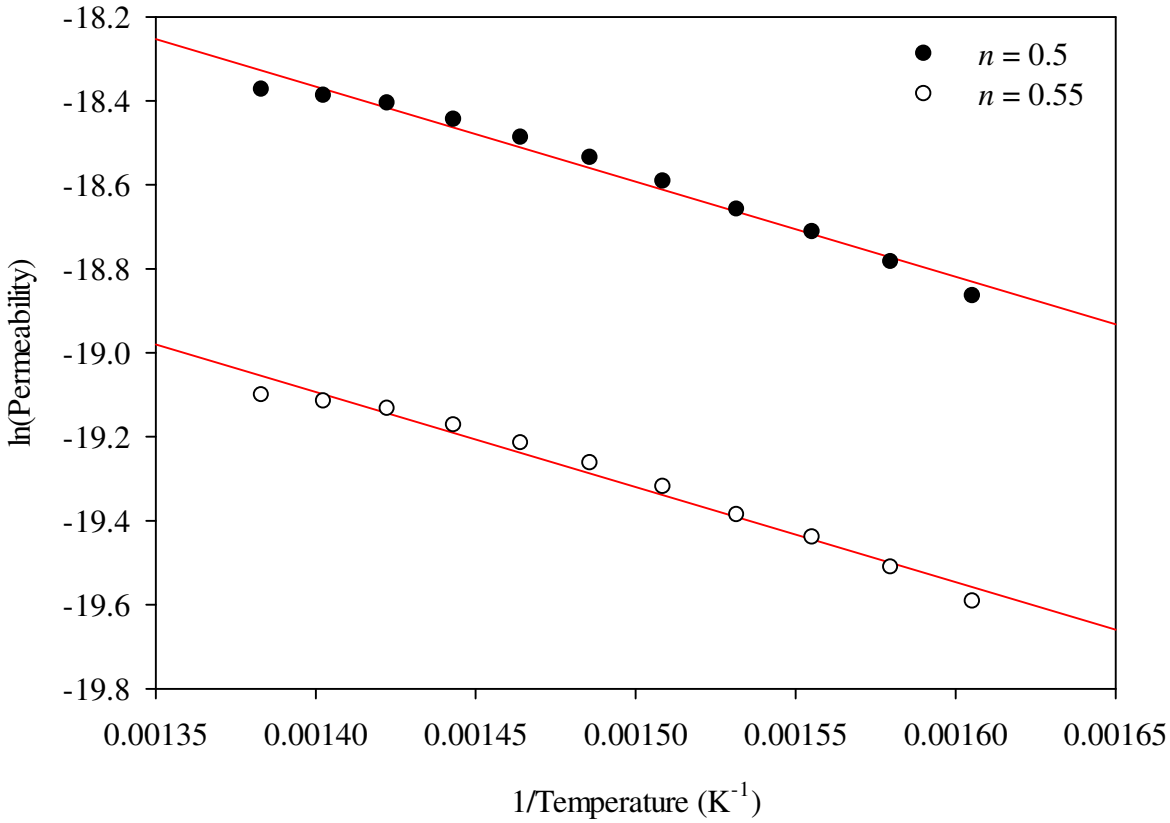

Figure 4.50 Arrhenius plot of the hydrogen permeability data shown in Figure 4.49 between 350 and 450 °C. The solid symbol curve was calculated using an *n*-value of 0.5 whereas the open symbol curve uses the best fit *n*-value of 0.55.

From Figure 4.50, the following general permeability formulae (350 – 450 °C) were derived for the Type A-B1-F membrane using an *n*-value of 0.5 and the best fit value of 0.55 as shown in Equation 4.14 and Equation 4.15, respectively.

$$\Phi_{n=0.5} = 2.15 \times 10^{-7} exp\left(\frac{-17.93 \times 10^{3}}{RT}\right) \qquad \text{Equation 4.14}$$

$$\Phi_{n=0.55} = 1.04 \times 10^{-7} exp\left(\frac{-17.93 \times 10^{3}}{RT}\right) \qquad \text{Equation 4.15}$$

In comparison to the general permeability formulae obtained for the Batch 1 Pd-Cu membrane (Equation 4.6 and Equation 4.7), the E_Φ has decreased almost a factor of three from 51.09 to

17.93 kJ mol^{-1} as result of positioning the Pd thin film on the feed side during MPR testing. Figure 4.51 demonstrates the variation of the *n*-value for the Type A-B1-F membrane with temperature. The largest increase happens at 375 °C achieving an *n*-value of 0.58 with a minor decrease to an *n*-value of 0.55 after which a steady rise occurs to an approximate *n*-value of 0.57. In comparison, Figure 4.19 shows that the Batch 1 Pd-Cu membrane undergoes a much more drastic increase with temperature achieving an *n*-value of 0.65 at 450 °C.

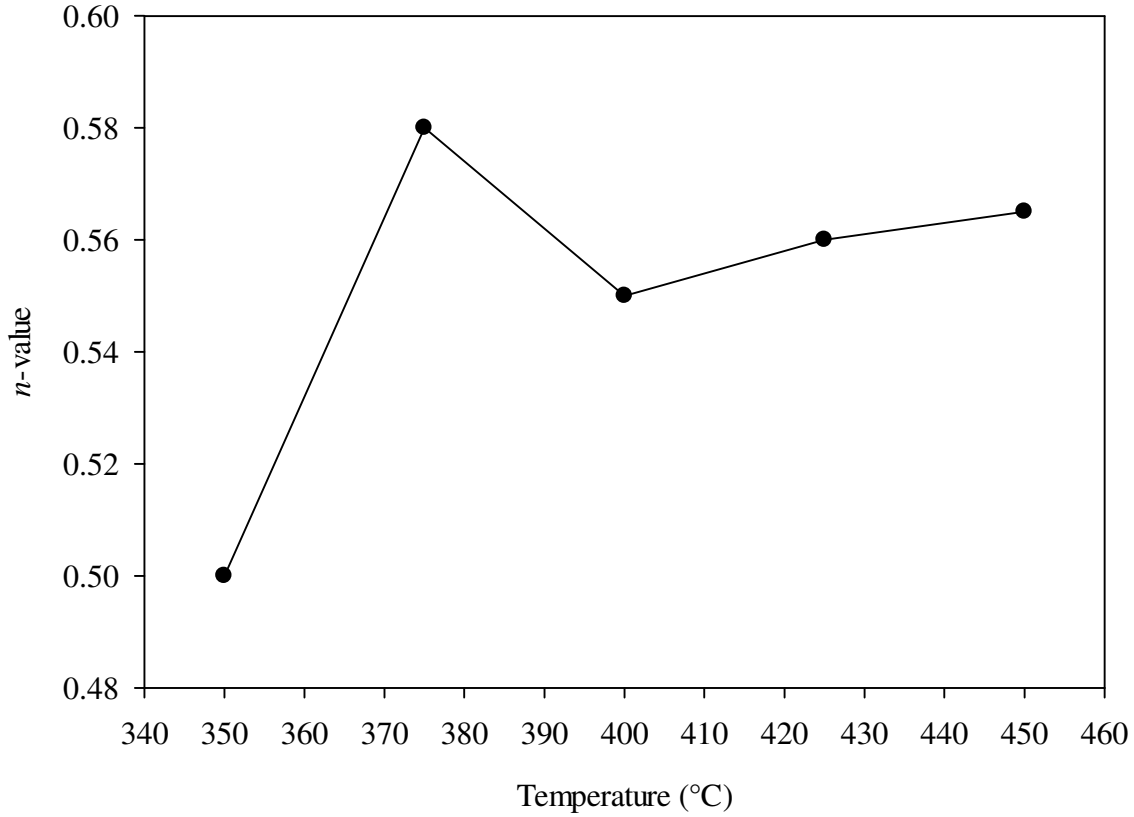

Figure 4.51 Variation of *n*-value as a function of temperature for the Type A-B1-F membrane.

Figure 4.52 demonstrates the first three cycles completed by the Type A-B2-F membrane. The first cycle completed by the Type A-B2-F membrane commences hydrogen permeation at 380 °C compared to the Batch 2 Pd-Cu membranes that started hydrogen permeation at 400 °C during the first cycle (Figure 4.25). The second and third cycles completed by the

Type A-B2-F membrane began hydrogen permeation at 270 and 260 °C, respectively. These temperatures are much lower than those demonstrated by the Batch 2 Pd-Cu membranes which began hydrogen permeation during the second and third cycle at 330 and 320 °C.

Moreover, the hydrogen permeability of the Type A-B2-F membrane varies similarly with temperature during the second and third cycle. The hydrogen permeability measured for the Type A-B2-F membrane at 450 °C during the third cycle is 8.82×10^{-9} mol m^{-1} s^{-1} Pa$^{-0.5}$ which is a 29% increase on the average value of $(6.86 \pm 0.6) \times 10^{-9}$ mol m^{-1} s^{-1} Pa$^{-0.5}$ achieved by the Batch 2 Pd-Cu membranes at the same temperature and cycle.

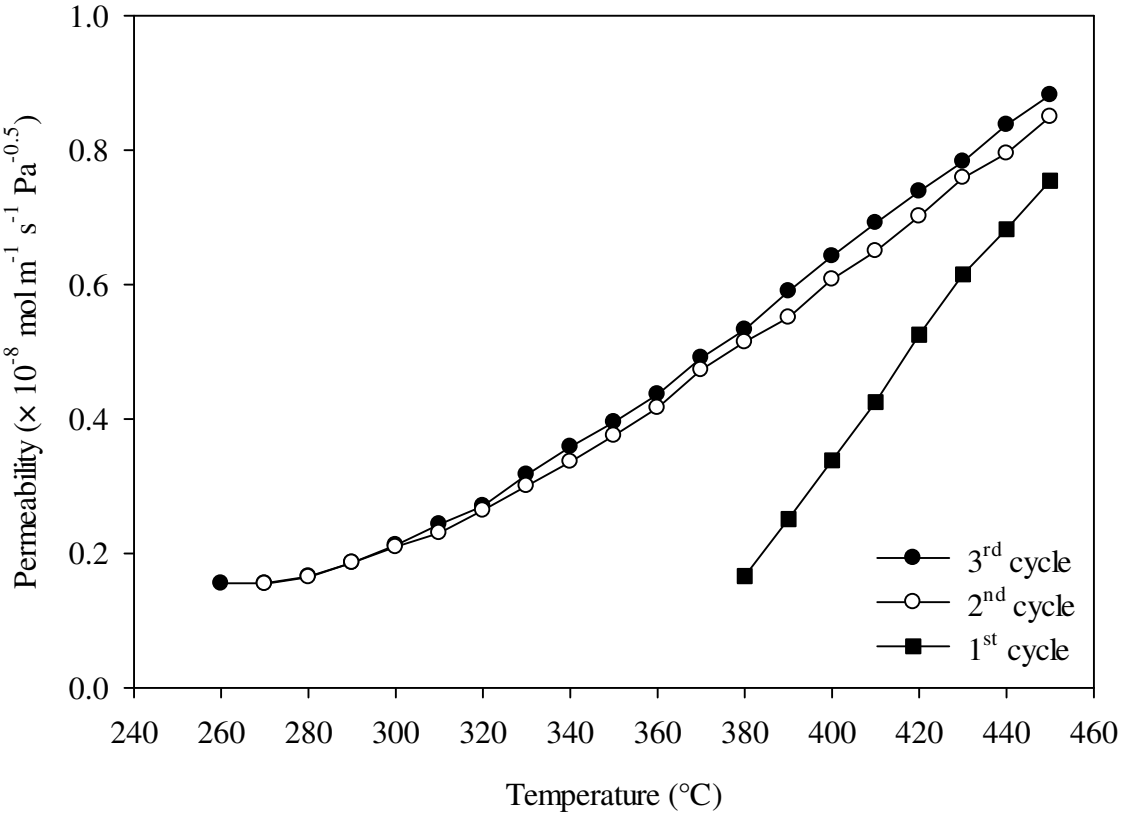

Figure 4.52 Hydrogen permeability as a function of temperature for the Type A-B2-F membrane. The plot shows the first three cycles heated between 50 and 450 °C using a hydrogen feed pressure of 445 kPa and permeate pressure of 100 kPa assuming an *n*-value of 0.5.

The results of the *n*-value measurements for the Type A-B2-F membrane are shown in Figure 4.53 with the data constrained to 0.5. As shown in Figure 4.54, the best fit *n*-value is 0.58 for the Type A-B2-F membrane.

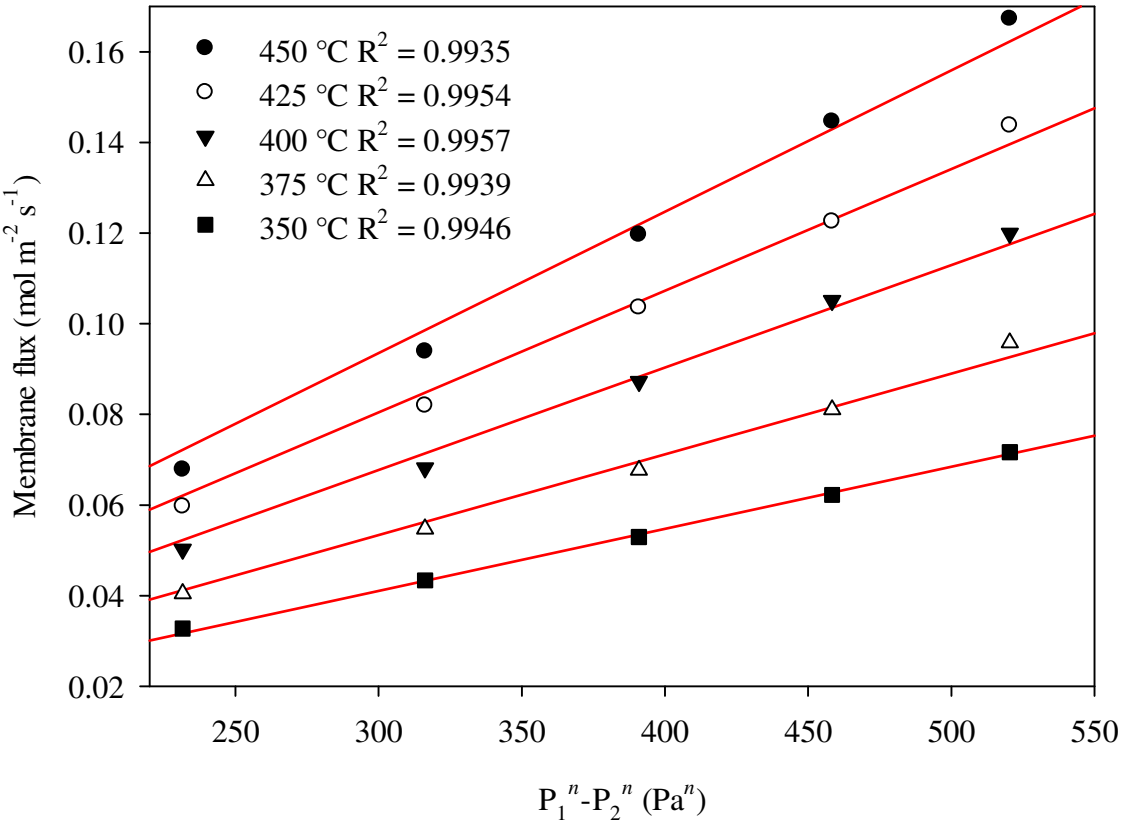

Figure 4.53 Membrane flux as a function of hydrogen differential pressure with *n* constrained to 0.5.

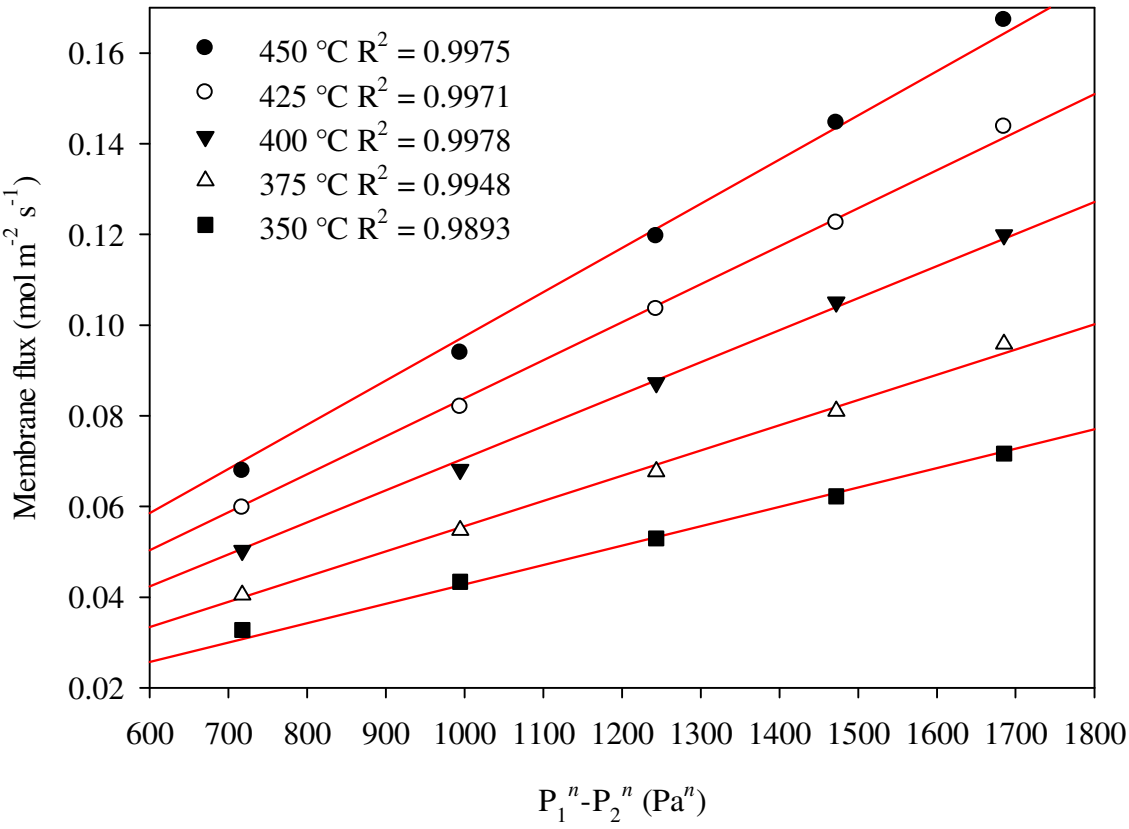

Figure 4.54 Membrane flux as a function of hydrogen differential pressure with *n* constrained to the best fit value of 0.58.

The third cycle completed by the Type A-B2-F membrane is shown in Figure 4.55 calculated using an *n*-value of 0.5 for the solid symbol curve and the best fit *n*-value of 0.58 for the open symbol curve. Figure 4.49 and Figure 4.55 demonstrate that positioning the Pd sputter-coated surface of the Type A-B1-F membrane and Type A-B2-F membrane on the feed side during MPR testing has no observable effect on the *n*-value. However, a marked improvement is seen in the hydrogen permeability when compared to their respective as-received batch of Pd-Cu membranes.

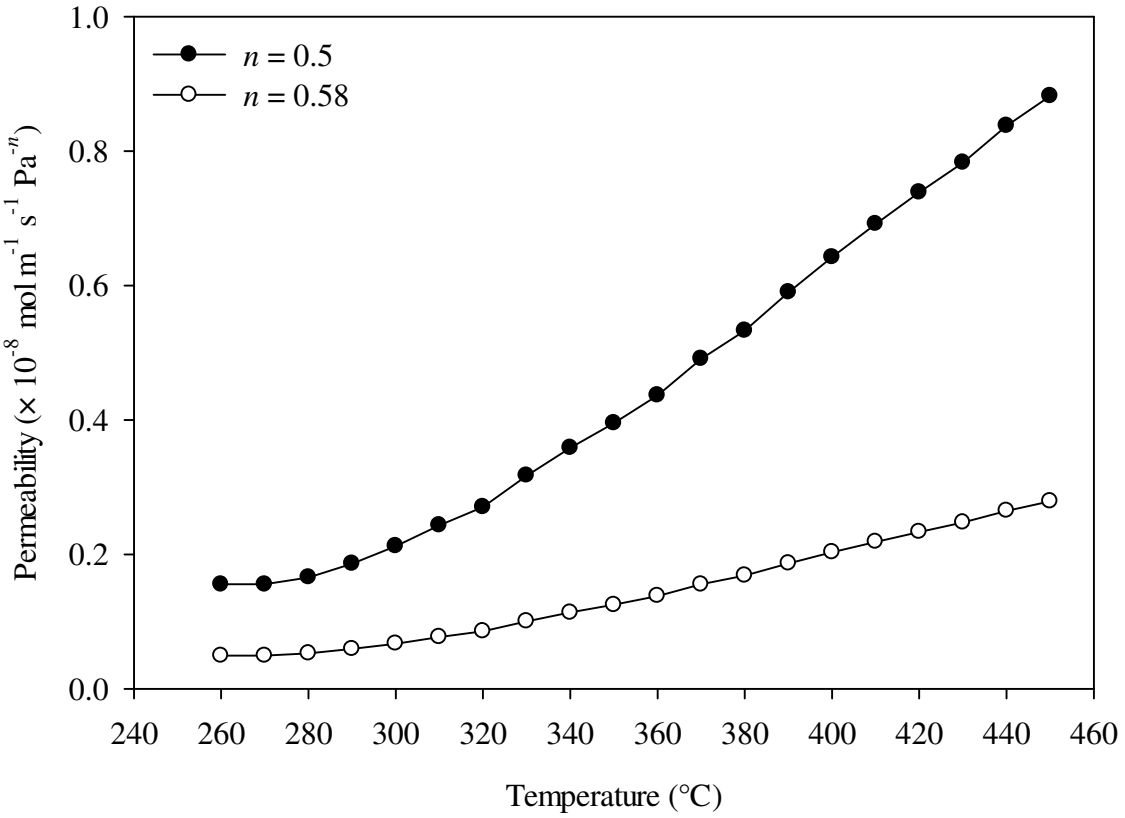

Figure 4.55 Hydrogen permeability as a function of temperature showing the third cycle for the Type A-B2-F membrane. A hydrogen feed pressure of 445 kPa and permeate pressure of 100 kPa was applied during measurements. The solid symbol curve was calculated using an *n*-value of 0.5 whereas the open symbol curve uses the best fit *n*-value of 0.58.

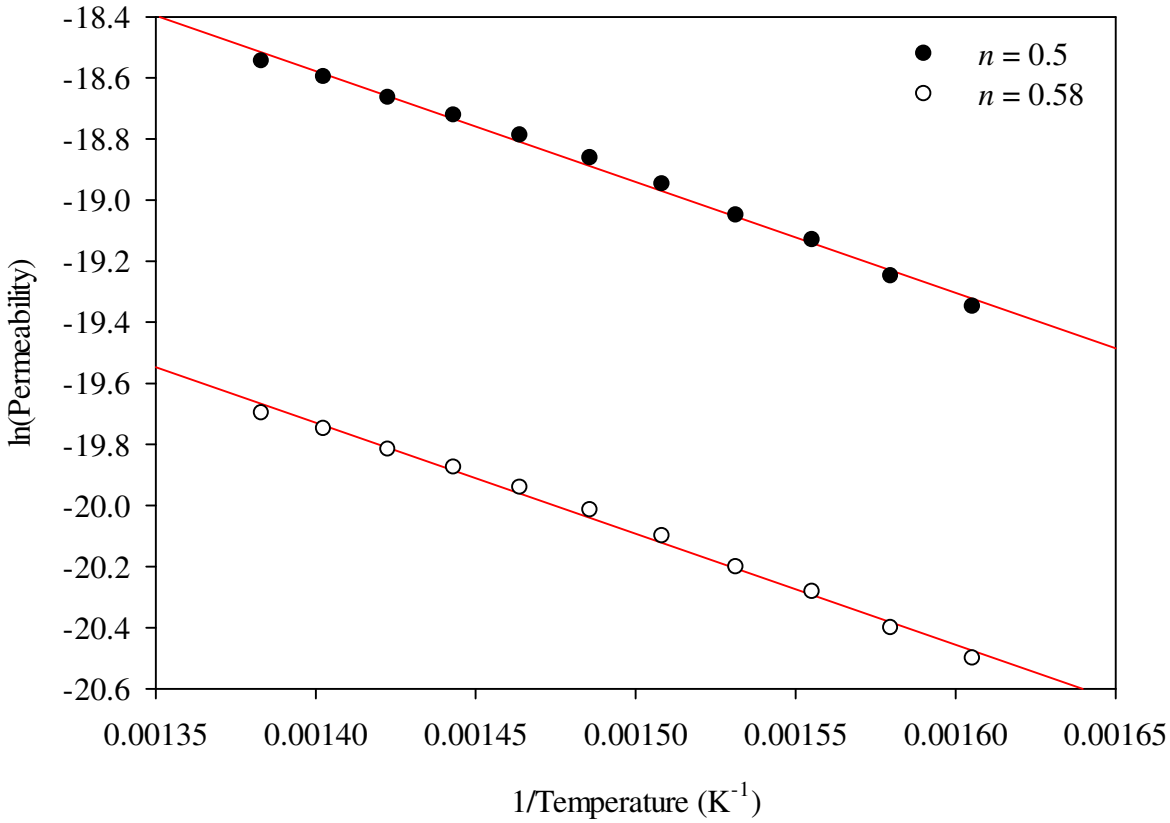

Figure 4.56 Arrhenius plot of the hydrogen permeability data shown in Figure 4.55 between 350 and 450 °C. The solid symbol curve was calculated using an *n*-value of 0.5 whereas the open symbol curve uses the best fit *n*-value of 0.58.

The following general permeability formulae (350 – 450 °C) has been derived from Figure 4.56 for the Type A-B2-F membrane using an *n*-value of 0.5 and the best fit value of 0.58 as shown in Equation 4.16 and Equation 4.17, respectively. Assuming an *n*-value of 0.5, the Pd thin film has appeared to decrease the E_Φ of the Batch 2 Pd-Cu membranes (41.67 ± 3.4 kJ mol^{-1}) to 29.95 kJ mol^{-1} as calculated for the Type A-B2-F membrane which is a 39% reduction.

$$\Phi_{n=0.5} = 1.33 \times 10^{-6} exp\left(\frac{-29.95 \times 10^3}{RT}\right) \qquad \text{Equation 4.16}$$

$$\Phi_{n=0.58} = 4.18 \times 10^{-7} exp\left(\frac{-29.93 \times 10^3}{RT}\right) \qquad \text{Equation 4.17}$$

Figure 4.57 reveals an almost linear increase in the *n*-value for the Type A-B2-F membrane across the temperature range showing a strong deviation from Sieverts' law as indicated by an *n*-value of approximately 0.66 at 450 °C.

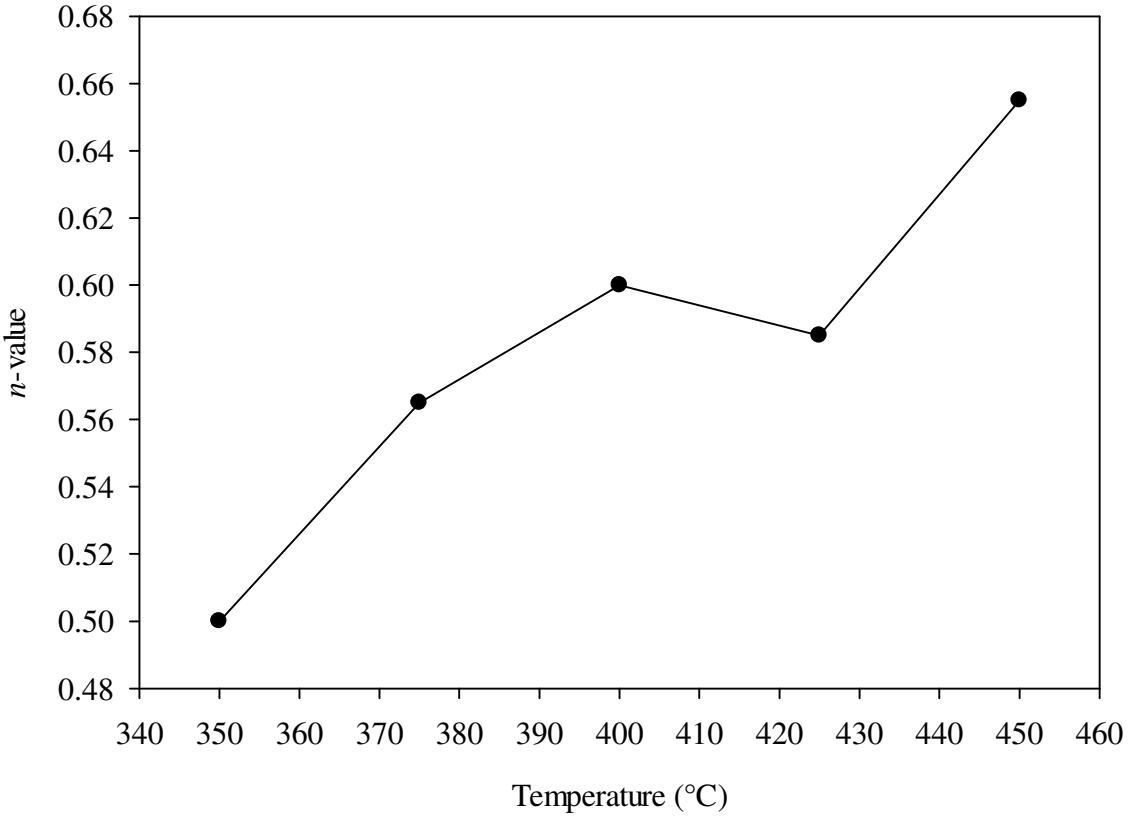

Figure 4.57 Variation of *n*-value as a function of temperature for the Type A-B2-F membrane.

4.4.2.2. Pd thin film positioned on the permeate side

A Type A-B1-P and Type A-B2-P membrane have been tested in the MPR with the Pd thin film positioned on the permeate side to investigate the effects on hydrogen permeability. Figure 4.58 depicts the first three cycles completed by the Type A-B1-P membrane. Similar to the Type A-B1-F membrane, hydrogen permeation commences in the first cycle at 350 °C, although this cycle exhibits a sharp rise in permeability compared to the subsequent cycles. This may be attributed to the temporary inability of the back-pressure regulator to accurately control the permeate pressure. This can lead to a gradual build up of pressure on the permeate

side of the membrane that could have been released over the remaining course of the cycle by the downstream MFC resulting in higher than normal hydrogen permeability measurements.

The second and third cycles both begin at 290 °C, which is lower than the corresponding cycles completed by the Batch 1 Pd-Cu membrane (410 and 370 °C). However, this is slightly higher than the temperatures associated with the second and third cycles completed by the Type A-B1-F which is 250 and 220 °C, respectively. The Type A-B1-P membrane achieves a hydrogen permeability of 7.45×10^{-9} mol m^{-1} s^{-1} $Pa^{-0.5}$ at 450 °C during the third cycle which is a 33% increase on the value obtained by the Batch 1 Pd-Cu membrane but a 29 % decrease on the value achieved by the Type A-B1-F membrane at the same temperature and cycle.

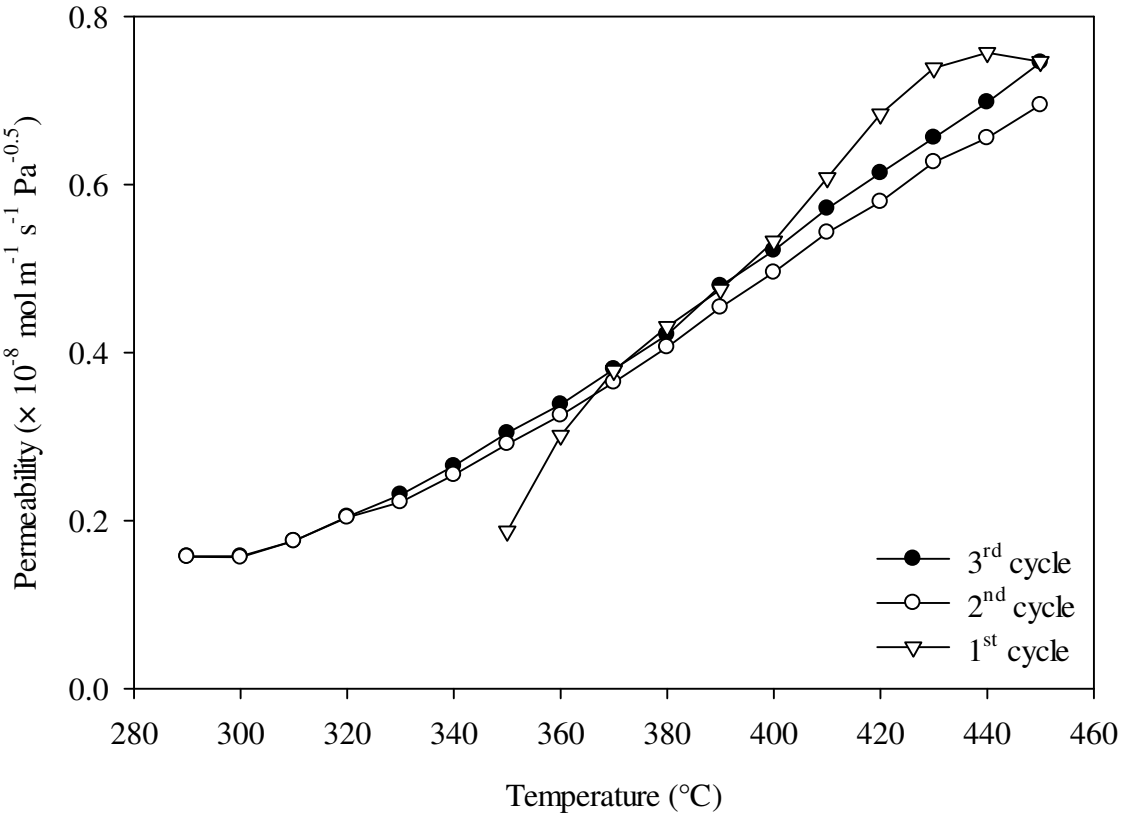

Figure 4.58 Hydrogen permeability as a function of temperature for the Type A-B1-P membrane. The plot shows the first three cycles heated between 50 and 450 °C using a hydrogen feed pressure of 445 kPa and permeate pressure of 100 kPa and assuming an *n*-value of 0.5.

The results of the *n*-value measurements for the Type A-B1-P membrane are shown in Figure 4.59 and Figure 4.60 whereby a best fit value of 0.60 was determined. The third cycle completed by the Type A-B1-P membrane is shown in Figure 4.61 where the solid symbol curve has been calculated using an *n*-value of 0.5 and the open symbol curve was computed using the best fit value of 0.60. This is a 9% increase on the *n*-value of 0.55 obtained for the Type-A-B1-F membrane, nevertheless hydrogen permeation is still limited by the diffusion process.

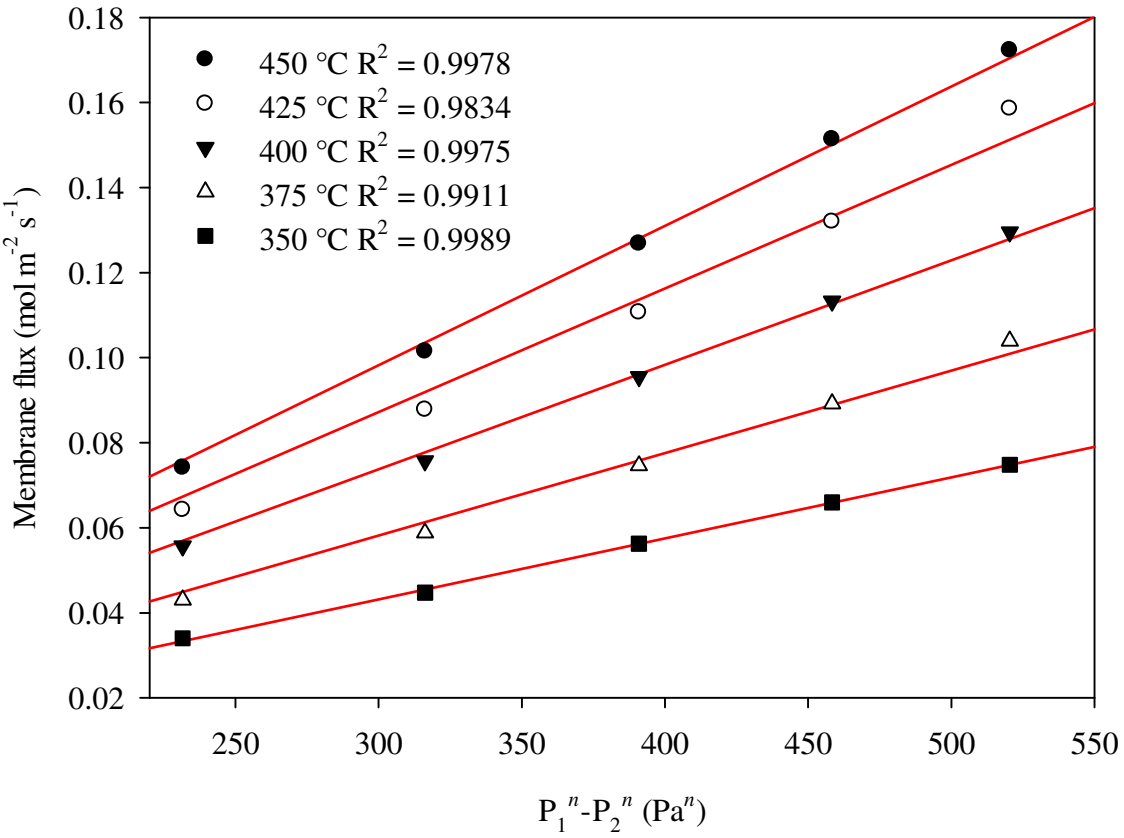

Figure 4.59 Membrane flux as a function of hydrogen differential pressure with *n* constrained to 0.5.

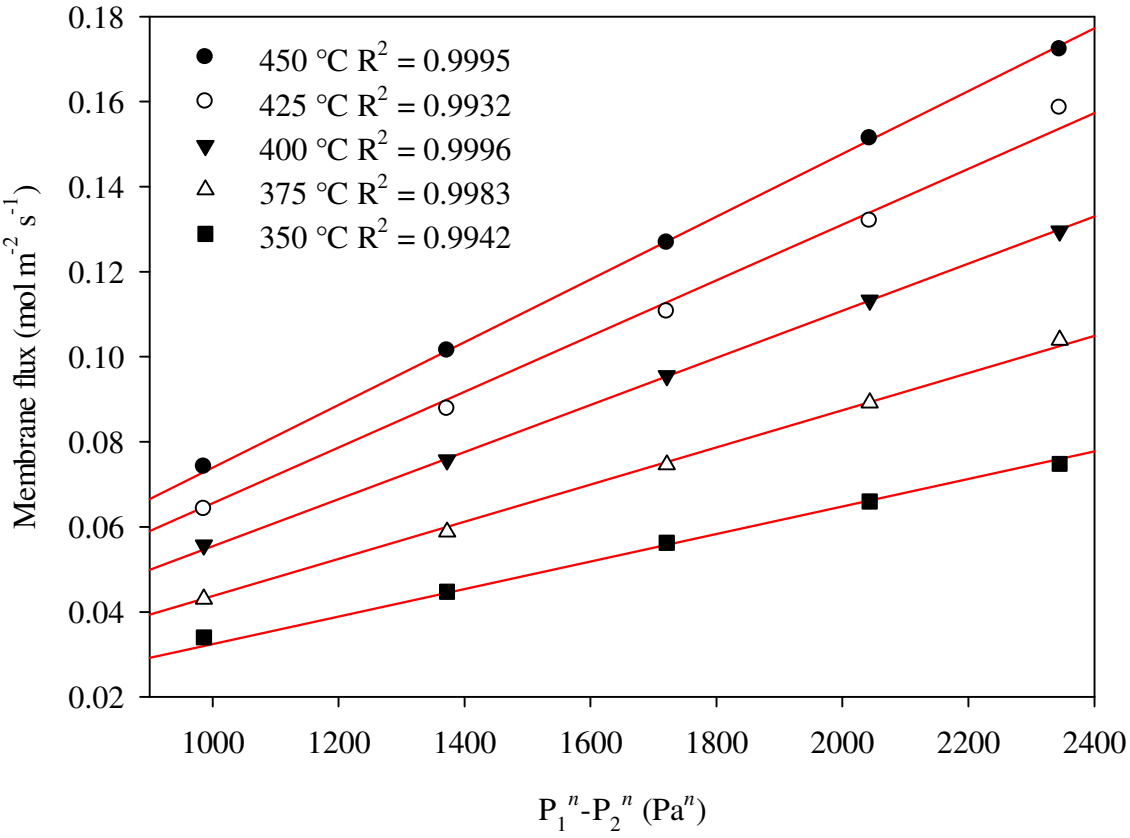

Figure 4.60 Membrane flux as a function of hydrogen differential pressure with *n* constrained to the best fit value of 0.60.

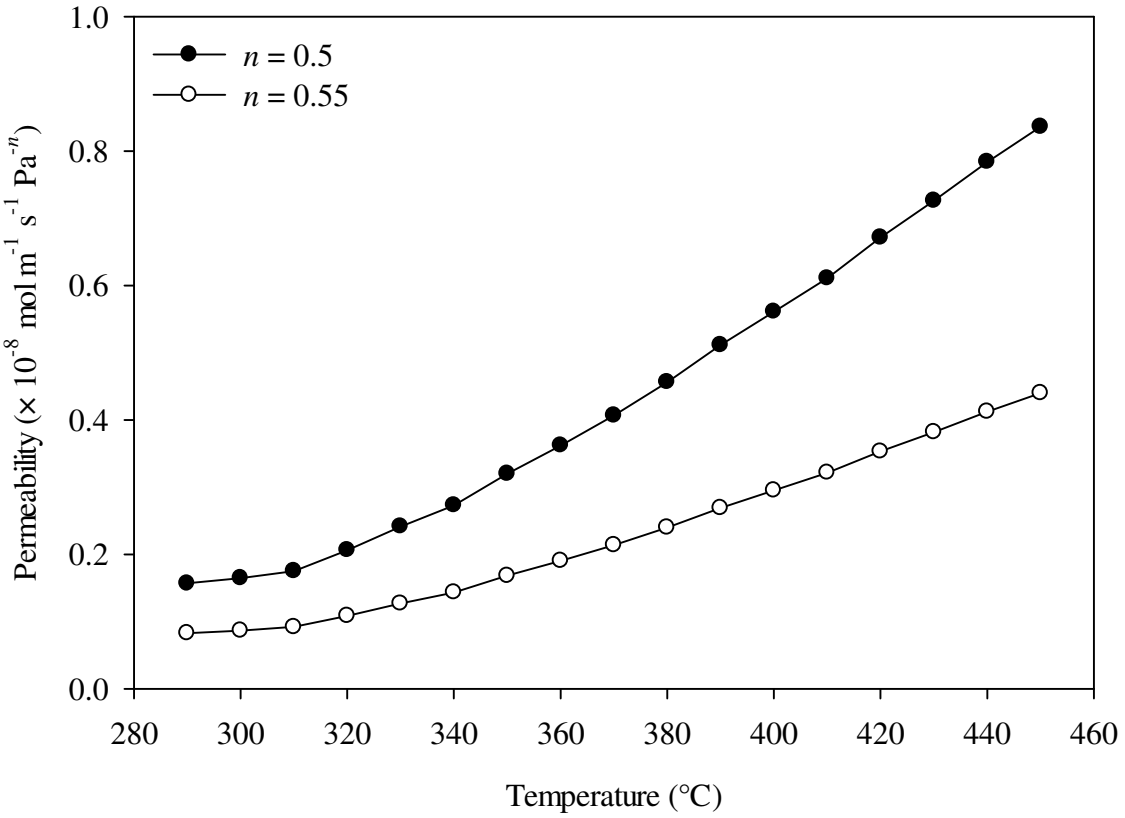

Figure 4.61 Hydrogen permeability as a function of temperature showing the third cycle for the Type A-B1-P membrane. A hydrogen feed pressure of 445 kPa and permeate pressure of 100 kPa was applied during measurements. The solid symbol curve was calculated using an *n*-value of 0.5 whereas the open symbol curve uses the best fit *n*-value of 0.60.

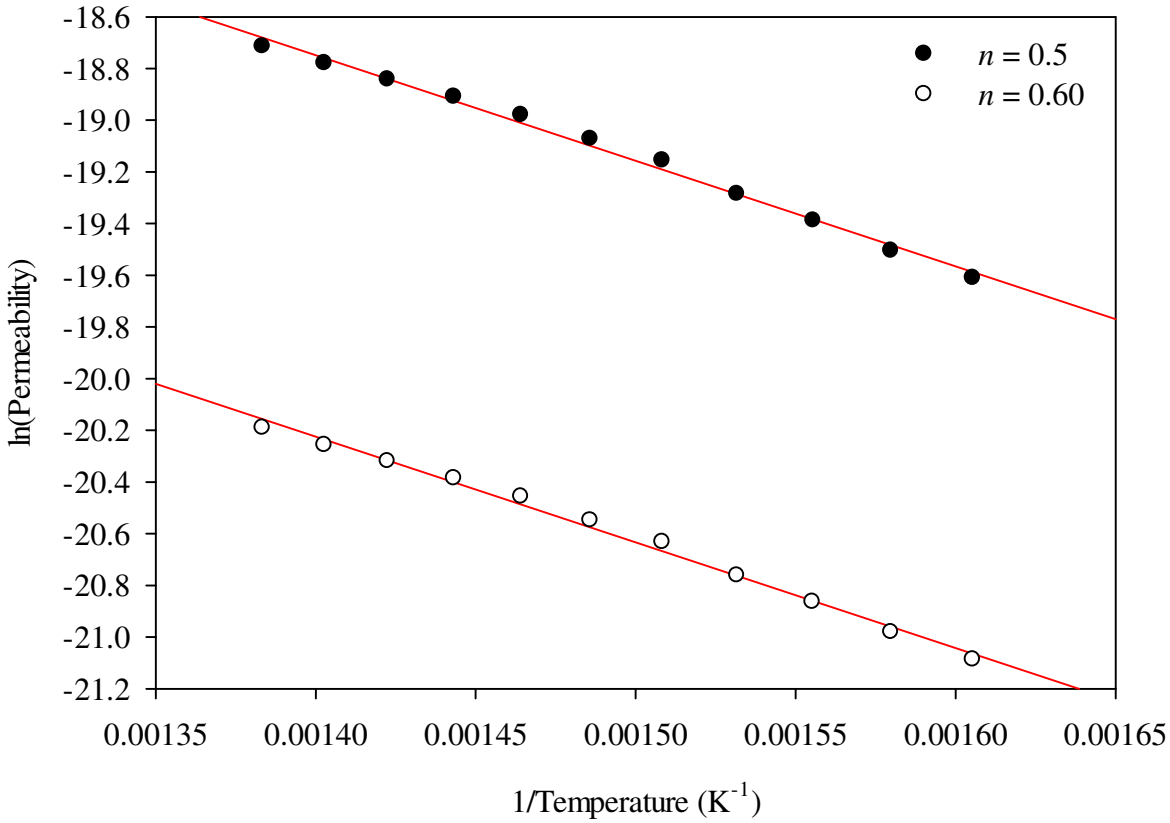

Figure 4.62 Arrhenius plot of the hydrogen permeability data shown in Figure 4.61 between 350 and 450 °C. The solid symbol curve was calculated using an *n*-value of 0.5 whereas the open symbol curve uses the best fit *n*-value of 0.60.

The general permeability formulae (350 – 450 °C) for the Type A-B1-P membrane are derived from Figure 4.62 using an *n*-value of 0.5 and the best fit value of 0.60 as shown in Equation 4.18 and Equation 4.19, respectively.

$$\Phi_{n=0.5} = 2.40 \times 10^{-6} exp\left(\frac{-34.44 \times 10^3}{RT}\right) \qquad \text{Equation 4.18}$$

$$\Phi_{n=0.60} = 5.46 \times 10^{-7} exp\left(\frac{-34.42 \times 10^3}{RT}\right) \qquad \text{Equation 4.19}$$

Assuming an *n*-value of 0.5, the E_Φ value of 34.44 kJ mol^{-1} for the Type A-B1-P membrane gives a 32% reduction on the value obtained for the Batch 1 Pd-Cu membrane, however this

value is almost double that of the value calculated for the Type A-B1-F membrane (17.93 kJ mol^{-1}).

A wide fluctuation in the *n*-value can be observed in Figure 4.63 for the Type A-B1-P membrane reaching a maximum value of approximately 0.71 at 425 °C, which is the largest deviation from Sieverts' law measured yet. The general trend is shown to be an increase in *n*-value over the experimental temperature range. The Type A-B1-F membrane showed a steadier rise in its *n*-value but only ever reaching a maximum of 0.58.

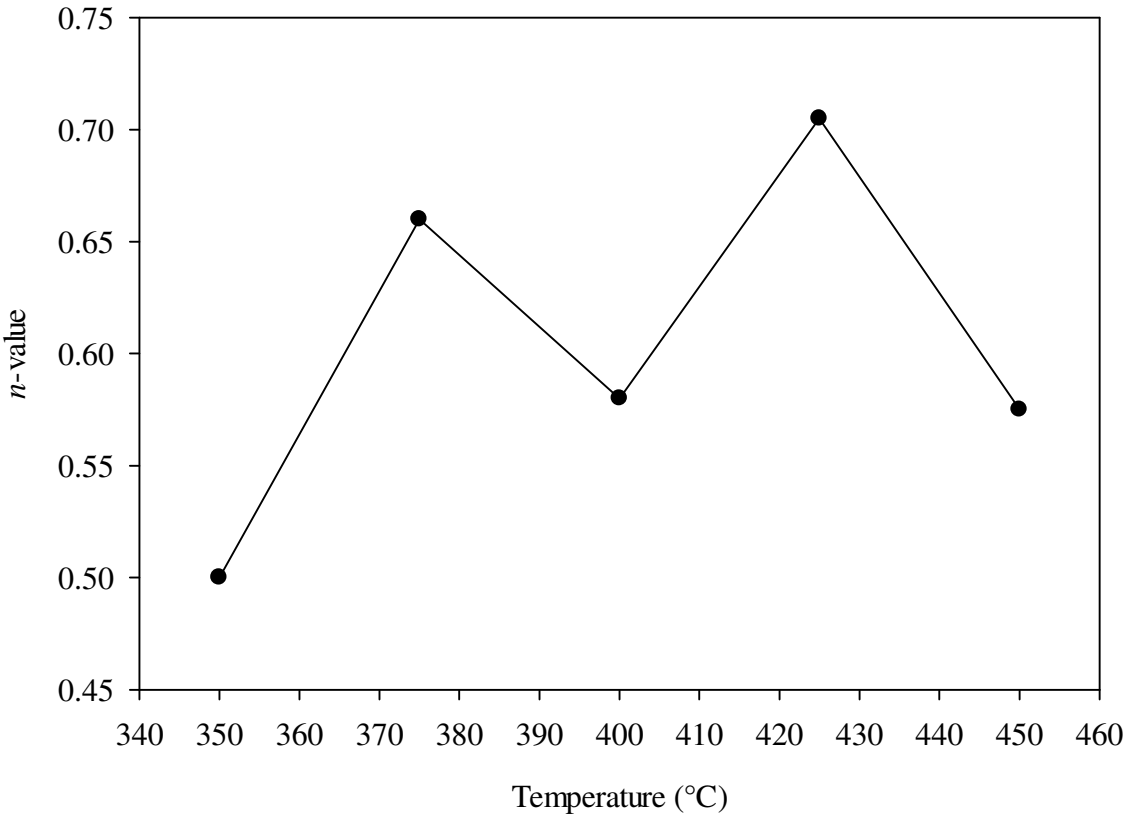

Figure 4.63 Variation of *n*-value as a function of temperature for the Type A-B1-P membrane.

Figure 4.64 illustrates the first three cycles completed by the Type A-B2-P membrane. The first cycle starts at 360 °C which is slightly lower than the hydrogen permeation start temperature of 380 °C for the Type A-B2-F membrane. The second and third cycles begin hydrogen permeation at 290 °C which is comparable to the corresponding cycles for the

Type A-B2-F membrane. Furthermore, this temperature is lower than the hydrogen permeation start temperature of 330 and 320 °C for the second and third cycles, respectively, associated with the Batch 2 Pd-Cu membranes. The Type A-B2-P membrane achieves a hydrogen permeability of 8.36×10^{-9} mol m^{-1} s^{-1} $Pa^{-0.5}$ at 450 °C during the third cycle which is 22% higher than the hydrogen permeability measured for the Batch 2 Pd-Cu membranes at the same temperature and cycle. Moreover, this figure is 5% lower than that measured for the Type A-B2-F membrane at the same temperature and cycle.

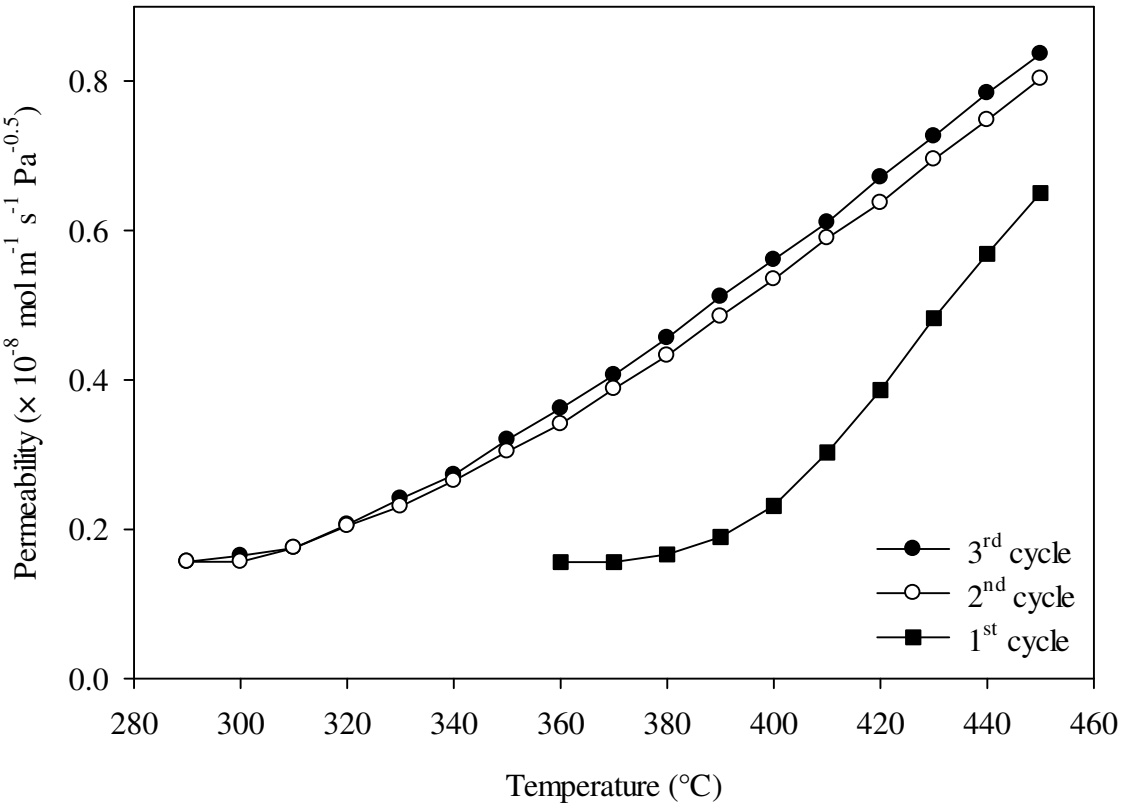

Figure 4.64 Hydrogen permeability as a function of temperature for the Type A-B2-P membrane. The plot shows the first three cycles heated between 50 and 450 °C using a hydrogen feed pressure of 445 kPa and permeate pressure of 100 kPa assuming an *n*-value of 0.5.

The data for the *n*-value measurements obtained for the Type A-B2-P membrane is displayed in Figure 4.65 and Figure 4.66. A best fit *n*-value of 0.55 was determined for the Type A-B2-P membrane which is comparable to the best fit *n*-value of 0.58 obtained for the

Type A-B2-F membrane. Figure 4.67 depicts the third cycle completed by the Type A-B2-P membrane where the solid symbol curve is calculated using an *n*-value of 0.5 and the open symbol curve is calculated using the best fit *n*-value of 0.55.

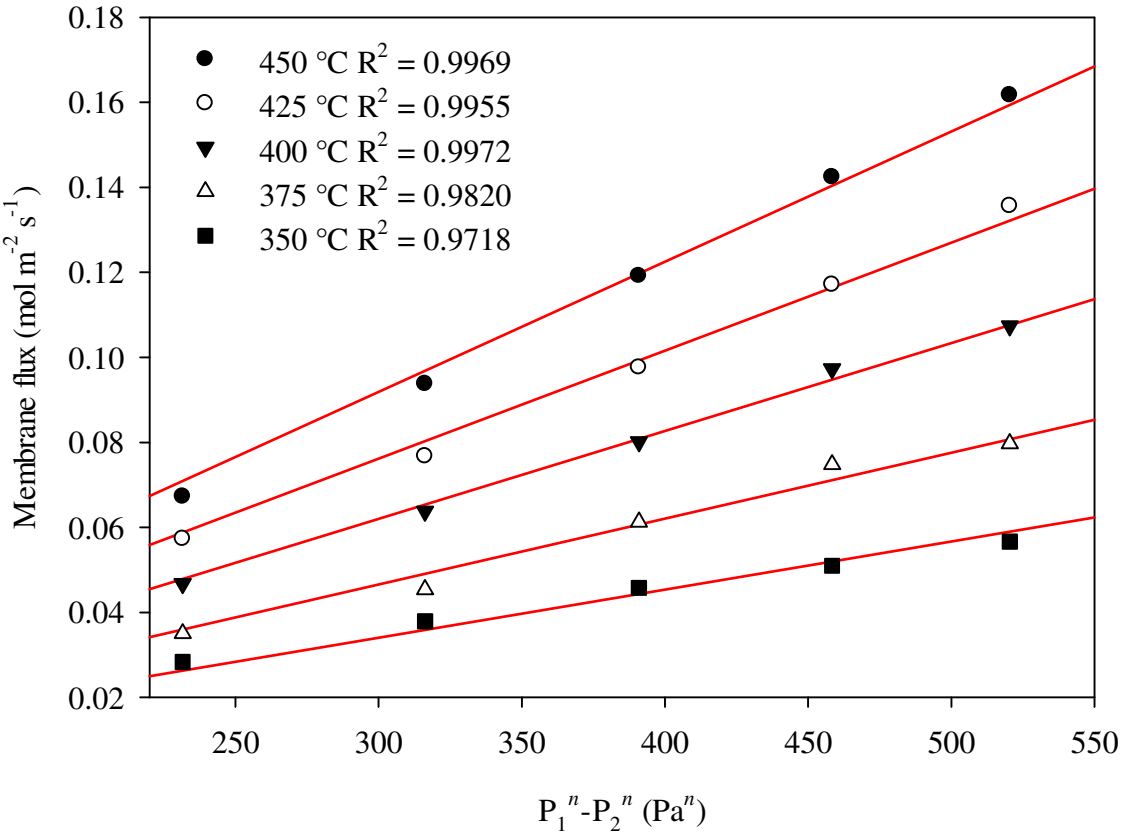

Figure 4.65 Membrane flux as a function of hydrogen differential pressure with *n* constrained to 0.5.

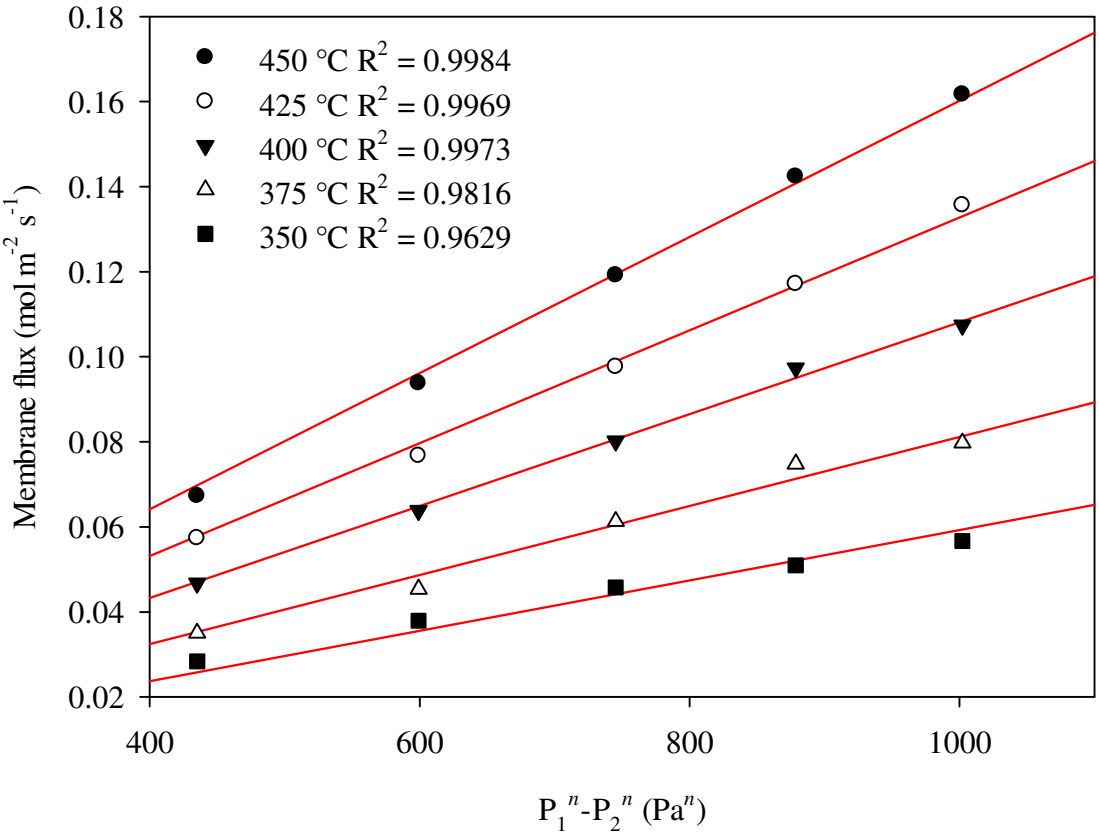

Figure 4.66 Membrane flux as a function of hydrogen differential pressure with *n* constrained to the best fit value of 0.55.

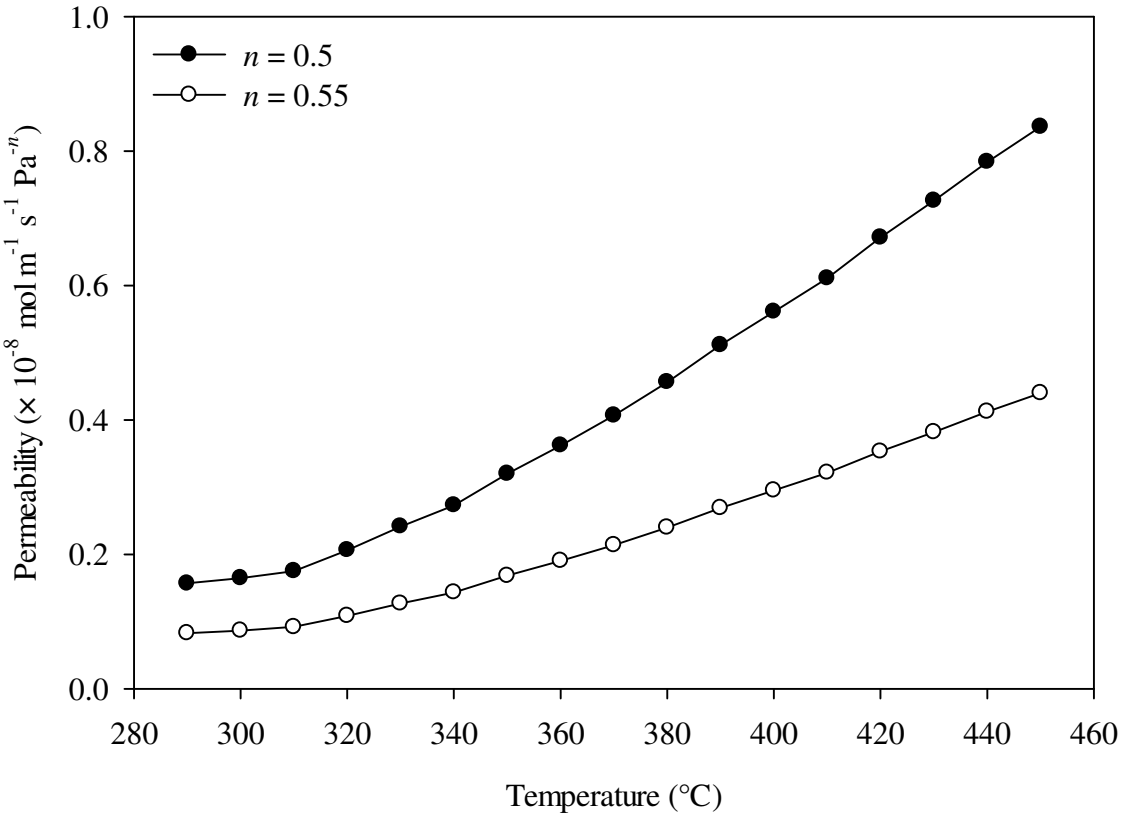

Figure 4.67 Hydrogen permeability as a function of temperature showing the third cycle for the Type A-B2-P membrane. A hydrogen feed pressure of 445 kPa and permeate pressure of 100 kPa was applied during measurements. The solid symbol curve was calculated using an *n*-value of 0.5 whereas the open symbol curve uses the best fit *n*-value of 0.55.

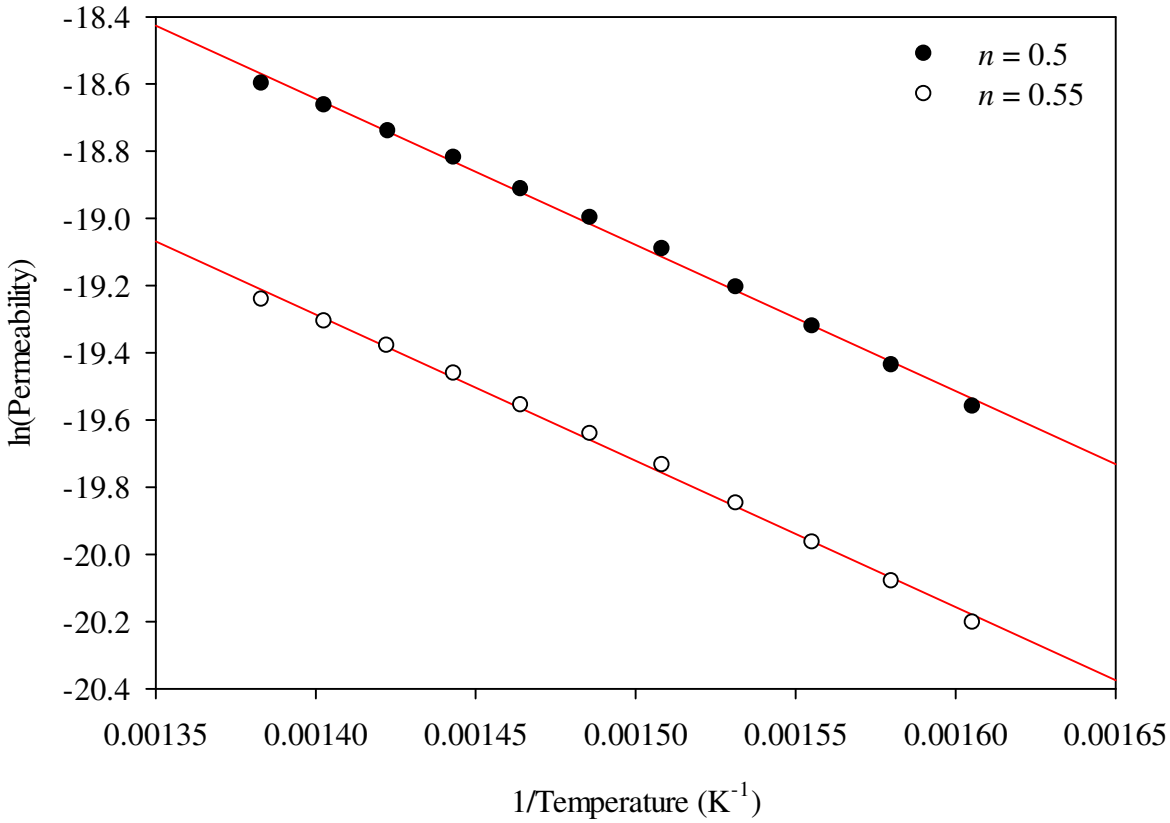

Figure 4.68 Arrhenius plot of the hydrogen permeability data shown in Figure 4.67 between 350 and 450 °C. The solid symbol curve was calculated using an *n*-value of 0.5 whereas the open symbol curve uses the best fit *n*-value of 0.55.

The general permeability formulae (350 – 450 °C) for the Type A-B2-P membrane have been derived from Figure 4.68 using an *n*-value of 0.5 and the best fit value of 0.55 as shown in Equation 4.20 and Equation 4.21, respectively.

$$\Phi_{n=0.5} = 3.69 \times 10^{-6} exp\left(\frac{-36.41 \times 10^3}{RT}\right) \qquad \text{Equation 4.20}$$

$$\Phi_{n=0.55} = 1.94 \times 10^{-6} exp\left(\frac{-36.41 \times 10^3}{RT}\right) \qquad \text{Equation 4.21}$$

The Type A-B2-P membrane has an E_Φ value of 36.41 kJ mol^{-1} and is 22% higher than the E_Φ value determined for the Type A-B2-F membrane yet is 13% lower than the E_Φ value

obtained for the Batch 2 Pd-Cu membranes. The *n*-value displays an almost linear increase with temperature reaching a maximum at approximately 0.60. The Type A-B2-F membrane exhibits a similar trend, however, it achieves a higher maximum *n*-value of 0.66.

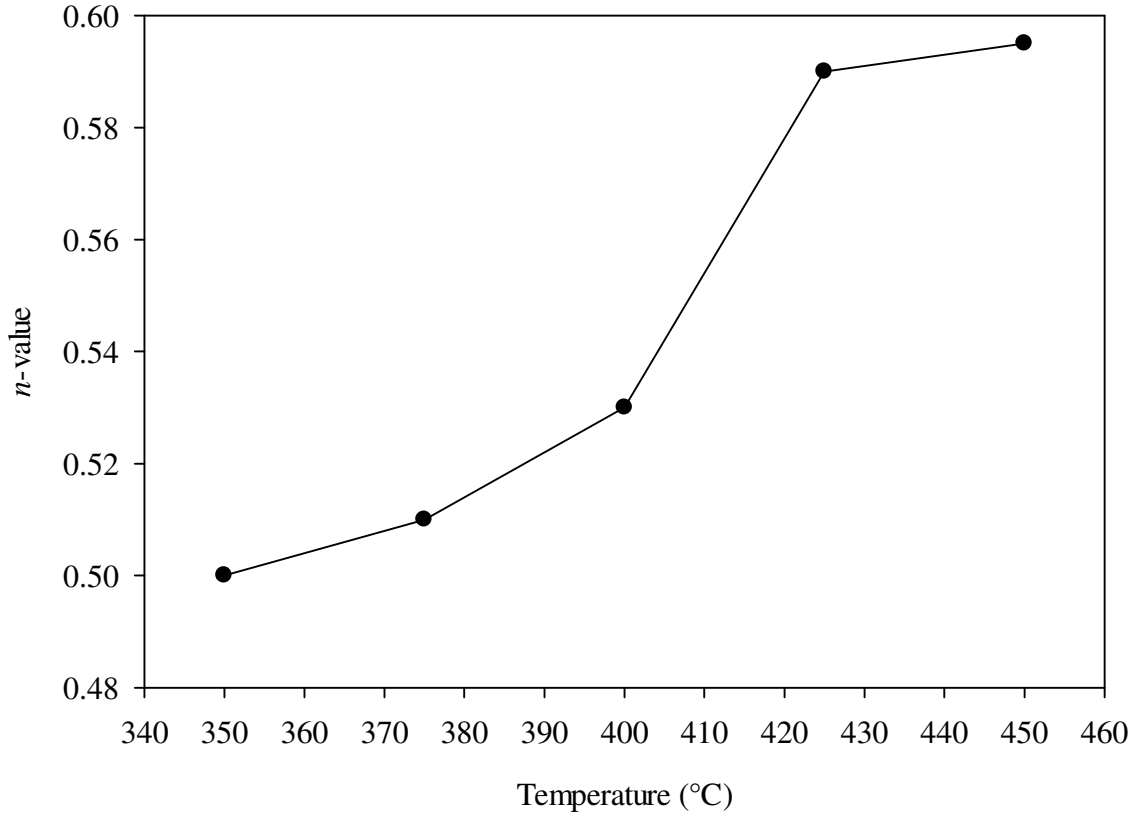

Figure 4.69 Variation of *n*-value as a function of temperature for the Type A-B2-P membrane.

It has become apparent that a 100 nm thick Pd thin film deposited onto one side of an as-received $Pd_{60}Cu_{40}$ wt% membrane has the ability to improve the hydrogen permeability. Moreover, it is found that positioning the Pd thin film on the feed side of the MPR enables the membrane to achieve a relatively higher hydrogen permeability by reducing the E_{Φ} compared to when the Pd thin film is positioned on the permeate side. An in depth discussion and explanation of these findings is made in Section 4.7.

4.4.3. Post-MPR characterisation

Following MPR testing, it was discovered that the Type A-B1/2-F/P membranes contain a mixture of the BCC and FCC phase as demonstrated in Figure 4.70 and Figure 4.72. The BCC phase originates from the bulk Pd-Cu membrane. As expected, the Pd-Cu membrane undergoes a phase change from the initial disordered FCC phase to the ordered BCC phase as a result of MPR testing. Furthermore, the remaining FCC phase belongs to the Pd thin film which had interdiffused with the bulk Pd-Cu membrane to produce a Pd-rich Pd-Cu FCC phase during MPR testing.

The composition of this newly formed phase can be determined using the method described in Section 4.3.1. Figure 4.71 shows the Pd-Cu(111) diffraction peak from Figure 4.70 in greater detail demonstrating asymmetry and therefore clear evidence of interdiffusion. The composition associated with points A to F in Figure 4.71 are displayed in Table 4.9 showing the range of compositions found on the Pd sputter-coated surface of the Type A-B1-F and Type A-B2-F membrane. The BCC phase composition on the feed side is $Pd_{60.8}Cu_{39.2}$ wt% whereas on the opposite permeate side a BCC phase composition of $Pd_{61.8}Cu_{38.2}$ wt% exists.

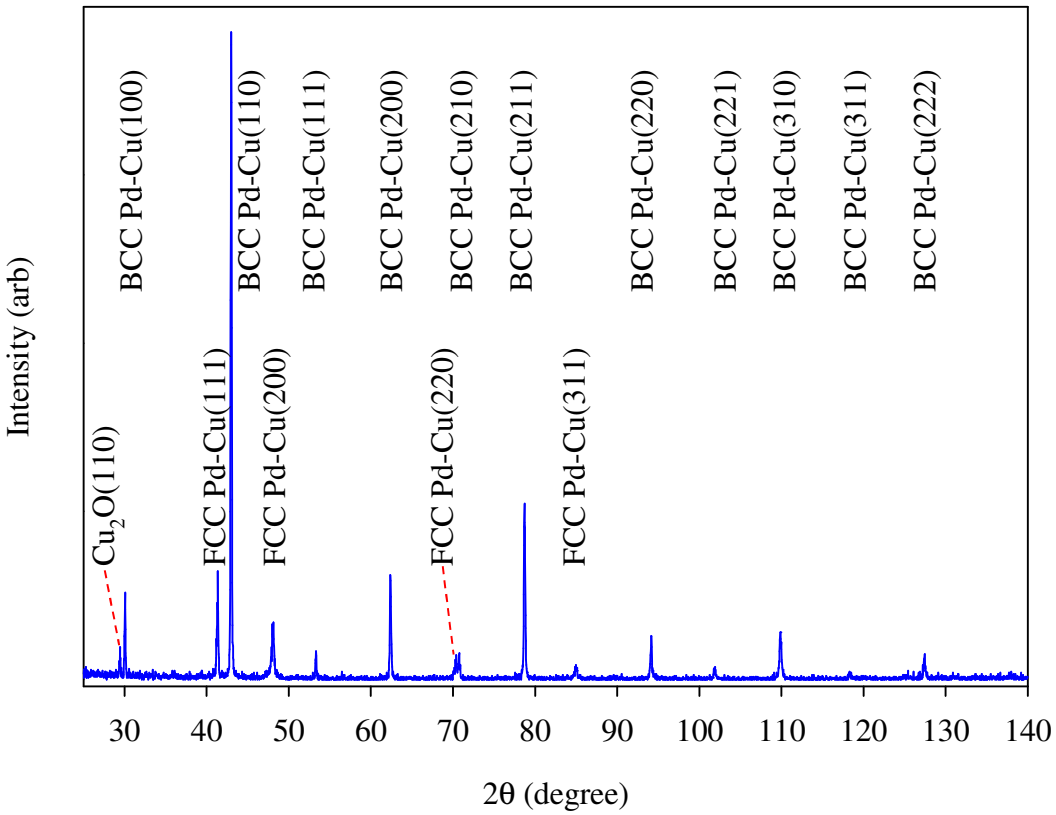

Figure 4.70 XRD pattern which is representative for the Pd sputter-coated side of a Type A-B1/2-F and Type A-B2-F membranes following MPR testing.

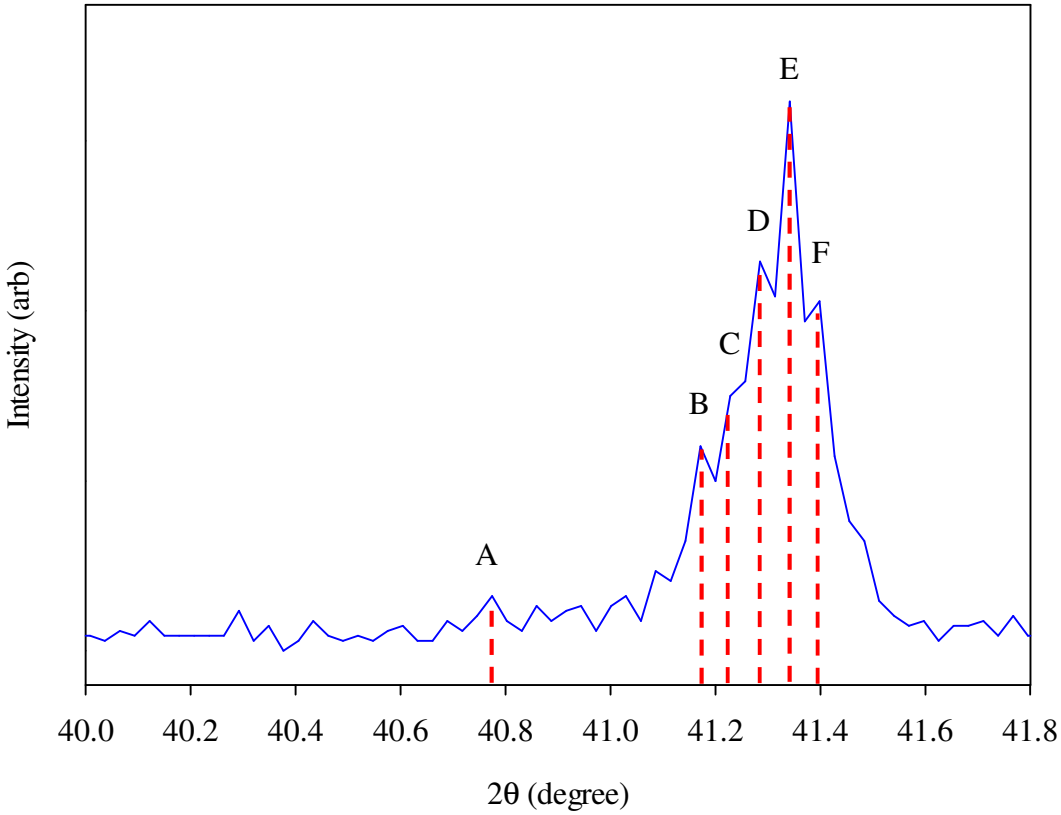

Figure 4.71 Magnification of the Pd-Cu(111) diffraction peak shown in Figure 4.70.

Table 4.9 Compositions determined for points A to F in Figure 4.71.

	Scattering angle, 2θ (degree)	Composition (wt%)
A	40.77	$Pd_{83.6}Cu_{16.4}$
B	41.17	$Pd_{73.6}Cu_{26.4}$
C	41.23	$Pd_{72.1}Cu_{27.9}$
D	41.28	$Pd_{70.5}Cu_{29.5}$
E	41.34	$Pd_{69.0}Cu_{31.0}$
F	41.40	$Pd_{67.4}Cu_{32.6}$

Similarly, Figure 4.73 shows a magnified view of the Pd-Cu(111) diffraction peak from Figure 4.72 which also shows signs of interdiffusion occurring on the Pd sputter-coated side of the Type A-B1-P and Type A-B2-P membrane. The compositions were calculated for points A to F shown in Figure 4.73 and are displayed in Table 4.10. The BCC phase composition on both sides of the membrane is $Pd_{61.7}Cu_{38.3}$ wt%.

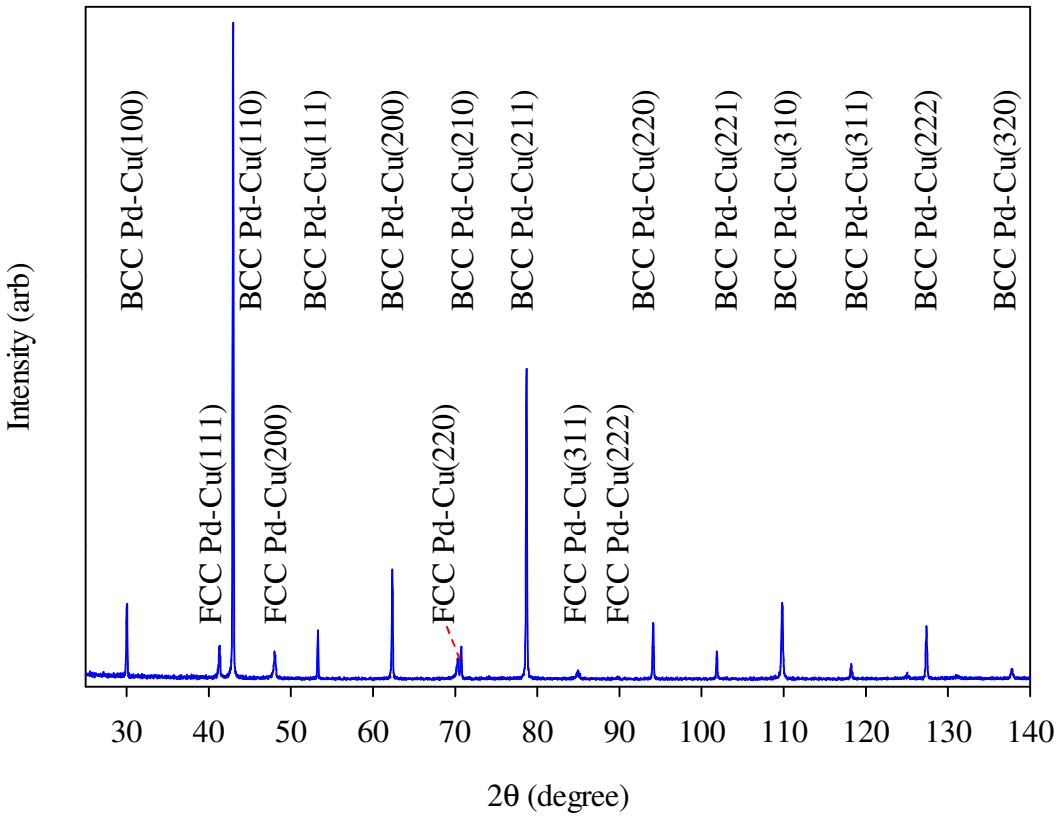

Figure 4.72 XRD pattern which is representative for the Pd sputter-coated side of the Type A-B1/2-P membranes following MPR testing.

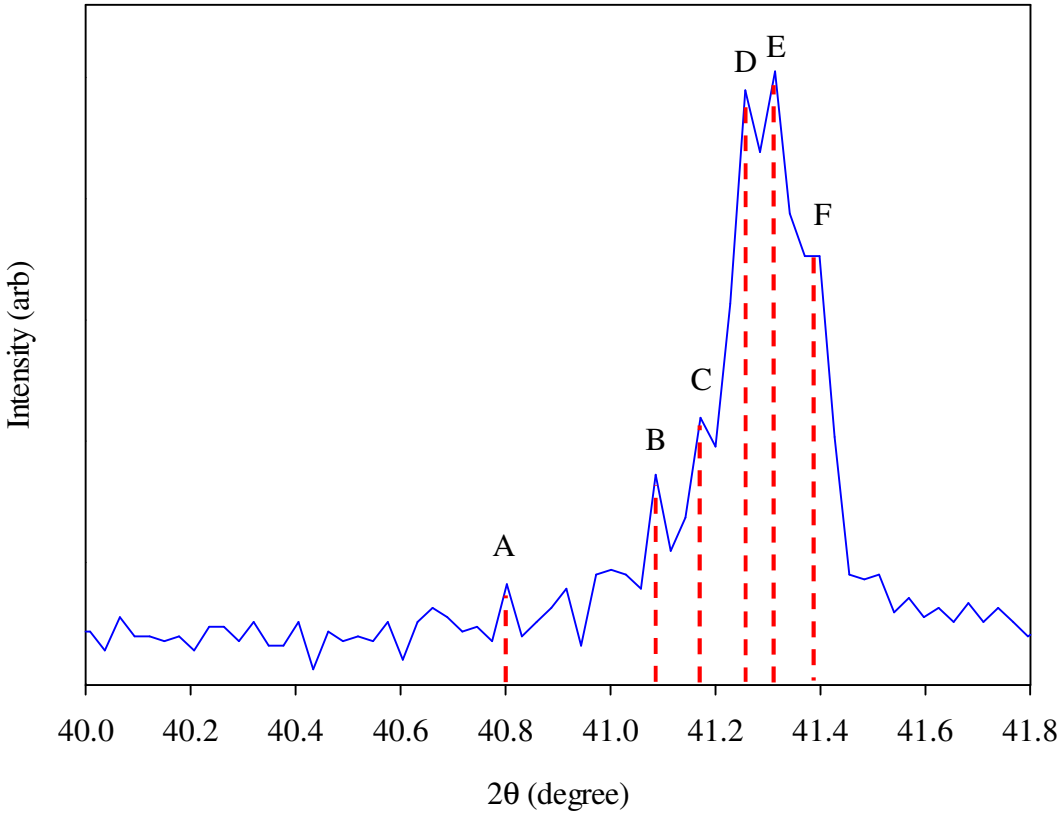

Figure 4.73 Magnification of the Pd-Cu(111) diffraction peak shown in Figure 4.72.

Table 4.10 Compositions determined for points A to F in Figure 4.73.

	Scattering angle, 2θ (degree)	Composition (wt%)
A	40.80	$Pd_{83.0}Cu_{17.0}$
B	41.09	$Pd_{75.8}Cu_{24.2}$
C	41.17	$Pd_{73.6}Cu_{26.4}$
D	41.26	$Pd_{71.3}Cu_{28.7}$
E	41.31	$Pd_{69.8}Cu_{30.2}$
F	41.40	$Pd_{67.4}Cu_{32.6}$

Both compositions of the Pd-rich Pd-Cu FCC phase agree well with those obtained using XPS depth profiling. Figure 4.74 and Figure 4.75 indicates a Pd-rich Pd-Cu FCC phase composition of $Pd_{89.5}Cu_{10.5}$ wt% and $Pd_{90.0}Cu_{10.0}$ wt%, respectively. This provides further proof that this new phase forms on the Pd sputter-coated surface of the Type A-B1/2-F/P membranes under the conditions tested in the MPR.

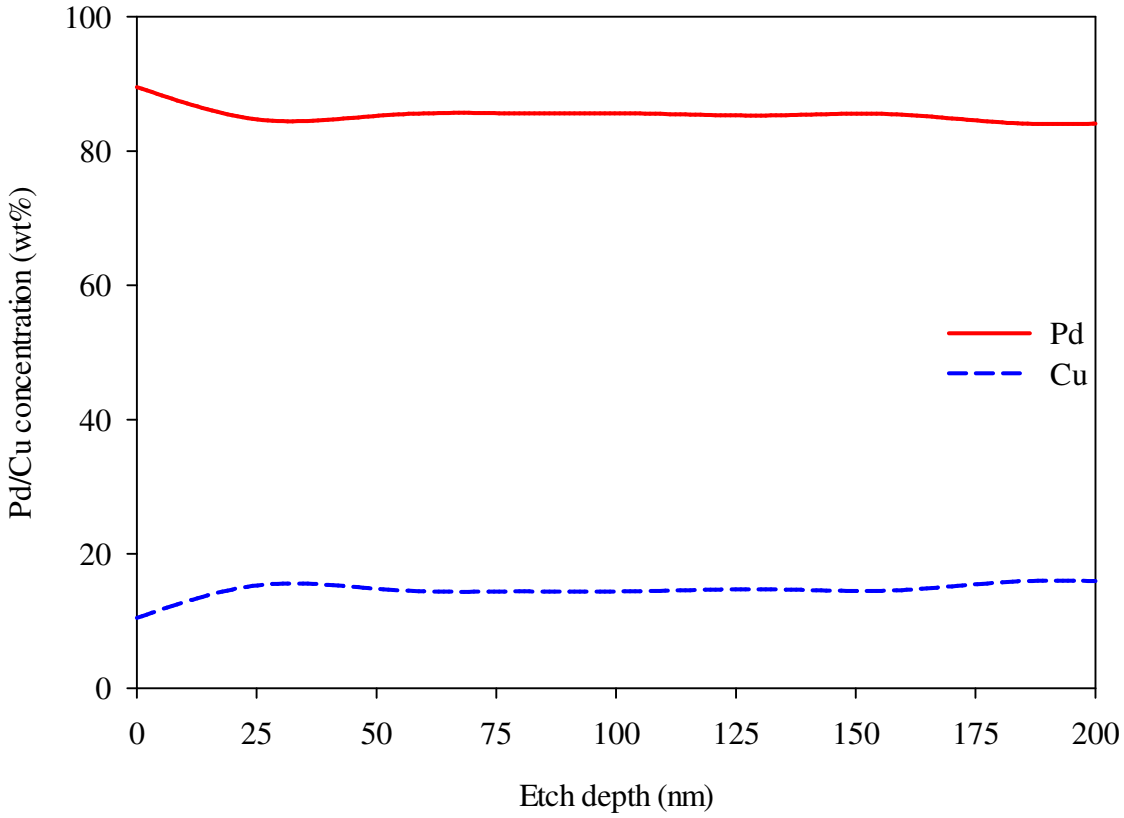

Figure 4.74 XPS depth profile analysis representative of a Type A-B1/2-F membrane following MPR testing. The etch depth was estimated using a reference etching rate of 0.21 nm s^{-1} for Ta_2O_5.

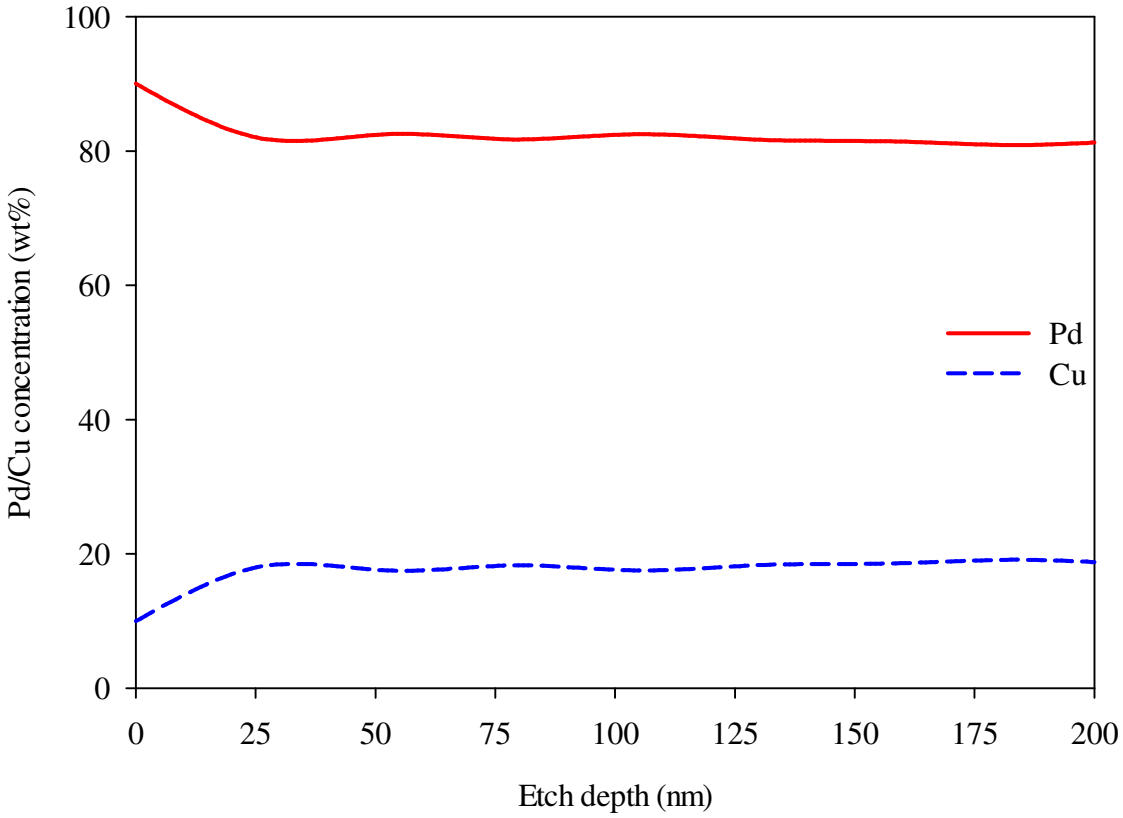

Figure 4.75 XPS depth profile analysis representative of a Type A-B1/2-P membrane following MPR testing. The etch depth was estimated using a reference etching rate of 0.21 nm s^{-1} for Ta_2O_5.

4.5. Type B membranes

4.5.1. Pre-MPR characterisation

Two Type B membranes were prepared for MPR testing by sputtering one side of the Batch 2 Pd-Cu membranes with Pd for 1,000 seconds in order to determine the effect of Pd thin film thickness on membrane performance. SEM images were captured of the Type B-B2 membranes in the as-deposited state (Figure 4.76(a) and (b)), showing grains that range between 50 and 250 nm in size. It is apparent that, depositing Pd with a 1 A target current for 1,000 seconds promotes significant grain growth which is a process favoured at high temperatures. It was not possible to directly measure the temperature of the Pd sputter-coated foil membranes and offcuts, however, it was evident that the Type B variety had undergone heating as a result of the deposition process. This effect would likely be the cause of the grain growth observed in Type B-B2 membranes/foil offcuts.

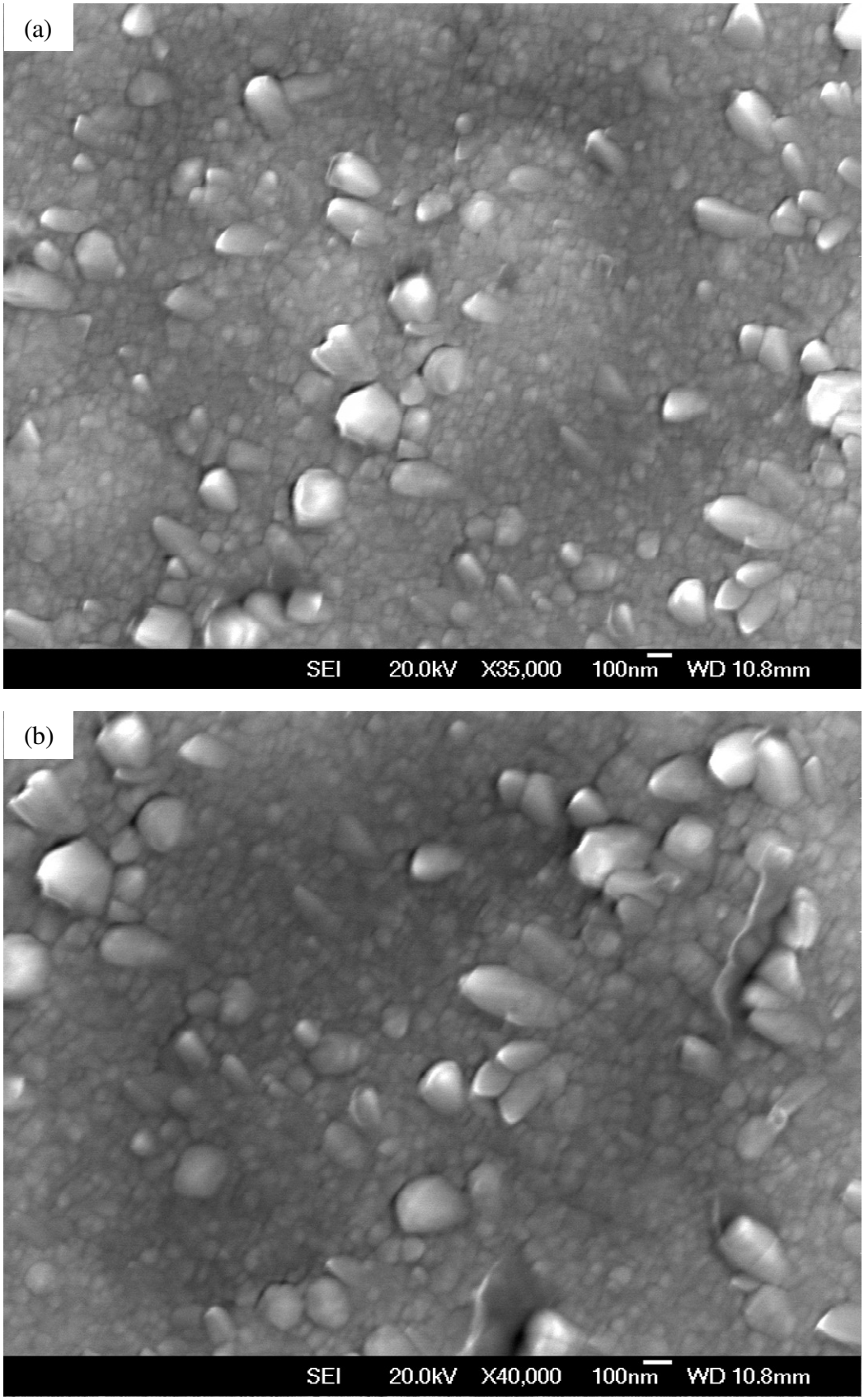

Figure 4.76 SEM micrographs showing the microstructure representative of a Type B-B2 membrane. Coating time was 1,000 seconds with a Pd target current of 1 A.

The thickness of the Pd thin film was estimated with Equation 3.1 to be 606 ± 26 nm assuming a fully dense film. Profilometry of the Pd sputter-coated glass slide (Figure 4.77) which was simultaneously coated with the Type B-B2 membranes and offcuts reveals a film thickness of approximately 797.4 ± 0.2 nm. The discrepancy in thickness suggests that the Pd thin film has some degree of porosity which could be attributed to the large grain boundary volume typical of a nanocrystalline microstructure.

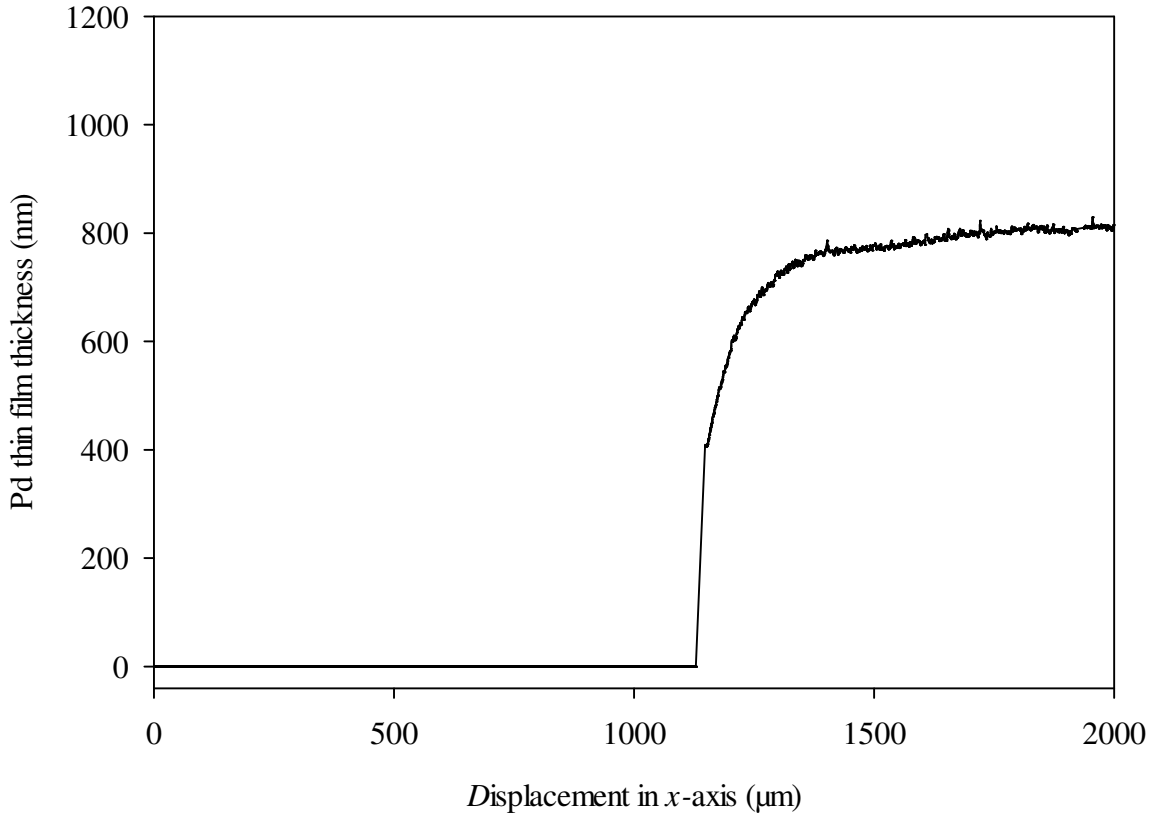

Figure 4.77 Profilometer trace for a glass slide that has been Pd sputter-coated for 1,000 seconds. The first 1,130 µm of the *x*-axis represents the area of the glass slide masked with Kapton tape during Pd deposition.

Figure 4.78 depicts a representative XRD pattern acquired from the Pd sputter-coated surface of a Type B-B2 membrane. As expected, in the as-deposited state the Type B-B2 membrane indicates the presence of only the FCC phase. The presence of the Pd thin film is clearly indicated by the Pd diffraction peaks. The relatively high intensity displayed by the low

scattering angle Pd(111) and Pd(200) diffraction peaks is due to the incident X-ray beam glancing the top surface of the Type B-B2 membrane collecting a majority of the information from the Pd thin film.

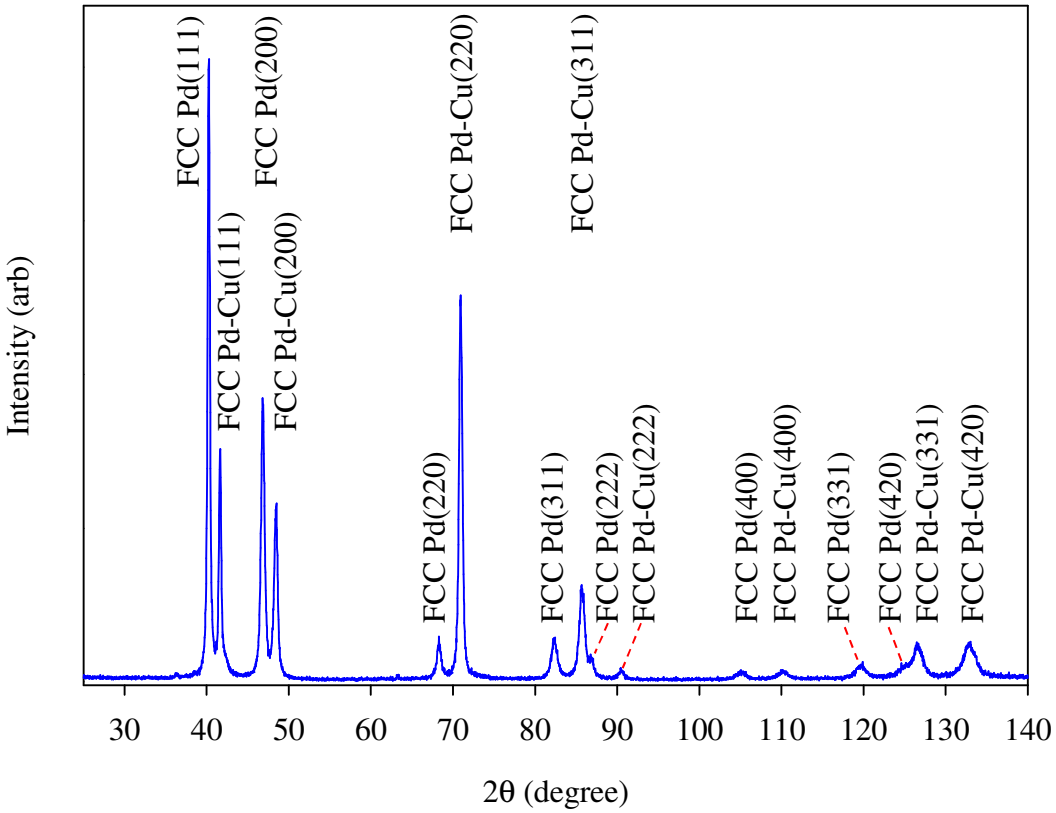

Figure 4.78 XRD pattern which is representative for the Pd sputter-coated side of a Type B-B2 membrane in the as-deposited state before MPR testing.

As the Pd thin film is deposited onto the Batch 2 Pd-Cu membrane, growth proceeds and the Pd adsorbed atoms (adatoms) have the tendency to arrange themselves into the most densely packed plane as this configuration has the lowest free energy. The most densely packed plane for the FCC crystal structure is the (111) plane. The relatively high intensity Pd(111) diffraction peak shown in Figure 4.78, indicates that the Pd adatoms have mainly assumed this arrangement.

Using the scattering angles associated with the Pd(*hkl*) diffraction peaks, the composition of the Pd thin film was calculated to be $Pd_{99.5}Cu_{0.5}$ wt% indicating that, although minute, there is evidence for interdiffusion of Cu atoms from the bulk Pd-Cu membrane into the Pd thin film occurring during the Pd deposition process. This seems plausible as the nanocrysalline nature of the Pd thin film shown in Figure 4.76(a) and (b) would facilitate interdiffusion during deposition.

Three Type B-B2 foil offcuts were prepared along with the Type B-B2 membranes referred to as Type B-B2 Foil 1, Type B-B2 Foil 2 and Type B-B2 Foil 3. Figure 4.79 displays the results of the XPS depth profile analysis performed on Type B-B2 Foil 1. An XPS scan resolution of 50 nm was implemented during the analysis. The Cu concentration begins to rise at an approximate depth of 890 nm and plateau at 1,050 nm indicating the interdiffusion region and providing further proof that interdiffusion occurs during the sputtering process.

Deeper into Type B-B2 Foil 1, a region resembling a bottleneck exists originating from the bulk Batch 2 Pd-Cu foil showing the Cu concentration decreasing to form a second plateau at a depth of 1,500 nm. This could be caused from the residual effects of coring whereby the relatively lower melting point Cu atoms diffuse towards the extremities of the foil and the Pd atoms concentrate towards the inner region. It should be noted that the total analysis depth is approximately 1,680 nm and that it may be necessary to analyse to greater depths in order to reach the original composition of the Batch 2 Pd-Cu foil (~$Pd_{60}Cu_{40}$ wt%).

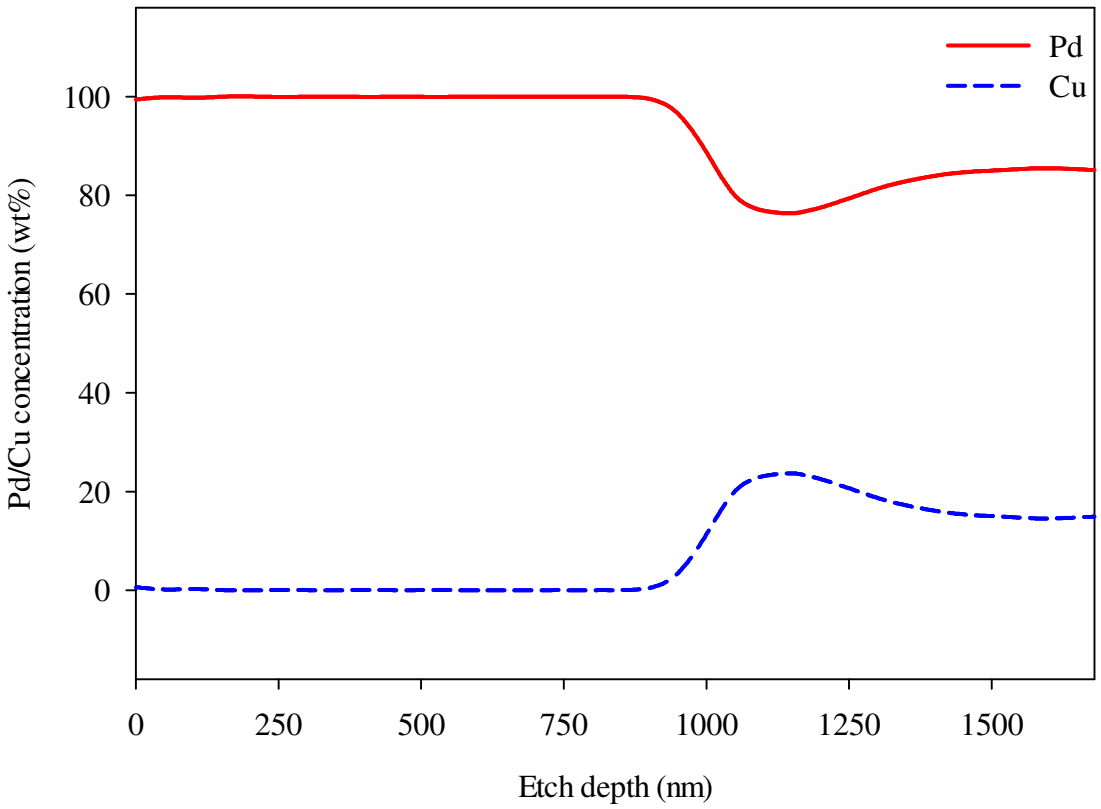

Figure 4.79 XPS depth profile analysis of Type B-B2 Foil 1 in the as-deposited state. The etch depth was estimated using a reference etching rate of 0.21 nm s^{-1} for Ta_2O_5.

4.5.1.1. Effects of temperature and hydrogen pressure on interdiffusion

The VTXRD results for Type B-B2 Foil 2 and Type B-B2 Foil 3 are displayed in Figure 4.80(a) and (b), respectively. Both foils are representative of the Type B-B2-F/P membranes. Type B-B2 Foil 2 readily forms the β-PdH phase at 30 °C under 445 kPa of hydrogen pressure as indicated by the β-PdH(111) diffraction peak positioned at 2θ = 38.41° as shown in Figure 4.80(a). This scattering angle corresponds to a lattice parameter of 4.056 Å indicating a 13.4% Pd lattice volume expansion which is comparable to the 14.3% Pd lattice volume expansion experienced by Type A-B2 Foil 2. Moreover, hydrogen desorption in Type B-B2 Foil 2 occurs at the same temperature as Type A-B2 Foil 2 (200 °C) forming the α-PdH phase as shown by the α-PdH(111) diffraction peak at 2θ = 39.81°.

At 400 °C, the α-PdH(111) diffraction peak moves to higher scattering angles to merge with the Pd-rich Pd-Cu(111) diffraction peak which appears above 400 °C. In addition, the Pd-Cu(111) diffraction peak associated with the bulk Pd-Cu foil disappears at 275 °C. In general, the Pd thin film seems to completely interdiffuse with the bulk Pd-Cu foil under the VTXRD conditions used.

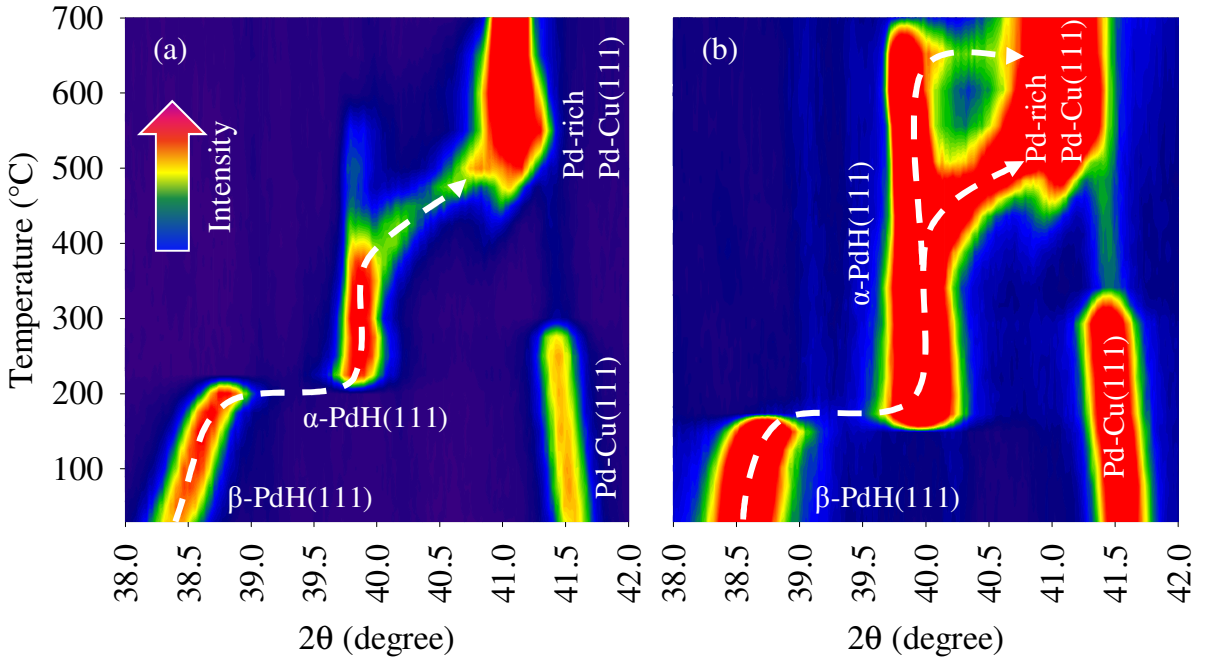

Figure 4.80 VTXRD contour plots tracking the movement of the (a) PdH(111) diffraction peak from the Pd thin film of Type B-B2 Foil 2 under 445 kPa of flowing hydrogen and (b) the PdH(111) diffraction peak from the Pd thin film of Type B-B2 Foil 3 under 100 kPa of flowing hydrogen whilst heating between 30 and 700 °C.

For Type B-B2 Foil 3, the β-PdH(111) diffraction peak appears at 2θ = 38.58° for a temperature of 30 °C and 100 kPa of hydrogen pressure as illustrated in Figure 4.80(b). This corresponds to a lattice parameter of 4.039 Å which represents a 12.0% Pd lattice volume expansion. Hydrogen desorption from the Pd thin film occurs at 150 °C which is identical to the temperature at which hydrogen desorbs from the Pd thin film of Type A-B2 Foil 3. This is represented by the movement of the β-PdH(111) diffraction peak to 2θ = 39.94° signalling the

formation of the α-PdH phase which is indicated by the α-PdH(111) diffraction peak. This particular phase remains stable to almost 700 °C. Under the VTXRD conditions, interdiffusion mainly occurs between 400 and 550 °C, ceases and then continues at 650 °C although the Pd thin film remains stable almost up to 700 °C. The Pd-Cu(111) diffraction peak originating from the bulk Pd-Cu foil drops in intensity between 325 °C and merges with the Pd-rich Pd-Cu(111) diffraction peak at 500 °C.

XPS depth profile analysis was performed on Type B-B2 Foil 2 and Type B-B2 Foil 3 following VTXRD analysis with the results displayed in Figure 4.81 and Figure 4.82, respectively. It is apparent that Type B-B2 Foil 2 contains the Pd-rich Pd-Cu FCC phase on the Pd sputter-coated surface giving a composition of $Pd_{85.6}Cu_{14.4}$ wt%. Moreover, Type B-B2 Foil 3 shows evidence of the Pd-rich Pd-Cu FCC phase with a composition of $Pd_{89.5}Cu_{10.5}$ wt%. The Pd-rich Pd-Cu FCC phase associated with Type B-B2 Foil 2 has a relatively higher Cu concentration likely caused through an increased rate of interdiffusion facilitated by the relatively higher hydrogen pressure.

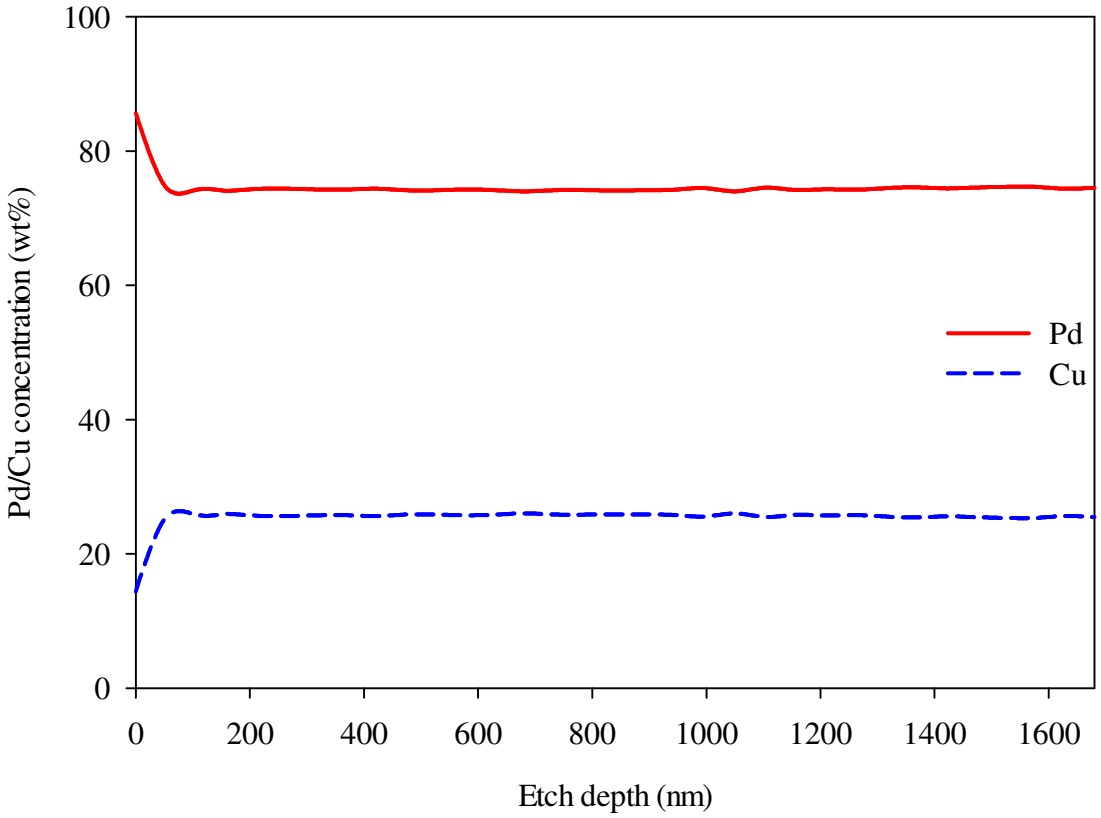

Figure 4.81 XPS depth profile analysis of Type B-B2 Foil 2 following VTXRD under 445 kPa of hydrogen pressure. The etch depth was estimated using a reference etching rate of 0.21 nm s^{-1} for Ta_2O_5.

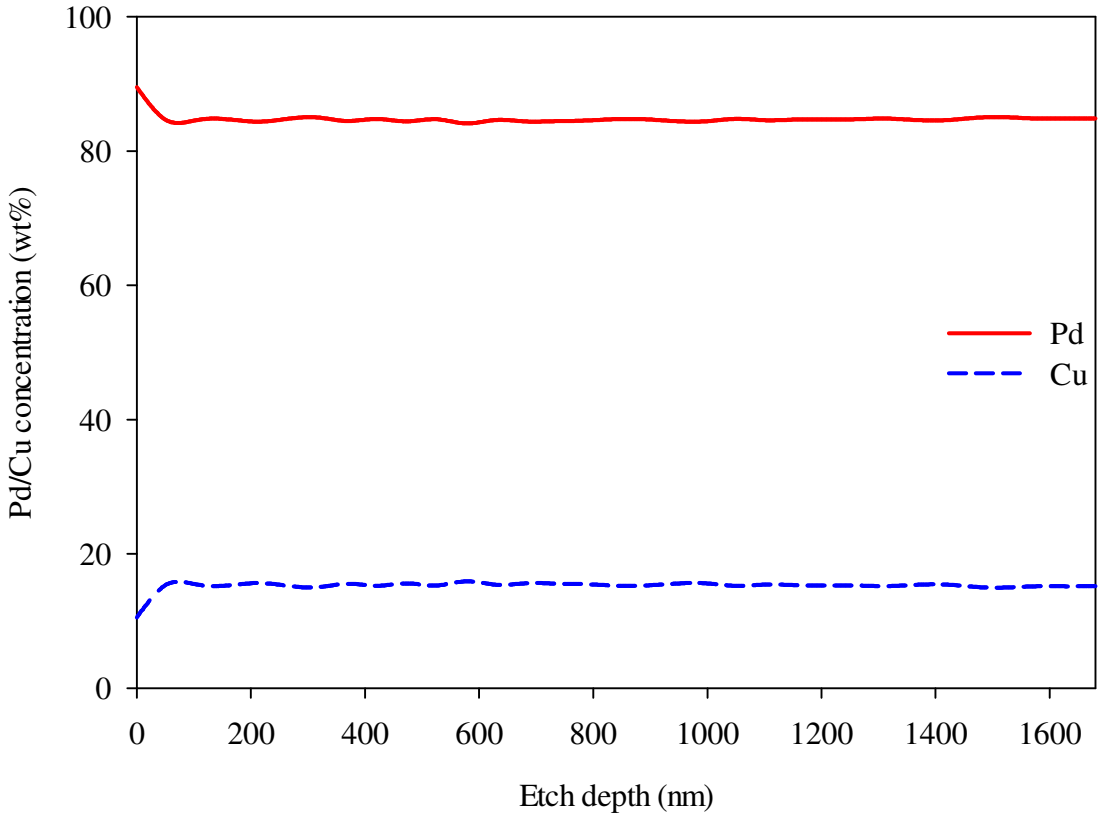

Figure 4.82 XPS depth profile analysis of Type B-B2 Foil 3 following VTXRD under 100 kPa of hydrogen pressure. The etch depth was estimated using a reference etching rate of 0.21 nm s^{-1} for Ta_2O_5.

4.5.2. MPR results

4.5.2.1. Pd thin film positioned on the feed side

For a valid comparison, the hydrogen permeability of the Type B-B2-F membrane will mainly be correlated with the Batch 2 Pd-Cu membranes that completed the initial cycles between 50 and 450 °C. The first three cycles completed by the Type B-B2-F membrane are shown in Figure 4.83. Hydrogen permeation begins during the first cycle at 390 °C comparable to the corresponding hydrogen permeation start temperatures of the Batch 2 Pd-Cu membranes (400 °C) and the Type A-B2-F membrane (380 °C). Hydrogen permeation commences at 210 and 200 °C during the second and third cycles, respectively. This is significantly lower than the corresponding hydrogen permeation start temperatures observed for the second and third

cycles completed by the Batch 2 Pd-Cu membranes (330 and 320 °C, respectively) and the Type A-B2-F membrane (270 and 260 °C, respectively).

The Type B-B2-F membrane achieves a hydrogen permeability of 1.00×10^{-8} mol m^{-1} s^{-1} Pa$^{-0.5}$ at 450 °C during the third cycle. This is a 46% increase on the average hydrogen permeability of $(6.86 \pm 0.6) \times 10^{-9}$ mol m^{-1} s^{-1} Pa$^{-0.5}$ achieved by the Batch 2 Pd-Cu membranes at the same temperature and cycle. This is also a 13% increase on the hydrogen permeability of 8.82×10^{-9} mol m^{-1} s^{-1} Pa$^{-0.5}$ achieved by the Type A-B2-F membrane at the same temperature and cycle.

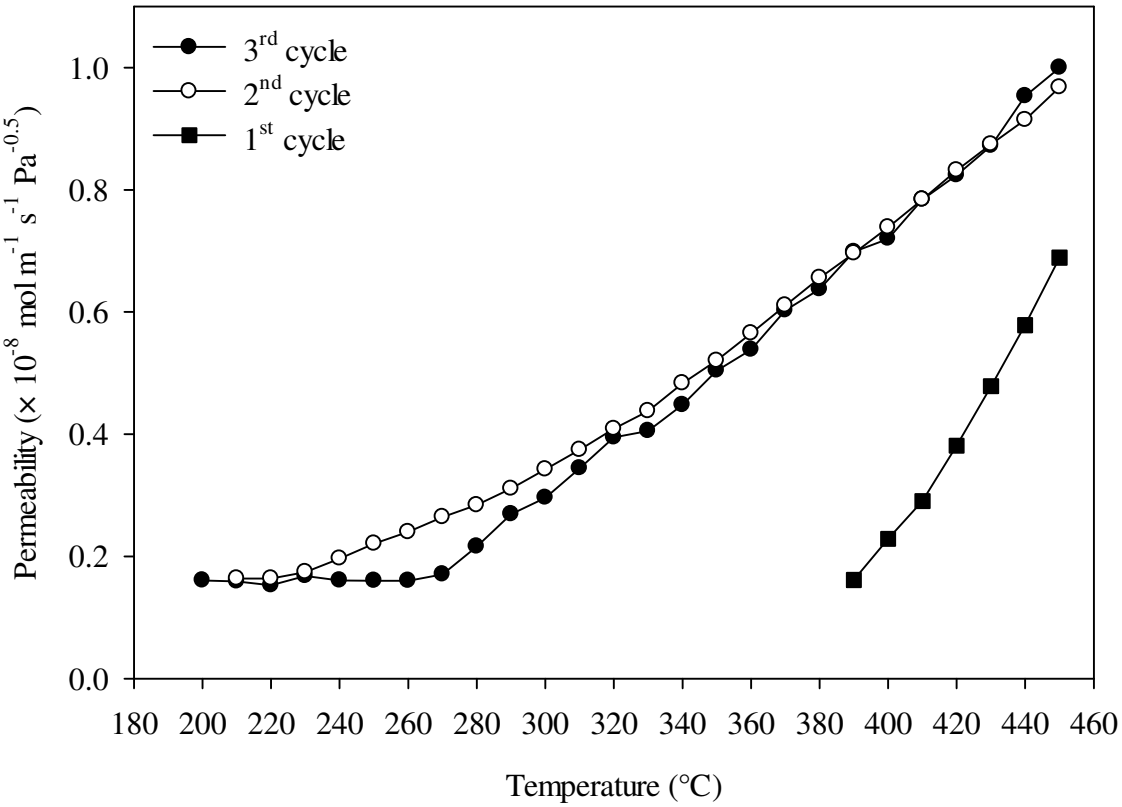

Figure 4.83 Hydrogen permeability as a function of temperature for the Type B-B2-F membrane. The plot shows the first three cycles heated between 50 and 450 °C using a hydrogen feed pressure of 445 kPa and permeate pressure of 100 kPa assuming an *n*-value of 0.5.

Figure 4.84 and Figure 4.85 illustrate the *n*-value measurement results for the Type B-B2-F membrane with the data constrained to 0.5 and the best fit value of 0.63, respectively. Figure 4.86 shows the third cycle completed by the Type B-B2-F membrane using an *n*-value of 0.5 for the solid symbol curve and the best fit value of 0.63 for the open symbol curve.

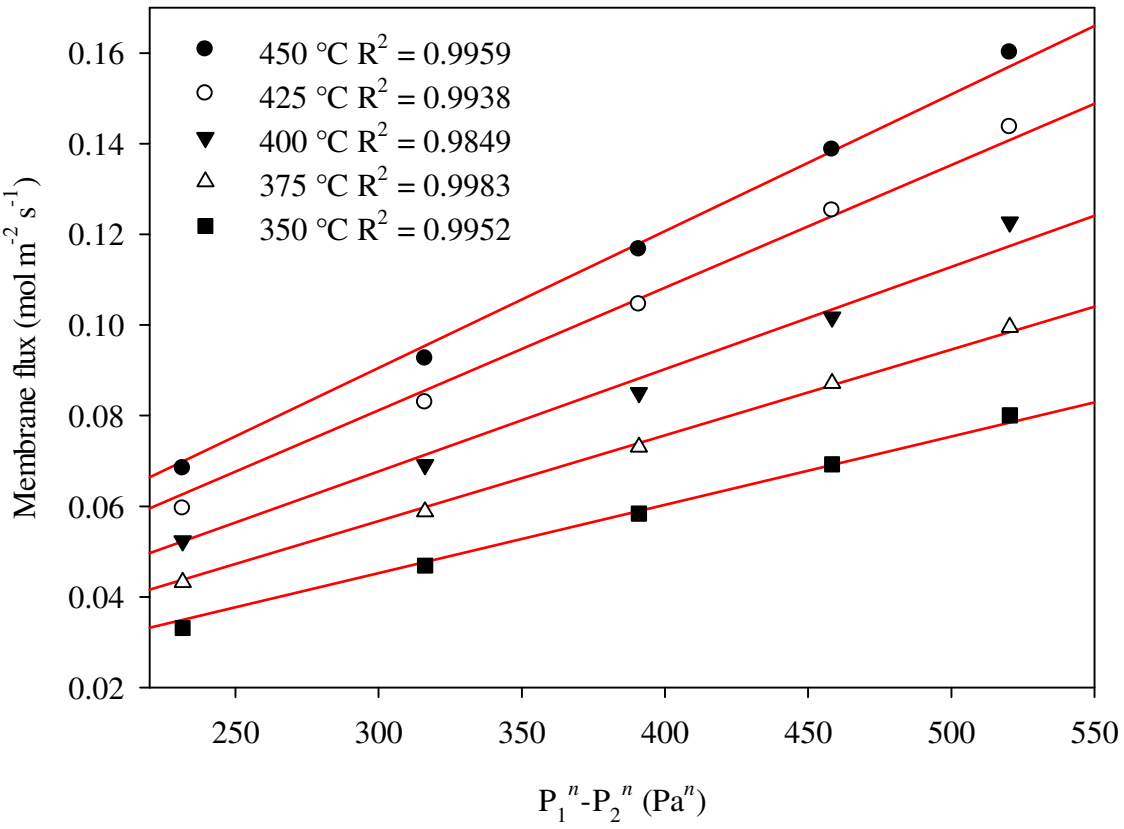

Figure 4.84 Membrane flux as a function of hydrogen differential pressure with *n* constrained to 0.5.

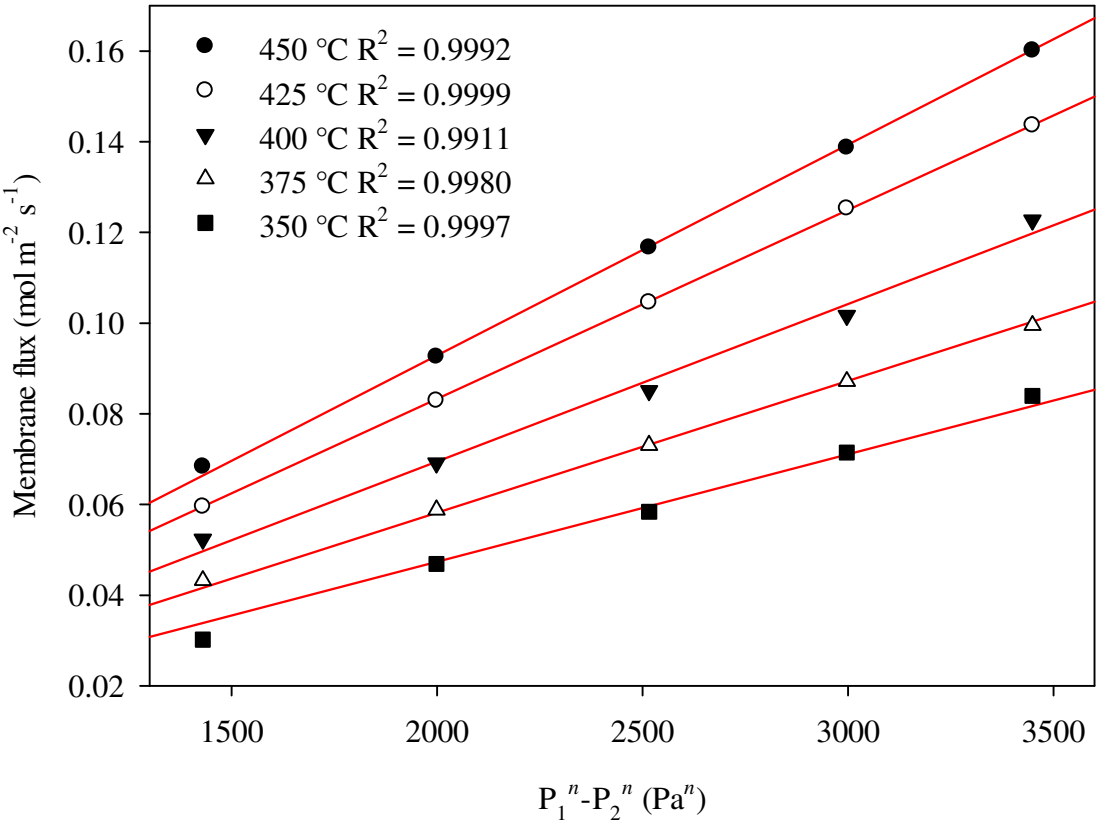

Figure 4.85 Membrane flux as a function of hydrogen differential pressure with *n* constrained to the best fit value of 0.63.

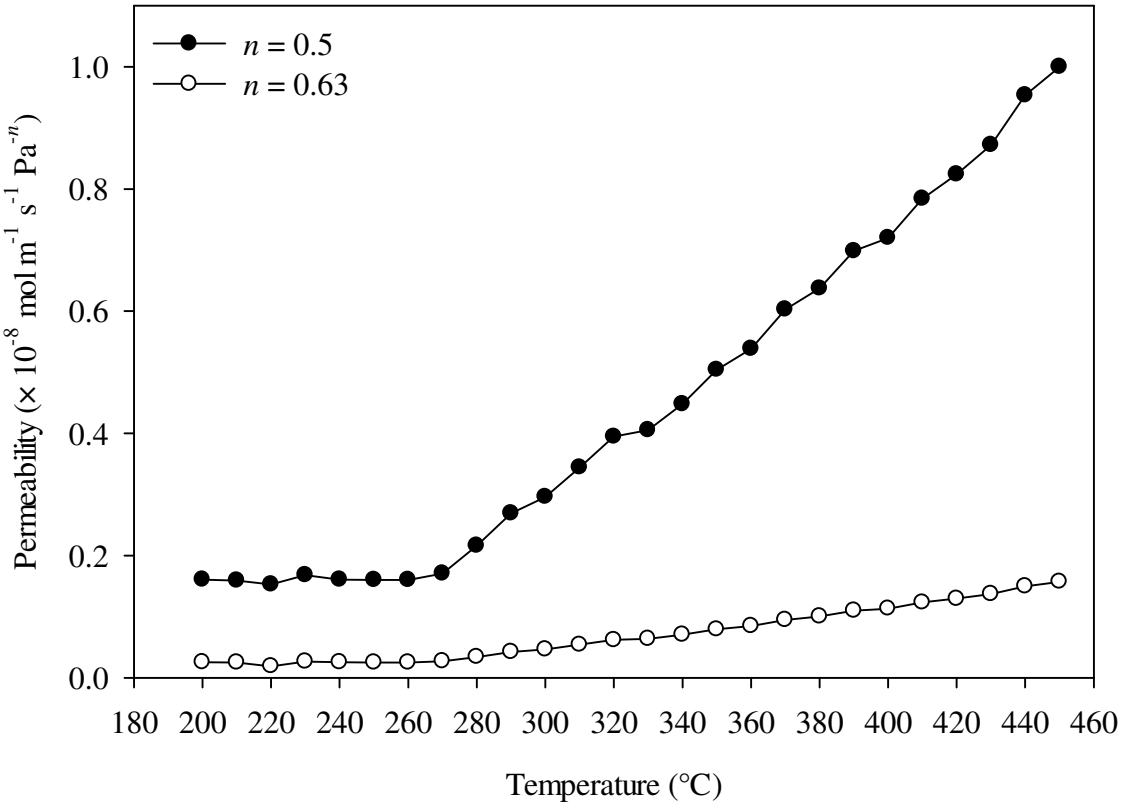

Figure 4.86 Hydrogen permeability as a function of temperature showing the third cycle for the Type B-B2-F membrane. A hydrogen feed pressure of 445 kPa and permeate pressure of 100 kPa was applied during measurements. The solid symbol curve was calculated using an *n*-value of 0.5 whereas the open symbol curve uses the best fit *n*-value of 0.63.

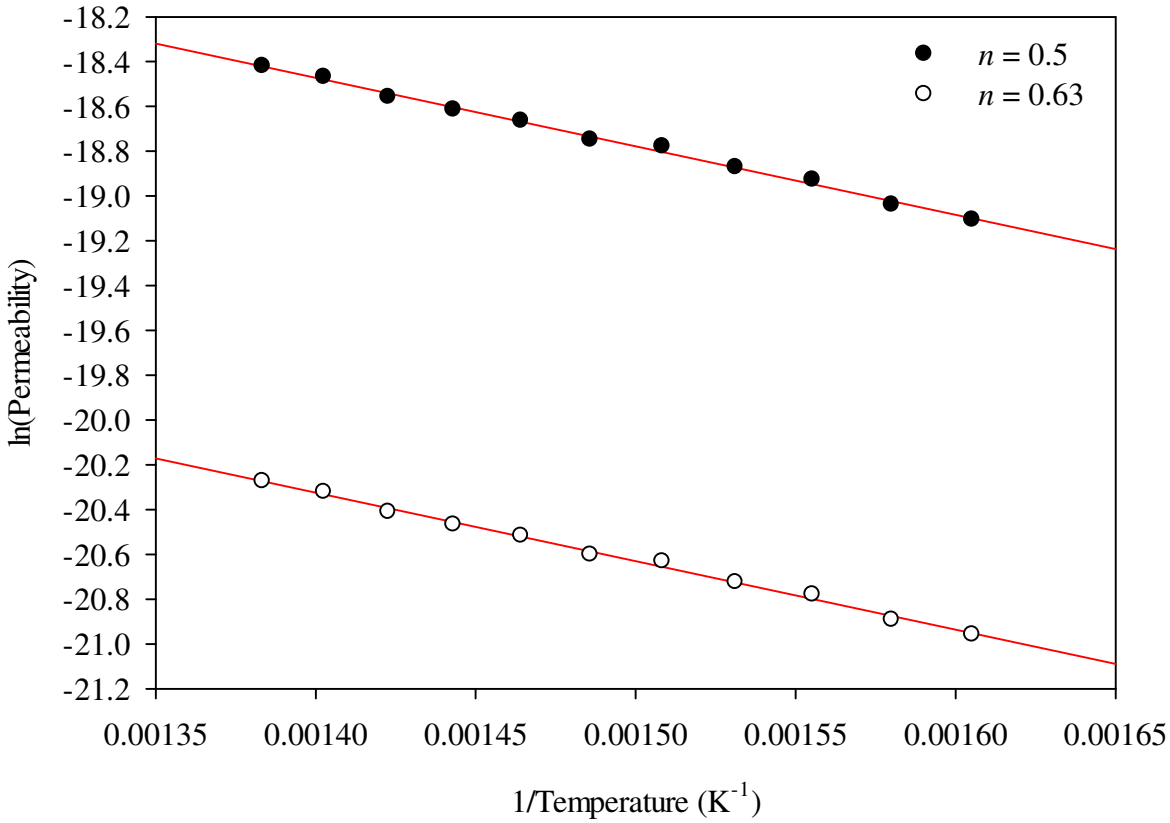

Figure 4.87 Arrhenius plot of the hydrogen permeability data shown in Figure 4.86 between 350 and 450 °C. The solid symbol curve was calculated using an *n*-value of 0.5 whereas the open symbol curve uses the best fit *n*-value of 0.63.

The general permeability formulae (350 – 450 °C) have been derived from Figure 4.87 for the Type B-B2-F membrane using an *n*-value of 0.5 and the best fit value of 0.63 as shown in Equation 4.22 and Equation 4.23, respectively. For an *n*-value of 0.5, the Type B-B2-F membrane gives an E_Φ value of 23.41 kJ mol^{-1} which is a 22% reduction on the E_Φ value obtained for the Type A-B2-F membrane and a 44% decrease on the E_Φ value obtained for the Batch 2 Pd-Cu membranes.

$$\Phi_{n=0.5} = 4.99 \times 10^{-7} exp\left(\frac{-23.41 \times 10^3}{RT}\right) \qquad \text{Equation 4.22}$$

$$\Phi_{n=0.63} = 7.83 \times 10^{-8} exp\left(\frac{-23.41 \times 10^3}{RT}\right) \qquad \text{Equation 4.23}$$

Figure 4.88 demonstrates the variation of the *n*-value with temperature for the Type B-B2-F membrane. To begin with, the *n*-value declines from 0.62 to just above 0.56 between 350 and 375 °C. Subsequently the *n*-value increase to 0.64 between 400 and 425 °C and finally declining to 0.60 at 450 °C. In general, it is apparent that the hydrogen permeation in the Type B-B2-F membrane is diffusion limited.

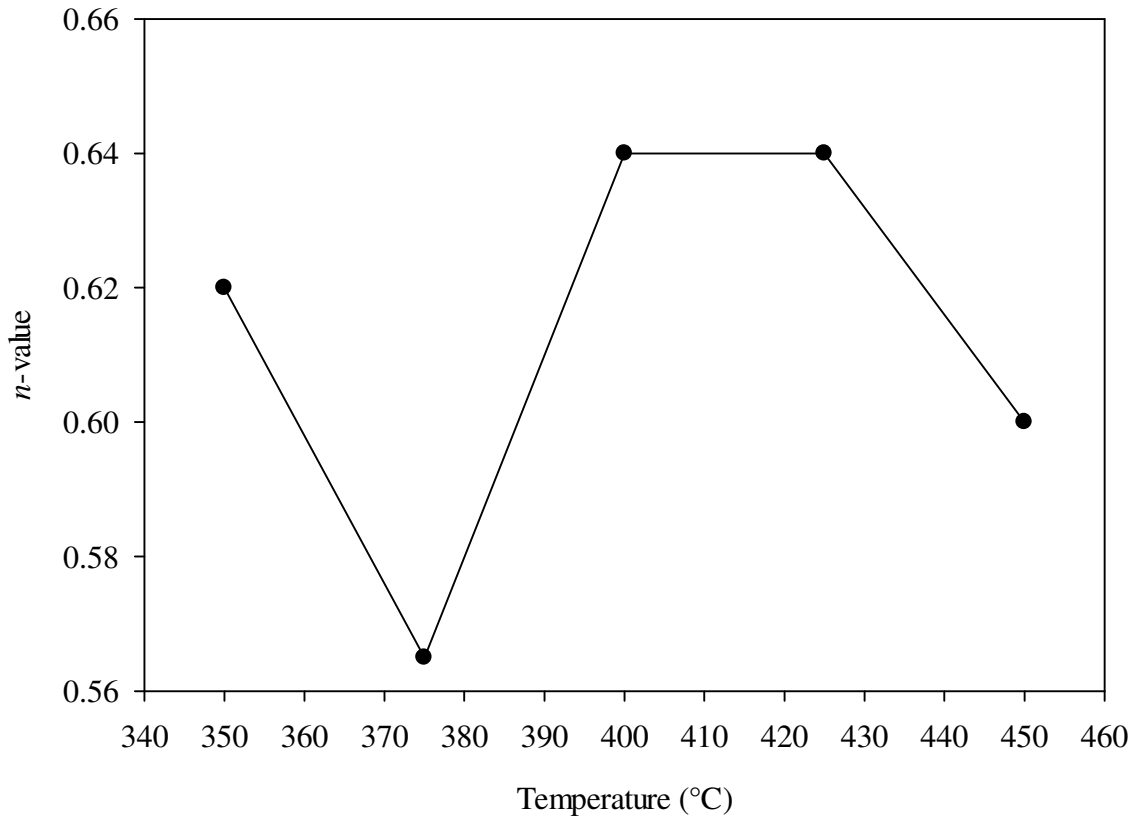

Figure 4.88 Variation of *n*-value as a function of temperature for the Type B-B2-F membrane.

4.5.2.2. Pd thin film positioned on the permeate side

Figure 4.89 shows the first three cycles completed by the Type B-B2-P membrane. For the first cycle, hydrogen permeation begins at 350 °C which is similar to the first cycle hydrogen permeation start temperature of 360 °C for the Type A-B2-P membrane yet lower than the Batch 2 Pd-Cu membranes which began at 400 °C. Subsequently, hydrogen permeation

begins at 300 °C for both second and third cycles completed by the Type B-B2-P membrane. Again, this is comparable to the second and third cycle hydrogen permeation start temperature of 290 °C for the Type A-B2-P membrane. Although, the second and third cycle hydrogen permeation start temperatures of 320 and 330 °C, respectively, for the Batch 2 Pd-Cu membranes is slightly higher in comparison.

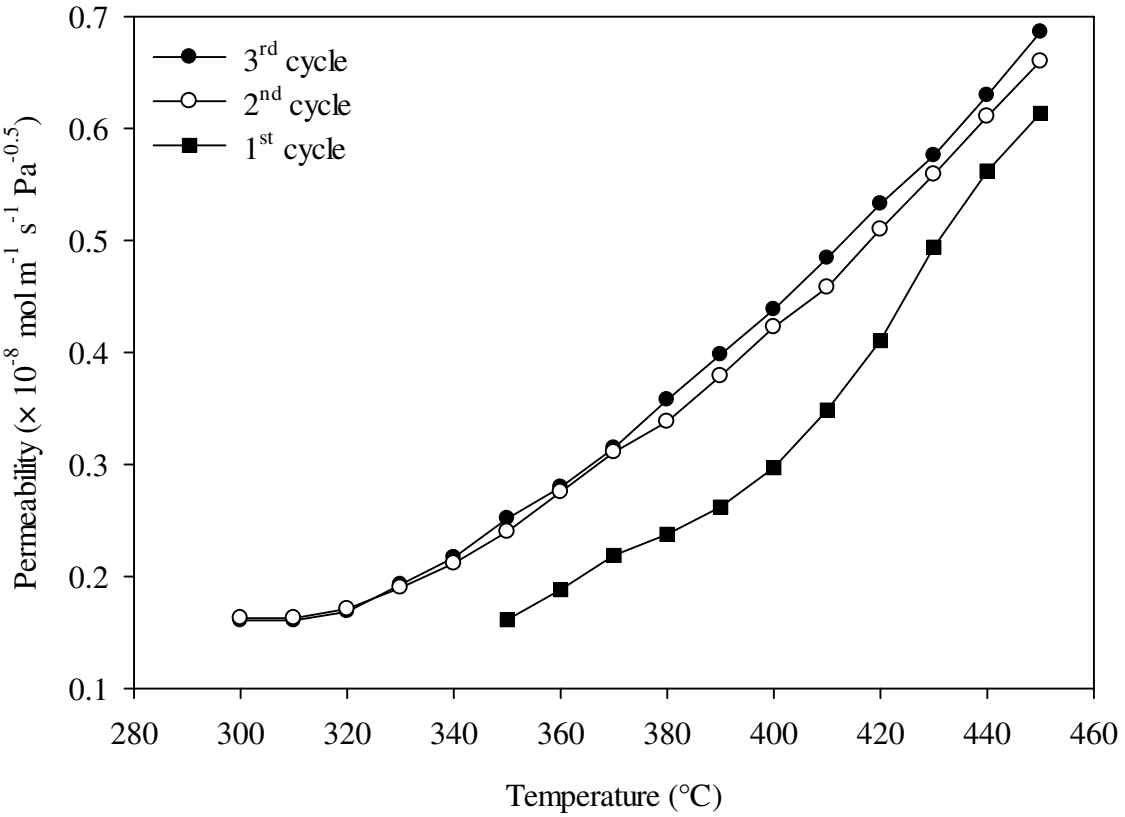

Figure 4.89 Hydrogen permeability as a function of temperature for the Type B-B2-P membrane. The plot shows the first three cycles heated between 50 and 450 °C using a hydrogen feed pressure of 445 kPa and permeate pressure of 100 kPa assuming an *n*-value of 0.5.

A hydrogen permeability of 6.86×10^{-9} mol m^{-1} s^{-1} $Pa^{-0.5}$ was measured at 450 °C during the third cycle for the Type B-B2-P membrane. This is identical to the hydrogen permeability value achieved by the Batch 2 Pd-Cu membranes during the same cycle and temperature indicating that a nearly 800 nm thick Pd thin film positioned on the permeate side provides no improvement on hydrogen permeability. Compared to the Type A-B2-P membrane and

Type B-B2-F membrane, this is a 24% and 31% reduction, respectively, in hydrogen permeability for the equivalent cycle and temperature.

In Figure 4.90, the *n*-value measurement data for the Type B-B2-P membrane is constrained to 0.5 while Figure 4.91 displays the data constrained to the best fit value of 0.60. In addition, Figure 4.92 shows the third cycle completed by the Type B-B2-P membrane where the solid symbol curve has been calculated using an *n*-value of 0.5 and the open symbol curve has been calculated using the best fit value of 0.60.

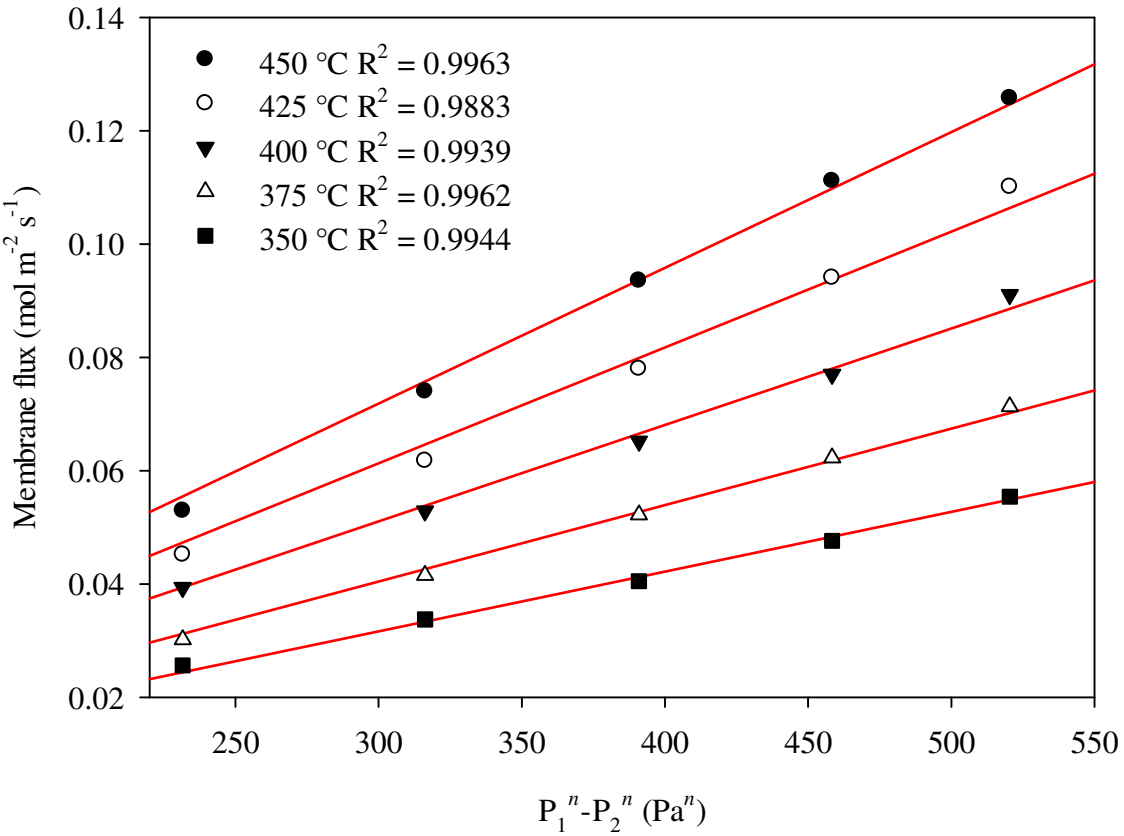

Figure 4.90 Membrane flux as a function of hydrogen differential pressure with *n* constrained to 0.5.

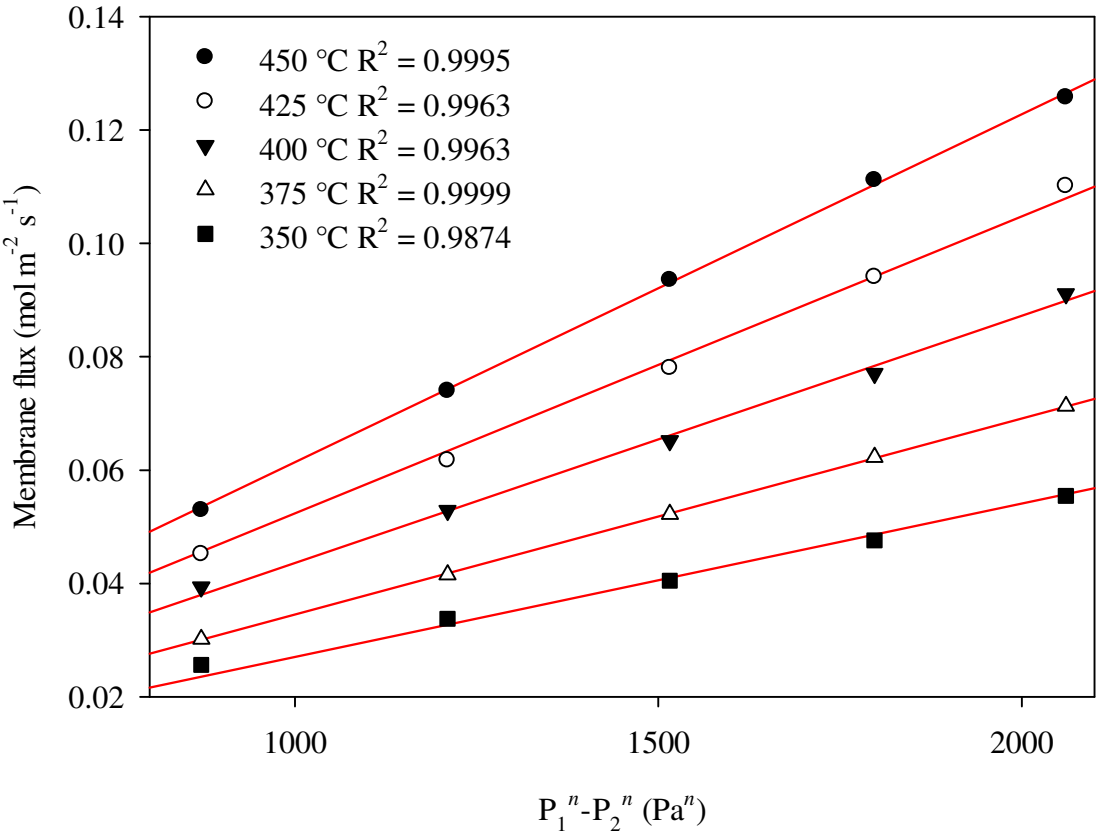

Figure 4.91 Membrane flux as a function of hydrogen differential pressure with *n* constrained to the best fit value of 0.60.

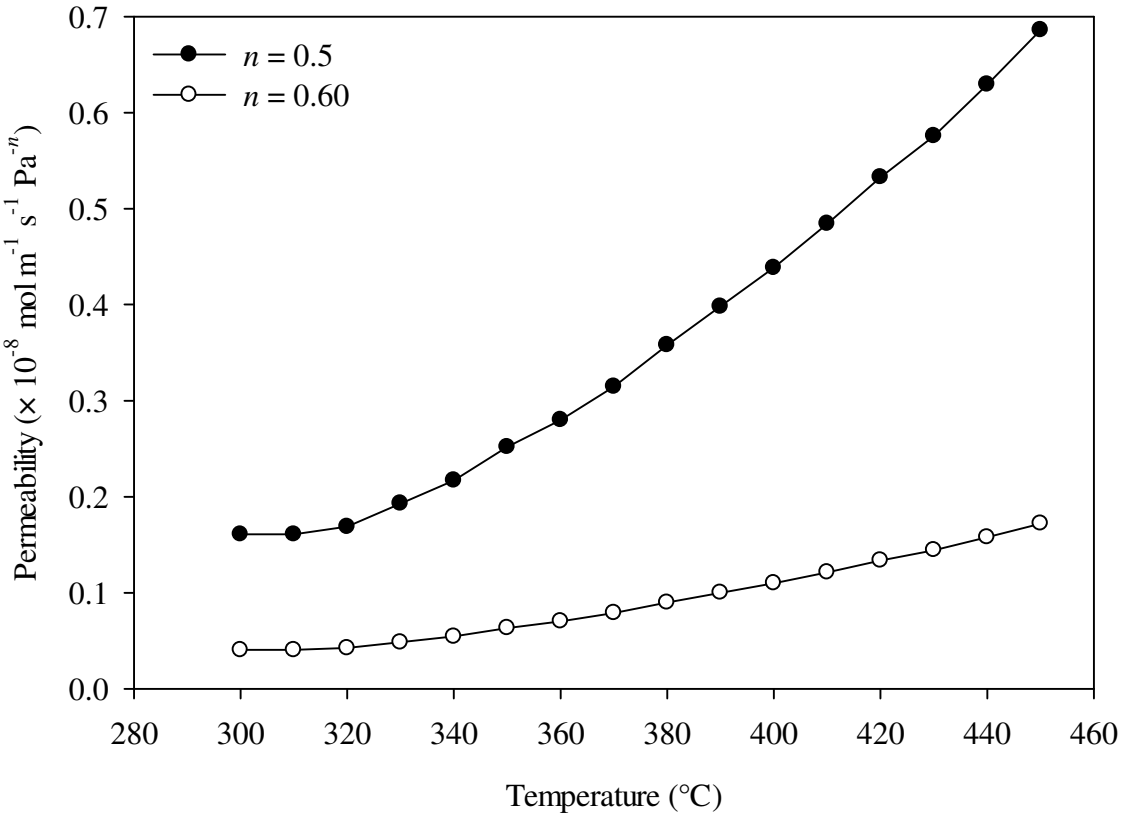

Figure 4.92 Hydrogen permeability as a function of temperature showing the third cycle for the Type B-B2-P membrane. A hydrogen feed pressure of 445 kPa and permeate pressure of 100 kPa was applied during measurements. The solid symbol curve was calculated using an *n*-value of 0.5 whereas the open symbol curve uses the best fit *n*-value of 0.60.

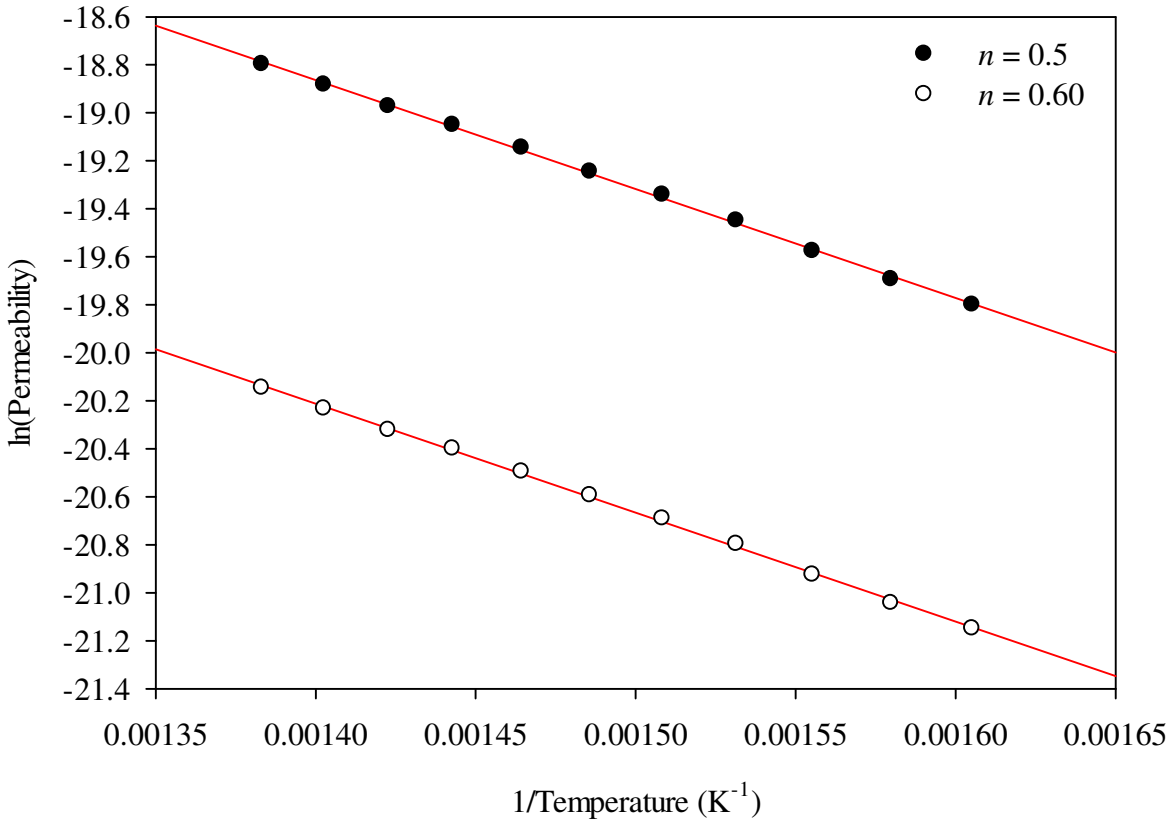

Figure 4.93 Arrhenius plot of the hydrogen permeability data shown in Figure 4.92 between 350 and 450 °C. The solid symbol curve was calculated using an *n*-value of 0.5 whereas the open symbol curve uses the best fit *n*-value of 0.60.

From Figure 4.93, the following general permeability formulae (350 – 450 °C) for the Type B-B2-P membrane have been derived for an *n*-value of 0.5 and the best fit *n*-value of 0.60 as demonstrated in Equation 4.24 and Equation 4.25, respectively.

$$\Phi_{n=0.5} = 3.88 \times 10^{-6} exp\left(\frac{-38.01 \times 10^3}{RT}\right) \qquad \text{Equation 4.24}$$

$$\Phi_{n=0.60} = 1.01 \times 10^{-6} exp\left(\frac{-38.01 \times 10^3}{RT}\right) \qquad \text{Equation 4.25}$$

The E_Φ value of 38.01 kJ mol^{-1} for the Type B-B2-P membrane is comparable to that determined for the Batch 2 Pd-Cu membranes (41.67 ± 3.40 kJ mol^{-1}) and the

Type A-B2-P membrane (36.41 kJ mol^{-1}). On the other hand, this is a 62% increase on the E_Φ value of 23.41 kJ mol^{-1} obtained for the Type B-B2-F membrane.

Figure 4.94 shows that, in general, the Type B-B2-P membrane *n*-value increases with temperature and remains around a value of 0.60 indicating that hydrogen permeation remains limited by the diffusion process.

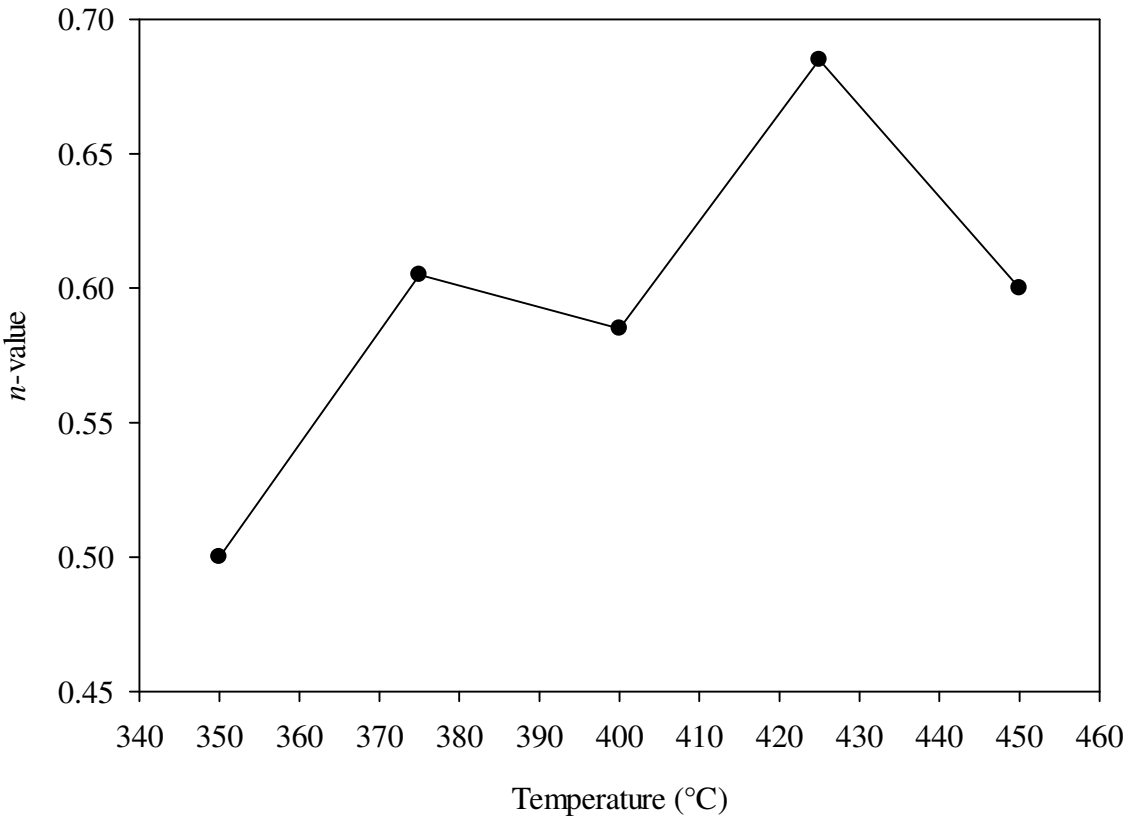

Figure 4.94 Variation of *n*-value as a function of temperature for the Type B-B2-P membrane.

4.5.3. Post-MPR characterisation

Similar to the Type A-B1/2-F/P membranes, the Type B-B2-F membrane and the Type B-B2-P membrane contain a mixture of the BCC phase and FCC phase following MPR testing as depicted in Figure 4.95 and Figure 4.97, respectively. In both cases, the BCC phase originates from Batch 2 Pd-Cu membrane while the FCC phase is attributed to the Pd thin film.

Note that the FCC diffraction peaks exhibit asymmetry revealing evidence of interdiffusion resulting in the formation of the Pd-rich Pd-Cu FCC phase. Figure 4.96 shows a magnified view of the Pd-Cu(111) diffraction peak displayed in the XRD scan acquired for the Type B-B2-F membrane (Figure 4.95). The compositions associated with points A to K are listed in Table 4.11 demonstrating the compositional range of the Pd-rich Pd-Cu FCC phase. The composition of the BCC phase found on the Pd sputter-coated side of the Type B-B2-F membrane is $Pd_{61.3}Cu_{38.7}$ wt%. The non-coated side contained only the BCC phase with a composition of $Pd_{60.8}Cu_{39.2}$ wt%.

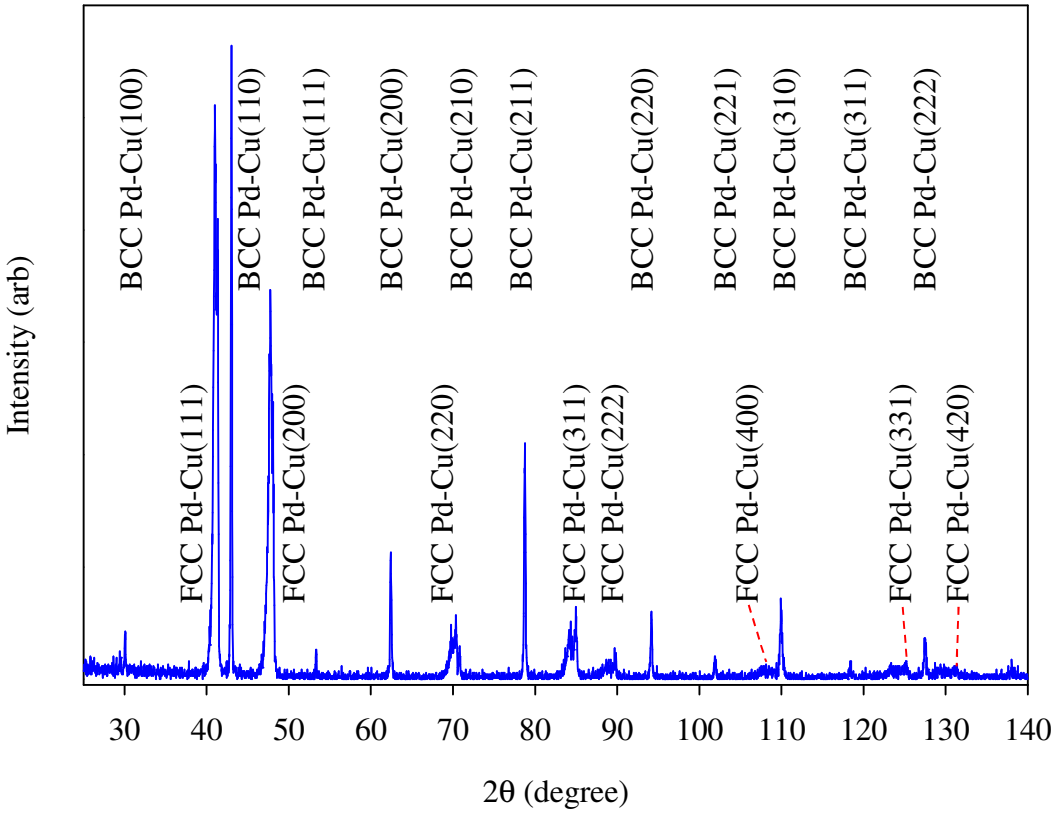

Figure 4.95 XRD pattern which is representative for the Pd sputter-coated side of the Type B-B2-F membrane following MPR testing.

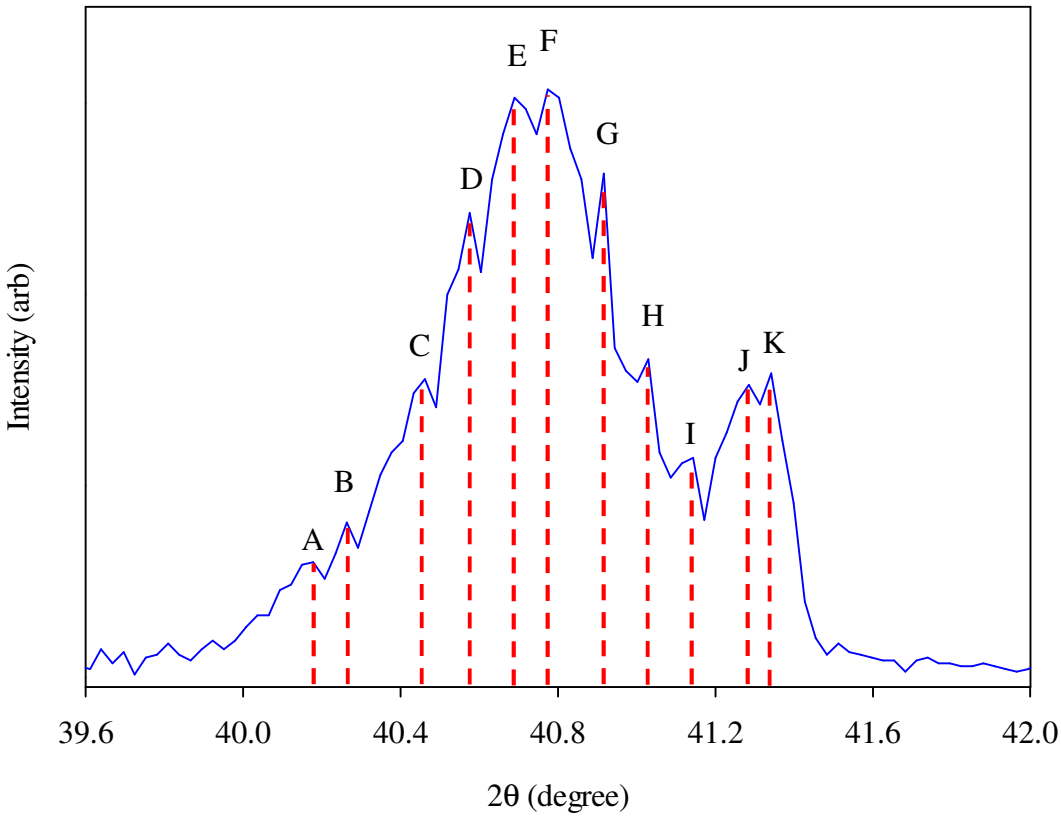

Figure 4.96 Magnification of the Pd-Cu(111) diffraction peak shown in Figure 4.95.

Table 4.11 Compositions determined for points A to K in Figure 4.96.

	Scattering angle, 2θ (degree)	Composition (wt%)
A	40.18	$Pd_{97.0}Cu_{3.0}$
B	40.26	$Pd_{95.2}Cu_{4.8}$
C	40.46	$Pd_{90.9}Cu_{9.1}$
D	40.58	$Pd_{88.3}Cu_{11.7}$
E	40.69	$Pd_{85.7}Cu_{14.3}$
F	40.77	$Pd_{83.6}Cu_{16.4}$
G	40.91	$Pd_{80.2}Cu_{19.8}$
H	41.03	$Pd_{77.3}Cu_{22.7}$
I	41.14	$Pd_{74.3}Cu_{25.7}$
J	41.28	$Pd_{70.5}Cu_{29.5}$
K	41.34	$Pd_{69.0}Cu_{31.0}$

In addition, Figure 4.98 shows the Pd-Cu(111) diffraction peak from the XRD scan acquired for the Type B-B2-P membrane (Figure 4.97). Again, peak asymmetry is clearly shown indicating signs of interdiffusion. The compositions corresponding to points A to L are

compiled in Table 4.12. Furthermore, the composition of the BCC phase detected on the Pd sputter-coated side of the Type B-B2-P membrane is $Pd_{62.4}Cu_{37.6}$ wt%. The non-coated side contained only the BCC phase with a composition of $Pd_{61.1}Cu_{38.9}$ wt%.

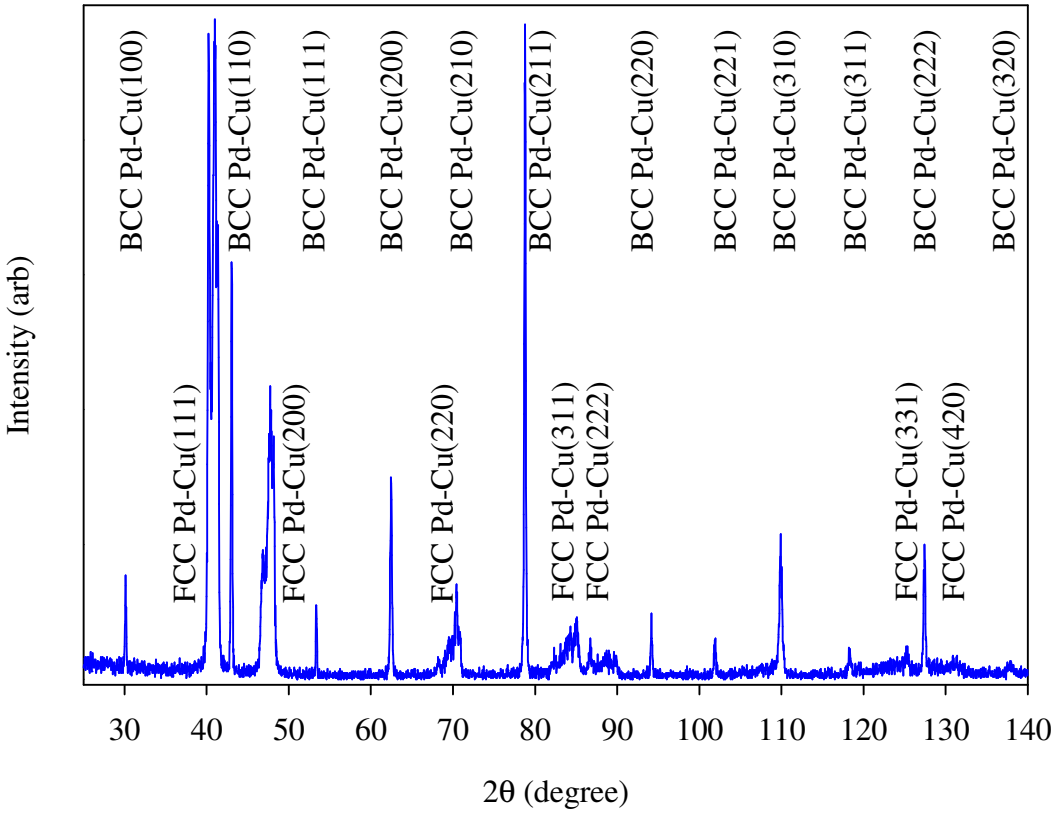

Figure 4.97 XRD pattern which is representative for the Pd sputter-coated side of the Type B-B2-P membrane following MPR testing.

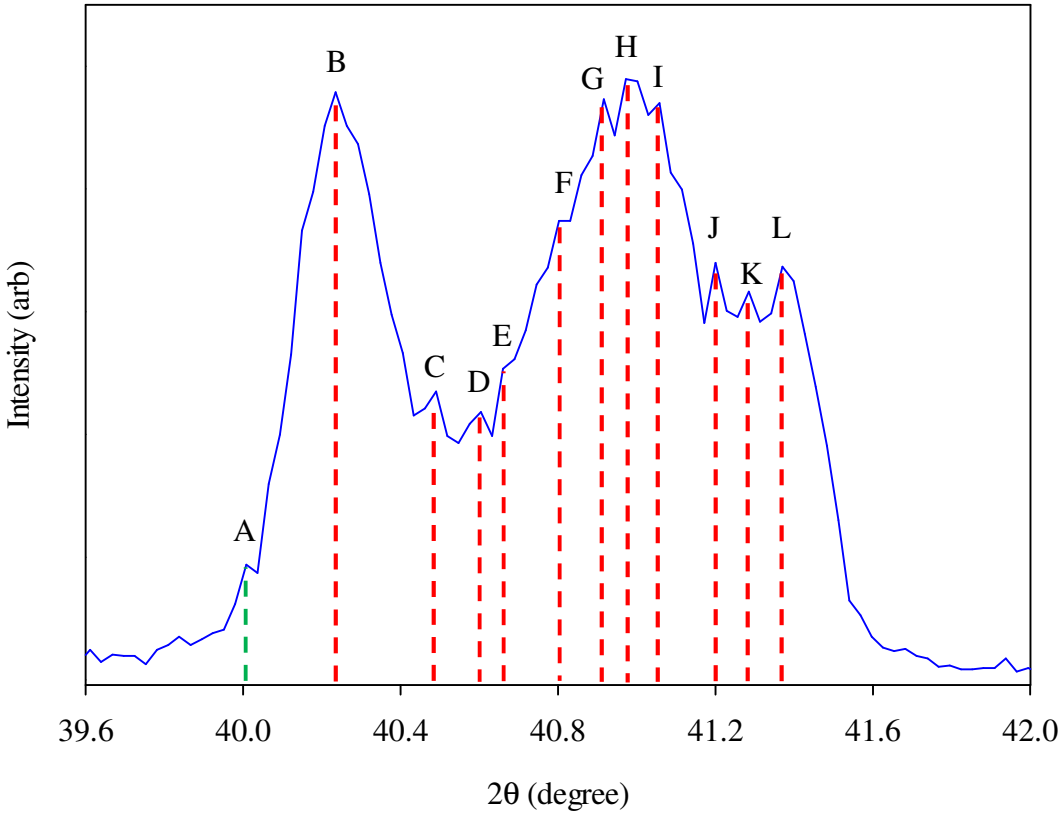

Figure 4.98 Magnification of the Pd-Cu(111) diffraction peak shown in Figure 4.97.

Table 4.12 Compositions determined for points A to L in Figure 4.98.

	Scattering angle, 2θ (degree)	Composition (wt%)
A	40.01	$Pd_{100.0}Cu_{0.0}$
B	40.24	$Pd_{95.8}Cu_{4.2}$
C	40.49	$Pd_{90.2}Cu_{9.8}$
D	40.60	$Pd_{87.6}Cu_{12.4}$
E	40.66	$Pd_{86.3}Cu_{13.7}$
F	40.80	$Pd_{83.0}Cu_{17.0}$
G	40.92	$Pd_{80.1}Cu_{19.9}$
H	40.97	$Pd_{78.7}Cu_{21.3}$
I	41.06	$Pd_{76.6}Cu_{23.4}$
J	41.20	$Pd_{72.8}Cu_{27.2}$
K	41.28	$Pd_{70.5}Cu_{29.5}$
L	41.37	$Pd_{68.2}Cu_{31.8}$

The XPS depth profile analysis for the Type B-B2-F membrane (Figure 4.99) and Type B-B2-P membrane (Figure 4.100) corroborate well with the composition of

Pd-rich Pd-Cu FCC phase determined using the XRD data. Figure 4.99 shows that the top surface of the Type B-B2-F membrane has a composition of $Pd_{95.0}Cu_{5.0}$ wt% whereby the Pd concentration gradually declines with depth and plateaus at 1,470 nm. In contrast, Figure 4.100 reveals a top surface composed of pure Pd for the Type B-B2-P membrane, however, the Pd concentration displays a sharp dip at an approximate depth of 50 nm and continues to gradually decrease and plateau at a depth of 1,500 nm similar to that observed in the Type B-B2-F membrane.

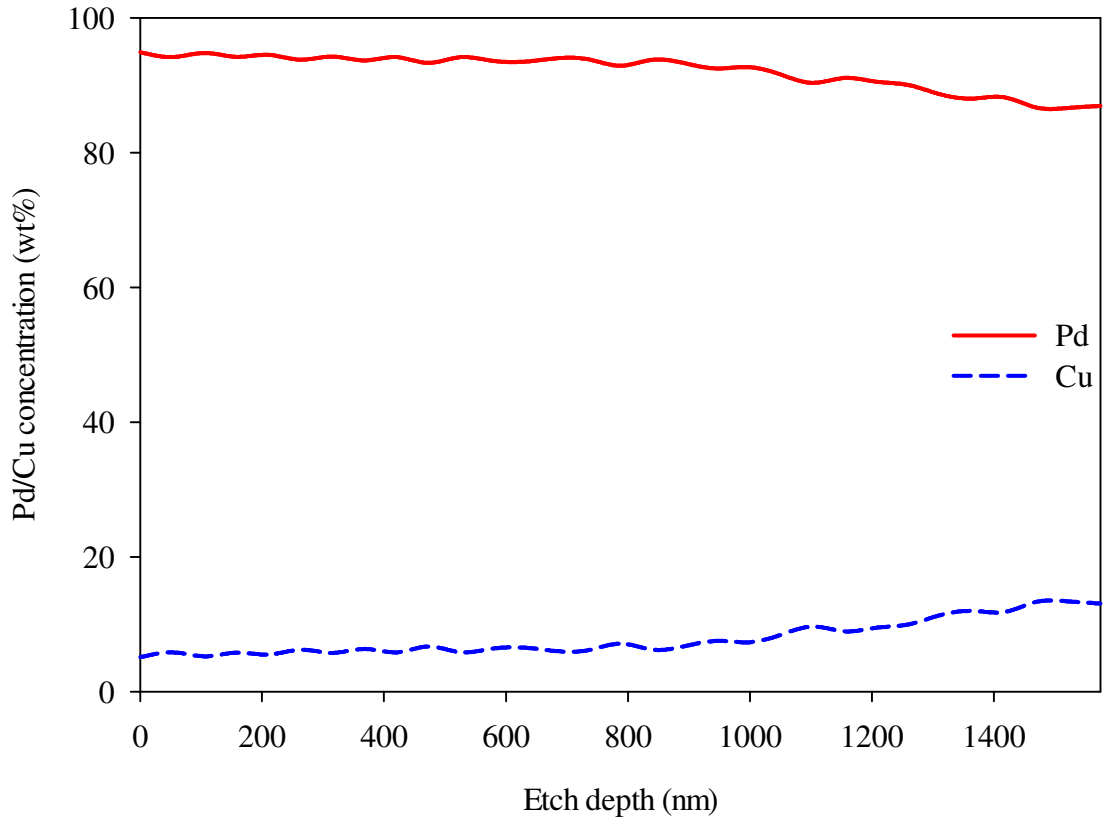

Figure 4.99 XPS depth profile analysis representative of a Type B-B2-F membrane following MPR testing. The etch depth was estimated using a reference etching rate of 0.21 nm s^{-1} for Ta_2O_5.

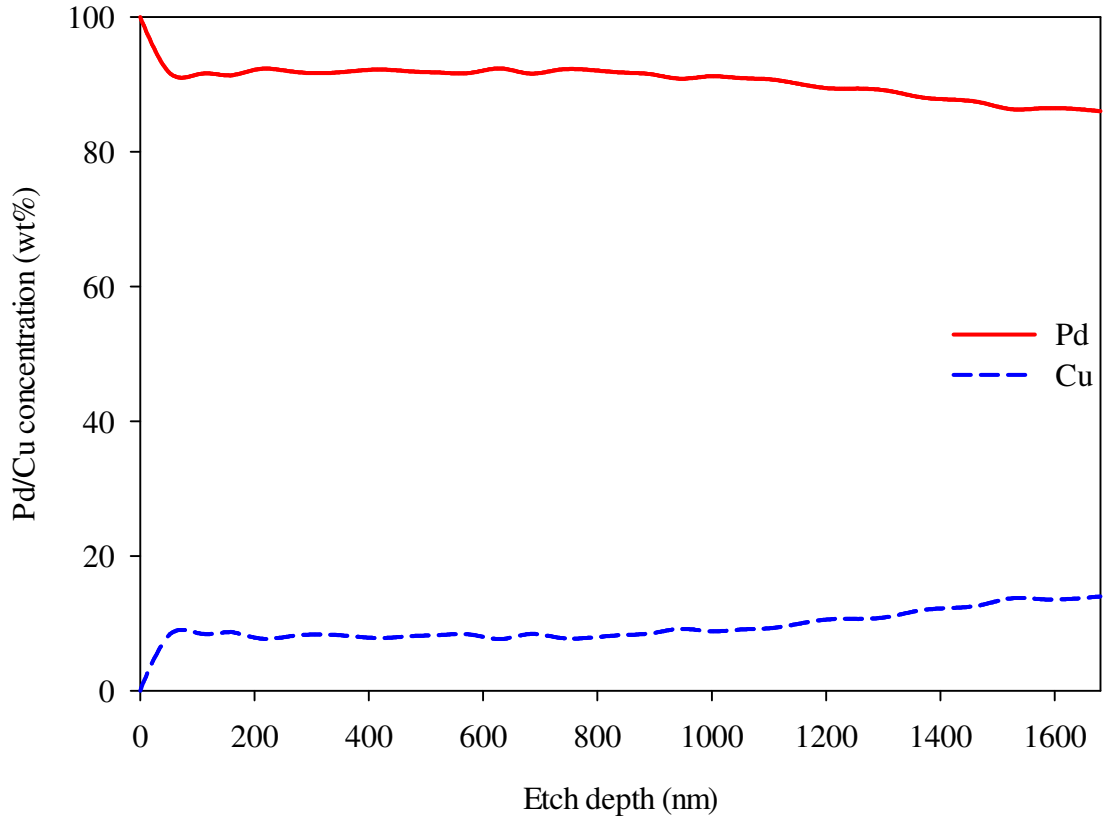

Figure 4.100 XPS depth profile analysis representative of a Type B-B2-P membrane following MPR testing. The etch depth was estimated using a reference etching rate of 0.21 nm s^{-1} for Ta_2O_5.

4.6. Type C membranes

4.6.1. Pre-MPR characterisation

Two Type C membranes were prepared for MPR testing by sputtering one side of the Batch 2 Pd-Cu membranes with Pd for 1,800 seconds in order to determine the effect of Pd thin film thickness on membrane performance. Figure 4.101(a) and (b) shows SEM images of a typical as-deposited Type C-B2 membrane revealing a microstructure containing equiaxed grains akin to that observed with the Type B-B2 membrane. The grain size ranges between 67 and 300 nm which is slightly larger than the grains found in the Type B-B2 membrane (50 – 250 nm) further indicating that grain growth occurs at elevated temperatures brought about by prolonged coating times. This seems logical, as the Type C-B2 series of membranes and foil offcuts had undergone heating during the deposition process so much so that it was necessary for the samples to cool sufficiently prior to handling.

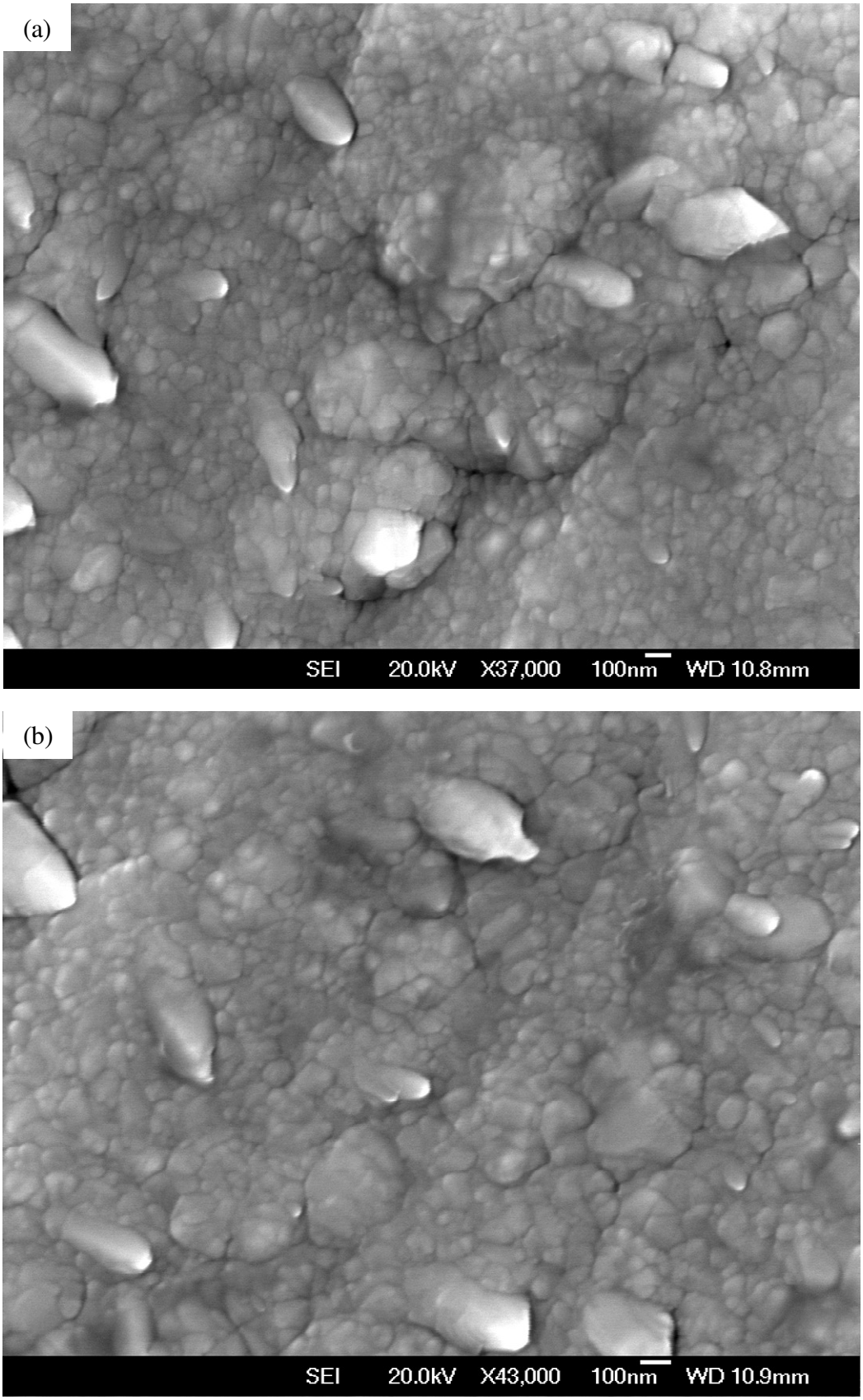

Figure 4.101 SEM micrographs showing the microstructure representative of a Type C-B2 membrane. Coating time was 1,800 seconds with a Pd target current of 1 A.

The thickness of the Pd thin film was approximated using Equation 3.1 to be 1,127 ± 39 nm assuming a fully dense film. A glass slide was routinely Pd sputter-coated alongside the Type C-B2 membranes and offcuts. Profilometry has been performed on this glass slide (Figure 4.102) revealing a Pd thin film thickness of approximately 1,409.6 ± 0.2 nm. Once again, the measured thickness is larger than the estimated figure which further suggests that the Pd thin film is not fully dense.

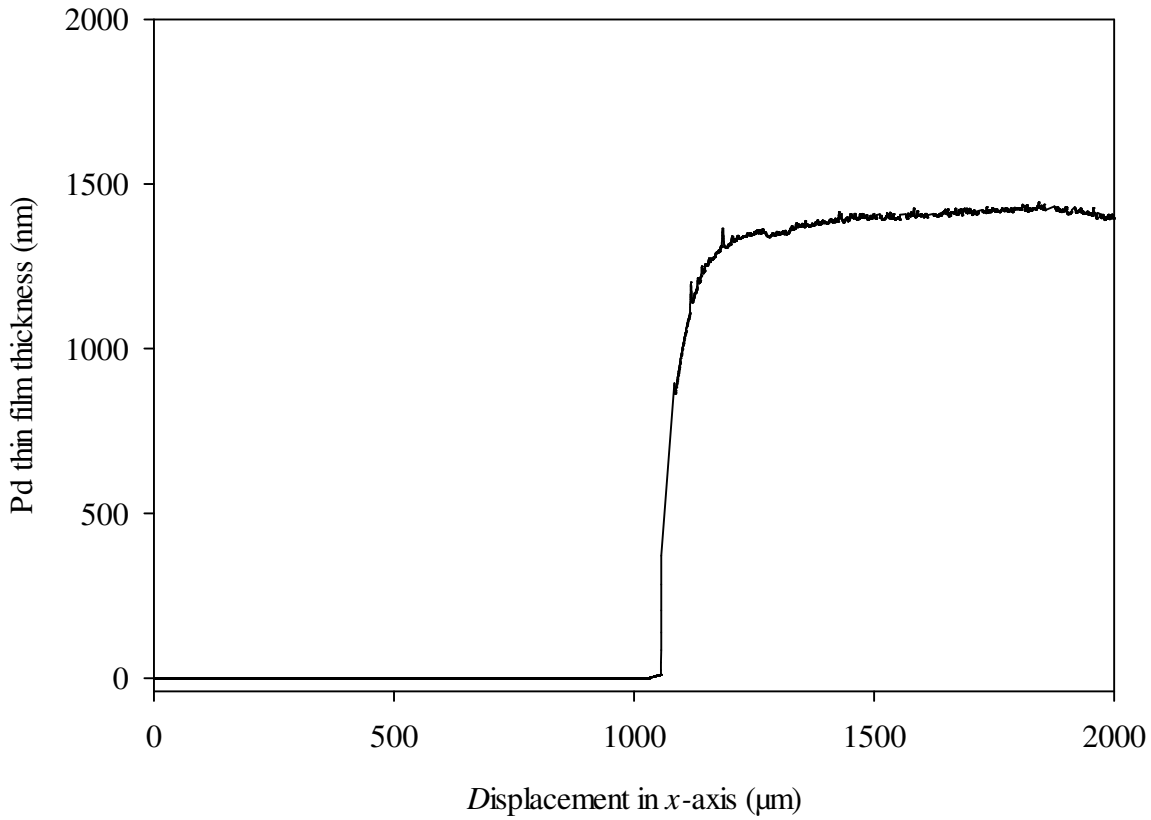

Figure 4.102 Profilometer trace for a glass slide that has been Pd sputter-coated for 1,800 seconds. The first 1,030 µm of the *x*-axis represents the area of the glass slide masked with Kapton tape during Pd deposition.

A representative XRD pattern is illustrated in Figure 4.103 for the Pd sputter-coated side of the Type C-B2 membrane in the as-deposited state indicating the presence of only the FCC phase. The Pd(111) diffraction peak associated with the Pd thin film has the highest relative

intensity giving evidence that the Pd adatoms are preferentially arranged in the most densely packed (111) plane.

A Pd thin film composition of $Pd_{98.1}Cu_{1.9}$ wt% was determined using the scattering angles associated with the Pd(*hkl*) diffraction peaks demonstrating again that interdiffusion between the deposited film and the bulk Pd-Cu membranes occur during the sputtering process owing to the nanocrystalline microstructure of the Type C-B2 membranes/foil offcuts.

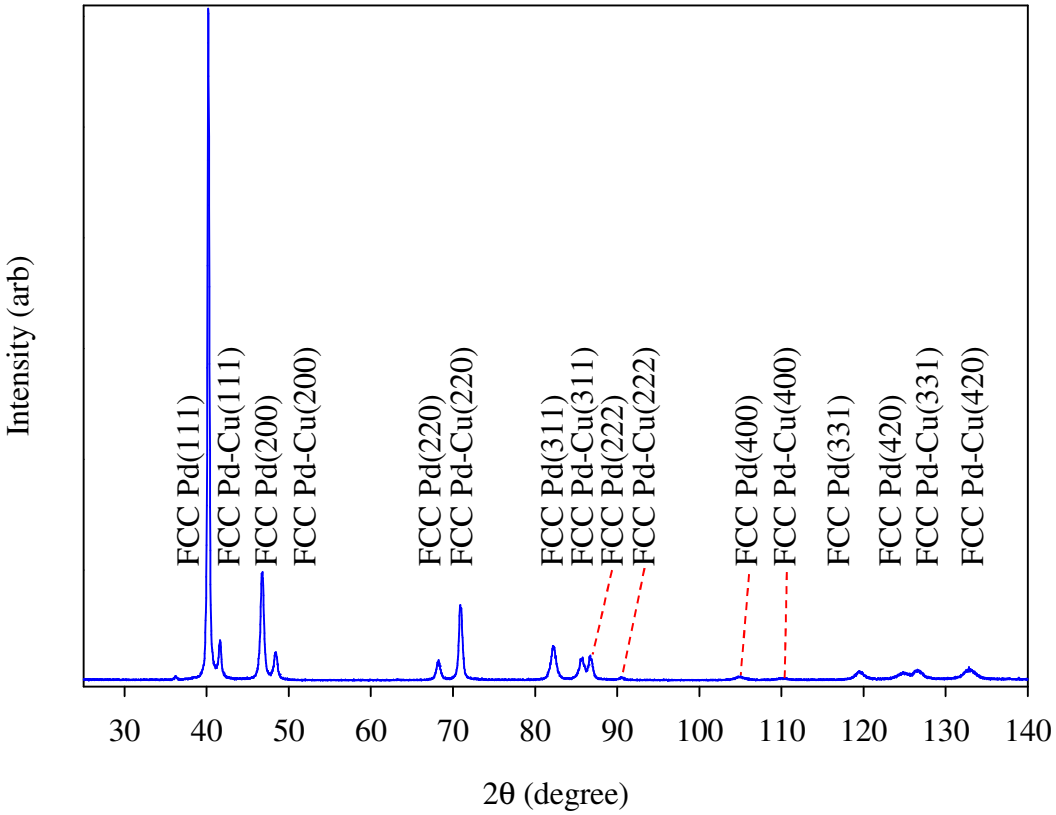

Figure 4.103 XRD pattern which is representative for the Pd sputter-coated side of a Type C-B2 membrane in the as-deposited state before MPR testing.

Alongside the Type C-B2 membranes, three Type C-B2 foil offcuts were prepared which are referred to as Type C-B2 Foil 1, Type C-B2 Foil 2 and Type C-B2 Foil 3. The XPS depth profile analysis for the Type C-B2 Foil 1 is displayed in Figure 4.104 which uses a 50 nm resolution. It is shown that the Cu concentration begins to increase at an approximate depth of

1,520 nm indicating the start of the interdiffusion region and plateaus at around 1,800 nm. It would seem necessary to continue analysis to greater depths in order to reach the end of the interdiffusion region.

Furthermore, it is important to note that the thickness of the Pd thin film determined by XPS (1,520 nm) is different from that measured via profilometry for two main reasons. Firstly, the etch depth is estimated from a Ta_2O_5 standard which may etch at a different rate to a Pd-Cu sample. Moreover, the membranes and foil offcuts were weighed before and after the sputtering process revealing relatively different deposited Pd masses for each sample. It was shown that the Pd sputter-coated membranes and foil offcuts had similar thin film thicknesses as demonstrated by the error margin associated with the estimated thickness (1,127 ± 39 nm).

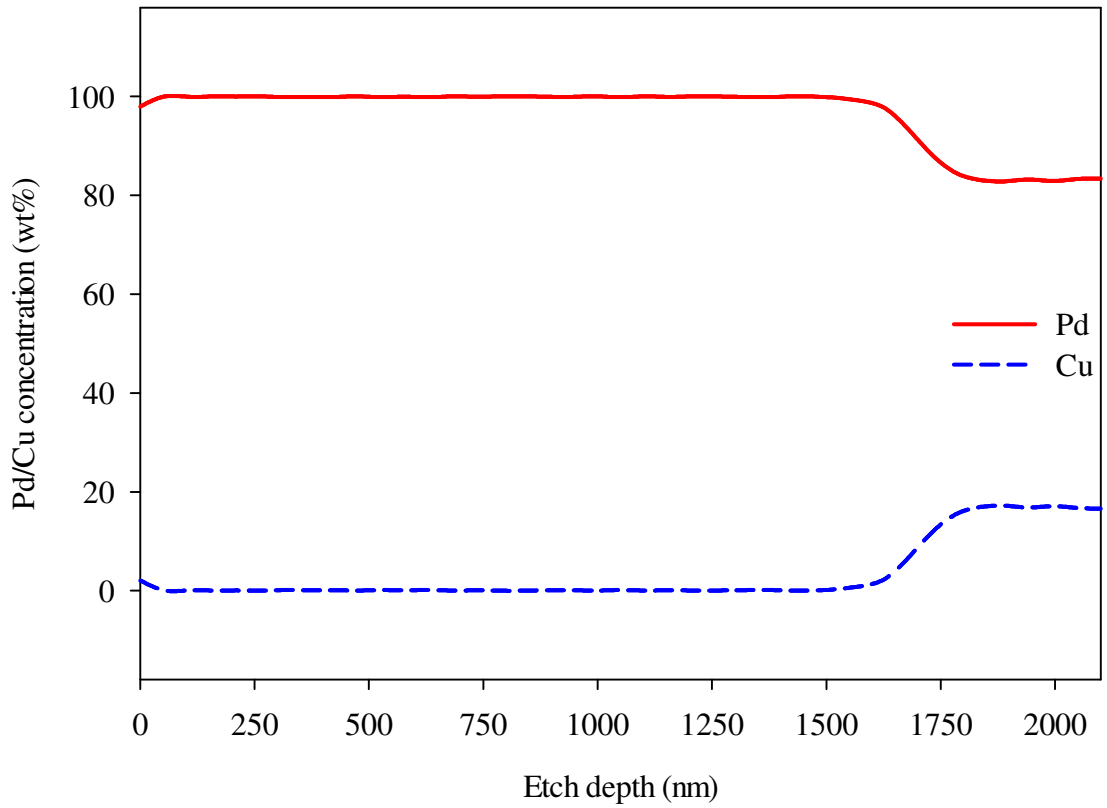

Figure 4.104 XPS depth profile analysis of Type C-B2 Foil 1 in the as-deposited state. The etch depth was estimated using a reference etching rate of 0.21 nm s^{-1} for Ta_2O_5.

4.6.1.1. Effects of temperature and hydrogen pressure on interdiffusion

Figure 4.105(a) and (b) show the VTXRD results for Type C-B2 Foil 2 and Type C-B2 Foil 3, respectively, and are both representative of the Type C-B2-F/P membranes. As evidenced in Figure 4.105(a) by the β-PdH(111) diffraction peak at 2θ = 38.38°, Type C-B2 Foil 2 readily forms the β-PdH phase at 30 °C under 445 kPa of hydrogen pressure. A lattice parameter of 4.059 Å can be calculated from this scattering angle demonstrating that the Pd lattice volume had expanded by 13.6%. This is similar to the lattice volume expansion observed for Type A-B2 Foil 2 (14.3%) and Type B-B2 Foil 2 (13.4%) at the same temperature and hydrogen pressure.

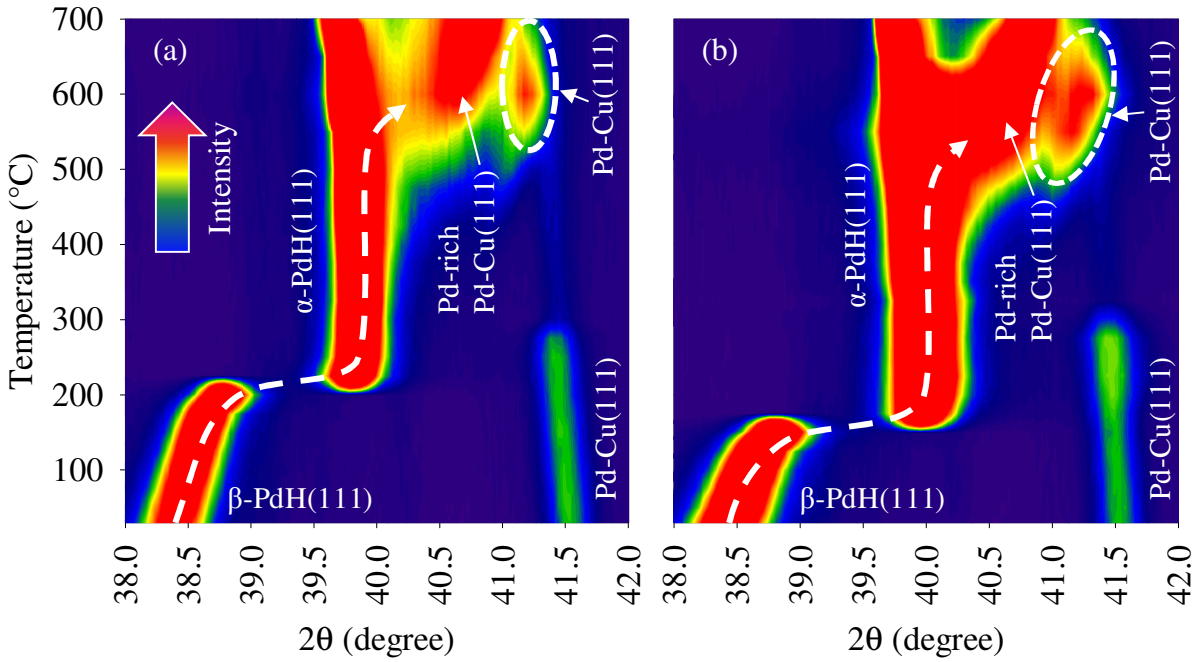

Figure 4.105 VTXRD contour plots tracking the movement of the (a) PdH(111) diffraction peak from the Pd thin film of Type C-B2 Foil 2 under 445 kPa of flowing hydrogen and (b) the PdH(111) diffraction peak from the Pd thin film of Type C-B2 Foil 3 under 100 kPa of flowing hydrogen whilst heating between 30 and 700 °C.

Similar to Type A-B2 Foil 2 and Type B-B2 Foil 2, hydrogen desorption from the Pd thin film in Type C-B2 Foil 2 occurs at 200 °C in order to accommodate the β-PdH → α-PdH phase transformation. This is indicated by the appearance of the α-PdH(111) diffraction peak

at 2θ = 39.79°. Significant interdiffusion takes place between 400 and 700 °C, however the α-PdH phase appears to be stable even up to 700 °C meaning that the Pd thin film does not completely interdiffuse with the bulk Pd-Cu foil under the conditions used in the VTXRD experiment. Furthermore, the Pd-Cu(111) diffraction peak associated with the bulk Pd-Cu foil disappears at 300 °C and reappears above 500 °C to merge with the Pd-rich Pd-Cu(111) diffraction peak at higher temperatures.

At 30 °C and 100 kPa of hydrogen pressure, Figure 4.105(b) reveals that in Type C-B2 Foil 3 the β-PdH(111) diffraction peak appears at 2θ = 38.45°. This scattering angle corresponds to a lattice parameter of 4.052 Å representing a 13.0% Pd lattice volume expansion. Like in Type A-B2 Foil 3 and Type B-B2 Foil 3, the β-PdH → α-PdH phase transformation occurs at 150 °C in Type C-B2 Foil 3 as demonstrated by the formation of the α-PdH(111) diffraction peak at 2θ = 39.96°. Similar to Type C-B2 Foil 2, interdiffusion in Type C-B2 Foil 3 takes place between 400 and 650 °C and the α-PdH phase remains stable up until 700 °C showing that the Pd thin film does not fully interdiffuse with the bulk Pd-Cu foil at a hydrogen pressure of 100 kPa. In addition, the Pd-Cu(111) diffraction peak originating from the bulk Pd-Cu foil disappears at 325 °C and reappears at 500 °C to finally merge with the Pd-rich Pd-Cu(111) diffraction peak.

Following the VTXRD runs, XPS depth profile analysis was performed on Type C-B2 Foil 2 and Type C-B2 Foil 3 with the results displayed in Figure 4.106 and Figure 4.107, respectively. Figure 4.106 shows that the Pd sputter-coated side of Type C-B2 Foil 2 has a Pd-rich Pd-Cu FCC phase composition of $Pd_{79.7}Cu_{20.3}$ wt%. The Cu concentration immediately increases and stabilises at a depth of around 50 nm and then steadily increases over the analysis depth. Figure 4.107 shows that the top surface of Type C-B2 Foil 3 has a

composition of $Pd_{76.1}Cu_{23.9}$ wt%. The Cu concentration experiences a slight dip at a depth of 50 nm after which the composition remains relatively constant across the analysis depth.

Interestingly, the Pd-rich Pd-Cu FCC phase compositions for Type C-B2 Foil 2 and Type C-B2 Foil 3 have a higher Cu content compared to the Pd-rich Pd-Cu FCC phase present in Type B-B2 Foil 2 ($Pd_{85.6}Cu_{14.4}$ wt%) and Type B-B2 Foil 3 ($Pd_{89.5}Cu_{10.5}$ wt%). This could be attributed to the existence of a larger Cu concentration gradient introduced by the relatively thicker Pd thin film (~1,400 nm) in Type C-B2 Foil 2 and Type C-B2 Foil 3 creating a greater driving force for Cu interdiffusion into the Pd thin film.

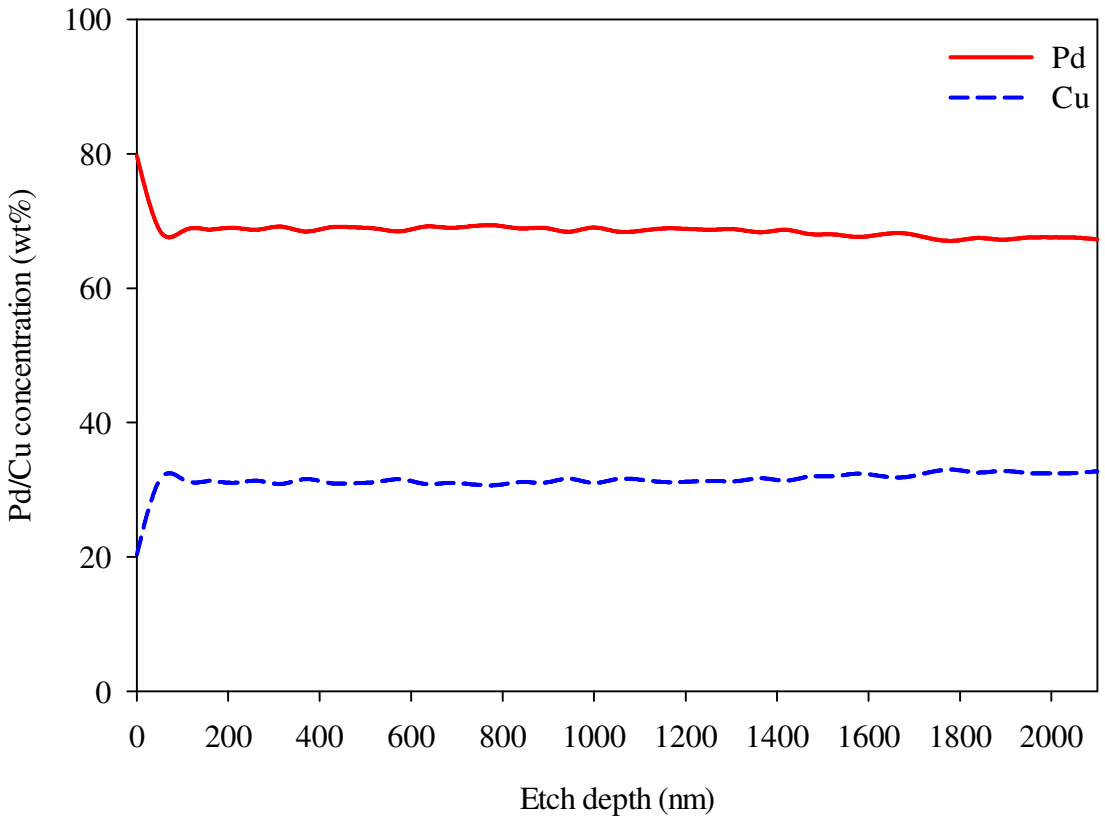

Figure 4.106 XPS depth profile analysis of Type C-B2 Foil 2 following VTXRD under 445 kPa of hydrogen pressure. The etch depth was estimated using a reference etching rate of 0.21 nm s^{-1} for Ta_2O_5.

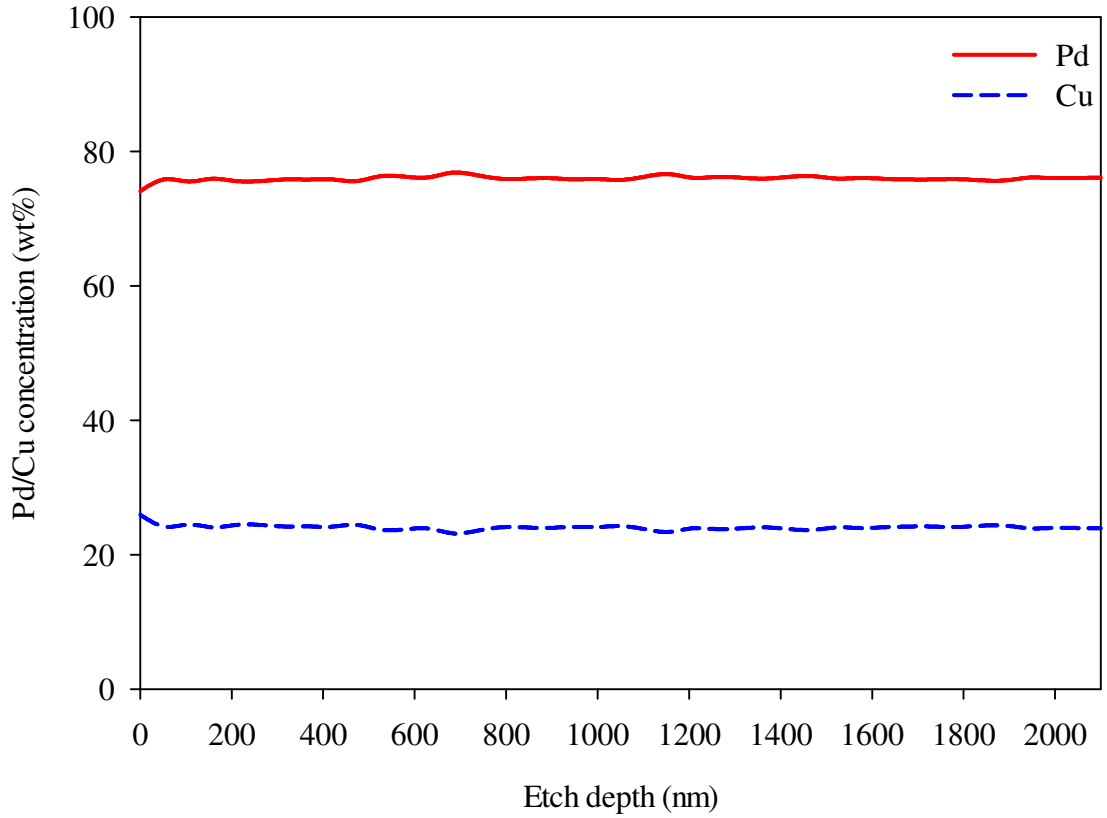

Figure 4.107 XPS depth profile analysis of Type C-B2 Foil 3 following VTXRD under 100 kPa of hydrogen pressure. The etch depth was estimated using a reference etching rate of 0.21 nm s^{-1} for Ta_2O_5.

4.6.2. MPR results

4.6.2.1. Pd thin film positioned on the feed side

Figure 4.108 shows the initial three cycles completed by the Type C-B2-F membrane. For the first cycle, hydrogen permeation commences at 340 °C which is a lower starting temperature in comparison to the Batch 2 Pd-Cu membranes (400 °C), Type A-B2-F membrane (380 °C) and the Type B-B2-F membrane (390 °C). Subsequently, hydrogen permeation begins at 200 °C during the second cycle and 190 °C during the third cycle. Also, this is relatively lower than the corresponding hydrogen permeation start temperatures for the second and third cycles completed by the Batch 2 Pd-Cu membranes (330 and 320 °C, respectively), Type A-B2-F membrane (270 and 260 °C, respectively) and the Type B-B2-F membrane (210 and 200 °C, respectively).

At 450 °C, the Type C-B2-F membrane achieves a hydrogen permeability of 1.09×10^{-8} mol m^{-1} s^{-1} Pa$^{-0.5}$ during the third cycle. This value is 59%, 24% and 9% higher than the values achieved at the same temperature and cycle by the Batch 2 Pd-Cu membranes, the Type A-B2-F membrane and the Type B-B2-F membrane, respectively.

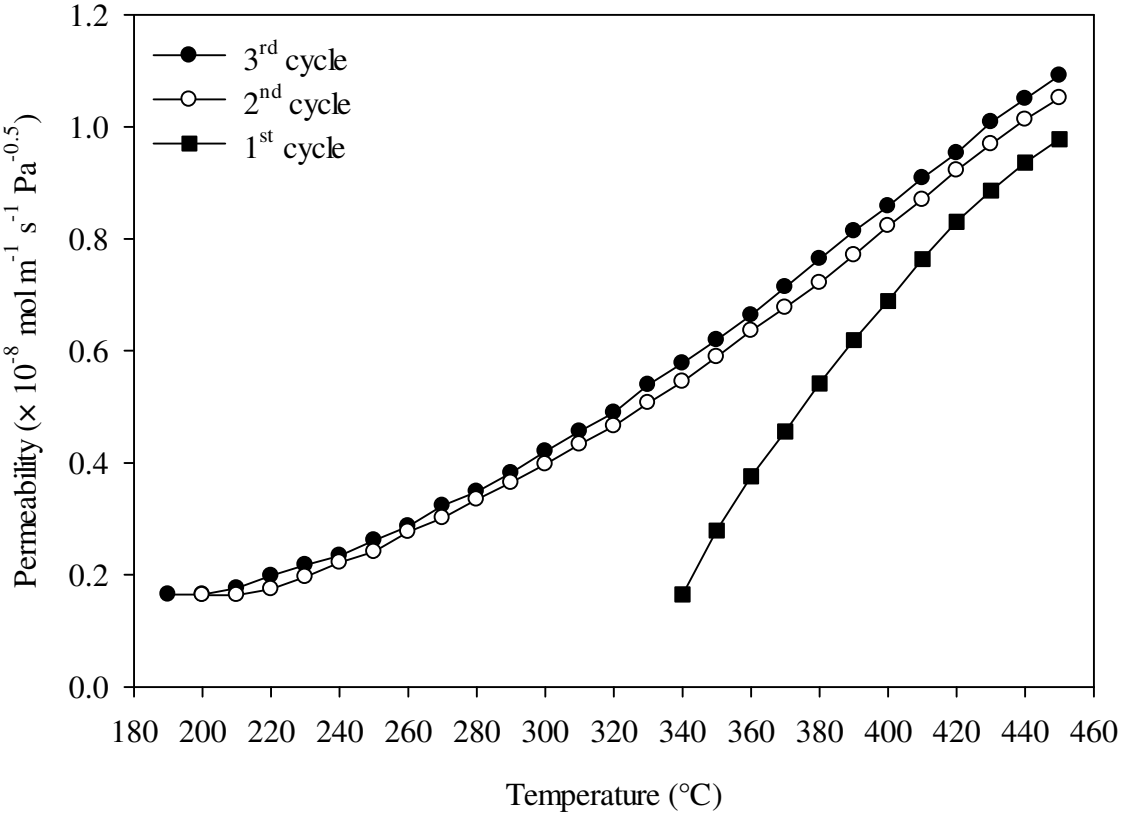

Figure 4.108 Hydrogen permeability as a function of temperature for the Type C-B2-F membrane. The plot shows the first three cycles heated between 50 and 450 °C using a hydrogen feed pressure of 445 kPa and permeate pressure of 100 kPa assuming an *n*-value of 0.5.

The *n*-value measurement results obtained from the Type C-B2-F membrane are depicted in Figure 4.109 and Figure 4.110 showing the data constrained to 0.5 and the best fit value of 0.56, respectively. In addition, Figure 4.111 illustrates the third cycle completed by the Type C-B2-F membrane where the solid symbol curve is calculated using an *n*-value of 0.5 and the open symbol curve utilises the best fit value of 0.56.

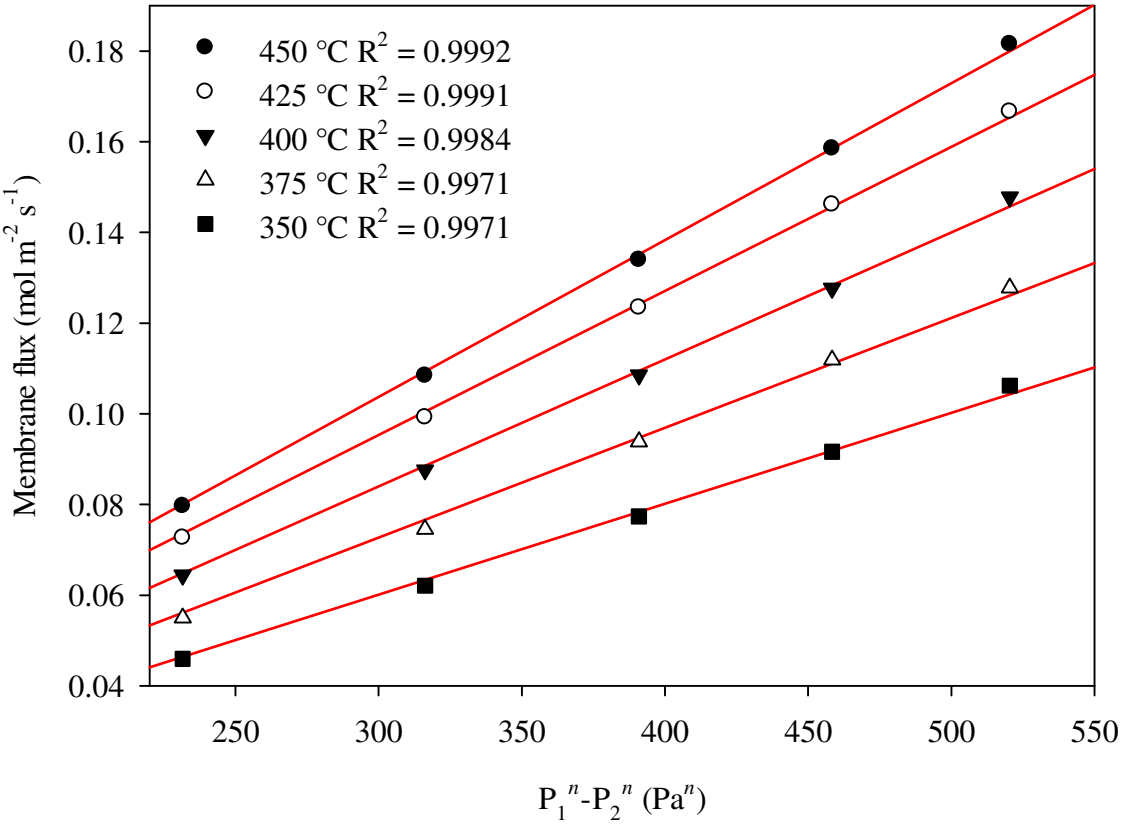

Figure 4.109 Membrane flux as a function of hydrogen differential pressure with *n* constrained to 0.5.

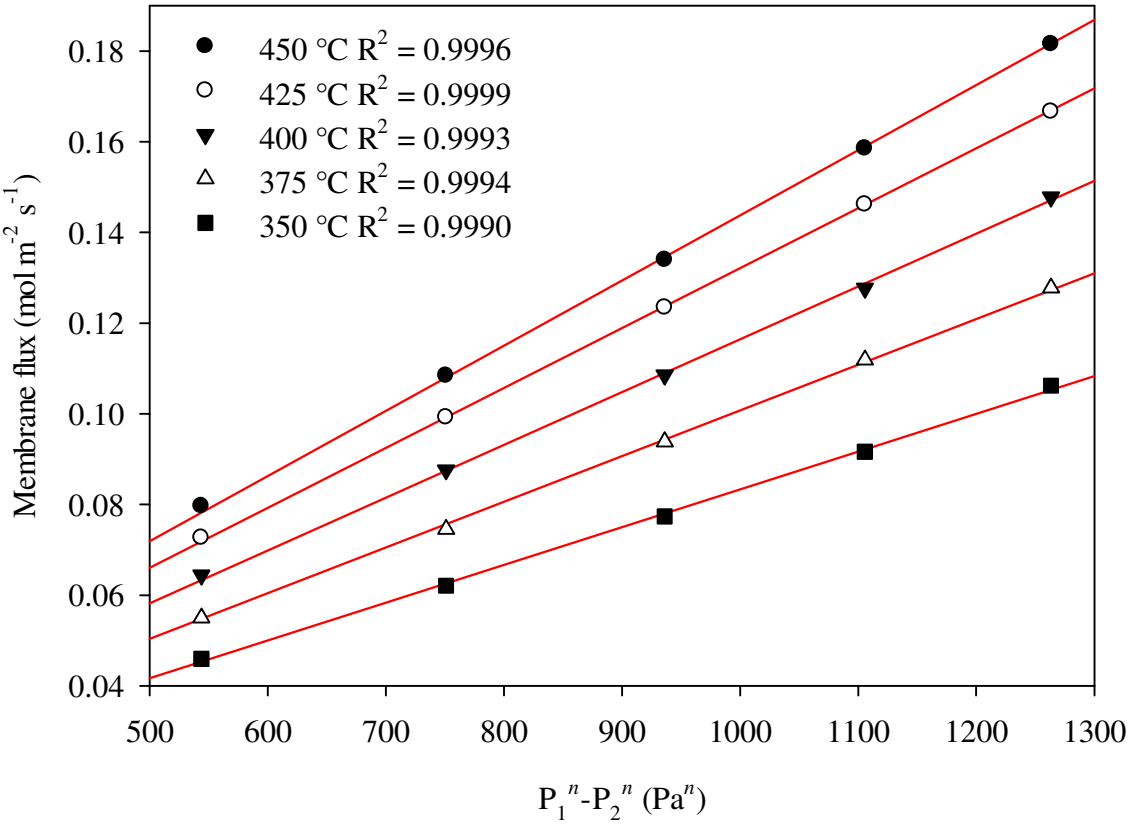

Figure 4.110 Membrane flux as a function of hydrogen differential pressure with *n* constrained to the best fit value of 0.56.

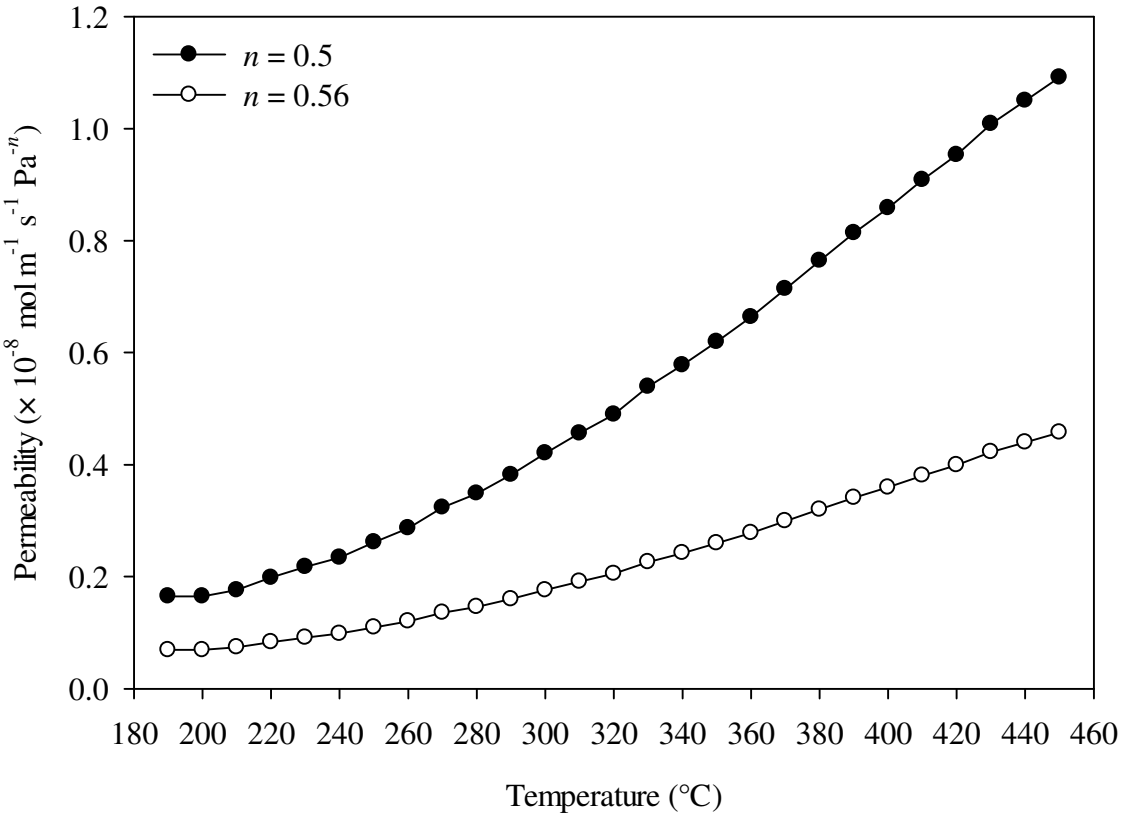

Figure 4.111 Hydrogen permeability as a function of temperature showing the third cycle for the Type C-B2-F membrane. A hydrogen feed pressure of 445 kPa and permeate pressure of 100 kPa was applied during measurements. The solid symbol curve was calculated using an *n*-value of 0.5 whereas the open symbol curve uses the best fit *n*-value of 0.56.

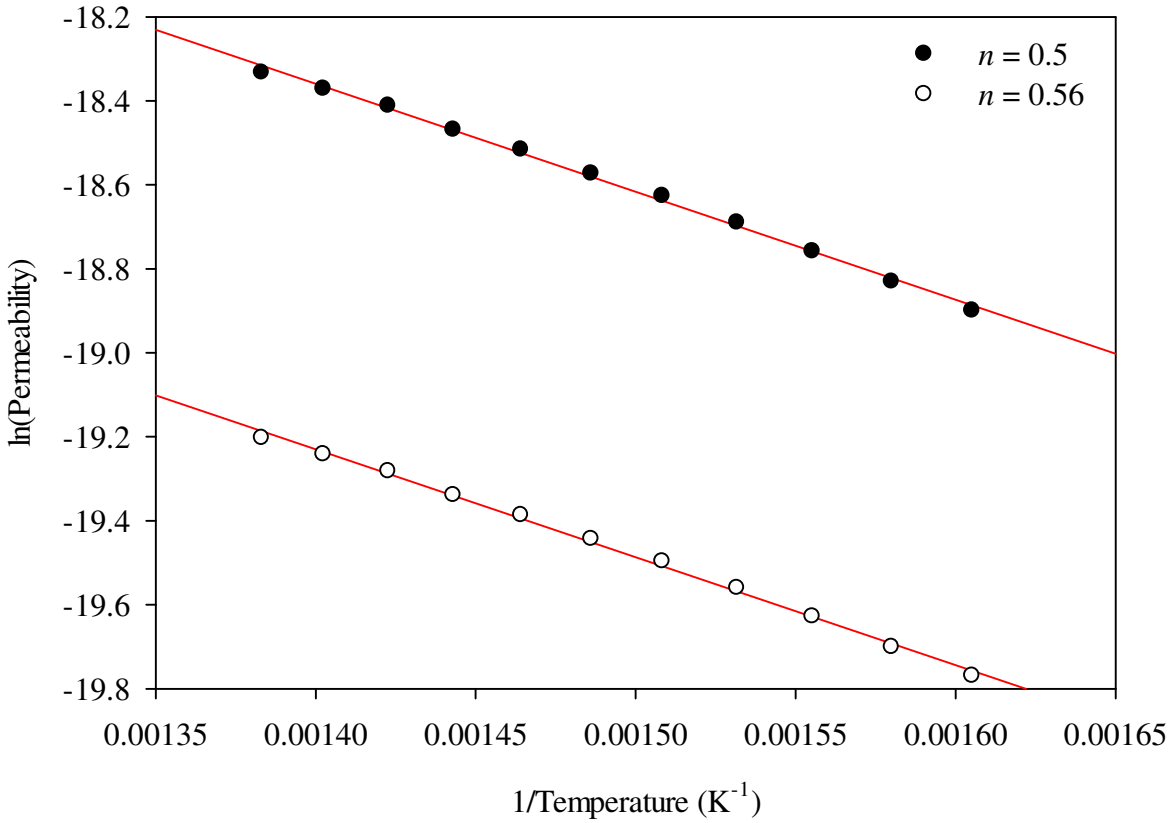

Figure 4.112 Arrhenius plot of the hydrogen permeability data shown in Figure 4.111 between 350 and 450 °C. The solid symbol curve was calculated using an *n*-value of 0.5 whereas the open symbol curve uses the best fit *n*-value of 0.56.

From Figure 4.112, the following general permeability formulae (350 – 450 °C) can be derived for the Type C-B2-F membrane using an *n*-value of 0.5 and the best fit value of 0.56 as demonstrated in Equation 4.26 and Equation 4.27, respectively. Assuming an *n*-value of 0.5, the E_Φ for the Type C-B2-F membrane is 20.52 kJ mol^{-1}. This value is 51%, 31% and 14% lower than those determined for the Batch 2 Pd-Cu membranes, Type A-B2-F membrane and Type B-B2-F membrane, respectively.

$$\Phi_{n=0.5} = 3.44 \times 10^{-7} exp\left(\frac{-20.52 \times 10^3}{RT}\right) \qquad \text{Equation 4.26}$$

$$\Phi_{n=0.56} = 1.44 \times 10^{-7} exp\left(\frac{-20.52 \times 10^3}{RT}\right) \qquad \text{Equation 4.27}$$

Contrary to the observed trend thus far, Figure 4.113 shows that the *n*-value generally decreases with temperature. This suggests that Sieverts' law is more favoured at higher temperatures when the ~1,400 nm thick Pd thin film of the Type C-B2-F membrane is positioned on the feed side during MPR testing.

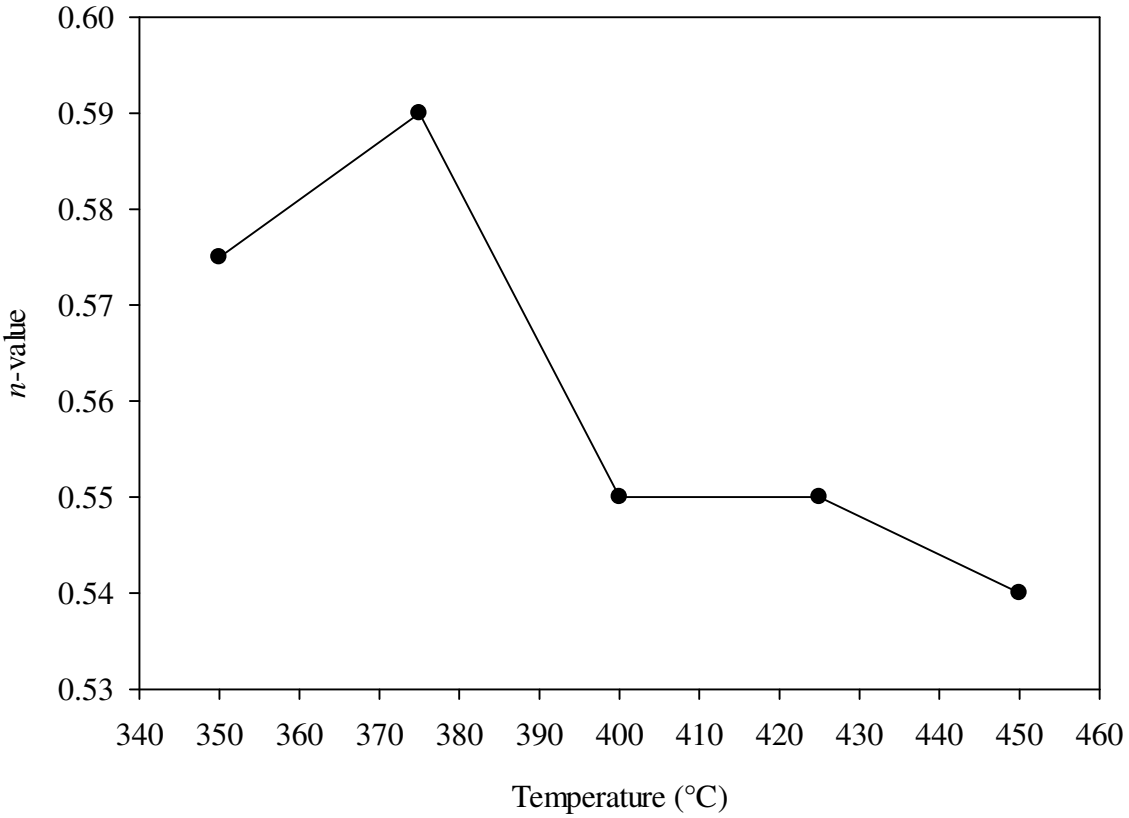

Figure 4.113 Variation of *n*-value as a function of temperature for the Type C-B2-F membrane.

4.6.2.2. Pd thin film positioned on the permeate side

The first three cycles completed by the Type C-B2-P membrane are displayed in Figure 4.114. During the first cycle, hydrogen permeation begins at 380 °C which is lower than the first cycle hydrogen permeation start temperature observed for the Batch 2 Pd-Cu membranes (400 °C) but higher than that observed for the Type A-B2-P membrane (360 °C) and the Type B-B2-P membrane (350 °C). A peculiar feature of this set of results is that the hydrogen permeability measured during the first cycle surpasses that measured in the second and third

cycle. A similar phenomenon was witnessed with the Type A-B1-F membrane as shown in Figure 4.58. As previously mentioned, this irregularity may be caused by the brief inability of the back pressure regulator to stabilise the permeate pressure.

The second and third cycle both begin hydrogen permeation at 300 °C displaying comparable hydrogen permeability values as a function of temperature. This hydrogen permeation start temperature is identical to the corresponding cycles for the Type B-B2-P membrane, similar to that shown for the Type A-B2-P membrane (290 °C) and is lower than that found for the Batch 2 Pd-Cu membranes (320 and 330 °C).

The Type C-B2-P membrane achieves a hydrogen permeability of 7.43×10^{-9} mol m^{-1} s^{-1} $Pa^{-0.5}$ at 450 °C during the third cycle. For the same temperature and cycle, this value is 8% higher than that achieved by the Batch 2 Pd-Cu membranes and Type B-B2-P membrane yet 11% lower compared to that measured for the Type A-B2-P membrane.

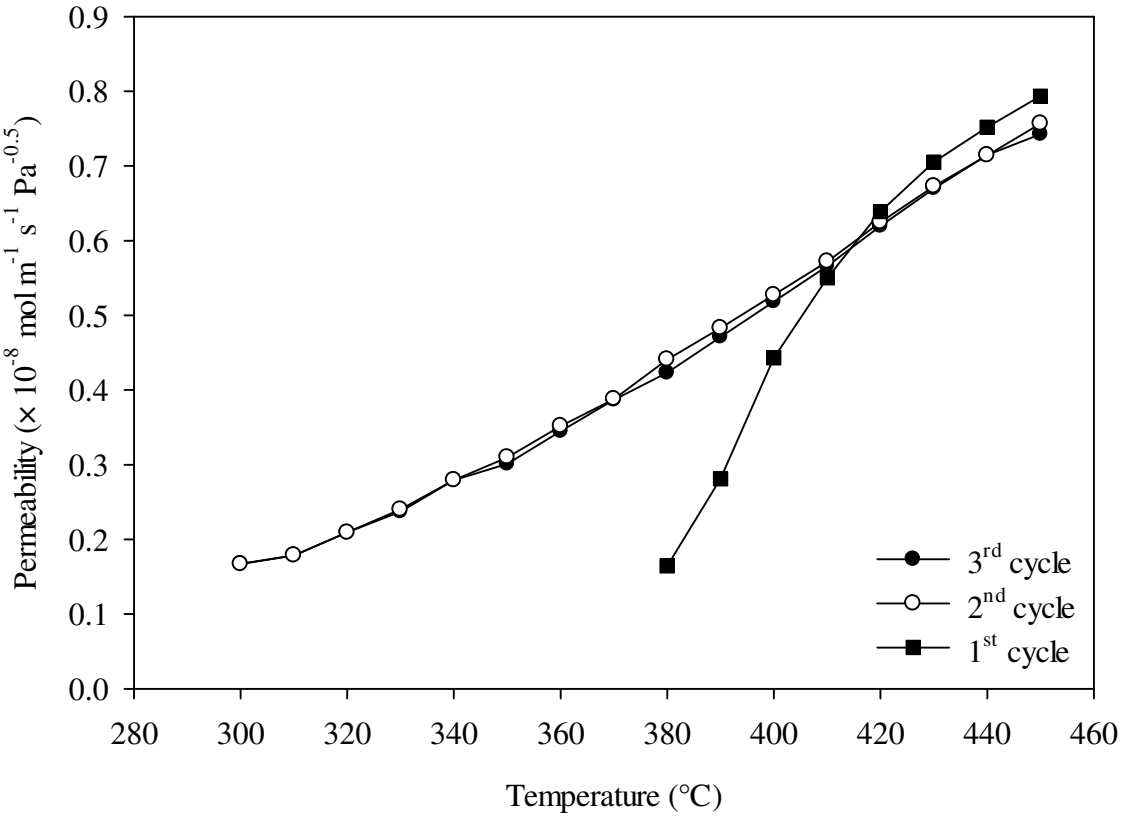

Figure 4.114 Hydrogen permeability as a function of temperature for the Type C-B2-P membrane. The plot shows the first three cycles heated between 50 and 450 °C using a hydrogen feed pressure of 445 kPa and permeate pressure of 100 kPa assuming an *n*-value of 0.5.

The *n*-value measurements for the Type C-B2-P membrane are displayed with the data constrained to 0.5 and the best fit value of 0.59 as shown in Figure 4.115 and Figure 4.116, respectively. Figure 4.117 illustrates the third cycle completed by the Type C-B2-P membrane whereby the solid symbol curve has been calculated using an *n*-value of 0.5 and the open symbol curve has been calculated using the best fit value of 0.59.

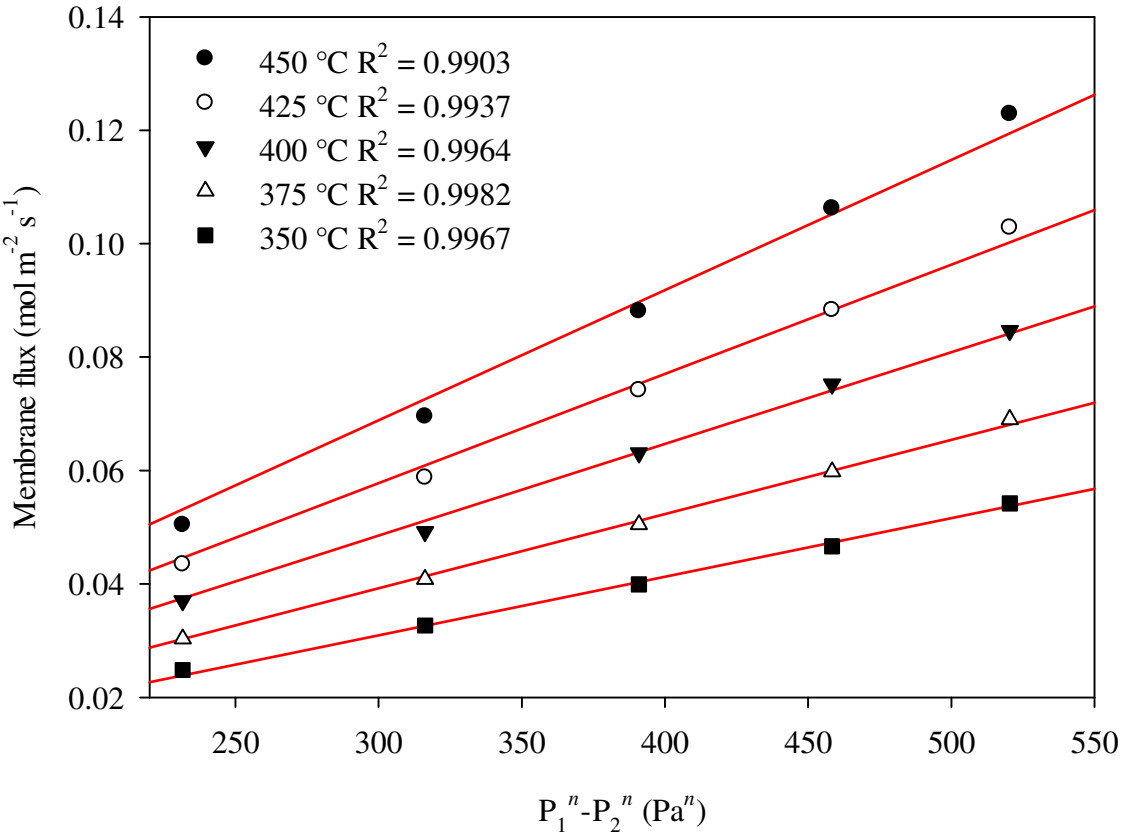

Figure 4.115 Membrane flux as a function of hydrogen differential pressure with *n* constrained to 0.5.

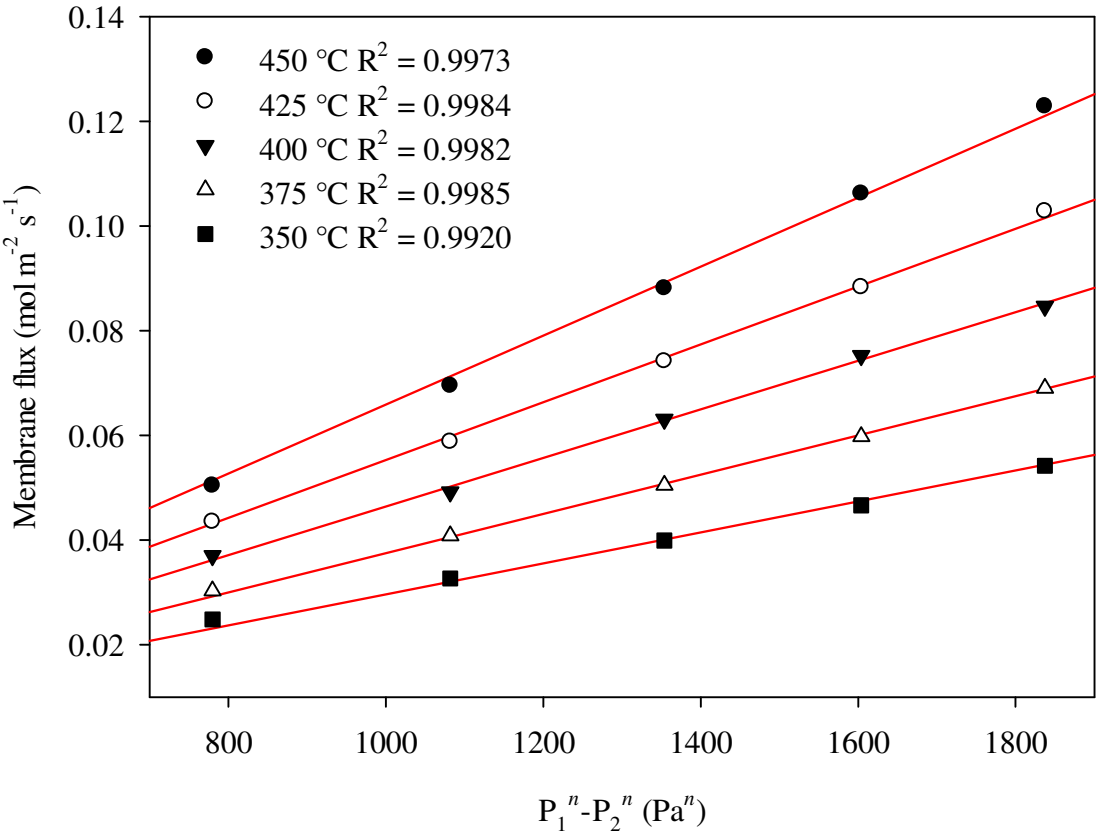

Figure 4.116 Membrane flux as a function of hydrogen differential pressure with *n* constrained to the best fit value of 0.59.

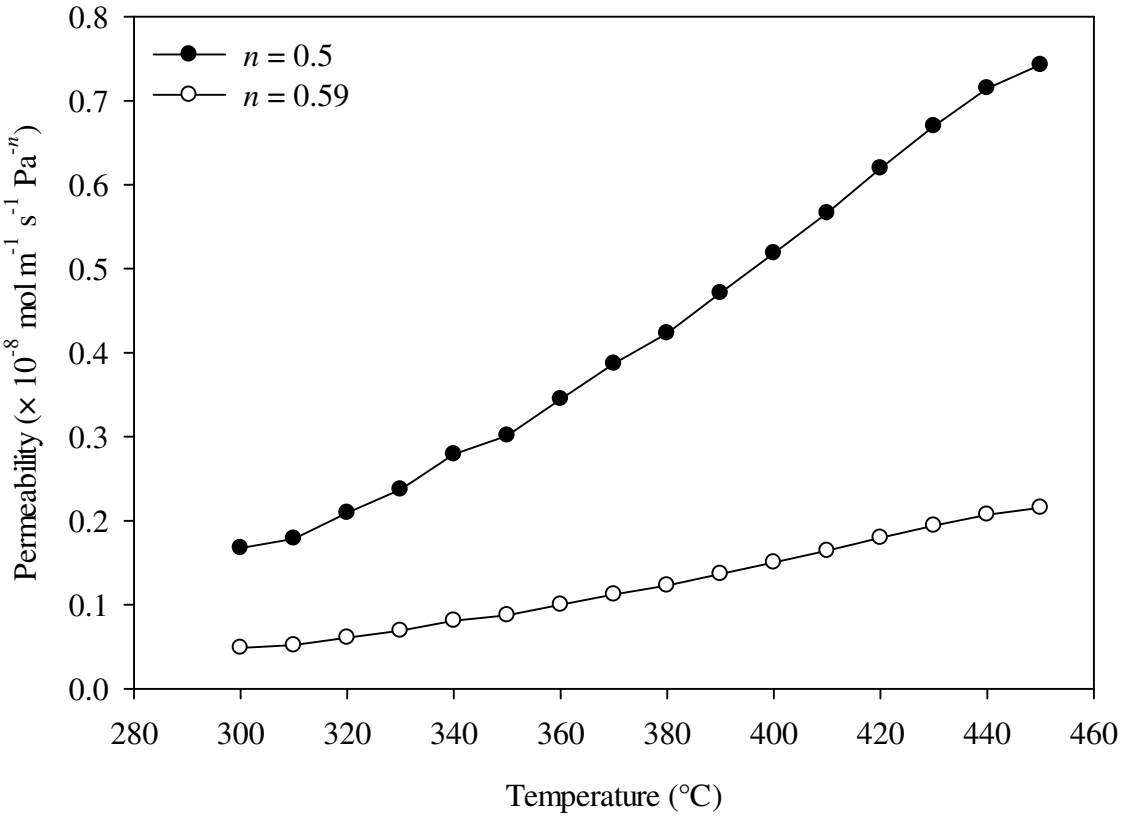

Figure 4.117 Hydrogen permeability as a function of temperature showing the third cycle for the Type C-B2-P membrane. A hydrogen feed pressure of 445 kPa and permeate pressure of 100 kPa was applied during measurements. The solid symbol curve was calculated using an *n*-value of 0.5 whereas the open symbol curve uses the best fit *n*-value of 0.59.

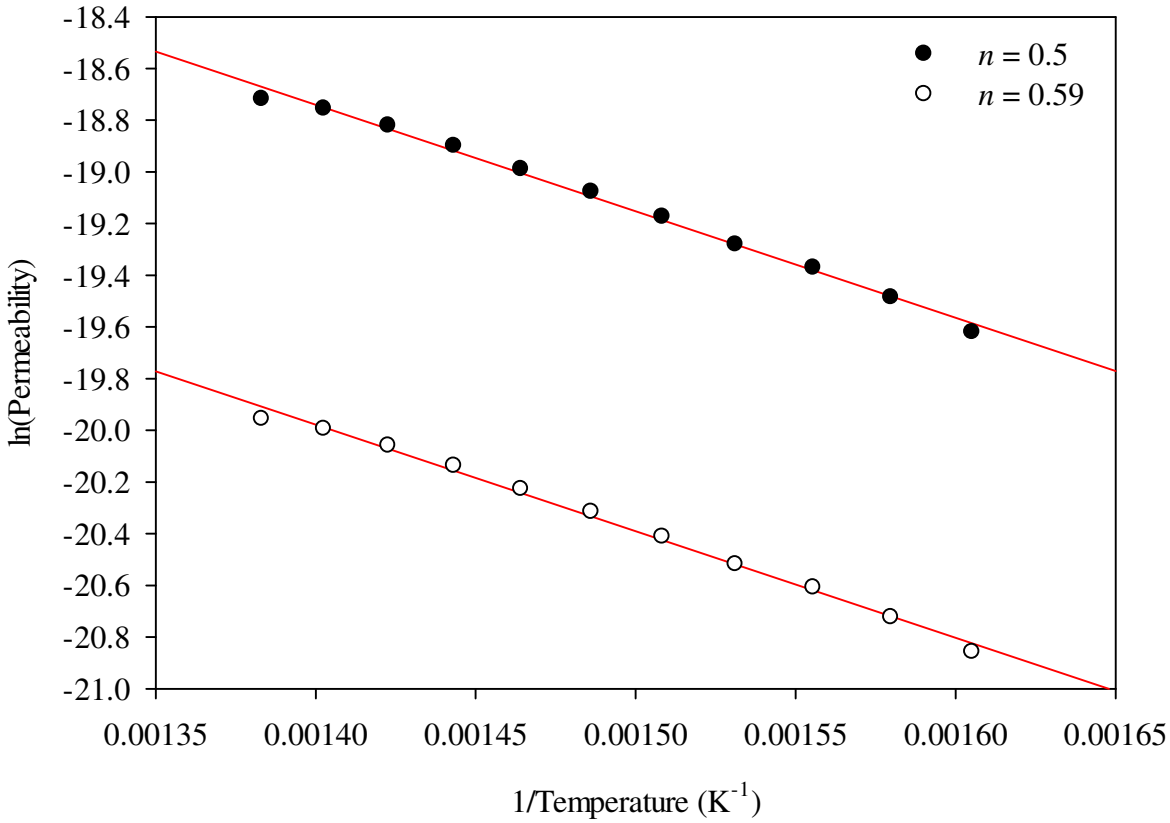

Figure 4.118 Arrhenius plot of the hydrogen permeability data shown in Figure 4.117 between 350 and 450 °C. The solid symbol curve was calculated using an *n*-value of 0.5 whereas the open symbol curve uses the best fit *n*-value of 0.59.

The following general permeability formulae (350 – 450 °C) for the Type C-B2-P membrane can be derived from Figure 4.118 for an *n*-value of 0.5 and the best fit value of 0.59 as shown in Equation 4.28 and Equation 4.29, respectively.

$$\Phi_{n=0.5} = 2.19 \times 10^{-6} exp\left(\frac{-33.91 \times 10^3}{RT}\right) \qquad \text{Equation 4.28}$$

$$\Phi_{n=0.59} = 6.35 \times 10^{-7} exp\left(\frac{-33.91 \times 10^3}{RT}\right) \qquad \text{Equation 4.29}$$

Assuming an *n*-value of 0.5, the E_Φ value calculated for the Type C-B2-P membrane is 33.91 kJ mol^{-1} which is 19%, 7% and 11% lower than the values calculated for the

Batch 2 Pd-Cu membranes, Type A-B2-P membrane and Type B-B2-P membrane, respectively.

In contrast to the Type C-B2-F membrane, Figure 4.119 demonstrates that the *n*-value for the Type C-B2-P membrane undergoes a drastic increase over the temperature range showing a significant deviation from Sieverts' law; however it is still evident that hydrogen diffusion remains the rate limiting step in the permeation process.

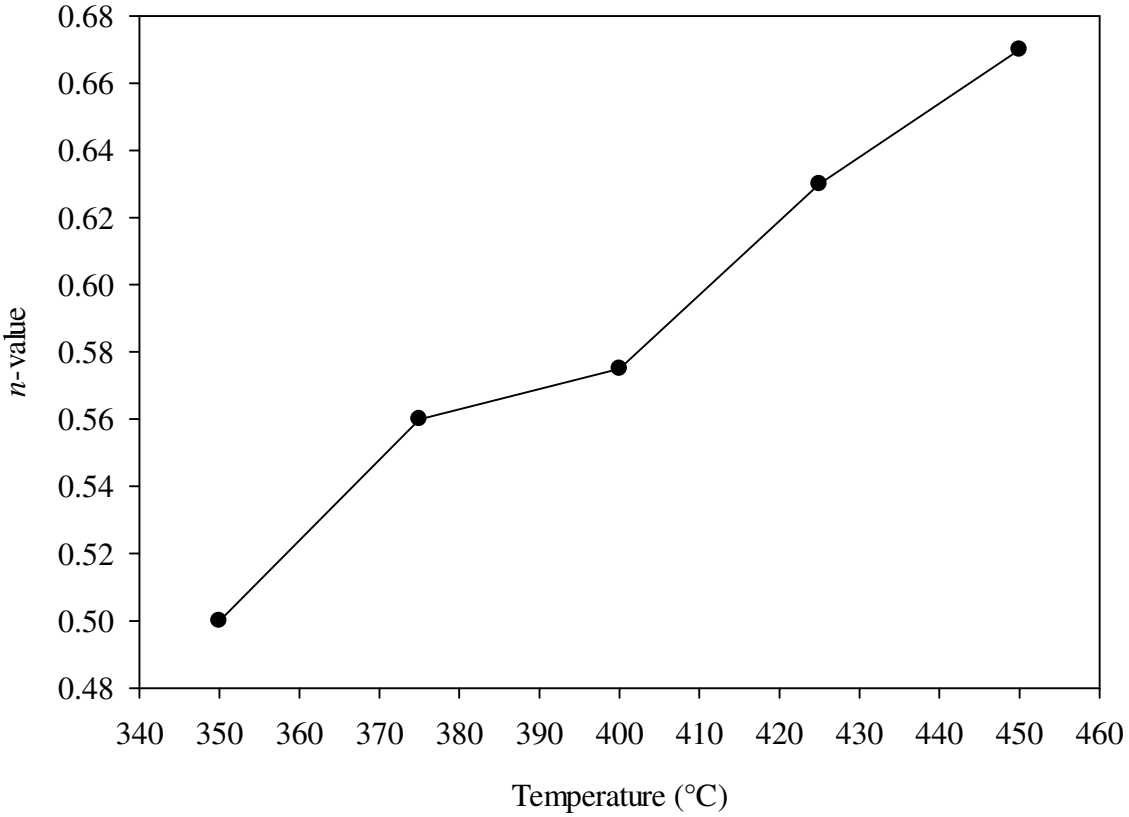

Figure 4.119 Variation of *n*-value as a function of temperature for the Type C-B2-P membrane.

4.6.3. Post-MPR characterisation

Similar to the Type A-B1-F/P and Type A/B-B2-F/P membranes, XRD reveals that the Type C-B2-F membrane and the Type C-B2-P membrane contain a mixture of the BCC phase and FCC phase following MPR testing as shown in Figure 4.120 and Figure 4.122, respectively.

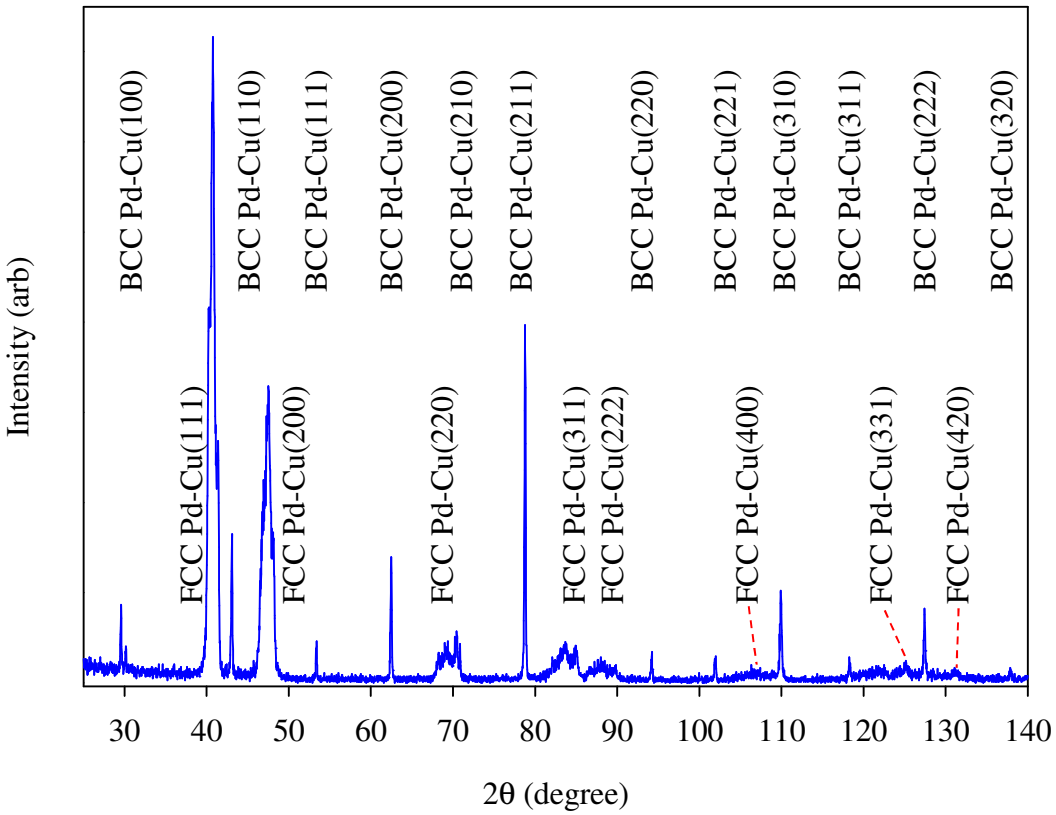

Figure 4.120 XRD pattern which is representative for the Pd sputter-coated side of the Type C-B2-F membrane following MPR testing.

Figure 4.121 shows a magnified view of the Pd-Cu(111) diffraction peak associated with the Pd-rich Pd-Cu FCC phase depicted in Figure 4.120. The asymmetry in the peak is a clear sign of interdiffusion occurring between the Pd thin film and bulk Pd-Cu membrane revealing a wide compositional gradient in the Pd sputter-coated side of the Type C-B2-F membrane as shown in Table 4.13. The composition of the BCC phase detected on the Pd sputter-coated side of the Type C-B2-F membrane is $Pd_{62.7}Cu_{37.3}$ wt%. The non-coated side contained only the BCC phase with a composition of $Pd_{63.0}Cu_{37.0}$ wt%.

Furthermore, Figure 4.123 gives a more detailed view of the Pd-Cu(111) diffraction peak corresponding to the Pd-rich Pd-Cu FCC phase displayed in Figure 4.122. This reveals a wide range of compositions detected on the Pd sputter-coated side of the Type C-B2-P membrane.

The compositions associated with the scattering angles shown in Figure 4.123 are compiled in Table 4.14 which indicates the remnants of the Pd thin film. Moreover, the composition of the BCC phase identified on the Pd sputter-coated side of the Type C-B2-P membrane is $Pd_{61.3}Cu_{38.7}$ wt%. The non-coated side contained only the BCC phase with a composition of $Pd_{61.6}Cu_{38.4}$ wt%.

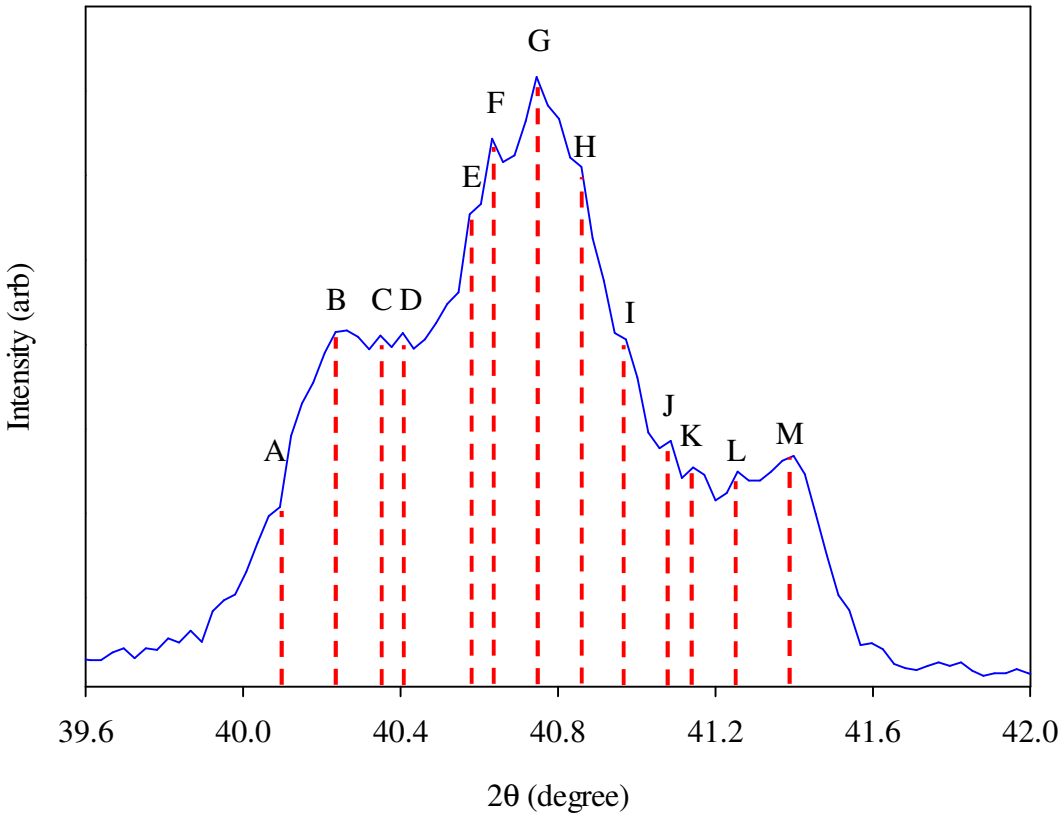

Figure 4.121 Magnification of the Pd-Cu(111) diffraction peak shown in Figure 4.120.

Table 4.13 Compositions determined for points A to M in Figure 4.121.

	Scattering angle, 2θ (degree)	Composition (wt%)
A	40.09	$Pd_{98.8}Cu_{1.2}$
B	40.24	$Pd_{95.8}Cu_{4.2}$
C	40.34	$Pd_{93.3}Cu_{6.7}$
D	40.41	$Pd_{92.1}Cu_{7.9}$
E	40.58	$Pd_{88.3}Cu_{11.7}$
F	40.63	$Pd_{87.0}Cu_{13.0}$
G	40.75	$Pd_{84.3}Cu_{15.7}$
H	40.86	$Pd_{81.6}Cu_{18.4}$
I	40.97	$Pd_{78.7}Cu_{21.3}$
J	41.09	$Pd_{75.8}Cu_{24.2}$
K	41.14	$Pd_{74.3}Cu_{25.7}$
L	41.26	$Pd_{71.3}Cu_{28.7}$
M	41.40	$Pd_{67.4}Cu_{32.6}$

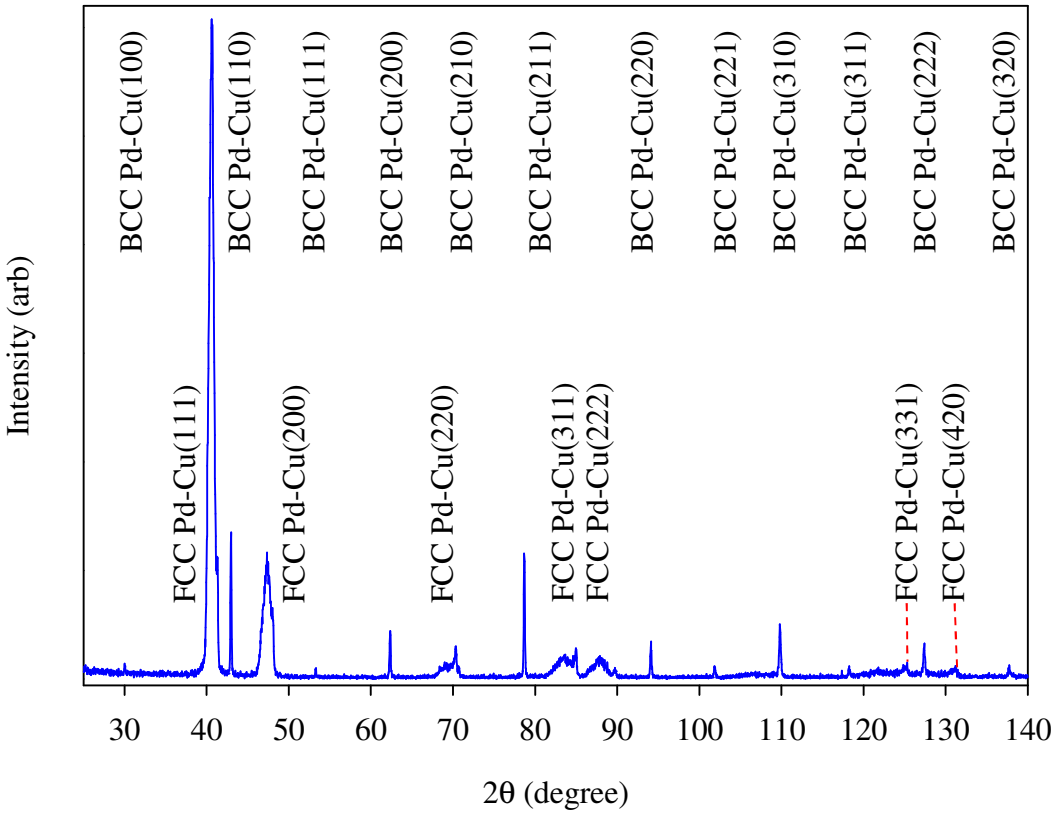

Figure 4.122 XRD pattern which is representative for the Pd sputter-coated side of the Type C-B2-P membrane following MPR testing.

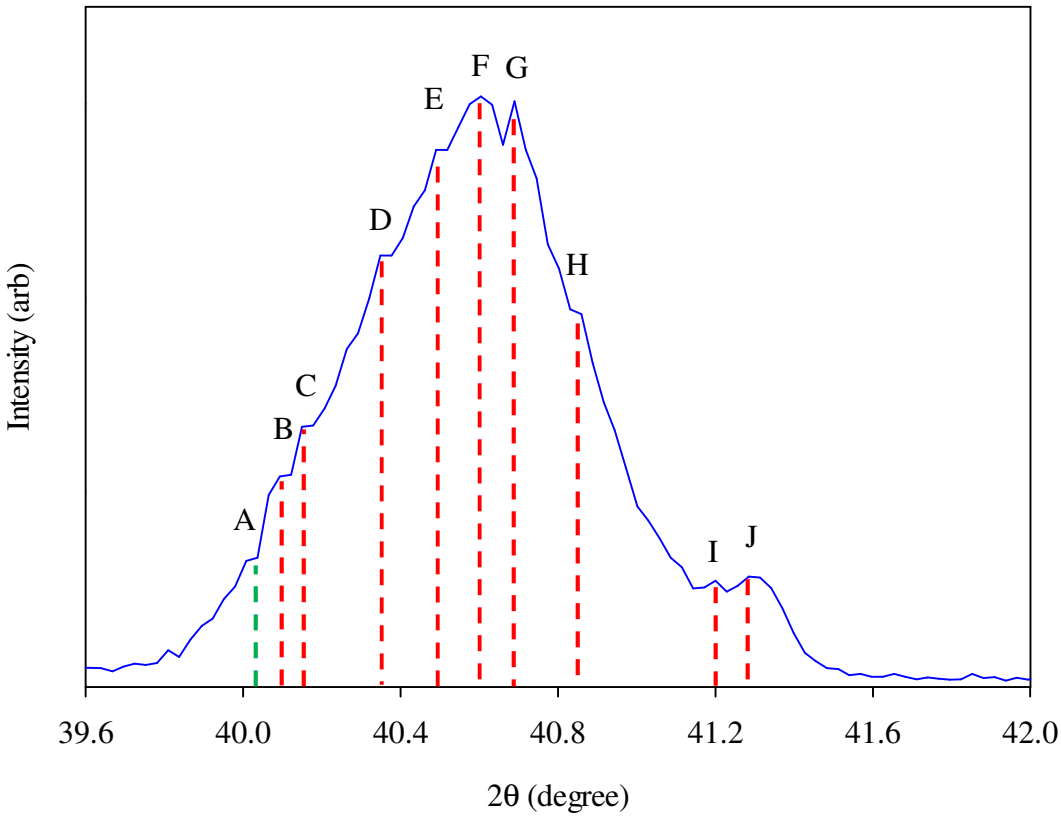

Figure 4.123 Magnification of the Pd-Cu(111) diffraction peak shown in Figure 4.122.

Table 4.14 Compositions determined for points A to J in Figure 4.123.

	Scattering angle, 2θ (degree)	Composition (wt%)
A	40.04	$Pd_{99.9}Cu_{0.1}$
B	40.09	$Pd_{98.8}Cu_{1.2}$
C	40.15	$Pd_{97.6}Cu_{2.4}$
D	40.35	$Pd_{93.4}Cu_{6.6}$
E	40.49	$Pd_{90.2}Cu_{9.8}$
F	40.60	$Pd_{87.6}Cu_{12.4}$
G	40.69	$Pd_{85.7}Cu_{14.3}$
H	40.86	$Pd_{81.6}Cu_{18.4}$
I	41.20	$Pd_{72.8}Cu_{27.2}$
J	41.28	$Pd_{70.5}Cu_{29.5}$

Figure 4.124 and Figure 4.125 show the XPS depth profile analysis results for the Type C-B2-F membrane and Type C-B2-P membrane, respectively. These results agree well with the compositions obtained using XRD analysis of the Pd-Cu(111) asymmetric diffraction

peaks for both membranes. Figure 4.124 shows that the top surface composition of the Type C-B2-F membrane is $Pd_{96.8}Cu_{3.2}$ wt% after which the Cu concentration steadily increases as a function of etch depth. Similarly, Figure 4.125 indicates that the Type C-B2-P membrane has a top surface composition of $Pd_{96.5}Cu_{3.5}$ wt% and subsequently the Cu concentration gradually increases over the analysis depth. In both cases, it seems evident that a near pure Pd surface remains on the Pd sputter-coated side of the Type C-B2-F membrane and Type C-B2-P membrane following MPR testing. Furthermore, it is apparent that the interdiffusion region in the Type C-B2-F membrane and Type C-B2-P membrane extends to much greater depths than 2,000 nm suggesting a compositional gradient has formed over a relatively large distance.

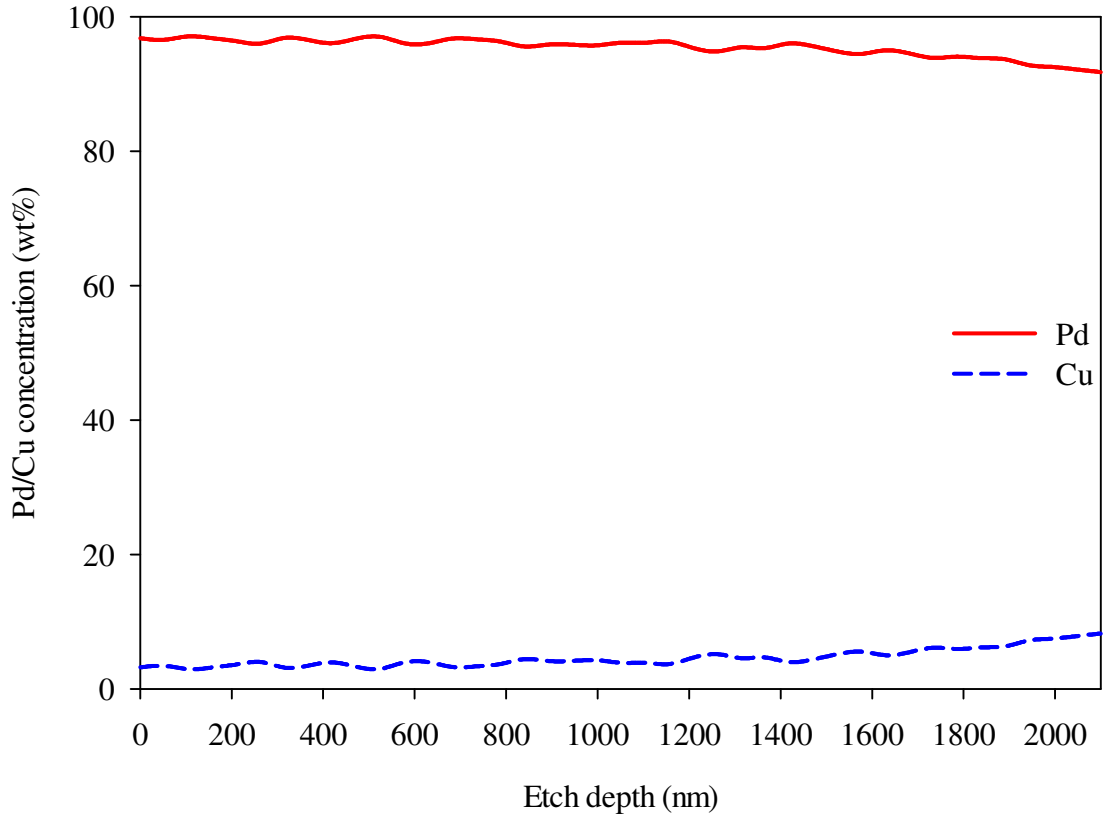

Figure 4.124 XPS depth profile analysis representative of a Type C-B2-F membrane following MPR testing. The etch depth was estimated using a reference etching rate of 0.21 nm s^{-1} for Ta_2O_5.

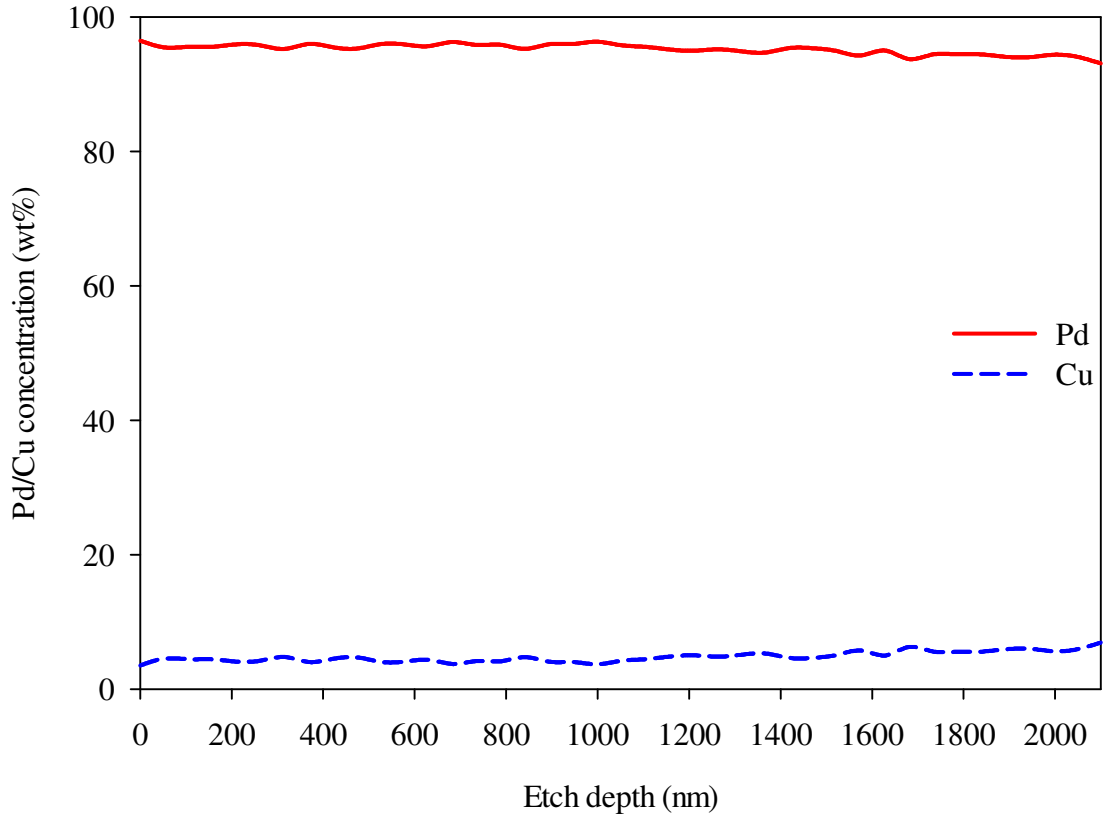

Figure 4.125 XPS depth profile analysis representative of a Type C-B2-P membrane following MPR testing. The etch depth was estimated using a reference etching rate of 0.21 nm s^{-1} for Ta_2O_5.

4.7. General discussion

The effects of hydrogen on the Pd-Cu alloy system have become more apparent throughout the course of this work. Table 4.15 summarises the results obtained from the VTXRD study. At 445 kPa of hydrogen pressure, the β-PdH phase in Type A/B/C-B2 Foil 2 readily forms at 30 °C and is stable up until 225 °C. The hydrogen depleted α-PdH phase forms at 200 °C signalling that hydrogen desorption from the hydrogen rich β-PdH phase takes place. It is evident that the α-PdH phase is stable to higher temperatures in the relatively thicker Pd thin film. For example, in Type A-B2 Foil 2 the α-PdH phase remains present up until 450 °C, whereas in Type B-B2 Foil 2 and Type C-B2 Foil 2 this phase disappears at 550 and 700 °C, respectively. This observation is plausible since a thicker Pd thin film which has a relatively larger amount of deposited Pd would require higher temperatures to completely interdiffuse

with the bulk Pd-Cu foil compared with thinner films under same durations and VTXRD test conditions.

At 100 kPa, the β-PdH phase forms between 30 and 150 °C in Type A-B2 Foil 3, while in Type B-B2 Foil 3 and Type C-B2 Foil 3 this phase is stable up to 175 °C. In the case of Type A-B2 Foil 3, the β-PdH phase may exist up to 175 °C, however, since the β-PdH(111) diffraction peak reduces in intensity during the phase transformation to the α-PdH phase this peak becomes indistinguishable from the background noise.

The α-PdH phase is detected up to 700 °C in Type A/B/C-B2 Foil 3 (100 kPa of hydrogen pressure) which is higher than the temperatures observed for Type A/B/C-B2 Foil 2 (445 kPa of hydrogen pressure) indicating that at higher hydrogen pressures interdiffusion is accelerated. Furthermore, under 100 kPa of hydrogen pressure the Pd-Cu FCC phase originating from the as-received Pd-Cu foil offcut is stable over a wider temperature range compared with 445 kPa of hydrogen pressure. This can both be attributed to the formation of the well known vacancy-hydrogen clusters [178, 179, 263, 264] that accelerate atomic diffusion responsible for rapid phase transformation and evidently increased rate of interdiffusion.

In Type A/B-B2 Foil 2/3, interdiffusion occurs at the same temperatures. Although, in the case of Type C-B2 Foil 2/3, this process starts at a higher temperature of 400 °C and potentially continues above 700 °C. This indicates that a portion of the Pd thin film in Type C-B2 Foil 2/3 remains stable under the conditions used during the VTXRD experiment likely due to its relatively large thickness compared with the Pd thin films in Type A/B-B2 Foil 2/3.

Table 4.15 Summary of the VTXRD results.

	Hydrogen pressure (kPa)	β-PdH temperature range (°C)	α-PdH temperature range (°C)	Pd-Cu FCC temperature range (°C)	Interdiffusion temperature range (°C)
Type A-B2 Foil 2	445	30 – 225	200 – 450	30 – 325, 500 – 700	350 – 600
Type A-B2 Foil3	100	30 – 150	150 – 700	30 – 700	350 – 600
Type B-B2 Foil 2	445	30 – 225	200 – 550	30 – 275, 450 – 700	350 – 600
Type B-B2 Foil 3	100	30 – 175	150 – 700	30 – 325, 450 – 700	350 – 600
Type C-B2 Foil 2	445	30 – 225	200 – 700	30 – 275, 475 – 700	400 – 700+
Type C-B2 Foil 3	100	30 – 175	150 – 700	30 – 300, 475 – 700	400 – 700+

An overall summary of the results are compiled in Table 4.16. In addition, Figure 4.126 displays a plot of hydrogen permeability as a function of temperature comparing the third cycle completed by each membrane studied in this work.

It is shown that the best fit *n*-value (BFN) is relatively unaffected by the presence or position of the Pd thin film during MPR testing. However, the Batch 1 Pd-Cu membrane demonstrates a decrease in the best fit *n*-value from 0.58 to 0.52 as a result of a series of cycles between 250 and 700 °C using hydrogen feed and permeate pressures of 445 and 100 kPa, respectively. An additional observation is that the Batch 1 Pd-Cu membrane *n*-value shows no significant change with increasing temperature following these cycles. The conditions used in these cycles facilitate rapid phase transformation, compositional homogenisation and ordering due to enhanced atomic mobility as evidenced by VTXRD studies and is likely responsible for the observed changes in the Batch 1 Pd-Cu membrane *n*-value.

One significant finding is the marked increase in the hydrogen permeability displayed by the Batch 1 and Batch 2 Pd-Cu membranes subsequent to cycling between 250 and 700 °C. The outcome for both membranes showed a more than 50% decrease in the E_{Φ} value and reduction in Φ_0 resulting in a doubling of the hydrogen permeability measured during the third cycle between 250 and 450 °C after completing the 250 to 700 °C cycles as shown in Figure 4.126. Such improvements can be attributed to the removal of residual coring effects due to gradual homogenisation of the membranes with each successive cycle enabling the Batch 1 and Batch 2 Pd-Cu membranes to achieve comparable or even higher permeability values than that observed for the pure palladium membrane.

Table 4.16 Summary of results obtained for the membranes investigated in this work. N.B. the permeability data has been determined between 350 and 450 °C.

Membrane	BFN	Permeability constant, Φ_0 ($\times 10^{-7}$ mol m^{-1} s^{-1} Pa^{-n})		Activation energy, E_Φ (kJ mol^{-1})		Permeability during third cycle at 450 °C ($\times 10^{-8}$ mol m^{-1} s^{-1} Pa^{-n})		Pd thin film surface composition post MPR testing (wt%) - XRD	Pd thin film surface composition post MPR testing (wt%) - XPS
		n-value		*n*-value		*n*-value			
		0.5	BFN	0.5	BFN	0.5	BFN		
Pd[a]	0.57	2.41	0.88	17.54	17.53	1.29	0.47	-	-
Batch 1 Pd-Cu[b]	0.58	288.33	88.68	51.09	51.09	0.56	0.17	-	-
	0.52*	2.71*	3.41*	19.86*	19.86*	1.19*	0.95*		
Batch 2 Pd-Cu[c]	-	88.13 ± 51.20	-	41.67 ± 3.40	-	0.69 ± 0.06	-	-	-
	0.59*	6.32 ± 4.74*	1.81 ± 1.36*	19.93 ± 6.12*	19.92 ± 6.12*	1.44 ± 0.08*	0.41 ± 0.02*	-	-
Type A-B1-F	0.55	2.15	1.04	17.93	17.93	1.05	0.51	$Pd_{83.6}Cu_{16.4}$	$Pd_{89.5}Cu_{10.5}$
Type A-B2-F	0.58	13.26	4.18	29.95	29.93	0.88	0.28		
Type A-B1-P	0.60	23.98	5.46	34.44	34.42	0.75	0.17	$Pd_{83.0}Cu_{17.0}$	$Pd_{90.0}Cu_{10.0}$
Type A-B2-P	0.55	36.93	19.42	36.41	36.41	0.84	0.44		
Type B-B2-F	0.63	4.99	0.78	23.41	23.41	1.00	0.16	$Pd_{97.0}Cu_{3.0}$	$Pd_{95.0}Cu_{5.0}$
Type B-B2-P	0.60	38.83	10.08	38.01	38.01	0.69	0.17	$Pd_{100.0}Cu_{0.0}$	$Pd_{100.0}Cu_{0.0}$
Type C-B2-F	0.56	3.44	1.44	20.52	20.52	1.09	0.46	$Pd_{98.8}Cu_{1.2}$	$Pd_{96.8}Cu_{3.2}$
Type C-B2-P	0.59	21.89	6.35	33.91	33.91	0.74	0.22	$Pd_{99.9}Cu_{0.1}$	$Pd_{96.5}Cu_{3.5}$

BFN = best fit *n*-value. Approximate Pd thin film thickness (nm) in Type A, B and C membranes is 95.5 ± 0.1, 797.4 ± 0.2 and 1,409.6 ± 0.2, respectively. Membrane thickness (µm) a = 67.8 ± 1.8, b = 31.0 ± 0.8, 31.3 ± 0.8. * indicates membrane permeability data acquired during the third cycle between 250 and 450 °C after cycling twice between 250 and 700 °C.

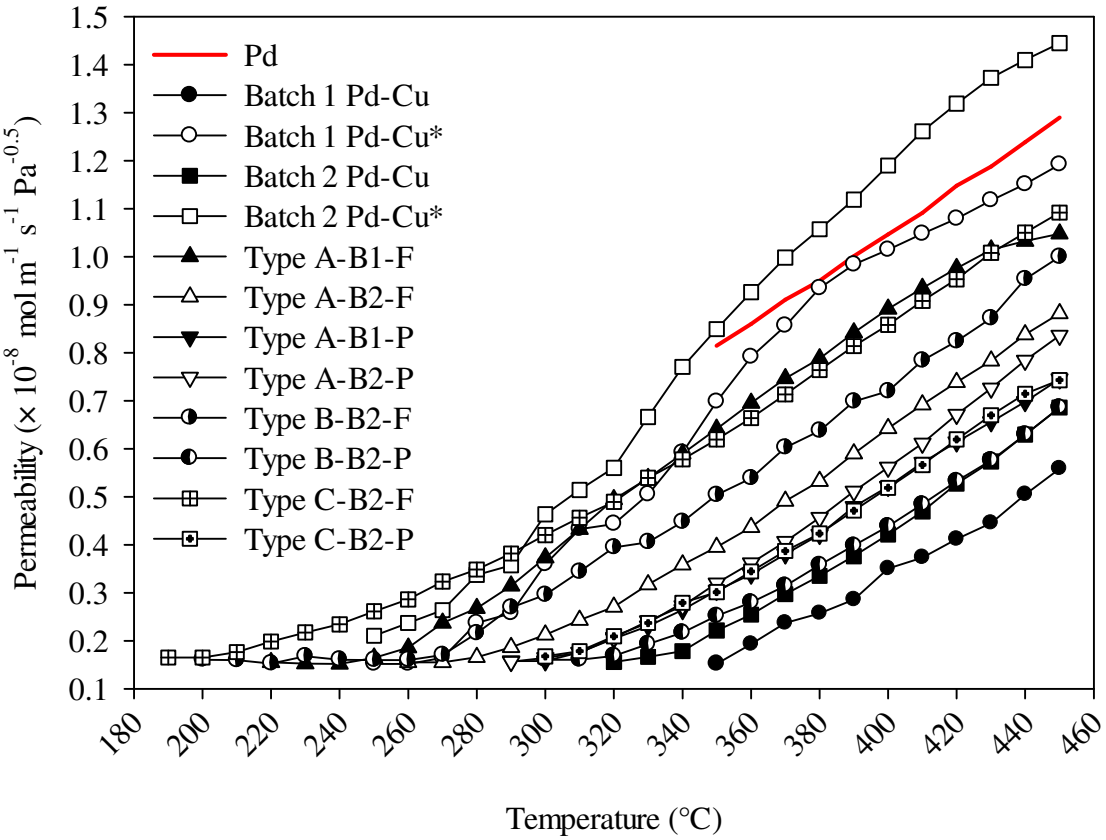

Figure 4.126 Hydrogen permeability as a function of temperature plot comparing each membrane investigated in this work. All curves show the third cycle completed by each membrane between 50 and 450 °C using a hydrogen feed pressure of 445 kPa and permeate pressure of 100 kPa assuming an *n*-value of 0.5. *indicates membrane permeability data acquired during the third cycle between 250 and 450 °C after cycling twice between 250 and 700 °C.

For a fair assessment, only membranes of the same batch that have completed the same number of cycles will be compared with each other. For example, the performance of the Type A-B1-F/P membranes will be compared with the Batch 1 Pd-Cu membrane which completed the initial three cycles between 50 and 450 °C prior to completing the cycles between 250 and 700 °C. As shown in Table 4.16 and Figure 4.126, the Type A-B1-F/P membranes achieve relatively higher hydrogen permeability values as compared with the Batch 1 Pd-Cu membrane. The presence of the 95.5 ± 0.1 nm thick Pd thin film has the effect of reducing the E_Φ value for the Batch 1 Pd-Cu membrane. The same can

be observed with the Type A/B/C-B2-F/P membranes whereby the E_{Φ} value is decreased due to the deposition of the Pd thin film on to the surface of the Batch 2 Pd-Cu membrane.

As evidenced by the XRD and XPS data, the Pd thin film interdiffuses with the bulk Pd-Cu membrane during MPR testing producing a compositional gradient on the Pd sputter-coated surface. Figure 4.127 clearly shows that at room temperature the hydrogen to metal ratio (H/M) otherwise known as the hydrogen solubility increases in a Pd-Cu alloy with increasing Pd content. Solubility data for the Pd-Cu at higher temperatures is not available in the literature although it is known that hydrogen solubility decreases in a Pd-Cu alloy with increasing temperature [137, 177].

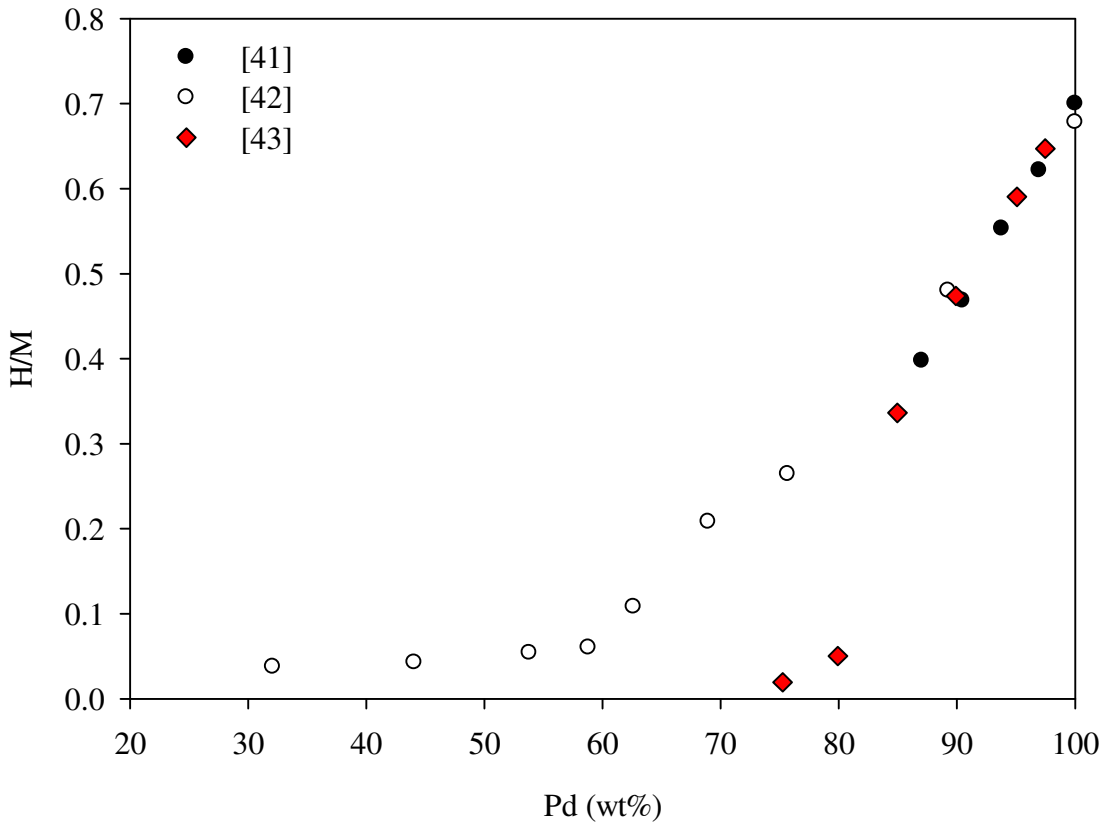

Figure 4.127 Hydrogen solubility data for the Pd-Cu alloy system at room temperature and 101.325 kPa compiled from literature [41-43].

As demonstrated by Sieverts' law (Equation 2.3), at a given temperature hydrogen solubility is proportional to concentration.

$$S = \frac{C}{P_{H_2}^{1/2}} \qquad \text{Equation 2.3}$$

It follows that if the Pd thin film introduces a compositional gradient during MPR testing, this will in turn produce a solubility gradient and therefore a concentration gradient ($\partial C/\partial x$) which, according to Fick's first law (Equation 2.1), is the driving force for diffusion and consequently permeability.

$$J = -D\frac{\partial C}{\partial x} \qquad \text{Equation 2.1}$$

Figure 4.128(a) is a schematic representation of the Batch 1 and Batch 2 Pd-Cu membranes during MPR testing which assumes a relatively uniform $Pd_{60}Cu_{40}$ wt% composition through the membrane thickness. Applying a hydrogen pressure differential across the membrane creates the concentration gradient necessary for conventional hydrogen diffusion.

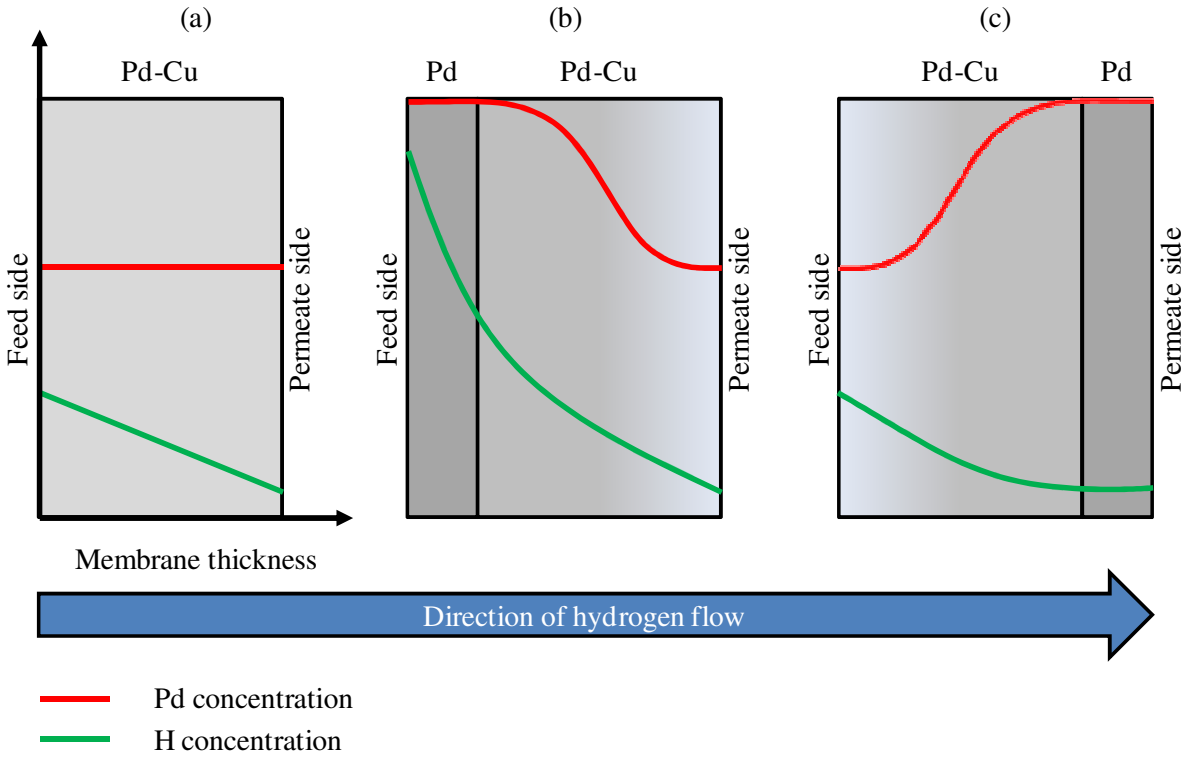

Figure 4.128 A schematic illustration showing the membrane composition, hydrogen pressure and concentration as a function of membrane thickness during MPR testing at a given temperature where (a) represents the Batch 1 and Batch 2 Pd-Cu membranes, (b) represents the Type A-B1-F and Type A/B/C-B2-F membranes and (c) represents the Type A-B1-P and Type A/B/C-B2-P membranes.

According to Table 4.16 and Figure 4.126, the Type A-B1-F and Type A/B/C-B2-F membranes achieve a relatively higher hydrogen permeability compared with the corresponding Batch 1 and Batch 2 Pd-Cu membranes due to a decrease in the E_{Φ} value. Figure 4.128(b) is a representation of the Type A-B1-F and Type A/B/C-B2-F membranes during MPR testing. Interdiffusion of the Pd thin film with the bulk Pd-Cu membrane during MPR testing creates a compositional gradient and produces a Pd-rich Pd-Cu FCC phase on the Pd sputter-coated surface of the membrane. This newly formed phase positioned on the feed side during MPR testing possesses a relatively higher hydrogen solubility thus introducing a much steeper concentration gradient which could be responsible for the observed increase in hydrogen permeability.

Comparing the Type A/B/C-B2-F membranes, the Type C-B2-F membrane has the highest hydrogen permeability, followed by the Type B-B2-F membrane and lastly the Type A-B2-F membrane. This is perhaps attributed to the thicker Pd thin film in the Type C-B2-F membrane producing a relatively richer Pd surface that increases hydrogen solubility and introduces a larger hydrogen concentration gradient responsible for the increase in hydrogen permeability.

Figure 4.128(c) is a representation of the Type A-B1-P and Type A/B/C-B2-P membranes whereby the Pd thin film is exposed to the permeate side. It is shown in Table 4.16 and Figure 4.126, that the Type A-B1-P and Type A/B/C-B2-P membranes achieve a higher hydrogen permeability than the corresponding Batch 1 and Batch 2 Pd-Cu membranes yet a lower hydrogen permeability compared to the Type A-B1-F and Type A/B/C-B2-F membranes. The applied pressure differential produces the concentration gradient necessary for hydrogen permeation, however, the high hydrogen solubility of the Pd-rich Pd-Cu FCC phase on the permeate side likely creates a plateau in the concentration profile causing the slight reduction in hydrogen permeability.

The Type B-B2-P membrane achieves the lowest hydrogen permeability of all the surface modified Pd-Cu membranes. This is possibly due to the Type B-B2-P membrane forming a pure Pd surface on the Pd sputter-coated side during MPR testing producing a larger plateau in the concentration profile which results in the observed decrease in hydrogen permeability.

In addition, the second and third cycles of the Type A-B1-P and Type A/B/C-B2-P membranes achieved very similar hydrogen permeability values as a function of temperature. As demonstrated in Figure 4.126, this group of membranes commence hydrogen permeation at relatively lower temperatures in comparison to the

Batch 1 and Batch 2 Pd-Cu membranes. This could be a sign that the Type A-B1-P and Type A/B/C-B2-P membranes achieve ordering in comparatively less time due to the increased hydrogen solubility introduced by the Pd thin film. This creates more vacancy-hydrogen clusters promoting atomic ordering so that the maximum hydrogen permeability of the Type A-B1-P and Type A/B/C-B2-P membranes is attained faster. However, with further cycling, the Batch 1 and Batch 2 Pd-Cu membranes will become more ordered and could begin to achieve higher hydrogen permeability values compared with the Type A-B1-P and Type A/B/C-B2-P membranes since a Pd thin film is not present to plateau the concentration profile which can reduce permeability.

The pure bulk Pd membrane used in this work was never cycled below the critical temperature (295 °C) in a hydrogen atmosphere during MPR testing in order to avoid the α-PdH → β-PdH phase transformation which involves a lattice volume expansion capable of causing membrane failure. However, it has been observed that the surface modified Pd-Cu membranes that maintain a relatively pure Pd surface during MPR testing (Type B/C-B2-P/F membranes) are capable of being cycled to temperatures as low as 50 °C without showing any evidence of film delamination or cracking. The bulk Pd-Cu membrane substrate appears to stabilise the Pd thin film preventing delamination under the conditions used during MPR testing.

5. Conclusions

For the first time, the hydrogen permeability of surface modified $Pd_{60}Cu_{40}$ wt% membranes has successfully been measured in this work. For a valid assessment, membranes which have completed the same number of cycles under the same test conditions in the MPR system are compared. The results confirm the hypothesis that modifying the surface of a Pd-Cu membrane using Pd sputter deposition can improve hydrogen permeability when the Pd thin film is positioned on the feed side during MPR testing.

Initially, hydrogen permeability was measured for the Batch 1 and Batch 2 Pd-Cu membranes in the as-received state by cycling between 50 and 450 °C. On the third cycle the hydrogen permeability for the Batch 1 and Batch 2 Pd-Cu membranes were determined at 450 °C to be 5.59×10^{-9} and $(6.86 \pm 0.6) \times 10^{-9}$ mol m^{-1} s^{-1} $Pa^{-0.5}$, respectively, which is relatively low compared with published data. However, it was observed that the Batch 1 and Batch 2 Pd-Cu membranes attained higher permeability values with each successive cycle. Moreover, it was found that cycling the Batch 1 and Batch 2 Pd-Cu membranes to temperatures as high as 700 °C, had the effect of reducing the E_Φ value by a factor of two and decreasing the n-value resulting in a hydrogen permeability at 450 °C of 1.19×10^{-8} and $(1.44 \pm 0.08) \times 10^{-8}$ mol m^{-1} s^{-1} $Pa^{-0.5}$, respectively. These new values are in good agreement with the published figures [37, 87, 97].

Coring was discovered to be the culprit for the initially low hydrogen permeability values demonstrated by the Batch 1 and Batch 2 Pd-Cu membranes. Coring likely occurred as a result of rapid cooling of the Pd-Cu alloy melt thus retaining the high temperature disordered FCC phase down to room temperature. Furthermore, this created compositional inhomogeneity as the component with the lowest melting point, in this case Cu atoms,

solidifies first and migrates to the outer extremities of the alloy leaving the Pd atoms to concentrate in the inner regions.

Prolonged cycling and exposure to elevated temperatures in hydrogen was found to be effective in homogenising the Batch 1 and Batch 2 Pd-Cu membranes and increasing their hydrogen permeability. Krueger [96] reports a similar observation with a Pd-Cu alloy membrane and proposes that annealing at temperatures close to the melting point of Cu in an atmosphere containing hydrogen is sufficient to reverse the effects of coring and significantly enhance hydrogen permeability.

Permeation hysteresis was also observed with the Batch 1 and Batch 2 Pd-Cu membranes upon cycling up to 700 °C. Yuan [97], attributes this to the presence of a metastable hydrogenated FCC Pd-Cu(H) phase that delays the FCC(H) ⇋ BCC(H) phase transformation. However, VTXRD analysis performed on offcuts of the Batch 1 Pd-Cu foil reveals that the FCC phase is stable to lower than normal temperatures in either a pure hydrogen atmosphere or pure helium atmosphere. Therefore, it is proposed that the stability of the FCC phase to lower than expected temperatures is more related to the cooling rate as opposed to the existence of a metastable hydrogenated FCC Pd-Cu(H) phase. Slower cooling rates will allow ample time for the phase transformation from the FCC to the BCC phase to occur and reach equilibrium.

Furthermore, VTXRD analysis of the Batch 1 and Batch 2 Pd-Cu foil offcuts showed that 445 kPa of hydrogen pressure moves the BCC | FCC + BCC and FCC + BCC | FCC phase boundaries to higher temperatures and Pd concentrations in the Pd-Cu binary phase diagram. This corresponds well to the observations reported by Piper [39]. This effect helps to explain

the ability of the BCC phase to remain stable past the position of the phase boundaries shown in the published Pd-Cu phase diagram [154].

It was revealed with the use of XRD and XPS depth profile analysis that interdiffusion between the Pd thin film and Pd-Cu foil substrate occurs in the Type A/B/C-B2 foil offcuts during the Pd deposition process. It is plausible to assume that interdiffusion occurs in the Type A-B1 and Type A/B/C-B2 membranes since they were sputter-coated under the same conditions as the Type A/B/C-B2 foil offcuts. The SEM micrographs of the Pd thin films in the as-deposited state reveal a nanocrystalline microstructure with equiaxed-shaped grains. Various authors [261, 270-274] postulate that the polycrystalline nature of a deposited thin film introduces grain boundary defects through which interdiffusion can be facilitated at relatively low temperatures. Apparently, a Pd target current of 1 A is sufficient in producing temperatures necessary to allow interdiffusion between the Pd thin film and Pd-Cu foil substrate during deposition.

Furthermore, it has been shown using VTXRD analysis of the Type A/B/C-B2 foil offcuts that the β-PdH phase is stable up to a maximum temperature of 175 °C under 100 kPa of hydrogen pressure. This limit is raised to 225 °C under 445 kPa of hydrogen pressure. The stability of the α-PdH phase depends on the thickness of the Pd thin film and hydrogen pressure. At 100 kPa of hydrogen pressure, the α-PdH phase remains stable up to 700 °C. Whereas, at 445 kPa of hydrogen pressure, the α-PdH phase disappears at 450 and 550 °C in Type A-B2 Foil 2 and Type B-B2 Foil 2, respectively, as a result of a reduction in hydrogen solubility caused by Cu interdiffusion into the Pd thin film. It was also found that the Pd-Cu FCC phase attributed to the bulk Pd-Cu foil substrate is stable over a wider temperature range under 100 kPa of hydrogen pressure compared with 445 kPa of hydrogen

pressure. This indicates that higher hydrogen pressures accelerate the Pd-Cu FCC to BCC phase transformation.

The Type A-B1 and Type A/B/C-B2 membranes achieved a relatively higher hydrogen permeability at 450 °C during the initial third cycle in comparison to the corresponding Batch 1 and Batch 2 Pd-Cu membranes at the same temperature and cycle. During MPR testing, interdiffusion between the Pd thin film and the bulk Pd-Cu membrane form both a Pd-rich Pd-Cu FCC phase and a compositional gradient on the Pd sputter-coated side of the Type A-B1 and Type A/B/C-B2 membranes. Positioning the Pd sputter-coated side of the Type A-B1 and Type A/B/C-B2 membranes on the feed side during MPR testing creates a larger than normal hydrogen concentration gradient due to the higher hydrogen solubility of the Pd-rich Pd-Cu FCC phase. This increased hydrogen concentration gradient is likely the cause of the relatively higher hydrogen permeability achieved by the Type A-B1-F and Type A/B/C-B2-F membranes.

In contrast, positioning the Pd sputter-coated side of the Type A-B1 and Type A/B/C-B2 membranes on the permeate side during MPR testing may have the opposite effect. The pressure differential across the membrane creates the hydrogen concentration gradient necessary for permeation, although the Pd-rich Pd-Cu FCC phase positioned on the permeate side introduces a hydrogen solubility gradient acting in the direction opposing hydrogen diffusion. This may have the effect of producing a plateau in the hydrogen concentration profile towards the permeate side of the membrane hence reducing the hydrogen permeability in Type A-B1-P and Type A/B/C-B2-P membranes.

The presence of the Pd thin film appears to have no effect on the bulk Pd-Cu membrane *n*-value. The overall trend demonstrates that the *n*-value increases with increasing

temperature. This ultimately means that the permeation process becomes less limited by hydrogen diffusion at higher temperatures. Such behaviour appears valid since at elevated temperatures the endothermic nature of hydrogen diffusion means that the rate of this process increases. Moreover, Doyle [123] attributes a deviation from Sieverts' law to the increase in hydrogen concentration. This results in the expansion of the host metal lattice by the dissolved hydrogen which may significantly affect hydrogen solubility. This can also alter the electronic properties of the metal-hydrogen system as more electrons are introduced by the dissolved hydrogen upon ionisation. This may also lead to an increase in repulsive interaction between protons (H^+) which may adversely affect the hydrogen dissociation process.

It was discovered that the Type B/C-B2 membranes retained an almost pure Pd surface following MPR testing and showed no signs of film delamination or disintegration as result of cycling between 50 and 450 °C in a hydrogen atmosphere. Typically, a bulk pure Pd membrane would rupture if cycled through the critical temperature (295 °C) in the presence of hydrogen due to the lattice volume expansion created by the α-PdH → β-PdH phase transformation. It seems that this expansion is suppressed in the deposited Pd thin film and stabilised by the bulk Pd-Cu membrane substrate.

Given reports of the Pd-rich Pd-Cu FCC phase exhibiting greater resistance to H_2S contamination [45, 87, 159], the surface modified Pd-Cu membranes investigated in this work may have the potential to separate hydrogen from a gas mixture containing H_2S under typical membrane operating conditions with improved durability.

5.1. Further work

Modifying the surface composition of a $Pd_{60}Cu_{40}$ wt% foil membrane via Pd sputter deposition shows great promise for the application of hydrogen separation and has scope for

further research and development. The following is a list of suggestions and recommendations for future work:

- Further studies should be conducted in order to determine the durability and stability of the Pd-rich Pd-Cu FCC phase. Additional cycles should be completed under varying hydrogen pressure differentials and temperatures to better understand the interdiffusion process.

- Different Pd thin film thicknesses can be explored in order to examine and identify the optimum Pd-rich Pd-Cu FCC phase composition.

- Additional work could be focussed on indentifying the nature of the decline observed in the E_Φ value for the Type A-B1-F/P and Type A/B/C-B2-F/P membranes. The E_Φ value is a sum of the activation energy for diffusion (E_D) and the enthalpy of solution of hydrogen (E_S). One or both of these values may vary in order for the E_Φ value to decrease. Therefore, diffusivity and solubility experiments can be performed on a new batch of surface modified $Pd_{60}Cu_{40}$ wt% membranes in order to determine whether E_D or E_S is responsible for changes in E_Φ.

- In order to fully eliminate the effects of coring in the as-received Pd-Cu foil, suitable conditions must be sought for annealing and homogenisation. A Pd-Cu membrane containing a fully ordered equilibrium BCC phase could make an ideal substrate for fabricating a new range of Type A, B and C membranes which could have enhanced hydrogen permeability.

- Test a new batch of surface modified $Pd_{60}Cu_{40}$ wt% membranes in a hydrogen atmosphere containing various concentrations of H_2S in order to assess the performance and durability of the Pd-rich Pd-Cu FCC phase.

6. Appendix

6.1. Method for calculating the Pd-Cu FCC and BCC phase composition

Vegard's law [249] has been initially used to accurately determine the phase composition of the as-received Pd-Cu foils. Literature data [137, 162, 164, 168, 171, 266, 275-282] has been compiled into a plot of FCC Pd-Cu lattice parameter as a function of Pd concentration (Figure 6.1).

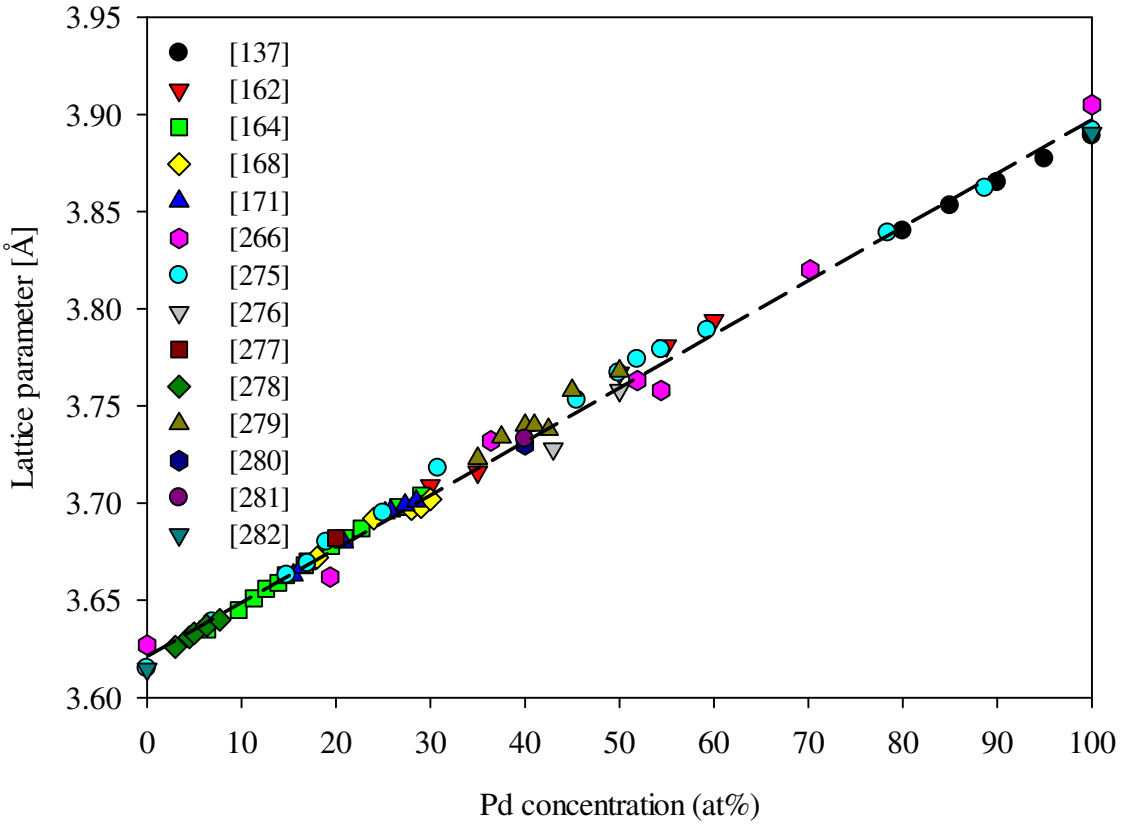

Figure 6.1 Lattice parameter of FCC Pd-Cu alloys as a function of Pd content featuring a dashed line of best fit.

Equation 6.1 was determined from a line of best fit for the Figure 6.1 data where x_{Pd} is the Pd concentration given in at%.

$$a = (2.75 \times 10^{-3})x_{Pd} + 3.62 \qquad \text{Equation 6.1}$$

Figure 6.2 is a plot of BCC Pd-Cu lattice parameter as a function of Pd concentration constructed using literature data [162, 168, 259, 266, 275, 276, 279, 281, 283]. Using this data, Equation 6.2 was derived.

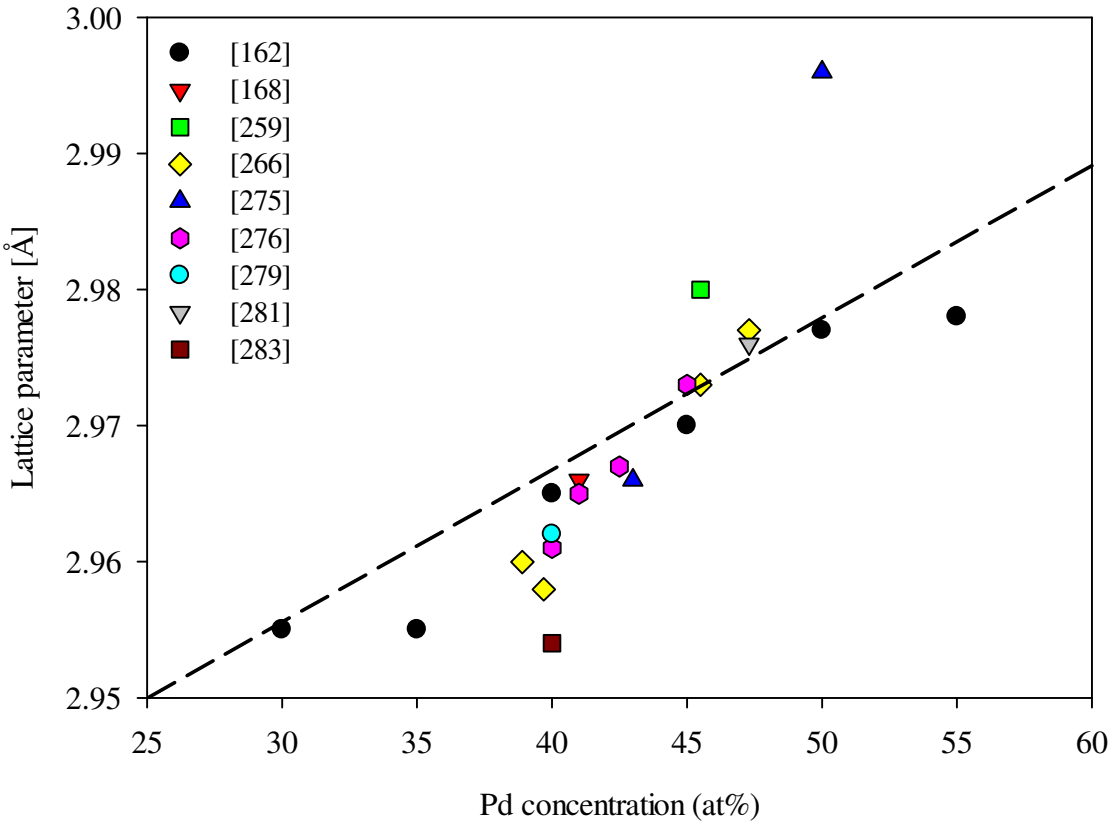

Figure 6.2 Lattice parameter of BCC Pd-Cu alloys as a function of Pd content featuring a dashed line of best fit.

$$a = (1.57 \times 10^{-3})x_{Pd} + 2.90 \qquad \text{Equation 6.2}$$

7. References

[1] C. Koroneos, A. Dompros, G. Roumbas, N. Moussiopoulos, Life cycle assessment of hydrogen fuel production processes, International Journal of Hydrogen Energy, 29 (2004) 1443-1450.

[2] M. Steinberg, H.C. Cheng, Modern and prospective technologies for hydrogen production from fossil fuels, International Journal of Hydrogen Energy, 14 (1989) 797-820.

[3] D.S. Newsome, The water-gas shift reaction, Catalysis Reviews Science and Engineering, 21 (1980) 275-318.

[4] U.S. Department of Energy Hydrogen, Fuel cells and infrastructure technologies program, multi-year research, development and demonstration plan: planned program activities for 2005–2015, Energy Efficiency and Renewable Energy, U.S. Department of Energy, Washington, DC, 2007.

[5] K.S. Lackner, A guide to CO_2 sequestration, Science, 300 (2003) 1677-1678.

[6] J.A. Turner, Sustainable hydrogen production, Science, 305 (2004) 972-974.

[7] D. Anderson, M. Leach, Harvesting and redistributing renewable energy: on the role of gas and electricity grids to overcome intermittency through the generation and storage of hydrogen, Energy Policy, 32 (2004) 1603-1614.

[8] J. Quakernaat, Hydrogen in a global long-term perspective, International Journal of Hydrogen Energy, 20 (1995) 485-492.

[9] S. Czernik, R. French, C. Feik, E. Chornet, Hydrogen by catalytic steam reforming of liquid byproducts from biomass thermoconversion processes, Industrial & Engineering Chemistry Research, 41 (2002) 4209-4215.

[10] F. Hawkes, R. Dinsdale, D. Hawkes, I. Hussy, Sustainable fermentative hydrogen production: challenges for process optimisation, International Journal of Hydrogen Energy, 27 (2002) 1339-1347.

[11] A. Léon, Hydrogen technology: mobile and portable applications, Springer, Berlin, 2008.

[12] S. Satyapal, J. Petrovic, C. Read, G. Thomas, G. Ordaz, The US department of energy's national hydrogen storage project: Progress towards meeting hydrogen-powered vehicle requirements, Catalysis Today, 120 (2007) 246-256.

[13] A.G. Wong-Foy, A.J. Matzger, O.M. Yaghi, Exceptional H_2 saturation uptake in microporous metal-organic frameworks, Journal of the American Chemical Society, 128 (2006) 3494-3495.

[14] R.K. Ahluwalia, T.Q. Hua, J.K. Peng, S. Lasher, K. McKenney, J. Sinha, M. Gardiner, Technical assessment of cryo-compressed hydrogen storage tank systems for automotive applications, International Journal of Hydrogen Energy, 35 (2010) 4171-4184.

[15] D. Mori, K. Hirose, Recent challenges of hydrogen storage technologies for fuel cell vehicles, International Journal of Hydrogen Energy, 34 (2009) 4569-4574.

[16] D. Gielen, G. Simbolotti, Prospects for hydrogen and fuel cells, International Energy Agency, Paris, 2005.

[17] A.U. Czaja, N. Trukhan, U. Muller, Industrial applications of metal-organic frameworks, Chemical Society Reviews, 38 (2009) 1284-1293.

[18] G. Marbán, T. Valdés-Solís, Towards the hydrogen economy?, International Journal of Hydrogen Energy, 32 (2007) 1625-1637.

[19] D. Stolten, Hydrogen and fuel cells: fundamentals, technologies and applications, Wiley-VCH, Weinheim, 2010.
[20] M. Panfilov, G. Gravier, S. Fillacier, Underground storage of H_2 and H_2-CO_2-CH_4 mixtures, 10th European Conference on the Mathematics of Oil Recovery, (2006).
[21] L. Schlapbach, A. Züttel, Hydrogen-storage materials for mobile applications, Nature, 414 (2001) 353-358.
[22] L. Schlapbach, Technology: Hydrogen-fuelled vehicles, Nature, 460 (2009) 809-811.
[23] F. Barbir, PEM fuel cells: theory and practice, Second Edition, Academic Press, Waltham, 2013.
[24] M.-B. Hägg, R. Quinn, Polymeric facilitated transport membranes for hydrogen purification, MRS Bulletin, 31 (2006) 750-755.
[25] T.M. Nenoff, R.J. Spontak, C.M. Aberg, Membranes for hydrogen purification: an important step toward a hydrogen-based economy, MRS Bulletin, 31 (2006) 735-744.
[26] M. Mulder, Basic principles of membrane technology, Kluwer Academic Publishers, Dordrecht, 2000.
[27] G. Grashoff, C. Pilkington, C. Corti, The purification of hydrogen, Platinum Metals Review, 27 (1983) 157-169.
[28] S. Fletcher, Thin film palladium – yttrium membranes for hydrogen separation (Ph.D Thesis), University of Birmingham, 2009.
[29] S. Tosti, L. Bettinali, S. Castelli, F. Sarto, S. Scaglione, V. Violante, Sputtered, electroless, and rolled palladium–ceramic membranes, Journal of Membrane Science, 196 (2002) 241-249.
[30] V. Starkov, A. Vyatkin, V. Volkov, H. Presting, J. Konle, U. Konig, Highly efficient to hydrogen permeability palladium membranes supported in porous silicon, Physica Status Solidi (c), 2 (2005) 3457-3460.
[31] S.-K. Ryi, J.-S. Park, S.-H. Kim, S.-H. Cho, J.-S. Park, D.-W. Kim, Development of a new porous metal support of metallic dense membrane for hydrogen separation, Journal of Membrane Science, 279 (2006) 439-445.
[32] S. Uemiya, Y. Kude, K. Sugino, N. Sato, T. Matsuda, E. Kikuchi, A palladium/porous-glass composite membrane for hydrogen separation, Chemistry Letters, 17 (1988) 1687-1690.
[33] D.-W. Lee, Y.-G. Lee, S.-E. Nam, S.-K. Ihm, K.-H. Lee, Study on the variation of morphology and separation behavior of the stainless steel supported membranes at high temperature, Journal of Membrane Science, 220 (2003) 137-153.
[34] P.P. Mardilovich, Y. She, Y.H. Ma, M.-H. Rei, Defect-free palladium membranes on porous stainless-steel support, American Institute of Chemical Engineers Journal, 44 (1998) 310-322.
[35] D.L. McKinley, Method for hydrogen separation and purification, U.S. Patent 3,439,474 (1969).
[36] D.L. McKinley, Metal alloy for hydrogen separation and purification, U.S. Patent 3,350,845 (1967).
[37] B. Howard, R. Killmeyer, K. Rothenberger, A. Cugini, B. Morreale, R. Enick, F. Bustamante, Hydrogen permeance of palladium–copper alloy membranes over a wide range of temperatures and pressures, Journal of Membrane Science, 241 (2004) 207-218.
[38] P. Kamakoti, D.S. Sholl, A comparison of hydrogen diffusivities in Pd and CuPd alloys using density functional theory, Journal of Membrane Science, 225 (2003) 145-154.

[39] J. Piper, Diffusion of hydrogen in copper-palladium alloys, Journal of Applied Physics, 37 (1966) 715-721.
[40] J. Völkl, G. Alefeld, Diffusion of hydrogen in metals, in: G. Alefeld, J. Völkl (Eds.) Hydrogen in metals I, Springer, Berlin (1978) 321-348.
[41] M.H. Martin, J. Galipaud, A. Tranchot, L. Roué, D. Guay, Measurements of hydrogen solubility in Cu_xPd_{100-x} thin films, Electrochimica Acta, 90 (2012) 615-622.
[42] T. Flanagan, D. Chisdes, Solubility of hydrogen (1 atm, 298 K) in some copper/palladium alloys, Solid State Communications, 16 (1975) 529-532.
[43] R. Burch, R. Buss, Absorption of hydrogen by palladium–copper alloys. Part 2.—Theoretical analysis, Journal of the Chemical Society, Faraday Transactions 1: Physical Chemistry in Condensed Phases, 71 (1975) 922-929.
[44] B. Morreale, M. Ciocco, B. Howard, R. Killmeyer, A. Cugini, R. Enick, Effect of hydrogen-sulfide on the hydrogen permeance of palladium–copper alloys at elevated temperatures, Journal of Membrane Science, 241 (2004) 219-224.
[45] N. Pomerantz, Y.H. Ma, Effect of H_2S on the performance and long-term stability of Pd/Cu membranes, Industrial & Engineering Chemistry Research, 48 (2009) 4030-4039.
[46] G.Q. Miller, J. Stocker, Selection of a hydrogen separation process, in: National Petrochemical Refiners Association, National Petroleum Refiners Association, San Francisco, CA, 1989.
[47] J.R. Longanbach, G.J. Steigel, M.D. Rutkowski, T.L. Buchanan, M.G. Klett, R.L. Schoff, Capital and operating cost of hydrogen production from coal gasification, National Energy Technology Laboratory, 2003 (Report DE-AM26-99FT-40465).
[48] A. Hinchliffe, K. Porter, A comparison of membrane separation and distillation, Chemical Engineering Research and Design, 78 (2000) 255-268.
[49] S.A. Steward, Review of hydrogen isotope permeability through materials, Lawrence Livermore National Laboratory, CA (USA), 1983.
[50] W. Koros, G. Fleming, Membrane-based gas separation, Journal of Membrane Science, 83 (1993) 1-80.
[51] S.C.A. Kluiters, Status review on membrane systems for hydrogen separation, Intermediate Report EU project MIGREYD NNE5-2001, 670 (2004).
[52] R.D. Noble, S.A. Stern, Membrane separations technology: principles and applications, Elsevier, Amsterdam, 1995.
[53] K. Malek, M.-O. Coppens, Knudsen self-and Fickian diffusion in rough nanoporous media, Journal of Chemical Physics, 119 (2003) 2801-2811.
[54] J.O. Hirschfelder, C.F. Curtiss, R.B. Bird, Molecular theory of gases and liquids, Wiley, New York, 1954.
[55] U. Beuscher, C.H. Gooding, Characterization of the porous support layer of composite gas permeation membranes, Journal of Membrane Science, 132 (1997) 213-227.
[56] B. Hosticka, P. Norris, J. Brenizer, C. Daitch, Gas flow through aerogels, Journal of Non-crystalline Solids, 225 (1998) 293-297.
[57] A. Kirchner, K. MacKenzie, I. Brown, T. Kemmitt, M. Bowden, Structural characterisation of heat-treated anodic alumina membranes prepared using a simplified fabrication process, Journal of Membrane Science, 287 (2007) 264-270.
[58] S. Uemiya, Brief review of steam reforming using a metal membrane reactor, Topics in Catalysis, 29 (2004) 79-84.
[59] S. Adhikari, S. Fernando, Hydrogen membrane separation techniques, Industry & Engineering Chemistry Research, 45 (2006) 875-881.

[60] T. Norby, Solid-state protonic conductors: principles, properties, progress and prospects, Solid State Ionics, 125 (1999) 1-11.
[61] T. Norby, The promise of protonics, Nature, 410 (2001) 877-878.
[62] J. Phair, S. Badwal, Review of proton conductors for hydrogen separation, Ionics, 12 (2006) 103-115.
[63] S.-J. Song, T. Lee, E. Wachsman, L. Chen, S. Dorris, U. Balachandran, Defect structure and transport properties of Ni–$SrCeO_{3-\delta}$ cermet for hydrogen separation membrane, Journal of the Electrochemical Society, 152 (2005) J125-J129.
[64] M. Schwartz, B.S. Berland, S.K. Gade, R.W. Schaller, Novel composite membranes for hydrogen separation from coal gasification streams, Abstracts of Papers of the American Chemical Society, 225, (2003) U864.
[65] R.E. Buxbaum, T.L. Marker, Hydrogen transport through non-porous membranes of palladium-coated niobium, tantalum and vanadium, Journal of Membrane Science, 85 (1993) 29-38.
[66] S.N. Paglieri, J.R. Wermer, R.E. Buxbaum, M.V. Ciocco, B.H. Howard, B.D. Morreale, Development of membranes for hydrogen separation: Pd coated V–10Pd, Energy Materials: Materials Science and Engineering for Energy Systems, 3 (2008) 169-176.
[67] J. Phair, S. Badwal, Materials for separation membranes in hydrogen and oxygen production and future power generation, Science and Technology of Advanced Materials, 7 (2006) 792-805.
[68] K. Buschow, P. Bouten, A. Miedema, Hydrides formed from intermetallic compounds of two transition metals: a special class of ternary alloys, Reports on Progress in Physics, 45 (1982) 937.
[69] T. Graham, On the absorption and dialytic separation of gases by colloid septa, Philosophical Transactions of the Royal Society of London, 156 (1866) 399-439.
[70] F. Sakamoto, Y. Kinari, F. Chen, Y. Sakamoto, Hydrogen permeation through palladium alloy membranes in mixture gases of 10% nitrogen and ammonia in the hydrogen, International Journal of Hydrogen Energy, 22 (1997) 369-375.
[71] M. Wise, J. Farr, I. Harris, X-ray studies of the α/β miscibility gaps of some palladium solid solution-hydrogen systems, Journal of the Less Common Metals, 41 (1975) 115-127.
[72] W. Huang, S.M. Opalka, D. Wang, T.B. Flanagan, Thermodynamic modelling of the Cu–Pd–H system, Calphad, 31 (2007) 315-329.
[73] H. Frieske, E. Wicke, Magnetic susceptibility and equilibrium diagram of PdH_n, Berichte der Bunsengesellschaft für Physikalische Chemie, 77 (1973) 48-52.
[74] R. Lässer, Isotope dependence of phase boundaries in the PdH, PdD, and PdT systems, Journal of Physics and Chemistry of Solids, 46 (1985) 33-37.
[75] R. Lässer, K.-H. Klatt, Solubility of hydrogen isotopes in palladium, Physical Review B, 28 (1983) 748.
[76] E. Wicke, H. Brodowsky, H. Züchner, Hydrogen in palladium and palladium alloys, in: G. Alefeld, J. Völkl (Eds.) Hydrogen in metals II: application-oriented properties, Springer, Berlin (1978) 73-155.
[77] M.D. Dolan, Non-Pd BCC alloy membranes for industrial hydrogen separation, Journal of Membrane Science, 362 (2010) 12-28.
[78] Palladium Price History [online]. Available from: http://palladiumprice.org/palladium-price-history.html [01/03/2015].

[79] F. Mazzolai, F. Lewis, Elastic energy dissipation in the palladium-silver-hydrogen (deuterium) system. I. Hydrogen-dislocation interaction effects, Journal of Physics F: Metal Physics, 15 (1985) 1249.
[80] S.N. Paglieri, J.D. Way, Innovations in palladium membrane research, Separation and Purification Methods, 31 (2002) 1-169.
[81] I. Harris, M. Norman, The electronic state of cerium in some palladium alloys, Journal of the Less Common Metals, 15 (1968) 285-298.
[82] W. Hume-Rothery, Electrons, atoms, metals and alloys, 3rd, Dover Publications, New York, 1963.
[83] O. Iyoha, R. Enick, R. Killmeyer, B. Morreale, The influence of hydrogen sulfide-to-hydrogen partial pressure ratio on the sulfidization of Pd and 70mol% Pd–Cu membranes, Journal of Membrane Science, 305 (2007) 77-92.
[84] S.M. Opalka, O.M. Løvvik, S.C. Emerson, Y. She, T.H. Vanderspurt, Electronic origins for sulfur interactions with palladium alloys for hydrogen-selective membranes, Journal of Membrane Science, 375 (2011) 96-103.
[85] G.L. Holleck, Diffusion and solubility of hydrogen in palladium and palladium-silver alloys, Journal of Physical Chemistry, 74 (1970) 503-511.
[86] R. Hurlbert, J. Konecny, Diffusion of hydrogen through palladium, The Journal of Chemical Physics, 34 (1961) 655-658.
[87] P. Kamakoti, B.D. Morreale, M.V. Ciocco, B.H. Howard, R.P. Killmeyer, A.V. Cugini, D.S. Sholl, Prediction of hydrogen flux through sulfur-tolerant binary alloy membranes, Science, 307 (2005) 569-573.
[88] H. Katsuta, R. Farraro, R. McLellan, The diffusivity of hydrogen in palladium, Acta Metallurgica, 27 (1979) 1111-1114.
[89] S.A. Koffler, J.B. Hudson, G.S. Ansell, Hydrogen permeation through alpha-palladium, Transactions of the Metallurgical Society of the American Institute of Mining, Metallurgical, and Petroleum Engineers, 245 (1969) 1735-1740.
[90] B.D. Morreale, M.V. Ciocco, R.M. Enick, B.I. Morsi, B.H. Howard, A.V. Cugini, K.S. Rothenberger, The permeability of hydrogen in bulk palladium at elevated temperatures and pressures, Journal of Membrane Science, 212 (2003) 87-97.
[91] G. Toda, Rate of permeation and diffusion coefficient of hydrogen through palladium, Journal of the Research Institute for Catalysis Hokkaido University, 6 (1958) 13-19.
[92] D. Fort, J. Farr, I. Harris, A comparison of palladium-silver and palladium-yttrium alloys as hydrogen separation membranes, Journal of the Less Common Metals, 39 (1975) 293-308.
[93] E. Serra, M. Kemali, A. Perujo, D. Ross, Hydrogen and deuterium in Pd-25 pct Ag alloy: permeation, diffusion, solubilization, and surface reaction, Metallurgical and Materials Transactions A, 29 (1998) 1023-1028.
[94] D.T. Hughes, I.R. Harris, A comparative study of hydrogen permeabilities and solubilities in some palladium solid solution alloys, Journal of the Less Common Metals, 61 (1978) P9-P21.
[95] C. Decaux, R. Ngameni, D. Solas, S. Grigoriev, P. Millet, Time and frequency domain analysis of hydrogen permeation across PdCu metallic membranes for hydrogen purification, International Journal of Hydrogen Energy, 35 (2010) 4883-4892.
[96] C. Krueger, Method of improving and optimizing the hydrogen permeability of a palladium-copper membrane and novel membranes manufactured thereby, U.S. Patent 6,372,363 B1 (2002).

[97] L. Yuan, A. Goldbach, H. Xu, Permeation hysteresis in PdCu membranes, Journal of Physical Chemistry B, 112 (2008) 12692-12695.
[98] Y. Sakamoto, F. Chen, M. Furukawa, M. Noguchi, Permeability and diffusivity of hydrogen in palladium-rich Pd-Y (Gd)-Ag ternary alloys, Journal of Alloys and Compounds, 185 (1992) 191-205.
[99] X. Ke, G.J. Kramer, O.M. Løvvik, The influence of electronic structure on hydrogen absorption in palladium alloys, Journal of Physics: Condensed Matter, 16 (2004) 6267-6277.
[100] Y. Ebisuzaki, M. O'Keeffe, The solubility of hydrogen in transition metals and alloys, Progress in Solid State Chemistry, 4 (1967) 187-211.
[101] Ö.A. Sacli, D.J. Emerson, D.F. Brewer, Rigid band behavior of platinum-vanadium alloys: Low-temperature specific heat, Journal of Low Temperature Physics, 18 (1975) 321-334.
[102] N.F. Mott, Electrons in transition metals, Advances in Physics, 13 (1964) 325-422.
[103] J. Friedel, Concept de niveau lié virtuel, Journal de Physique et Le Radium, 23 (1962) 692-700.
[104] R. Kleber, On the electronic density of states of the transition metals, Zeitschrift für Physik, 264 (1973) 301-308.
[105] F. Brouers, J.V.d. Rest, H.R. Khan, Density of states and superconductivity of vanadium-based alloys, Journal of Physics F: Metal Physics, 14 (1984) 2625-2629.
[106] R. Haydock, V. Heine, M.J. Kelly, Electronic structure based on the local atomic environment for tight-binding bands, Journal of Physics C: Solid State Physics, 5 (1972) 2845-2858.
[107] S. Komura, Y. Hamaguchi, N. Kunitomi, Experimental test of rigid band models for Cr by means of Cr-V-Mn ternary dilute alloys, Journal of the Physical Society of Japan, 23 (1967) 171-179.
[108] P. Kamakoti, D.S. Sholl, Towards first principles-based identification of ternary alloys for hydrogen purification membranes, Journal of Membrane Science, 279 (2006) 94-99.
[109] O.M. Løvvik, R.A. Olsen, Density functional calculations on hydrogen in palladium–silver alloys, Journal of Alloys and Compounds, 330–332 (2002) 332-337.
[110] A. Bhargav, G.S. Jackson, Thermokinetic modeling and parameter estimation for hydrogen permeation through $Pd_{0.77}Ag_{0.23}$ membranes, International Journal of Hydrogen Energy, 34 (2009) 5164-5173.
[111] S. Aboud, E. Ozdogan, J. Wilcox, Ab initio studies of palladium-niobium alloys for hydrogen separation, Abstracts of Papers of the American Chemical Society 237, (2009) 91.
[112] L. Semidey-Flecha, S. Hao, D.S. Sholl, Predictions of H isotope separation using crystalline and amorphous metal membranes: A computational approach, Journal of the Taiwan Institute of Chemical Engineers, 40 (2009) 246-252.
[113] S. Hao, D.S. Sholl, Comparison of first principles calculations and experiments for hydrogen permeation through amorphous ZrNi and ZrNiNb films, Journal of Membrane Science, 350 (2010) 402-409.
[114] S. Hao, D.S. Sholl, Self-diffusion and macroscopic diffusion of hydrogen in amorphous metals from first-principles calculations, Journal of Chemical Physics, 130 (2009) 244705.
[115] B. Bhatia, X. Luo, C. Sholl, D.S. Sholl, Diffusion of hydrogen in cubic Laves phase $HfTi_2H_x$, Journal of Physics: Condensed Matter, 16 (2004) 8891-8903.

[116] S.V. Alapati, J.K. Johnson, D.S. Sholl, Identification of destabilized metal hydrides for hydrogen storage using first principles calculations, Journal of Physical Chemistry B, 110 (2006) 8769-8776.
[117] S.V. Alapati, J.K. Johnson, D.S. Sholl, Stability analysis of doped materials for reversible hydrogen storage in destabilized metal hydrides, Physical Review B, 76 (2007) 104108.
[118] B. Svensson, Die magnetische Suszeptibilität der elektrolytisch aufgeladenen Palladium-Wasserstofflegierungen, Annalen der Physik, 410 (1933) 299-304.
[119] H.J. Bauer, E. Schmidbauer, Über den Einfluß elektrolytischer Wasserstoffbeladung auf die Magnetisierung von Nickel, Zeitschrift für Physik, 164 (1961) 367-373.
[120] N. Mott, H. Jones, The theory of the properties of metals and alloys, Oxford University Press, Oxford, 1936.
[121] J. Franck, Ueber den Lösungszustand des Wasserstoff im Palladium und Hydrierungskatalyse, Nachrichten von der Gesellschaft der Wissenschaften zu Göttingen, Mathematisch-Physikalische Klasse, 1933 (1933) 293-296.
[122] T.L. Ward, T. Dao, Model of hydrogen permeation behavior in palladium membranes, Journal of Membrane Science, 153 (1999) 211-231.
[123] M. Doyle, Order-Disorder solid state transformations and hydrogen solubility in a range of Pd-Y solid solution alloys (Ph.D Thesis), University of Birmingham, 1989.
[124] J. Simons, T.B. Flanagan, Effects of the electronic band shape of palladium metal on the proton model for hydrogen absorption, Canadian Journal of Chemistry, 43 (1965) 1665-1671.
[125] R. Burch, Theoretical aspects of the absorption of hydrogen by palladium and its alloys. Part 2.—Possible effects of lattice expansion on the solubility of hydrogen in palladium, Transactions of the Faraday Society, 66 (1970) 749-755.
[126] J. Fisher, Elastic interaction of interstitial atoms in body-centered cubic crystals, Acta Metallurgica, 6 (1958) 13-18.
[127] V.A. Blagojević, D.G. Minić, D.M. Minic, J.G. Novaković, Hydrogen economy: modern concepts, challenges and perspectives, in: D. Minic (Ed.) Hydrogen economy: modern concepts, challenges and perspectives, INTECH Open Access Publisher, 2012.
[128] K. Christmann, Hydrogen sorption on pure metal surfaces, in: Z. Paal, P. Menon (Eds.) Hydrogen effects in catalysis, M. Dekker, New York (1988).
[129] M. Cattania, V. Penka, R. Behm, K. Christmann, G. Ertl, Interaction of hydrogen with a palladium (110) surface, Surface Science, 126 (1983) 382-391.
[130] M. Baumberger, W. Stocker, K. Rieder, Investigations of the selective population of hydrogen subsurface sites on Pd (110) using He diffraction and thermal-desorption spectroscopy, Applied Physics A, 41 (1986) 151-156.
[131] E. Protopopoff, P. Marcus, Surface effects on hydrogen entry into metals, in: P. Marcus (Ed.) Corrosion mechanisms in theory and practice, CRC Press, Boca Raton (2011) 105-148.
[132] T. Kiriyama, T. Tanabe, Interaction of hydrogen atoms with metals, Journal of Nuclear Materials, 220 (1995) 873-877.
[133] P. Cotterill, The hydrogen embrittlement of metals, Progress in Materials Science, 9 (1961) 205-301.
[134] B. Baranowski, S. Majchrzak, T. Flanagan, The volume increase of fcc metals and alloys due to interstitial hydrogen over a wide range of hydrogen contents, Journal of Physics F: Metal Physics, 1 (1971) 258-261.

[135] A.G. Knapton, Palladium alloys for hydrogen diffusion membranes, Platinum Metals Review, 21 (1977) 44-50.
[136] H. Brodowsky, E. Poeschel, Wasserstoff in Palladium/Silber-Legierungen, Zeitschrift für Physikalische Chemie, 44 (1965) 143-159.
[137] R. Burch, R. Buss, Absorption of hydrogen by palladium–copper alloys. Part 1.—Experimental measurements, Journal of the Chemical Society, Faraday Transactions 1: Physical Chemistry in Condensed Phases, 71 (1975) 913-921.
[138] G. Zeng, A. Goldbach, H. Xu, Impact of support mass flow resistance on low-temperature H_2 permeation characteristics of a $Pd_{95}Ag_5/Al_2O_3$ composite membrane, Journal of Membrane Science, 326 (2009) 681-687.
[139] M. Yoshihara, R. McLellan, The thermodynamics of hydrogen in palladium-yttrium solid solutions, Acta Metallurgica, 36 (1988) 385-391.
[140] D. Hughes, I. Harris, A comparative study of hydrogen permeabilities and solubilities in some palladium solid solution alloys, Journal of the Less Common Metals, 61 (1978) P9-P21.
[141] O. Yoshinari, H. Matsuda, K. Fukuhara, K. Tanaka, Hydrogen diffusivity and solubility in Pd-Y alloys, Materials Transactions, 38 (1997) 508-513.
[142] M. Doyle, R.C. Wileman, I.R. Harris, Electrical resistance and hydrogen solubility anomalies in a PdY_8 at% solid solution alloy, Journal of the Less Common Metals, 130 (1987) 79-87.
[143] K.W. Kehr, Theory of the diffusion of hydrogen in metals, in: G. Alefeld, J. Völkl (Eds.) Hydrogen in metals I, Springer, Berlin (1978) 197-226.
[144] C. Wert, C. Zener, Interstitial atomic diffusion coefficients, Physical Review, 76 (1949) 1169-1175.
[145] Y. Fukai, H. Sugimoto, Diffusion of hydrogen in metals, Advances in Physics, 34 (1985) 263-326.
[146] W. Gissler, H. Rother, Theory of the quasielastic neutron scattering by hydrogen in bcc metals applying a random flight method, Physica, 50 (1970) 380-390.
[147] A. Latgé, R.M. Ribeiro-Teixeira, J. Iglesias, Binding energy of a hydrogen impurity in an fcc lattice, Solid State Communications, 52 (1984) 87-91.
[148] M. Khan, J. Parlebas, C. Demangeat, Electronic structure and ordering of hydrogen in fcc transition metals, Journal of the Less Common Metals, 77 (1981) P1-P8.
[149] K.G. McLennan, E.M. Gray, J.F. Dobson, Deuterium occupation of tetrahedral sites in palladium, Physical Review B, 78 (2008) 014104.
[150] J. Völkl, G. Alefeld, Diffusion of hydrogen in metals, in: G. Alefeld, J. Völkl (Eds.) Hydrogen in metals I, Springer, Berlin (1978) 321-348.
[151] D.S. Sholl, Using density functional theory to study hydrogen diffusion in metals: A brief overview, Journal of Alloys and Compounds, 446–447 (2007) 462-468.
[152] P.G. Sundell, G. Wahnström, Self-trapping and diffusion of hydrogen in Nb and Ta from first principles, Physical Review B, 70 (2004) 224301.
[153] M. Li, Z. Du, C. Guo, C. Li, A thermodynamic modeling of the Cu–Pd system, Calphad, 32 (2008) 439-446.
[154] P. Subramanian, D. Laughlin, Cu-Pd (copper-palladium), Journal of Phase Equilibria, 12 (1991) 231-243.
[155] H. Barlag, L. Opara, H. Züchner, Hydrogen diffusion in palladium based fcc alloys, Journal of Alloys and Compounds, 330 (2002) 434-437.
[156] R.C. Wileman, A study of the uses of some Pd alloy membranes for use in hydrogen isotope separation (Ph.D Thesis), University of Birmingham, 1987.

[157] H. Buchold, G. Sicking, E. Wicke, Hydrogen diffusion and appearance potential spectroscopy for examination of electronic structures in alloys of d-metals, Journal of the Less Common Metals, 49 (1976) 85-96.
[158] K.S. Rotherberg, B.H. Howard, R.P. Killmeyer, M.V. Ciocco, B.D. Morreale, R.M. Enick, Palladium-copper alloy membrane performance under continuous exposure, National Hydrogen Association, Washington, DC, (2005) 1-10.
[159] N. Pomerantz, Y.H. Ma, Novel method for producing high H_2 permeability Pd membranes with a thin layer of the sulfur tolerant Pd/Cu fcc phase, Journal of Membrane Science, 370 (2011) 97-108.
[160] R. Ruer, On the alloys of palladium with copper, Zeitschrift für Anorganische und Allgemeine Chemie, 51 (1906) 223-230.
[161] R. Taylor, Transformations in the copper-palladium alloys, The Journal of the Institute of Metals, 54 (1934) 255-273.
[162] F.W. Jones, C. Sykes, The transformations in the copper-palladium alloys, Journal of the Institute of Metals, 65 (1939) 419-433.
[163] V. Nemilov, A. Rudnitskii, R. Polyakova, Alloys of palladium with copper, Izvestiya Sektora Platiny i Drugikh Blagorodnykh Metallov, 24 (1949) 26-34.
[164] F. Jaumot, A. Sawatzky, An isothermal anneal study of quenched and cold-worked copper-palladium alloys, Acta Metallurgica, 4 (1956) 118-126.
[165] M. Hansen, K.P. Anderko, R.P. Elliott, Constitution of binary alloys, McGraw-Hill, New York, 1958.
[166] F. Jaumot, A. Sawatzky, Order-disorder and cold-work phenomena in Cu-Pd alloys, Physical Review, 94, (1954) 1429-1429.
[167] K. Schubert, B. Kiefer, M. Wilkens, Ordered phases with long periods in alloys, Zeitschrift für Naturforschung A, 9 (1954) 987-988.
[168] K. Schubert, B. Kiefer, M. Wilkens, R. Haufler, On some metallic ordered phases with long periods, Zeitschrift für Metallkunde, 46 (1955) 692-715.
[169] D. Watanabe, M. Hirabayashi, S. Ogawa, On the super-structure of the alloy Cu_3Pd, Acta Crystallographica, 8 (1955) 510-512.
[170] D. Watanabe, S. Ogawa, On the superstructure of the ordered alloy Cu_3Pd. 1. Electron diffraction study, Journal of the Physical Society of Japan, 11 (1956) 226-239.
[171] M. Hirabayashi, S. Ogawa, On the superstructure of the ordered alloy Cu_3Pd. II. X-ray diffraction study, Journal of the Physical Society of Japan, 12 (1957) 259-271.
[172] K. Okamura, Lattice modulation in the long period ordered alloys studied by X-ray diffraction. III. Cu_3Pd (alpha"), Journal of the Physical Society of Japan, 28 (1970) 1005-1014.
[173] A. Soutter, J. Hertz, Periodic antiphase structures of the alloy Cu_3Pd studied by X-ray diffraction in powders and electron microdiffraction in ultra-thin samples, Comptes Rendus B, 271 (1970) 378-381.
[174] A. Soutter, A. Colson, J. Hertz, Crystallographic analysis of the long-range-order phases and of the mono-periodic and bi-periodic antiphase structures in binary Cu-Pd alloys, Memoires Scientifiques de la Revue de Metallurgie, 68 (1971) 575-593.
[175] O. Terasaki, D. Watanabe, Two-dimensional antiphase structures of the 2d-Cu_3Pd type studied by high voltage, high resolution electron microscopy, Japanese Journal of Applied Physics, 20 (1981) L381-L384.
[176] T. Eguchi, Y. Tomokiyo, N. Kuwano, Configuration of antiphase domains in one-dimensional long period superstructure alloys, Transactions of the Japan Institute of Metals, 24 (1983) 369-377.

[177] R. Burch, R. Buss, Pressure-composition isotherms in the palladium-copper-hydrogen system, Solid State Communications, 15 (1974) 407-409.
[178] N. Fukumuro, M. Yokota, S. Yae, H. Matsuda, Y. Fukai, Hydrogen-induced enhancement of atomic diffusion in electrodeposited Pd films, Journal of Alloys and Compounds, 580, Supplement 1 (2013) S55-S57.
[179] T.B. Flanagan, C.-N. Park, Hydrogen-induced rearrangements in Pd-rich alloys, Journal of Alloys and Compounds, 293 (1999) 161-168.
[180] A. Goldbach, L. Yuan, H. Xu, Impact of the fcc/bcc phase transition on the homogeneity and behavior of PdCu membranes, Separation and Purification Technology, 73 (2010) 65-70.
[181] J. Shu, B. Grandjean, S. Kaliaguine, P. Ciavarella, A. Giroir-Fendler, J.A. Dalmon, Gas permeation and isobutane dehydrogenation over very thin Pd/ceramic membranes, Canadian Journal of Chemical Engineering, 75 (1997) 712-720.
[182] A. Damle, S. Gangwal, V. Venkataraman, A simple model for a water gas shift membrane reactor, Gas Separation & Purification, 8 (1994) 101-106.
[183] E. Kikuchi, Membrane reactor application to hydrogen production, Catalysis Today, 56 (2000) 97-101.
[184] S. Uemiya, N. Sato, H. Ando, T. Matsuda, E. Kikuchi, Steam reforming of methane in a hydrogen-permeable membrane reactor, Applied Catalysis, 67 (1990) 223-230.
[185] D. Edlund, A membrane reactor for H_2S decomposition, Advanced Coal-Fired Power Systems' 96 Review Meeting, Morgantown, WV, (1996) 1-9.
[186] A. Kulprathipanja, G.O. Alptekin, J.L. Falconer, J.D. Way, Pd and Pd–Cu membranes: inhibition of H_2 permeation by H_2S, Journal of Membrane Science, 254 (2005) 49-62.
[187] D.R. Alfonso, A.V. Cugini, D. Sorescu, Density functional theory study of adsorption and decomposition of H_2S on Pd (111), Cu (111), and PdCu (110), Preprints of Papers- American Chemical Society, Division of Fuel Chemistry, 48 (2003) 512-513.
[188] C.P. O'Brien, B.H. Howard, J.B. Miller, B.D. Morreale, A.J. Gellman, Inhibition of hydrogen transport through Pd and $Pd_{47}Cu_{53}$ membranes by H_2S at 350 °C, Journal of Membrane Science, 349 (2010) 380-384.
[189] D.J. Edlund, W.A. Pledger, Thermolysis of hydrogen sulfide in a metal-membrane reactor, Journal of Membrane Science, 77 (1993) 255-264.
[190] J. Milliken, Hydrogen, fuel cells and infrastructure technologies program: Multiyear research, development and demonstration plan, National Renewable Energy Laboratory (NREL), Golden, CO, 2007.
[191] V. Jayaraman, Y. Lin, Synthesis and hydrogen permeation properties of ultrathin palladium-silver alloy membranes, Journal of Membrane Science, 104 (1995) 251-262.
[192] J. Tong, Y. Matsumura, H. Suda, K. Haraya, Thin and dense Pd/CeO_2/MPSS composite membrane for hydrogen separation and steam reforming of methane, Separation and Purification Technology, 46 (2005) 1-10.
[193] J. Keuler, L. Lorenzen, S. Miachon, Preparing and testing Pd films of thickness 1–2 micrometer with high selectivity and high hydrogen permeance, Separation Science and Technology, 37 (2002) 379-401.
[194] I.P. Mardilovich, E. Engwall, Y.H. Ma, Dependence of hydrogen flux on the pore size and plating surface topology of asymmetric Pd-porous stainless steel membranes, Desalination, 144 (2002) 85-89.

[195] G. Xomeritakis, Y.S. Lin, CVD synthesis and gas permeation properties of thin palladium/alumina membranes, American Institute of Chemical Engineers Journal, 44 (1998) 174-183.
[196] O. Altinisik, M. Dogan, G. Dogu, Preparation and characterization of palladium-plated porous glass for hydrogen enrichment, Catalysis Today, 105 (2005) 641-646.
[197] R. Bhandari, Y.H. Ma, Pd–Ag membrane synthesis: the electroless and electro-plating conditions and their effect on the deposits morphology, Journal of Membrane Science, 334 (2009) 50-63.
[198] S. Yun, S. Ted Oyama, Correlations in palladium membranes for hydrogen separation: a review, Journal of Membrane Science, 375 (2011) 28-45.
[199] J. Okazaki, D.A.P. Tanaka, M.A.L. Tanco, Y. Wakui, F. Mizukami, T.M. Suzuki, Hydrogen permeability study of the thin Pd–Ag alloy membranes in the temperature range across the α–β phase transition, Journal of Membrane Science, 282 (2006) 370-374.
[200] T.-C. Huang, M.-C. Wei, H.-I. Chen, Preparation of hydrogen-permselective palladium–silver alloy composite membranes by electroless co-deposition, Separation and Purification Technology, 32 (2003) 239-245.
[201] J. Shu, B. Grandjean, E. Ghali, S. Kaliaguine, Simultaneous deposition of Pd and Ag on porous stainless steel by electroless plating, Journal of Membrane Science, 77 (1993) 181-195.
[202] J.N. Keuler, L. Lorenzen, Developing a heating procedure to optimise hydrogen permeance through Pd–Ag membranes of thickness less than 2.2 μm, Journal of Membrane Science, 195 (2002) 203-213.
[203] M.L. Bosko, D. Yepes, S. Irusta, P. Eloy, P. Ruiz, E.A. Lombardo, L.M. Cornaglia, Characterization of Pd–Ag membranes after exposure to hydrogen flux at high temperatures, Journal of Membrane Science, 306 (2007) 56-65.
[204] K. Hou, R. Hughes, The effect of external mass transfer, competitive adsorption and coking on hydrogen permeation through thin Pd/Ag membranes, Journal of Membrane Science, 206 (2002) 119-130.
[205] K. Hou, R. Hughes, Preparation of thin and highly stable Pd/Ag composite membranes and simulative analysis of transfer resistance for hydrogen separation, Journal of Membrane Science, 214 (2003) 43-55.
[206] D. Yepes, L. Cornaglia, S. Irusta, E. Lombardo, Different oxides used as diffusion barriers in composite hydrogen permeable membranes, Journal of Membrane Science, 274 (2006) 92-101.
[207] S. Uemiya, T. Matsuda, E. Kikuchi, Hydrogen permeable palladium-silver alloy membrane supported on porous ceramics, Journal of Membrane Science, 56 (1991) 315-325.
[208] Y.H. Ma, B.C. Akis, M.E. Ayturk, F. Guazzone, E.E. Engwall, I.P. Mardilovich, Characterization of intermetallic diffusion barrier and alloy formation for Pd/Cu and Pd/Ag porous stainless steel composite membranes, Industrial & Engineering Chemistry Research, 43 (2004) 2936-2945.
[209] P.M. Thoen, F. Roa, J.D. Way, High flux palladium–copper composite membranes for hydrogen separations, Desalination, 193 (2006) 224-229.
[210] H. Gao, J.Y. S. Lin, Y. Li, B. Zhang, Electroless plating synthesis, characterization and permeation properties of Pd–Cu membranes supported on ZrO_2 modified porous stainless steel, Journal of Membrane Science, 265 (2005) 142-152.

[211] F. Roa, J.D. Way, R.L. McCormick, S.N. Paglieri, Preparation and characterization of Pd–Cu composite membranes for hydrogen separation, Chemical Engineering Journal, 93 (2003) 11-22.
[212] F. Roa, J.D. Way, The effect of air exposure on palladium–copper composite membranes, Applied Surface Science, 240 (2005) 85-104.
[213] H. Honma, K. Kanemitsu, Electroless nickel plating on alumina ceramics, Plating and Surface Finishing, 74 (1987) 62-67.
[214] J. Shu, B. Grandjean, A.v. Neste, S. Kaliaguine, Catalytic palladium-based membrane reactors: A review, Canadian Journal of Chemical Engineering, 69 (1991) 1036-1060.
[215] H. Hsieh, Inorganic membranes for separation and reaction, Elsevier, Amsterdam, 1996.
[216] S.-E. Nam, K.-H. Lee, A study on the palladium/nickel composite membrane by vacuum electrodeposition, Journal of Membrane Science, 170 (2000) 91-99.
[217] J. Ye, G. Dan, Q. Yuan, The preparation of ultrathin palladium membrane, Key Engineering Materials, 61 (1992) 437-442.
[218] N. Itoh, T. Akiha, T. Sato, Preparation of thin palladium composite membrane tube by a CVD technique and its hydrogen permselectivity, Catalysis Today, 104 (2005) 231-237.
[219] G. Xomeritakis, Y. Lin, Fabrication of a thin palladium membrane supported in a porous ceramic substrate by chemical vapor deposition, Journal of Membrane Science, 120 (1996) 261-272.
[220] C.-S. Jun, K.-H. Lee, Palladium and palladium alloy composite membranes prepared by metal-organic chemical vapor deposition method (cold-wall), Journal of Membrane Science, 176 (2000) 121-130.
[221] D.M. Mattox, Handbook of physical vapor deposition (PVD) processing, Second Edition, William Andrew, Oxford, 2010.
[222] G. Xomeritakis, Y. Lin, Fabrication of thin metallic membranes by MOCVD and sputtering, Journal of Membrane Science, 133 (1997) 217-230.
[223] L. Xiong, S. Liu, L. Rong, Fabrication and characterization of Pd/$Nb_{40}Ti_{30}Ni_{30}$/Pd/porous nickel support composite membrane for hydrogen separation and purification, International Journal of Hydrogen Energy, 35 (2010) 1643-1649.
[224] B. McCool, G. Xomeritakis, Y. Lin, Composition control and hydrogen permeation characteristics of sputter deposited palladium–silver membranes, Journal of Membrane Science, 161 (1999) 67-76.
[225] J. Yang, C. Nishimura, M. Komaki, Preparation and characterization of Pd–Cu/V–15Ni composite membrane for hydrogen permeation, Journal of Alloys and Compounds, 431 (2007) 180-184.
[226] A.L. Mejdell, H. Klette, A. Ramachandran, A. Borg, R. Bredesen, Hydrogen permeation of thin, free-standing Pd/Ag23% membranes before and after heat treatment in air, Journal of Membrane Science, 307 (2008) 96-104.
[227] S.-K. Ryi, J.-S. Park, S.-H. Kim, S.-H. Cho, D.-W. Kim, K.-Y. Um, Characterization of Pd–Cu–Ni ternary alloy membrane prepared by magnetron sputtering and Cu-reflow on porous nickel support for hydrogen separation, Separation and Purification Technology, 50 (2006) 82-91.
[228] Y. Zhang, T. Ozaki, M. Komaki, C. Nishimura, Hydrogen permeation of Pd–Ag alloy coated V–15Ni composite membrane: effects of overlayer composition, Journal of Membrane Science, 224 (2003) 81-91.

[229] Y. Zhang, M. Komaki, C. Nishimura, Morphological study of supported thin Pd and Pd–25Ag membranes upon hydrogen permeation, Journal of Membrane Science, 246 (2005) 173-180.
[230] Y. Zhang, R. Maeda, M. Komaki, C. Nishimura, Hydrogen permeation and diffusion of metallic composite membranes, Journal of Membrane Science, 269 (2006) 60-65.
[231] H. Zhao, G. Xiong, N. Stroh, H. Brunner, Preparation and characterization of Pd-Ag alloy composite membrane with magnetron sputtering, Science in China Series B: Chemistry, 42 (1999) 581-588.
[232] M. Pick, M. Greene, M. Strongin, Uptake rates for hydrogen by niobium and tantalum: effect of thin metallic overlayers, Journal of the Less Common Metals, 73 (1980) 89-95.
[233] M. Dolan, S. Hara, N. Dave, K. Haraya, M. Ishitsuka, A. Ilyushechkin, K. Kita, K. McLennan, L. Morpeth, M. Mukaida, Thermal stability, glass-forming ability and hydrogen permeability of amorphous $Ni_{64}Zr_{36-x}M_x$ (M= Ti, Nb, Mo, Hf, Ta or W) membranes, Separation and Purification Technology, 65 (2009) 298-304.
[234] R.E. Buxbaum, Space group Cp2 alloys for the use and separation of hydrogen, U.S. Patent 7,323,034 (2008).
[235] S.E. Roark, R. Mackay, M.V. Mundschau, Dense, layered membranes for hydrogen separation, U.S. Patent 7,001,446 (2006).
[236] D.J. Edlund, Hydrogen-permeable composite metal membrane, U.S. Patent 5,259,870 (1992).
[237] D.J. Edlund, J. McCarthy, The relationship between intermetallic diffusion and flux decline in composite-metal membranes: implications for achieving long membrane lifetime, Journal of Membrane Science, 107 (1995) 147-153.
[238] Y. Hatano, K. Ishiyama, H. Homma, K. Watanabe, Improvement in high temperature stability of Pd coating on Nb by Nb_2C intermediate layer, International Journal of Hydrogen Energy, 32 (2007) 615-619.
[239] R.C. Dye, R.C. Snow, Thermally tolerant multilayer metal membrane, U.S. Patent 6,214,090 (2001).
[240] S. Martin, Recent advances in the study of fast ionically conducting glasses using nuclear magnetic resonance techniques, Materials Chemistry and Physics, 23 (1989) 225-265.
[241] A. Karthikeyan, C. Martindale, S.W. Martin, Preparation and characterization of new proton conducting chalcogenide glasses, Journal of Non-crystalline Solids, 349 (2004) 215-222.
[242] A. Karthikeyan, C.A. Martindale, S.W. Martin, Proton conductivity in a new class of H_2S modified thioborate-based glasses and ceramics, Solid State Ionics, 175 (2004) 655-659.
[243] Y.H. Ma, I.P. Mardilovich, E.E. Engwall, Composite gas separation modules having intermediate porous metal layers, U.S. Patent 7,175,694 (2007).
[244] M.A. Alvin, J.R. Babcock, Metal gas separation membrane, U.S. Patent 7,018,446 (2006).
[245] D.J. Edlund, Composite hydrogen separation element and module, U.S. Patent 5,498,278 (1996).
[246] J.N. Armor, Membrane catalysis: Where is it now, What needs to be done?, Catalysis Today, 25 (1995) 199-207.

[247] K. Cooke, J. Hamsphire, W. Southall, D. Teer, The industrial application of pulsed DC bias power supplies in closed field unbalanced magnetron sputter ion plating, Surface and Coatings Technology, 177 (2004) 789-794.
[248] R.C.J. Wileman, I.R. Harris, The permeability behaviour of protium and deuterium through a Pd-7.5at.%Y membrane, Journal of the Less Common Metals, 109 (1985) 367-374.
[249] L. Vegard, Die konstitution der mischkristalle und die raumfüllung der atome, Zeitschrift für Physik A Hadrons and Nuclei, 5 (1921) 17-26.
[250] B.D. Morreale, Evaluation of inorganic, hydrogen membranes at elevated temperatures and pressures (M.S. Thesis), University of Pittsburgh, 2002.
[251] A. DeRosset, Diffusion of hydrogen through palladium membranes, Industrial & Engineering Chemistry, 52 (1960) 525-528.
[252] S.K. Gade, P.M. Thoen, J.D. Way, Unsupported palladium alloy foil membranes fabricated by electroless plating, Journal of Membrane Science, 316 (2008) 112-118.
[253] S. Uemiya, N. Sato, H. Ando, E. Kikuchi, The water gas shift reaction assisted by a palladium membrane reactor, Industrial & Engineering Chemistry Research, 30 (1991) 585-589.
[254] J. Kleiner, E. Sevilla, R. Cotts, Diffusion of hydrogen in α'-VH_x, Physical Review B, 33 (1986) 6662-6666.
[255] D. Peterson, C. Jensen, Diffusion of hydrogen in niobium-tantalum alloys at 296 K, Metallurgical Transactions A, 11 (1980) 627-631.
[256] A. Pundt, R. Kirchheim, Hydrogen in metals: microstructural aspects, Annual Review of Materials Research, 36 (2006) 555-608.
[257] S.Ö. Kart, A. Erbay, H. Kılıç, T. Cagin, M. Tomak, Molecular dynamics study of Cu-Pd ordered alloys, Journal of Achievements in Materials and Manufacturing Engineering, 31 (2008) 41-46.
[258] S. Nayebossadri, J. Speight, D. Book, Effects of low Ag additions on the hydrogen permeability of Pd–Cu–Ag hydrogen separation membranes, Journal of Membrane Science, 451 (2014) 216-225.
[259] L. Yuan, A. Goldbach, H. Xu, Segregation and H_2 transport rate control in body-centered cubic PdCu membranes, Journal of Physical Chemistry B, 111 (2007) 10952-10958.
[260] P.L. Gai, B.C. Smith, Dynamic electron microscopy of copper-palladium intermetallic compound catalysts, Ultramicroscopy, 34 (1990) 17-26.
[261] S. Nakahara, J.A. Abys, S.M. Abys, Room-temperature diffusion-induced grain boundary migration in the fine-grained Pd side of Cu-Pd diffusion couples, Materials Letters, 2 (1983) 155-159.
[262] A. Zetkin, G. Kagan, A. Varaksin, E. Levin, J. Caffrey, Diffusion and penetrability of deuterium in the alloy Pd−53 at.% Cu, Soviet Physics Solid State, 34 (1992) 83-85.
[263] E. Hayashi, Y. Kurokawa, Y. Fukai, Hydrogen-induced enhancement of interdiffusion in Cu-Ni diffusion couples, Physical Review Letters, 80 (1998) 5588-5590.
[264] Y. Fukai, Formation of superabundant vacancies in M–H alloys and some of its consequences: a review, Journal of Alloys and Compounds, 356 (2003) 263-269.
[265] J.R. Davis, ASM specialty handbook: copper and copper alloys, ASM International, Materials Park, OH, 2001.
[266] J.O. Linde, The lattice constants of Cu-Pd binary alloys, Annals of Physics, 15 (1932) 249-251.

[267] F. Roa, J.D. Way, Influence of alloy composition and membrane fabrication on the pressure dependence of the hydrogen flux of palladium-copper membranes, Industrial & Engineering Chemistry Research, 42 (2003) 5827-5835.
[268] V. Jayaraman, Y. Lin, M. Pakala, R. Lin, Fabrication of ultrathin metallic membranes on ceramic supports by sputter deposition, Journal of Membrane Science, 99 (1995) 89-100.
[269] R. Merkle, J. Maier, On the Tammann–Rule, Zeitschrift für Anorganische und Allgemeine Chemie, 631 (2005) 1163-1166.
[270] Y. Kuru, M. Wohlschlögel, U. Welzel, E.J. Mittemeijer, Interdiffusion and stress development in Cu–Pd thin film diffusion couples, Thin Solid Films, 516 (2008) 7615-7626.
[271] J. Chakraborty, U. Welzel, E. Mittemeijer, Mechanisms of interdiffusion in Pd–Cu thin film diffusion couples, Thin Solid Films, 518 (2010) 2010-2020.
[272] J. Chakraborty, U. Welzel, E. Mittemeijer, Interdiffusion, phase formation, and stress development in Cu–Pd thin-film diffusion couples: Interface thermodynamics and mechanisms, Journal of Applied Physics, 103 (2008) 113512.
[273] A. Bukaluk, Influence of depth resolution on interdiffusion measurements in polycrystalline Cu/Pd multilayers, Surface and Interface Analysis, 30 (2000) 597-602.
[274] A. Bukaluk, AES studies of interdiffusion in thin-film copper–palladium multilayer structures, Vacuum, 54 (1999) 279-283.
[275] S. Holgersson, E. Sedstrom, Experimental investigation on the lattice structure of certain metallic alloys, Annalen der Physik (Leipzig), 75 (1924) 143-162.
[276] L. Graf, Kinetics and mechanism of transformation in the system palladium-copper (X-ray investigation of single crystals with 40-50 at.% Pd), Zeitschrift für Physik A Hadrons and Nuclei, 36 (1935) 489-498.
[277] A.H. Geisler, J.B. Newkirk, Ordering reaction of the Cu_4Pd alloy, Transactions of the American Institute of Mining, Metallurgical and Petroleum Engineers, 200 (1954) 1076-1082.
[278] A.A. Presnyakov, A.A. Karpenyuk, E.A. Dzhanbusinov, Features of the ordering of a dilute solid solution of palladium in copper, Trudy Instituta Yaderno Fiziki Nauk Kazakhstan SSR, 10 (1969) 45-51.
[279] E. Raub, O.L. Jr., W. Plate, H. Krill, The structure of ternary copper-nickel-palladium alloys between temperatures of 400 to 700 °C, Zeitschrift für Metallkunde, 62 (1971) 826-830.
[280] V.V. Sanadze, M.V. Dzhibuti, Study of disordering process in a copper-palladium alloy, Izvestiya Vysshikh Uchebnykh Zavedenii Fizika, 16 (1973) 51-56.
[281] K. Imakuma, Phase transformations in $Cu_{0.6}Pd_{0.4}$ alloy (Dissertation), Instituto de Energia Atomica, 1978.
[282] T.B. Massalski, H. Okamoto, P. Subramanian, L. Kacprzak, Binary alloy phase diagrams, ASM International, Materials Park, OH, 1990.
[283] V.V. Sanadze, M.V. Dzhibuti, Disordering process in a Cu-Pd alloy, Trudy Gruzii Politekhnicheskogo Instituta, 6 (1972) 70-75.